High-performance computing and numerical simulation for laser wakefield acceleration with realistic laser profiles

Imene Zemzemi

To cite this version:

Imene Zemzemi. High-performance computing and numerical simulation for laser wakefield acceleration with realistic laser profiles. Plasma Physics [physics.plasm-ph]. Institut Polytechnique de Paris, 2020. English. NNT : 2020IPPAX111 . tel-03155101

HAL Id: tel-03155101

https://tel.archives-ouvertes.fr/tel-03155101

Submitted on 1 Mar 2021

INSTITUT
POLYTECHNIQUE
DE PARIS

Laboratoire
Leprince-Ringuet

ÉCOLE
POLYTECHNIQUE

IP PARIS

NNT : 2020IPPAX111

Thèse de doctorat

High performance computing and numerical simulation for laser wakefield acceleration with realistic laser profiles

Thèse de doctorat de l'Institut Polytechnique de Paris
préparée à l'École polytechnique

École doctorale n°626 : École doctorale de l'Institut Polytechnique de Paris (EDIPP)
Spécialité de doctorat: Optique, laser et plasma

Thèse présentée et soutenue à Palaiseau, le 16 Décembre, par

IMENE ZEMZEMI

Composition du Jury :

Jean-Luc Vay Directeur de recherche, LBNL, Berkeley	Président
Gilles Maynard Directeur de recherche CNRS, LPGP, Orsay	Rapporteur
Emmanuel d'Humières Professeur, Université de Bordeaux/CELIA, Bordeaux	Rapporteur
Rachel Nuter Ingénieure-chercheuse CEA, CELIA, Bordeaux	Examinatrice
Xavier Davoine Ingénieur-chercheur, CEA DAM, Bruyères-le-châtel	Examinateur
Arnaud Beck Ingénieur de recherche CNRS, LLR, Palaiseau	Directeur de thèse

Acknowledgements

The last three years that I spent working on this thesis were very enriching, yet challenging. I would like to thank those who stood by me and helped me through this journey.

Firstly, I would like to dedicate this work and the success that I have achieved so far to the one and only, my beloved father. He believed in me and raised me to be the strong and independent woman I have become today. I wish he was here for me to witness my defense and be proud of me. May his soul rest in peace!

I am thankful to the people from my laboratory who contributed to making this work possible. In particular, I am grateful to my Ph.D. advisor for his guidance and for the freedom he granted me. I would like to also thank Arnd Specka and Francesco Massimo for the insightful discussions throughout my thesis, Andrea Sartirana for his reactivity to solve the problems related to computational resources, Michel Lastes and Michael Mellin for providing me with the materials I needed for my work, and Philippe Bruel for the numerous discussions around the lunch table. Finally, I would like to thank the head of our laboratory Yves Sirois and the administration staff: Marie Thérèse Teordora, Alimata Bagayoko and Michel Hoarau for ensuring a good working environment. I am also thankful for the other Ph.D. students and post-doctoral researchers from my laboratory for sharing advice and experiences during these 3 years.

I am extremely grateful to Gilles Maynard and Emmanuel d'Humières for thoroughly reviewing my manuscript and to Jean-Luc Vay, Rachel Nuter and Xavier Davoine as well for being part of my Ph.D. defense jury and for their very interesting questions and remarks. I am also thankful for everyone who attended virtually the defense and congratulated me for my success, despite the special circumstances related to Covid-19 that did not allow for an in-person presence.

I wish to express my gratitude to Jean-Luc Vay for hosting me in his Accelerator Modeling Program and sponsoring our collaboration on developing the spectral solver in PICSAR library during my visit to LBNL. In this regard, I am thankful to Remi Lehe for the fruitful discussions around the implementation and to Haithem Kallala for introducing me to PICSAR environment. I would like also to thank Jaehong Park, Maxence Thévenet and Olga Shapoval for making my stay pleasant scientifically and culturally.

I would like also to thank the experimenters who are working on the Apollon laser for providing me with the experimental data and the laser measurements that I used for my numerical study on the impact of the laser imperfections in laser wakefield acceleration, in particular Dimitris Papadopoulos and Mélanie Chabanis.

Finally, I am grateful for my mom Aljia Ltaief and my sisters Amal and Intissar for their unconditional support during these three years, and throughout the path that led to it. I would like to thank my friends who encouraged me, in particular Hajer for being there when I needed someone to talk to. Last but not least, I would like to express my warmest thanks to my partner Haithem for standing by me through the good and the bad moments. Although he was busy with his own thesis, he contributed to this achievement in many ways from encouragement and support to technical discussions about the core of my thesis subject.

Contents

Introduction **1**

Chapter 1 Physics of laser-wakefield acceleration **5**

1.1 UHI laser 7
  1.1.1 Gaussian beam formalism 8
1.2 Plasma 12
  1.2.1 Plasma parameters 12
  1.2.2 Electromagnetic waves propagation in a plasma 12
  1.2.3 Kinetic description of plasmas 14
  1.2.4 Fluid description of plasmas 15
1.3 Wakefield generation by a laser pulse 15
  1.3.1 Ponderomotive force 15
  1.3.2 Plasma waves driven by a laser pulse 16
1.4 Regimes of plasma wave excitation 17
  1.4.1 Linear regime 18
  1.4.2 Non-linear regime 22
1.5 Laser-wakefield acceleration 27
  1.5.1 Electrons trapping 27
  1.5.2 Electrons injection schemes 29
  1.5.3 Laser propagation and modulation in plasma 32
  1.5.4 Limits of acceleration 34
  1.5.5 Properties of the accelerated electron bunch 36

Chapter 2 Numerical modeling and simulation tools for laser-wakefield acceleration **43**

2.1 Numerical resolution of Maxwell-Vlasov system 44
  2.1.1 Overview of numerical methods 44
  2.1.2 Particle-In-Cell method 44
2.2 Overview of the Particle-In-Cell algorithm 46

2.2.1 Particle dynamics . . . 46
2.2.2 Yee method . . . 48
2.2.3 The PIC cycle . . . 50
2.3 The PIC code Smilei . . . 55
2.3.1 Parallelization strategy of the PIC algorithm with the FDTD scheme . . 55
Chapter 3 Azimuthal Fourier decomposition in cylindrical geomerty 61
3.1 Theory and mathematical derivation of azimuthal Fourier field decomposition . . 63
3.1.1 Maxwell's equations in azimuthal geometry . . . 65
3.2 FDTD scheme . . . 65
3.2.1 Discretized Maxwell equations in the Yee grid . . . 66
3.2.2 On axis condition . . . 66
3.2.3 Boundary conditions . . . 71
3.2.4 Esirkepov algorithm for charge conserving current deposition . . . 75
3.2.5 Interpolation . . . 77
3.2.6 Numerical dispersion relation and stability condition for FDTD . . . 78
3.2.7 limits of the FDTD . . . 81
3.3 Pseudo Spectral Analytical Time Domain scheme . . . 82
3.3.1 Spectral Cartesian representation . . . 83
3.3.2 Spectral quasi-cylindrical representation . . . 84
3.3.3 Overview of the quasi-cylindrical spectral algorithm . . . 85
3.4 Parallelization strategy of the PIC algorithm with the PSATD scheme . . . 91
3.4.1 Domain decomposition and parallelization of the PSATD solver . . . 91
3.4.2 Single domain multiple decompositions (SDMD) . . . 92
3.5 Advantages of PSATD . . . 93
3.5.1 Comparison between FDTD and PSATD schemes . . . 94
3.5.2 Discussion . . . 95
Chapter 4 High fidelity simulations using realistic Apollon laser profile 99
4.1 Propagation using Fresnel integration . . . 101
4.2 Study on the presence of a hole in the laser's near-field with a theoretical fit . . . 103
4.2.1 Laser profile fitting with super-Gaussians in the near-field . . . 105
4.2.2 Choice of the laser profiles . . . 107
4.2.3 Results and discussion . . . 109
4.2.4 Conclusions . . . 119
4.3 Influence of experimental laser imperfections on laser wakefield acceleration . . . 119
4.3.1 Motivation . . . 119

4.3.2 Effect of realistic laser profiles on 3D Cartesian simulations 120
4.3.3 Effect of realistic laser profiles on quasi-cylindrical simulations 128

Conclusion **147**

Appendixs **151**

Appendix A Theory of plasma waves excitation by a laser pulse **151**

Appendix B Comoving coordinates **155**

Appendix C One dimensional model of plasma waves excitation theory in the case of a laser pulse driver **157**

Introduction

Context

Plasma-based accelerator: an alternative to the conventional accelerator

The continuous upgrade in laser technology has permitted the investigation of a wide range of applications related to laser-matter interaction. In this context, Laser WakeField Acceleration (LWFA)[Tajima and Dawson, 1979][Esarey et al., 2009] [Malka et al., 2002] has been proven to be a promising and efficient path for producing high energy electron beams.

When an ultra-short ultra-intense laser pulse propagates trough an under-dense plasma, a large amplitude plasma wave is excited, in which electrons can be trapped and accelerated to relativistic energies over very short distances of the order of few millimeters. These plasma waves support very high accelerating gradients of 100 GeV/m, which is three orders of magnitude higher than the maximum field in conventional radio-frequency accelerators. As a result, LWFA paved the way to interesting prospects towards more compact accelerators. The plasma wave generation is the result of the laser ponderomotive force, which perturbs locally the plasma density by pushing radially outward the electrons from the intense region of the laser pulse while keeping the background-plasma ions practically immobile thus creating charge separation. The space charge force of the ions recalls the electrons back, hence forming the wake.

With the currently available laser powers, it became possible to achieve a complete ponderomotive blowout of the electrons which are completely expelled thus forming an ion cavity surrounded by a thin electrons sheath behind the laser pulse. This so-called bubble regime [Pukhov and Meyer-ter Vehn, 2002; Rosenzweig et al., 1991a; Lu et al., 2007a] is characterized by its nonlinear plasma waves created by an intense laser with a spot size comparable to the wake's wavelength. Nowadays, most of the LWFA experiments are operating in the bubble regime in which the highest acceleration gradients are reached. This regime is particularly interesting thanks to its linear focusing forces that do not vary in the longitudinal direction and its accelerating forces that are independent of the transverse coordinates. Therefore, it ensures a quite stable propagation of low phase-space-volume electron bunches over several Rayleigh lengths.

Over the past two decades, LWFA has witnessed a significant progress thanks to the development of the laser technique called Chirped Pulse Amplification (CPA). Particularly, in 2004 the field has reached a major milestone with the experimental demonstration of the first quasi-monoenergetic beam in three groups from the UK [Mangles et al., 2004a], USA [Geddes et al., 2004a] and France [Faure et al., 2004a]. These ~ 100 MeV electron beams were produced by ~ 10 TW lasers in ~ 1 mm plasmas of densities $n_0 \sim 10^{19}$ cm^{-3}. Subsequently, the observation of the first beam beyond 1 GeV was reported in [Leemans et al., 2006]. A sea change in the field of laser plasma acceleration has occurred with the success in constructing petawatt class lasers that allow to reach unprecedented electron energies of few GeVs [Kim et al., 2013; Wang et al., 2013; Leemans et al., 2014]. The latest record in this race is the production of a 7.8 GeV electron beam [Gonsalves et al., 2019] by guiding a 0.85 PW laser over 20 cm-long capillary of $n_0 = 3.410^{17} \times cm^{-3}$.

These laser-driven electron sources are of great interest because the generated electron bunches have a very short duration reaching down to few femtoseconds only, a small transverse size, and a high peak intensity. The tremendous progress in LWFA opens up the way to several practical applications such as high-resolution gamma radiography [Ben-Ismail et al., 2011] in material science, cancer treatment [Glinec et al., 2006] in medicine, phase-contrast imaging [Fourmaux et al., 2011] in biology. Moreover, the use of laser plasma accelerators as potential future light sources is identified by the scientific community. In particular, LWFA is a promising technique to develop compact and affordable synchrotrons and free-electron lasers.

Numerical modeling and the role of simulations in plasma based accelerators research

Theory and experiments play a complementary role: from the observations we make and the understanding we develop to the problem, we create an analytical model and we derive equations from fundamental physics that describe the observed phenomena to the best of our knowledge. Then, by its implications, the accuracy and the precision of this model are verified when compared to the results from experience. The consistency or deviancy of its estimation from the measured results will guide us to review the assumptions made for this model in order to enhance it. If the model prediction does not agree with a measured result then either the theory that gave rise to the prediction, or the manner in which the prediction was inferred from the theory has to be modified. Thereby creating a loop of mutual influence and control based on reciprocal feedback: it's what we call a scientific method.

In some cases, the system we are studying is very complicated and the processes that are involved are highly non linear and it is hard to break it into a simple practically usable set of governing equations that can be solved directly. It is the case for example in plasma physics where the governing equations of Maxwell-Vlasov do not have an explicit analytical solution except under some specific statements and assumptions that can not be generalized in the case of most applications. With numerical models, we can use a multitude of methods ranging from numerical analysis to linear algebra to approximate the solutions of these equations. Therefore numerical modeling, which is a mathematical representation of a physical behavior, based on relevant hypothesis and simplifying assumptions [Sirois and Grilli, 2015], plays a crucial role to bridge this gap. It is often considered as an intermediate branch between theoretical and experimental physics.

In plasma physics, numerical modeling is a widely adopted technique to tackle complex problems with computational simulations of physical scenarios. In particular, the understanding and developing of LWFA relies on the strong coupling between experiments and numerical modeling. In order to investigate the different experimental set-ups and to determine the optimal parameters to achieve this goal, simulation is the key to perform a parametric scan and analyze regimes that haven't been explored yet.

Particle-In-Cell codes

That one may model correctly the interaction between the laser and the plasma, a full kinetic description of the plasma is needed. Particle-in-Cell algorithm is ubiquitously used as an established tool that solves Vlasov equation for the different species presented in the plasma coupled with Maxwell's equations. It is a powerful method that gives an accurate description of the plasma response to the laser and captures a wide range of physical phenomena [Birdsall and Langdon, 2004]. Nevertheless, precise and realistic results are obtained only with full 3D descriptions and high resolutions. Even though 2D simulations are used in the context of 2D Cartesian slab or in the cylindrical geometry r-z to illuminate the physics, there is a qualitative and quantitative difference with the 3D simulations especially in the case of LWFA when studying non linear regime. This is mainly because self focus and self modulation of the phase are not well described by a 2D simulation [Davoine et al., 2008]. In spite of the necessity of using well resolved 3D simulations for the accurate description, this type of simulations is computationally very expensive and pushes the existent computing resources, available nowadays, to the limit in order to have the simulation results in a reasonable amount of time. Therefore, there have been many methods suggested to overcome this obstacle among which we mention the moving window, the quasi-static approximation [Mora and Antonsen, 1997], the ponderomative guiding center or envelope description [Benedetti et al., 2010, 2017] and the boosted frame [Vay, 2007].

Azimuthal Fourier field decomposition

A particularly interesting method that leverages the azimuthale symmetry of the LWFA, is the Fourier field decomposition in cylindrical geometry [Lifschitz et al., 2009]. It combines an accurate modeling of the physics at stake and a significant speed-up. In fact, with a cylindrically symmetric laser envelope like a Gaussian one, the laser pulse is fully described by the azimuthal mode 1 and the wakefield is described by the azimuthal mode 0. Therefore, the cost of the simulation is roughly 2 times the cost of a 2D simulation.

Realistic lasers in simulations

So far, most of the simulations have dealt with Gaussian or Laguerre-Gaussian laser pulses. However, realistic lasers have a more complicated asymmetric structure due to the imperfections in the laser system thus leading to aberrations in the intensity and wave front profiles. Presently, the highest acceleration gradients are achieved in the bubble regime with the self-injection scheme. However, self-injection process is very sensitive to shot-to-shot fluctuations and to the laser's condition [Beaurepaire et al., 2015; Ferri et al., 2016] . In order to realize practical devices based on LWFA, it is crucial to understand the system sensitivity to the laser aberrations and their implications on the performance of the accelerator.

Objectives and outline

In this context, the objective of this thesis consists in two parts: on the one hand, I implemented the Fourier field decomposition method in cylindrical geometry with finite differences and pseudo-spectral schemes in the PIC code Smilei. On the other hand, I studied the impact of laser aberrations on the electrons acceleration and the quality of the injected bunch via 3D numerical simulations with realistic laser profiles measured from the Apollon facility. The simulations are then reproduced in the quasi-cylindrical geometry, after determining the optimal number of azimuthal modes required to correctly model the laser. The importance of including higher modes in such simulations is evaluated by varying the number of modes and analyzing the differences. The reliability of the algorithm in this case is analyzed by comparing the results of simulations run with different number of modes with the ones from 3D Cartesian simulations. The manuscript is organized as follows:

Chapter 1 introduces some of the main theoretical concepts of the underlying physics in laser wakefield acceleration that are used later throughout the thesis. Figures of merit used to quantify the quality of the electron bunches are also presented.

Chapter 2 describes the numerical modeling tools for laser-wakefield acceleration simulations. It sums up the principle of PIC method and its features in the framework of Smilei code.

Chapter 3 details the implementation of the Fourier field decomposition method in cylindrical geometry with finite differences in Smilei and highlights the limits of this discretization scheme. It also presents the implementation of this method with the pseudo-spectral scheme in PICSAR library and explains the parallelization technique that enables the coupling of the library with the Smilei code.

Finally, chapter 4 is dedicated to the study of the effect of experimental laser imperfections on laser wakefield acceleration and the quality of the generated electron bunches using 3D and quasi-cylindrical geometries. In particular, it analyzes the impact of including higher modes in quasi-cylindrical geometry and emphasizes the importance of using experimentally measured laser profiles to accurately model the experiments.

Chapter 1

Physics of laser-wakefield acceleration

The development of shorter, more powerful lasers thanks to novel technologies such as the Chirped Pulse Amplification (CPA) [Strickland and Mourou, 1985], has been spurring an increasing interest in related research work. In particular, it allowed a breakthrough in Laser Wakefield Acceleration (LWFA) where the achievement of high acceleration gradients on the order of 100 GeV/m became possible. Therefore, it paved the way to interesting prospects towards more compact and cost-efficient plasma-based accelerators.

The intent of this chapter is to introduce some important theories and concepts pertaining to LWFA which will be used throughout the rest of this dissertation. Sections 1.1 and 1.2, introduce the basic field equations and approximations which are used to describe respectively the laser and the plasma. In section 1.3, the properties of linear and nonlinear plasma waves are discussed. In section 1.5, methods for injection and trapping electrons in plasma waves are reviewed. Basic physics of laser pulse evolution in underdense plasmas is summarized such as the propagation, and self-focusing of the laser pulse. Limits to the electron energy gain are outlined, including laser pulse diffraction, electron dephasing, laser pulse energy depletion, and beam loading limitations. Finally, the emittance of the accelerated beam is defined and the principal sources of its degradation are presented.

Contents

1.1 UHI laser 7
  - 1.1.1 Gaussian beam formalism 8

1.2 Plasma 12
  - 1.2.1 Plasma parameters 12
  - 1.2.2 Electromagnetic waves propagation in a plasma 12
  - 1.2.3 Kinetic description of plasmas 14
  - 1.2.4 Fluid description of plasmas 15

1.3 Wakefield generation by a laser pulse 15
  - 1.3.1 Ponderomotive force 15
  - 1.3.2 Plasma waves driven by a laser pulse 16

1.4 Regimes of plasma wave excitation 17
  - 1.4.1 Linear regime 18
  - 1.4.2 Non-linear regime 22

1.5 Laser-wakefield acceleration 27
  - 1.5.1 Electrons trapping 27

1.5.2 Electrons injection schemes 29
1.5.3 Laser propagation and modulation in plasma 32
1.5.4 Limits of acceleration 34
1.5.5 Properties of the accelerated electron bunch 36

1.1 UHI laser

Laser pulses used in LWFA are characterized by a very short duration ($\sim 15 - 30$ fs) which allows to achieve high powers (TW-PW) with relatively low energies ($\sim 1-10$ J). In this section, we will try to briefly summarize the baseline of the mathematical description of an ultra-short laser pulse.

A laser pulse is an electromagnetic wave characterized by its electric field $\boldsymbol{E}$ and magnetic field $\boldsymbol{B}$. The propagation of the laser pulse is governed by Maxwell's equations:

$$\boldsymbol{\nabla} \times \boldsymbol{E}(\boldsymbol{x}, t) = -\frac{\partial \boldsymbol{B}(\boldsymbol{x}, t)}{\partial t} \tag{1.1}$$

$$\boldsymbol{\nabla} \times \boldsymbol{B}(\boldsymbol{x}, t) = \mu_0 \, \boldsymbol{J}(\boldsymbol{x}, t) + \frac{1}{c^2}\frac{\partial \boldsymbol{E}(\boldsymbol{x}, t)}{\partial t} \tag{1.2}$$

$$\boldsymbol{\nabla} \cdot \boldsymbol{E}(\boldsymbol{x}, t) = \frac{\rho(\boldsymbol{x}, t)}{\epsilon_0} \tag{1.3}$$

$$\boldsymbol{\nabla} \cdot \boldsymbol{B}(\boldsymbol{x}, t) = 0 \tag{1.4}$$

Where ρ, $\boldsymbol{J}$ are respectively the charge and current densities of the medium (in vacuum $\rho = 0$ and $\boldsymbol{J} = 0$), μ_0 and ϵ_0 are the permittivity and permeability of vacuum. c is the speed of light.

An alternative but equivalent way to write Maxwell's equations is the potential formalism where the calculation of the electric and magnetic fields is based on the associated scalar electric potential ϕ and vector magnetic potential $\boldsymbol{A}$:

$$\boldsymbol{E}(\boldsymbol{x}, t) = -\frac{\partial \boldsymbol{A}(\boldsymbol{x}, t)}{\partial t} - \boldsymbol{\nabla}\Phi \tag{1.5}$$

$$\boldsymbol{B}(\boldsymbol{x}, t) = \boldsymbol{\nabla} \times \boldsymbol{A} \tag{1.6}$$

These relations can be substituted into Maxwell's equations to express the latter in terms of the potentials.

$$\boldsymbol{\nabla}^2\Phi + \frac{\partial}{\partial t}(\boldsymbol{\nabla} \cdot \boldsymbol{A}) = -\,\frac{\rho}{\epsilon_0} \tag{1.7}$$

$$\left(\boldsymbol{\nabla}^2\boldsymbol{A} - \frac{1}{c^2}\frac{\partial^2 \boldsymbol{A}}{\partial t^2}\right) - \boldsymbol{\nabla}\left(\boldsymbol{\nabla} \cdot \boldsymbol{A} + \frac{1}{c^2}\frac{\partial \Phi}{\partial t}\right) = -\,\mu_0\boldsymbol{J} \tag{1.8}$$

These potentials are not described uniquely i.e for any choice of a twice-differentiable scalar function of position and time λ, if $(\Phi, \boldsymbol{A})$ is a solution then $(\Phi', \boldsymbol{A}')$ is also a solution given that it verifies :

$$\Phi' = \Phi - \frac{\partial \lambda}{\partial t}$$

$$\boldsymbol{A}' = \boldsymbol{A} + \boldsymbol{\nabla}\lambda$$

In the Lorenz gauge $\boldsymbol{\nabla} \cdot \boldsymbol{A} + \frac{1}{c^2}\frac{\partial \Phi}{\partial t} = 0$, the potentials solve the following equations:

$$\left(\boldsymbol{\nabla}^2 - \frac{1}{c^2}\frac{\partial^2}{\partial t^2}\right)\boldsymbol{A} = -\mu_0\boldsymbol{J} \tag{1.9}$$

$$\left(\boldsymbol{\nabla}^2 - \frac{1}{c^2}\frac{\partial^2}{\partial t^2}\right)\Phi = -\frac{1}{\epsilon_0}\rho \tag{1.10}$$

In the Coulomb gauge, we impose $\nabla \cdot \boldsymbol{A} = 0$. By combining (1.5) and (1.3), we obtain : $\frac{\partial \nabla \cdot \boldsymbol{A}}{\partial t} - \Delta\Phi = \frac{\rho}{\epsilon_0}$. Together with Coulomb gauge , we can find Poisson equation:

$$\Delta\Phi = -\frac{\rho}{\epsilon_0} \tag{1.11}$$

1.1.1 Gaussian beam formalism

Gaussian beam formalism [Siegman, 1986] constitutes a simplified analytical description of beams propagation and a keystone to develop models of laser-plasma interactions. The subsequent derivation follows the one presented in [Kallala, 2020].

From Maxwell equations 1.2 and 1.1, one can derive the wave equation in vacuum. We assume in the following a linearly-polarized laser propagating in the z direction which can be completely characterized by its transverse electric component $E_\perp(x, y, z, t)$. Therefore, it propagates in vacuum according to the following equation:

$$\Delta E_\perp - \frac{\partial^2}{c^2 \partial t^2} E_\perp = 0 \tag{1.12}$$

We consider a laser pulse with a wave length λ_0 propagating dominantly in the longitudinal z-direction and that solutions to eq. (1.12) are of the general form:

$$E_\perp(x, y, z, t) = E_0(x, y, z, t)\exp(ik_0 z - i\omega_0 t) \tag{1.13}$$

where $k_0 = \omega_0/c$ is the wave number, $\omega_0 = 2\pi c/\lambda_0$ is the angular frequency and $E_0(x, y, z, t)$ is the spatio-temporal envelope. By replacing the laser expression (1.13) in the propagation equation (1.12), we obtain the following PDE for E_0:

$$\Delta E_0 - k_0^2 E_0 + 2ik_0\frac{\partial E_0}{\partial z} - \frac{1}{c^2}\left(\frac{\partial^2 E_0}{\partial t^2} - \omega_0^2 E_0 - 2i\omega_0\frac{\partial E_0}{\partial t}\right) = 0 \tag{1.14}$$

The *slowly varying envelope approximation* assumes that the electric field envelope amplitude E_0 varies slowly with both z and t variables. As a result, when taking derivatives, the highest-order derivatives in the z-direction and time may be neglected. Precisely, the approximation reads:

$$\left|\frac{\partial^2 E_0}{\partial^2 z}\right| \ll \left|k_0 \frac{\partial E_0}{\partial z}\right| \tag{1.15}$$

$$\left|\frac{\partial^2 E_0}{\partial^2 t}\right| \ll \left|\omega_0 \frac{\partial E_0}{\partial t}\right| \tag{1.16}$$

The previous expanded propagation equation (1.14) is reduced to the following parabolic wave equation:

$$k_0\left(\frac{\partial E_0}{\partial z} + \frac{\partial E_0}{c\partial t}\right) - \frac{i}{2}\Delta_\perp E_0 = 0 \tag{1.17}$$

where $\Delta_\perp = \frac{\partial^2}{\partial x^2} + \frac{\partial^2}{\partial y^2}$ is the transverse Laplace operator. Admissible solutions to equation (1.17) can be expressed in the form of the product of a transverse spatial envelope $f(x, y, z)$ and a temporal envelope $g(z, t)$ of the electric field:

$$E_0(x, y, z, t) = f(x, y, z)g(z, t)$$

When replacing the latter electric field expression in the parabolic wave equation (1.17), we obtain:

$$k_0 \left(\frac{\partial f}{\partial z} g + f \frac{\partial g}{\partial z} + \frac{1}{c} f \frac{\partial g}{\partial t} \right) - g \frac{i}{2} \Delta_\perp f = 0 \tag{1.18}$$

$$g \left(k_0 \frac{\partial f}{\partial z} - \frac{i}{2} \Delta_\perp f \right) + k_0 f \left(\frac{\partial g}{\partial z} + \frac{1}{c} \frac{\partial g}{\partial t} \right) = 0 \tag{1.19}$$

$$\Longrightarrow \left\{ \begin{array}{l} k_0 \frac{\partial f}{\partial z} - \frac{i}{2} \Delta_\perp f = 0 \\ \frac{\partial g}{\partial z} + \frac{1}{c} \frac{\partial g}{\partial t} = 0 \end{array} \right. \tag{1.20}$$

The first equation in 1.20 represents the Helmoltz equation under the paraxial approximation. Gaussian beam is among valid solutions to this equation.

$$f(x, y, z) = \frac{w_0}{w(z)} exp \left[- \frac{(x^2 + y^2)}{w(z)^2} \right] exp \left[-ik_0 \frac{(x^2 + y^2)}{2R(z)} - i\phi_0 \right] \tag{1.21}$$

We define the following terms involved in the previous expression (see fig. 1.1):

- $w(z) = w_0 \sqrt{1 + (z/Z_r)^2}$ is the laser radius at the position z.
- w_0 is the laser waist. It is the minimum value of the laser radius w which is reached in the focal plane.
- $Z_r = \pi w_0^2 / \lambda_0$ the laser Rayleigh length. This physical parameter represents the length where the laser intensity on axis drops by a factor 2 compared to the intensity in the focal plane ($z = 0$). This is also the distance over which the phase fronts are approximately flat.
- $R(z) = z[1 + (Z_r/z)^2]$ the laser radius of curvature. It is infinite in the focal plane.
- $\phi_0 = \arctan(z/Zr)$ is the Gouy phase which shifts of π when a Gaussian beam goes through a focus (from the far field to the far field on the other side of the focus).

We can also define the laser beam divergence θ, which represents the angle covered by the laser cone of the light far from the laser focus:

$$\tan \theta = \lim_{z \to +\infty} \frac{\omega(z)}{z} \tag{1.22}$$

The second equation in the system 1.20 is simply an homogeneous transport equation whose solutions are given by:

$$g(z, t) = g(z - ct, t = 0) \tag{1.23}$$

A possible representation of g is a Gaussian temporal envelope:

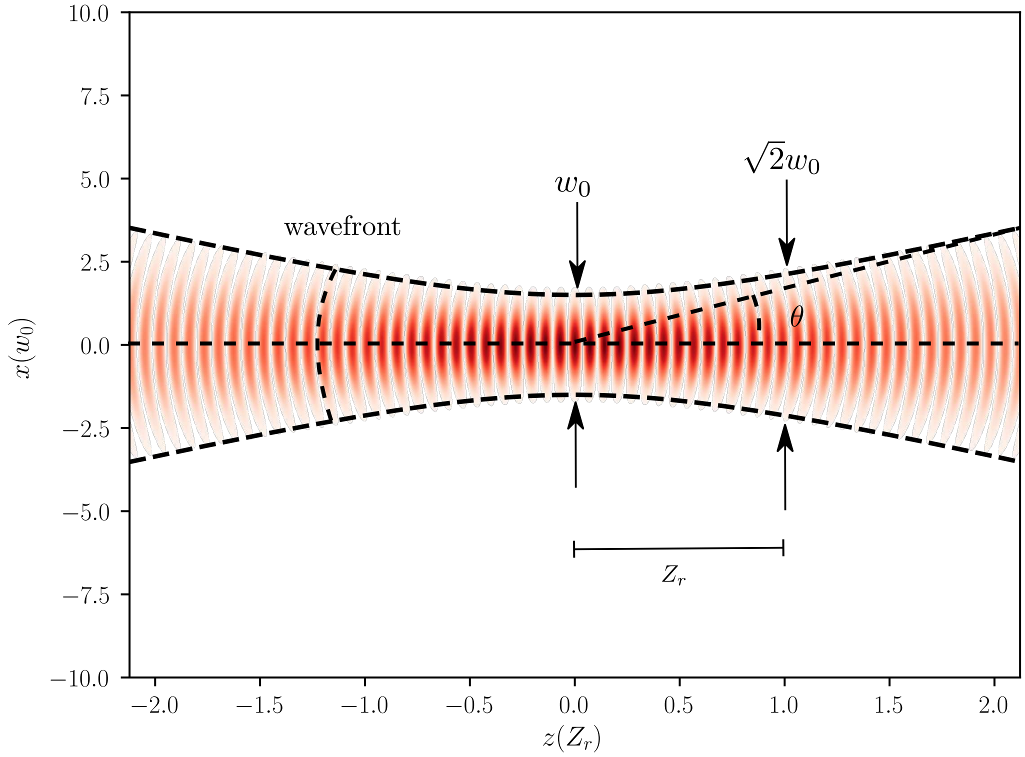

Figure 1.1: Evolution of the Gaussian beam radius $w(z)$ as a function of the propagation distance z in vacuum. $z = 0$ is the focal plan, where the beam has its minimum spot size w_0. After propagating to a distance of one Rayleigh length Z_r away from the focal plan, the spot size increases to $\sqrt{2}w_0$.

$$g(z,t) = E_{max} \exp\left[-\left(\frac{t - z/c}{\tau_0}\right)^2\right] \tag{1.24}$$

where E_{max} is the laser maximum amplitude and τ_0 is the temporal laser duration.

The slowly varying envelope approximation in time requires that the laser duration τ_0 to be larger than the laser period $T_0 = 2\pi/\omega_0$ ($\tau_0 \gg T_0$). The laser intensity full width at half maximum: $\text{FWHM}_{\text{I}} = \sqrt{2\log(2)}\tau_0 = 1.177\tau_0$ is often used to characterize the temporal duration of ultra-short lasers. The intensity I of a linearly-polarized laser pulse can be introduced as the average of the Poynting vector in vacuum $\boldsymbol{S} = c^2\epsilon_0 \boldsymbol{E} \wedge \boldsymbol{B}$ over a laser period T_0.

$$I = \langle |S| \rangle_{T_0} = \frac{c\epsilon_0}{2}|E_0|^2 \tag{1.25}$$

where brackets designate the temporal average over a laser period $\langle |S| \rangle_{T_0} = \frac{1}{T}\int_{-T_0/2}^{T_0/2} |S| dt$.

Therefore, we can deduce the expression of the intensity for a Gaussian laser beam:

$$I(x,y,z,t) = I_0 \frac{w_0^2}{w(z)^2} \exp\left[-2\frac{(x^2+y^2)}{w(z)^2}\right] \exp\left[-2\left(\frac{(t-z/c)}{\tau_0}\right)^2\right] \quad \text{where} \quad I_0 = \frac{\epsilon_0 c}{2} E_{max} \tag{1.26}$$

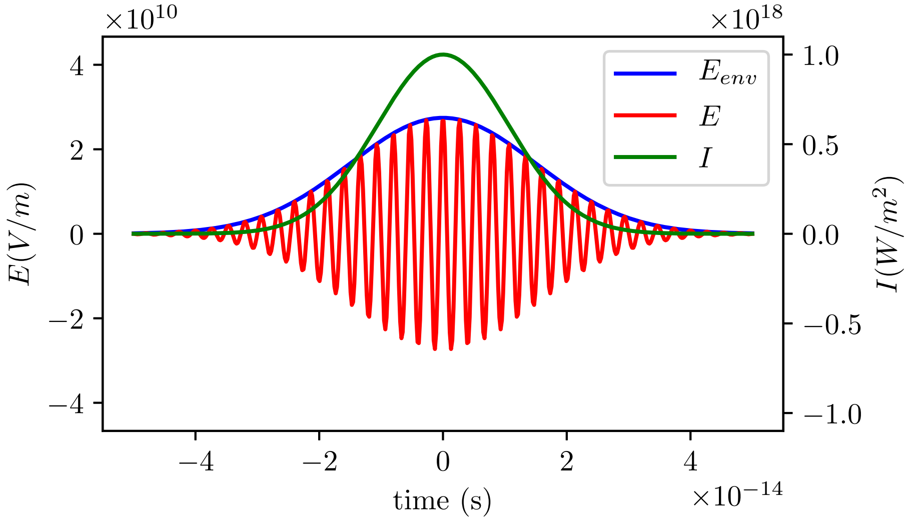

Figure 1.2: The intensity profile I and the related electric field E and its temporal envelope E_{env} of a laser pulse with a wavelength $\lambda_0 = 0.8\mu m$, and duration $\tau_0 = 25 fs$.

The quantities usually measured during experiments are the laser energy U and its distribution in space, and the pulse duration τ_0. They are used to evaluate the laser intensity, which is a key parameter for laser plasma interaction. The laser peak power for a Gaussian pulse in time is written as :

$$P = 2\sqrt{\frac{2}{\pi}} \frac{ln(2)U}{\tau_0} \simeq \frac{U}{\tau_0} \tag{1.27}$$

And the corresponding peak laser intensity of a laser with a Gaussian transverse envelope in the focal plane is:

$$I_0 = \frac{2P}{\pi w_0^2} \simeq \frac{2U}{\pi \tau_0 w_0^2} \tag{1.28}$$

It is useful to define the normalized vector potential $\boldsymbol{a}$ by:

$$\boldsymbol{a} = \frac{e\boldsymbol{A}}{m_e c} = \frac{e\boldsymbol{E}}{m_e c \omega_0} \tag{1.29}$$

where e is the electron charge and m_e its mass. Its peak value a_0, also called the normalized laser amplitude can be expressed as a function of the intensity:

$$a_0 = \frac{eE_{max}}{m_e \omega_0 c} = \lambda_0[\mu m]\sqrt{I_0[W.cm^{-2}]/(1.37 \times 10^{18})} \tag{1.30}$$

The critical value $a_0 = 1$ is the threshold around which an electron oscillating in a laser field reaches a relativistic velocity. This dimensionless parameter differentiates the non-relativistic regime $a_0 \ll 1$ and the relativistic regime $a_0 > 1$. In the context of laser plasma interaction processes, the normalized laser amplitude is a key parameter that determines the nature of the interaction regime [TAJIMA, 2010].

1.2 Plasma

A plasma is a state of matter made of a collection of unbound positively and negatively charged particles that exhibit a collective behavior through electromagnetic fields induced by the motion of free charged particles. It can be generated by heating or subjecting a neutral gas to a strong electromagnetic field to the point where the medium is ionized [Mor, 2012].

1.2.1 Plasma parameters

Debye length

We consider a globally neutral, non-isothermic plasma. Due to their larger mass, ions are supposed to be immobile on the time scale of electron motion. As a consequence, the current in the plasma is mainly generated by the electrons motion [Tonks and Langmuir, 1929].

In the presence of a large collection of charged particles, each one of them simultaneously interacts with many nearby charged particles through the associated Coulomb potential, resulting in the collective behavior of the plasma.

When a local perturbation occurs, the influence of the electrostatic field of an individual charged particle, felt by the other charged particles inside the plasma is damped over a characteristic length called Debye length λ_D [Hückel and Debye, 1923] given by:

$$\lambda_D = \sqrt{\frac{\epsilon_0 k_B T_e}{n_e^2}} \tag{1.31}$$

where ϵ_0 is the vacuum permittivity, k_B is Boltzmann constant, T_e is the temperature and n_e is the electron density.

Plasma frequency

Slightly displacing a sheath of electrons from its equilibrium position generates an electrostatic field $\boldsymbol{E}$ resulting from the charge separation and creating a force $\boldsymbol{F} = -e\boldsymbol{E}$ that pulls it back to restore the initial equilibrium. The kinetic energy gain from this shift results in a harmonic oscillation with a characteristic frequency often referred to as the plasma frequency (or Langmuir frequency) ω_p [Rax, 2005].

$$w_p = \sqrt{\frac{n_e e^2}{\epsilon_0 m_e}} \tag{1.32}$$

This parameter sets the time scale of relaxation of internal electrostatic perturbations. Hence, high-density plasmas respond more quickly to an external perturbation than low-density ones. The associated plasma wavelength is defined by:

$$\lambda_p = 2\pi c/\omega_p \simeq \frac{3.34 \times 10^{10}}{\sqrt{n_e[cm^{-3}]}} \tag{1.33}$$

1.2.2 Electromagnetic waves propagation in a plasma

Let us consider an electromagnetic monochromatic plane wave $\boldsymbol{E} = \boldsymbol{E_0} e^{i(\omega_0 t - kz)}$ propagating in a cold homogeneous collision-less plasma of density n_e where ions are considered immobile. For small perturbations in the case of non relativistic regime, the fluid description of the plasma can be used and non linear terms in the equation of motion of the electrons can be neglected :

$$\frac{\partial \boldsymbol{v}}{\partial t} = -\frac{e}{m_e}\boldsymbol{E} \tag{1.34}$$

Considering the current density $\boldsymbol{J} = -en_e\boldsymbol{v}$, eq. (1.34) can be rewritten as :

$$\frac{\partial \boldsymbol{J}}{\partial t} = \epsilon_0\omega_p^2\boldsymbol{E} \tag{1.35}$$

By combining Faraday's eq. (1.1) and Ampere's eq. (1.2) and with taking into account eq. (1.35) the usual wave equation is found

$$(c^2k^2 - \omega_0^2)\boldsymbol{E} = -\frac{n_e e^2}{\epsilon_0 m_e}\boldsymbol{E} \tag{1.36}$$

where we recognize the plasma frequency in the right side term. Therefore, we can derive the dispersion relation for an electromagnetic wave in a cold plasma:

$$\omega_0^2 = \omega_p^2 + c^2k^2 \qquad k = \frac{\omega_0}{c}\sqrt{1-\frac{\omega_p^2}{\omega_0^2}} = \frac{\sqrt{\omega_0^2-\omega_p^2}}{c} \tag{1.37}$$

In order to understand the propagation of a laser in a plasma, one should distinguish between two cases where the plasma frequency ω_p is compared to the laser frequency ω_0. The transition limit between the two cases corresponds to $\omega_p = \omega_0$. The plasma density corresponding to $\omega_p = \omega_0$ is defined as the critical plasma density $n_c = \frac{m_e\epsilon_0\omega_0^2}{e^2}$. It can be approximated as: $n_c[cm^{-3}] = \frac{1.1\times10^{21}}{\lambda_0[\mu m]}$.

Overdense plasma In the case of $\omega_p > \omega_0$ or equivalently $n_e > n_c$, k in eq. (1.37) is imaginary and corresponds to an evanescent wave with a skin depth of $1/|k|$. The density is too high for the laser to propagate through: the collective response of the plasma electrons to the incoming electromagnetic field is faster than its wave oscillation. The effect of the incident laser oscillations inside the plasma is canceled by the generated currents from the plasma so that the overall field is 0 within the skin depth. This kind of plasma is known as overdense, it reflects totally or partially the incident electromagnetic field.

Underdense plasma In the case of $\omega_p < \omega_0$ or equivalently $n_e < n_c$, k in eq. (1.37) is real which means that the electromagnetic wave can propagate in the plasma: the collective response of the plasma electrons to the incoming electromagnetic field is longer than the optical period of the incoming laser pulse and it is unable to cancel its effect. This kind of plasma is known as underdense and transparent to the incident electromagnetic field field which can propagate in it. However, the plasma modifies the laser propagation since it is a dispersive medium with a dispersion relation eq. (1.37) that is different from the one in vacuum $\omega_0 = kc$.

One can define the phase and group velocity of the laser in the plasma denoted respectively by v_ϕ and v_g thanks to the index of refraction η:

$$v_\phi = \frac{\omega_0}{k} = \frac{c}{\eta} \tag{1.38}$$

$$v_g = \frac{d\omega_0}{dk} = \eta c \tag{1.39}$$

$$\text{where} \quad \eta = \sqrt{1 - \frac{\omega_p^2}{\omega_0^2}} = \sqrt{1 - \frac{n_e}{n_c}} < 1 \tag{1.40}$$

In laser wakefield experiments, the plasma is very under-dense $n_e \ll n_c$ thus $\omega_p \ll \omega_0$, so that $\eta \approx 1$ and $v_\phi \approx v_g \approx c$.

1.2.3 Kinetic description of plasmas

In theory, a full description of a plasma should take into account the position and speed of each of the N particles composing it. However, due to the complexity of resolving an N-body problem when $N \gg 1$, a statistical description is usually employed [Krall and Trivelpiece, 1973]. In this approach, the plasma is described by the distribution functions f_s of each species s in the phase space $(\boldsymbol{x}, \boldsymbol{p})$. For a non-collisional plasmas [1], the corresponding kinetic equation that governs the evolution of the distribution functions is the Vlasov equation given by:

$$\frac{\partial f_s}{\partial t} + \frac{d\boldsymbol{x}}{dt} \cdot \frac{\partial f_s}{\partial \boldsymbol{x}} + \frac{d\boldsymbol{p}}{dt} \cdot \frac{\partial f_s}{\partial \boldsymbol{p}} = 0 \tag{1.41}$$

where $f_s(\boldsymbol{x}, \boldsymbol{p}, t)$ is the distribution function pertaining to a given species s of mass m_s and charge q_s. It is defined as the number density per element of the phase space or the probability of finding a particle of species s in a volume of size $\boldsymbol{dx} \times \boldsymbol{dp}$ around a certain phase space point $(\boldsymbol{x}, \boldsymbol{p})$ with charge q_s. The position is denoted by $\boldsymbol{x}$ and the momentum by $\boldsymbol{p}$. The Vlasov equation is simply an advection equation whose characteristic lines $(\boldsymbol{x}, \boldsymbol{p})$ are solutions to the following equations:

$$\begin{aligned} \frac{d\boldsymbol{p}}{dt} &= \boldsymbol{F} \\ \frac{d\boldsymbol{x}}{dt} &= \boldsymbol{v} = \frac{\boldsymbol{p}}{\sqrt{m_s^2 + |\boldsymbol{p}^2|/c^2}} \end{aligned} \tag{1.42}$$

where $\boldsymbol{F} = q_s(\boldsymbol{E} + \boldsymbol{v} \wedge \boldsymbol{B})$ is the Lorentz force acting on a particle with velocity $\boldsymbol{v}$ with $\boldsymbol{E}$ and $\boldsymbol{B}$ are respectively the electric and magnetic field satisfying Maxwell's eqs. (1.1) to (1.4).

The Vlasov-Maxwell system describes the evolution of the plasma in a self-consistent way. The Maxwell's equations are coupled to the density distribution functions $f_s(\boldsymbol{x}, \boldsymbol{p}, t)$ via the source terms ρ and $\boldsymbol{J}$ given by:

$$\begin{aligned} \rho(\boldsymbol{x}, t) &= \sum_s q_s \int f_s(\boldsymbol{x}, \boldsymbol{p}, t) d\boldsymbol{p} \\ \boldsymbol{J}(\boldsymbol{x}, t) &= \sum_s q_s \int \boldsymbol{v} f_s(\boldsymbol{x}, \boldsymbol{p}, t) d\boldsymbol{p} \end{aligned} \tag{1.43}$$

---

[1] In the context of laser and plasma wakefield experiments, the collisions between particles can be neglected [P., 2013].

1.2.4 Fluid description of plasmas

A more tractable and simplified model can be obtained by describing the particles of each species through their averaged densities n_s and $\boldsymbol{v_s}$. This approach is called fluid description of the plasma. By integrating the equation (1.41) over the different momentum, we obtain the continuity equation that describes particle conservation for each species:

$$\frac{\partial n_s}{\partial t} + \nabla \cdot (n_s \boldsymbol{v_s}) = 0 \tag{1.44}$$

The equation of motion for a specie s in the scope of fluid description for a cold plasma becomes:

$$\frac{\partial \boldsymbol{p}_s}{\partial t} + (\boldsymbol{v}_s \cdot \nabla)\boldsymbol{p}_s = -q_s(\boldsymbol{E} + \boldsymbol{v} \times \boldsymbol{B}) \tag{1.45}$$

1.3 Wakefield generation by a laser pulse

1.3.1 Ponderomotive force

Looking at poisson equation (1.11), Φ represents the potential in the plasma due to charge separation while, the vector potential $\boldsymbol{A}$ in the potential formalism (1.5) and (1.6) represents almost exclusively the laser field. Therefore, the electric field $\boldsymbol{E}$ can be decomposed in two components: $\boldsymbol{E} = \boldsymbol{E}_L + \boldsymbol{E}_p$ where the laser component $\boldsymbol{E}_L = -\frac{\partial \boldsymbol{A}}{\partial t}$ and the plasma field $\boldsymbol{E}_p = -\nabla\Phi$.

In order to emphasize the role of the laser on particles dynamics, we will assume in the following that the electrons only witness the laser field by neglecting the plasma field.

Under this assumption, the electron fluid momentum equation in an under-dense cold [2] plasma where ions are supposed to be immobile[3] can be written as :

$$\frac{\partial \boldsymbol{p}}{\partial t} + \frac{1}{\gamma m_e}(\boldsymbol{p} \cdot \nabla)\boldsymbol{p} = -e(\boldsymbol{E}_L + \boldsymbol{v} \times \boldsymbol{B}_L) \tag{1.46}$$

where $\boldsymbol{p} = \gamma m_e \boldsymbol{v}$ is the momentum, $\boldsymbol{v}$ is the velocity and $\gamma = \sqrt{1 + (\boldsymbol{p}/m_e c)^2}$ is the Lorentz factor.

The movement of electrons upon interacting with the laser pulse can be decomposed on two time scales: on a short time scale, the electrons wiggle in response to the fast oscillating electric and magnetic field of the laser pulse and acquire from it a momentum known as the quiver momentum on a time scale of ω_0^{-1}. On a long time scale, they respond to the low frequency corresponding to the average force over fast oscillations associated with the laser pulse envelope variation known as ponderomotive force [Startsev and McKinstrie, 1997; Bauer et al., 1995] which pushes the electrons away from the pulse creating a wake on a scale of ω_p^{-1} [4] . Since $\omega_p \ll \omega_0$, we can separate the time scales of the electron motion into $\boldsymbol{p} = \boldsymbol{p}^f + \boldsymbol{p}^s$, with $\boldsymbol{p}^f$ is the fast component considered as first order and hence vanish when averaging over one laser period

---

[2] In LWFA, this is justified because in an under-dense plasma the thermal velocity: $v_{th} = \sqrt{k_B T_e/m_e}$ is neglected because the temperature remains small (few eV) compared to the typical oscillation energy (multi-keV) that the electrons acquire from the quiver velocity of electrons in the laser field.

[3] While the laser duration is comparable with the plasma electrons response time $\tau_0 \sim 2\pi/\omega_p$, the typical time for ion motion $2\pi/\omega_{pi}$ is large compared to the driver pulse duration $\tau_0 \ll 2\pi/\omega_{pi}$.

[4] In LWFA, we typically use lasers with duration $\tau_0 \sim 2\pi/\omega_p$. Therefore, the slow motion scales like the temporal envelope of the laser pulse $\sim \omega_p^{-1}$ while fast motion scales like the laser frequency $\sim \omega_0^{-1}$.

($\langle \boldsymbol{p}^f \rangle = 0$), and $\boldsymbol{p}^s$ the slow component considered as second order and constant over a laser period ($\langle \boldsymbol{p}^s \rangle = \boldsymbol{p}^s$).

By linearizing the previous equation 1.46, one gets to the first order:

$$\frac{\partial \boldsymbol{p}^f}{\partial t} = -e\boldsymbol{E}_L \tag{1.47}$$

Using the expression of $\boldsymbol{E}_L = -\frac{m_e c}{e}\frac{\partial \boldsymbol{a}}{\partial t}$ where $\boldsymbol{a}$ is the normalized vector potential defined in (1.29), we deduce the corresponding momentum $\boldsymbol{p}^f = m_e c\boldsymbol{a}$.

Since $\nabla \times \boldsymbol{E}_L = -\partial \boldsymbol{B}_L/\partial t$, one can write: $\boldsymbol{B}_L = \frac{1}{e}\nabla \times \boldsymbol{p}^f = \frac{m_e c}{e}\nabla \times \boldsymbol{a}$. By taking into account $\boldsymbol{B}_L$ expression, one can write the second order or slow components of the equation of motion:

$$\frac{\partial \boldsymbol{p}^s}{\partial t} + \frac{m_e c^2}{\gamma}(\boldsymbol{a}\cdot\nabla)\boldsymbol{a} = -\frac{m_e c^2}{\gamma}\boldsymbol{a}\times\nabla\times\boldsymbol{a} \tag{1.48}$$

Using the identity $\boldsymbol{a}\times\nabla\times\boldsymbol{a} = \nabla|\boldsymbol{a}|^2/2 - (\boldsymbol{a}\cdot\nabla)\boldsymbol{a}$ in the right-hand term of eq. (1.48), we obtain:

$$\boldsymbol{F}_p = \frac{\partial \boldsymbol{p}^s}{\partial t} = -\frac{m_e c^2}{2\gamma}\nabla|\boldsymbol{a}|^2 \tag{1.49}$$

The term $\boldsymbol{F}_p$, proportional to the gradient of the laser intensity, is the ponderomotive force. The negative sign implies that the ponderomotive force, introduced by the spatial distribution of the laser intensity, tends to expel electrons from regions of locally higher intensity to lower ones. This movement of electrons upon interacting with the laser pulse creates a rarefaction zone of electrons behind the laser pulse. However, the ions remain almost immobile and the global electron density remain unchanged. The electric field induced by the charge separation pulls back the electrons causing quasi-periodic oscillations in the electron density behind the laser pulse. Thus, a plasma wave that co-moves with the laser pulse similar to the wake behind a speedboat, is generated.

1.3.2 Plasma waves driven by a laser pulse

When a high intensity laser pulse is focused in an under-dense plasma, the non linear ponderomotive force of the pulse expels a large amount of plasma electrons and can excite large amplitude plasma waves behind the laser [Akhiezer and Polovin, 1956].

The system of equations that governs this mechanism is presented in the following. A detailed derivation of these equations can be found in appendix A. It is based on the Lorentz equation of motion for the electrons in a cold fluid plasma, in addition to the Maxwell's equations in the potential formalism in the Coulomb gauge $\nabla\cdot\boldsymbol{A} = 0$. This description rests upon several assumptions: we consider a cold, collisionless underdense ($\omega_p \ll \omega_0$) fully-ionized plasma. Therefore, under the coulomb gauge, the electromagnetic laser field $\boldsymbol{A}$ corresponding to the high frequencies ω_0 can be separated from the electrostatic plasma field Φ corresponding to the low frequencies ω_p. Recombination of electrons with ions are neglected on the considered time scale. The ions are considered motionless in the plasma and treated as a homogeneous neutralizing background: $n_0 = Zn_i$ with Z the atomic number and n_i the ion number density whereas n_e is the displaced electron density. Thus, we can express the charge density and current as: $\rho = -e(n_e - n_0)$ and $\boldsymbol{J} = -en_e\boldsymbol{v}$ where $\boldsymbol{v}$ is the electrons velocity. We suppose that there is no trajectory crossing in the motion of the electrons. Therefore, these equations are valid in the limit of the cold fluid description presented in section 1.2.4 [5].

---

[5] Note that in this case, kinetic effects like electrons trapping are neglected.

$$\nabla^2 \Phi = \frac{e}{\epsilon_0}(n_e - n_0) \tag{1.50}$$

$$\frac{\partial n_e}{\partial t} + \nabla \cdot (n_e \boldsymbol{v}) = 0 \tag{1.51}$$

$$\left(\nabla^2 - \frac{1}{c^2}\frac{\partial^2}{\partial t^2}\right)\boldsymbol{A} = \frac{e n_e}{\epsilon_0 c^2}\boldsymbol{v} + \frac{1}{c^2}\frac{\partial}{\partial t}\nabla\Phi \tag{1.52}$$

$$\frac{\partial \boldsymbol{p}}{\partial t} = e\nabla\Phi + e\frac{\partial \boldsymbol{A}}{\partial t} - m_e c^2 \nabla\gamma \tag{1.53}$$

where $\gamma = \sqrt{1 + (\boldsymbol{p}/m_e c)^2}$. Here $\nabla\Phi$ is the space charge force and $\boldsymbol{F}_p = -m_e c^2 \nabla\gamma$ represents the generalized nonlinear ponderomotive force [6].

In order to simplify these equations we use the following normalization: $\phi = e\Phi/mc^2$, $\boldsymbol{a} = e\boldsymbol{A}/mc$, $\boldsymbol{u} = \boldsymbol{p}/mc = \gamma\boldsymbol{v}/c = \gamma\boldsymbol{\beta}$ and $\gamma = (1 + \boldsymbol{u}^2)^{1/2}$, we obtain the following system of equations:

$$\nabla^2 \phi = k_p^2 \left(\frac{n_e}{n_0} - 1\right) \tag{1.54}$$

$$\frac{\partial n_e}{\partial t} + c\nabla \cdot \left(\frac{n_0 \boldsymbol{u}}{\gamma}\right) = 0 \tag{1.55}$$

$$\left(\nabla^2 - \frac{1}{c^2}\frac{\partial^2}{\partial t^2}\right)\boldsymbol{a} = k_p^2 \frac{n_e \boldsymbol{u}}{\gamma n_0} + \frac{1}{c}\frac{\partial}{\partial t}\nabla\phi \tag{1.56}$$

$$\frac{\partial \boldsymbol{u}}{\partial t} = c\nabla(\phi - \gamma) + \frac{\partial \boldsymbol{a}}{\partial t} \tag{1.57}$$

where $k_p = \omega_p/c = \sqrt{e^2 n_0/\epsilon_0 m_e c^2}$ is the wave number of the plasma.

1.4 Regimes of plasma wave excitation

The ponderomotive force resulting in electrons motion leads to a charge density modulation, which in return introduces a coulomb restoring force to the electrons. This process leads to the creation of the wakefield which strongly depends on the strength parameter of the laser pulse a_0. In pratice, two limiting cases are particularly insightful [Esarey et al., 2009] : the linear regime and the non-linear regime.

Theories and analytical models of the wakefield established so far, are valid only in certain regimes. In the previous section, the behavior of plasma wakefield generated in the case of a laser pulse driver was analytically described based on plasma fluid theory [Sprangle et al., 1988; Esarey et al., 1989; Gorbunov and Kirsanov, 1987]. This theory is valid in the linear regime even in three dimensions. Yet, it is restricted to one dimensional description when it comes to the nonlinear regime [Akhiezer and Polovin, 1956]. For sufficiently high laser intensities ($\gtrsim 10^{18} W/cm^2$), relativistic effects become very important and crossings occur in electron trajectories. In this case, the fluid theory fails to describe accurately these relativistic and kinetic effects and the self-consistent evolution of the driver laser pulse. Therefore, multi-dimensional effects in the non linear regime must be modeled numerically.

---

[6] Note that if we consider $\boldsymbol{p} = m_e c \boldsymbol{a}$ we retrieve the expression for the ponderomotive force in eq. (1.49)

1.4.1 Linear regime

In the linear regime, the laser strength is sufficiently low $a_0^2 \ll 1$ [Kruer, 2003; Gibbon, 2005] to not trigger almost any relativistic effects. It only drives small perturbations in the quiescent background electronic density. All the plasma parameters $X = (n_e, \phi, \gamma, \boldsymbol{u})$ can be written as: $X = X_0 + \delta X$ where $\delta X \ll X_0$. Thus, they can be considered as first-order quantities in Taylor development. The trajectories of the electrons, in this case, are laminar (i.e. there are no trajectory crossing). Therefore, the use of cold fluid theory is justified.

Since $\omega_p \ll \omega_0$, we can separate the quantities in high frequencies ($\sim \omega_0$) and low frequencies ($\sim \omega_p$). Therefore, quantities pertaining to the plasma are considered as low frequencies denoted by the exponent s ($\phi = \phi^s$ and $n_e = n_e^s$), while those related to the laser field are considered as high frequencies denoted by the exponent f ($\boldsymbol{a} = \boldsymbol{a}^f$). The electrons motion has both components: $\boldsymbol{u} = \boldsymbol{u}^s + \boldsymbol{u}^f$ where $\boldsymbol{u}^f = \boldsymbol{a}$ as demonstrated previously in section 1.3.1.

Thus, the equation of motion (1.57) for the slow component reads:

$$\frac{\partial \boldsymbol{u}^s}{\partial t} = c\nabla(\phi - \langle\gamma\rangle)$$

where$\langle\gamma\rangle \simeq 1 + \langle\boldsymbol{a}^2\rangle/2$ is the average of γ over the fast oscillations [7]. The equation of motion in the linear regime becomes:

$$\frac{\partial \boldsymbol{u}^s}{\partial t} = c\nabla\phi - c\nabla\frac{\langle\boldsymbol{a}^2\rangle}{2} \tag{1.58}$$

where $-\nabla\langle\boldsymbol{a}^2\rangle/2$ is the expression of the normalized ponderomotive force in the linear weakly relativistic regime. The electrons motion resulting from the ponderomotive force will lead to a charge density modulation. This density modulation in return will introduce a coulomb restoring force to the electrons that can be described with Poisson's equation (1.54):

$$\nabla^2\phi = k_p^2\frac{\delta n_e}{n_0} \tag{1.59}$$

The plasma density can be described with the continuity equation (1.55), which can be linearized in the case of weak density perturbation:

$$\frac{\partial}{\partial t}\frac{\delta n_e}{n_0} + c\nabla\cdot\boldsymbol{u}^s = 0 \tag{1.60}$$

Deriving (1.60) in time and using (1.58) and (1.59), we get :

$$\frac{\partial^2}{\partial t^2}\frac{\delta n_e}{n_0} + c\nabla\cdot(\frac{\partial \boldsymbol{u}^s}{\partial t}) = \frac{\partial^2}{\partial t^2}\frac{\delta n_e}{n_0} + c^2\nabla^2\phi - c^2\nabla^2\frac{\langle\boldsymbol{a}^2\rangle}{2}$$

We finally obtain:

$$\left(\frac{\partial^2}{\partial t^2} + \omega_p^2\right)\frac{\delta n_e}{n_0} = c^2\nabla^2\frac{\langle a^2\rangle}{2} \tag{1.61}$$

By substituting (1.61) in Poisson's equation (1.59), one obtains the plasma wave potential equation:

---

[7] By linearization, the expression becomes : $\langle\gamma\rangle \simeq 1 + \langle(\boldsymbol{u}^f)^2\rangle/2 + (\boldsymbol{u}^s)^2/2$. However, $\boldsymbol{u}^s$ can be neglected in this expression because it is on the order of $\boldsymbol{a}^2$ as it will be demonstrated later on, hence $\langle\gamma\rangle \simeq 1 + \langle\boldsymbol{a}^2\rangle/2$.

$$\left(\frac{\partial^2}{\partial t^2} + \omega_p^2\right)\phi = \omega_p^2 \frac{\langle \boldsymbol{a}^2 \rangle}{2} \tag{1.62}$$

From equations (1.61) and (1.62), we can see that $\delta n_e/n_0$ and ϕ are on the order of $\langle \boldsymbol{a}^2 \rangle$ and hence $\boldsymbol{u}^s$ too, which justify the assumption we made earlier in Taylor development for γ.

In an under-dense plasma, it is assumed that the laser driver and the corresponding wakefield propagate very close to the speed of light i.e $v_g \sim c$ and $v_\phi \sim c$ [Sprangle et al., 1990] [8], so it is practical to use the copropagating coordinates $\tau = t$ and $\xi = z - ct$ (where z is the spatial coordinate along the axis of propagation) in order to follow the laser pulse. The partial derivatives under this transformation are detailed in appendix B, in both cases of $v_g \sim c$ and $v_g \neq c$.

Furthermore, we assume that the changes in the driving laser during its propagation, occur on timescales much larger than the pulse duration and the plasma period λ_p. Actually, changes in the laser envelope start occurring at propagation distances on the order of Z_r. Consequently, we can consider that the laser envelope remains unchanged throughout its propagation (any change in the laser field induced by the plasma is neglected). It is also assumed that the pulse duration is much longer than the laser period: $\tau_0 \gg T_0 = 2\pi/\omega_0$ where τ_0 is the laser duration and ω_0 is its frequency. Therefore, the laser pulse and the plasma wave can be considered stationary during the time a plasma electron needs to slip through the pulse (quasi-static approximation [9]). This allows us to neglect derivatives in τ compared to the ones in ξ, i.e $\partial/\partial\tau = 0$. The quasi-static approximation is only valid for plasma electrons with sufficiently low energy. It fails to describe electrons which have been accelerated to high energies and traveling with the laser pulse.

Applying this approximation, one finally gets the potential equation with the quasi-static approximation in the co-moving coordinates:

$$\left(\frac{\partial^2}{\partial \xi^2} + k_p^2\right)\phi = k_p^2 \frac{\langle a(\xi)^2 \rangle}{2} \tag{1.63}$$

This equation simply shows that the plasma electrons behave like harmonic oscillator driven by the laser ponderomotive force which generates a periodic oscillation of the electron density with a wavelength $\lambda_p = 2\pi/k_p$ where $k_p = \omega_p/c$.

Equation (1.63) can be solved using Green functions:

$$\phi = -\frac{k_p}{2}\int_{\xi}^{\infty} \langle a(\xi')^2 \rangle \sin(k_p(\xi - \xi'))d\xi' \tag{1.64}$$

The above expression determines the wakefield components which are zero at an infinite distance ξ (no plasma perturbation before the driver pulse). We are interested in perturbations behind the laser pulse ($\xi < 0$). Let us express these fields explicitly in the case where the driver is a linearly polarized femtosecond Gaussian laser pulse:

$$\boldsymbol{a} = \hat{\boldsymbol{a}}(r,\xi)\cos(k_0\xi)\boldsymbol{e_x}$$

with

$$\hat{\boldsymbol{a}}(r,\xi) = a_0 \exp(-\xi^2/L_0^2)\exp(-r^2/\sigma^2)$$

---

[8] The generalization of the theory for velocities different from c such as the laser group velocity $\boldsymbol{v}_g$ or the wake phase velocity $\boldsymbol{v}_\phi$ was the focus of many works presented in the following references [Esarey et al., 1997; Mori et al., 1993].

[9] Also called frozen field approximation by Whittum [Whittum, 1997]

where $L_0 = c\tau_0$ is the pulse length and $\sigma = w_0/\sqrt{2}$ with w_0 is the Gaussian waist. In this case $\langle \boldsymbol{a}^2 \rangle = \hat{\boldsymbol{a}}/2$ and

$$\phi = -\sqrt{\pi} a_0^2 \frac{k_p L_0}{4} \exp\left(-\frac{k_p^2 L_0^2}{4}\right) \exp\left(-\frac{r^2}{\sigma^2}\right) \sin(k_p \xi) \tag{1.65}$$

As we can see from this equation, in the linear regime the laser pulse triggers a sinusoidal oscillation of the plasma electron density behind the laser pulse with a wavelength $\lambda_p = 2\pi/k_p$. The above expression of ϕ entirely determines the wakefield since:

$$\frac{\boldsymbol{E}}{E_0} = -\frac{1}{k_p}\nabla\phi = -\frac{1}{k_p}\left(\frac{\partial\phi}{\partial\xi}\boldsymbol{e_z} + \frac{\partial\phi}{\partial r}\boldsymbol{e_r}\right)$$

and

$$\frac{\delta n_e}{n_0} = -\frac{1}{k_p E_0}\left(\frac{\partial E_z}{\partial \xi} + \frac{1}{r}\frac{\partial (r E_r)}{\partial r}\right)$$

where $E_0 = m_e c \omega_p / e$ is the maximal electric field in the linear regime, when the density perturbation is total and the resonance condition is fulfilled. It quantifies how efficiently the laser pulse excites the wakefield.

The expressions for the longitudinal and transverse electric fields E_z and E_r for $\xi < 0$ can thus be written :

$$\frac{E_z}{E_0} = \sqrt{\pi} a_0^2 \frac{k_p L_0}{4} \exp\left(-\frac{k_p^2 L_0^2}{4}\right) \exp\left(-\frac{r^2}{\sigma^2}\right) \cos(k_p \xi) \tag{1.66}$$

$$\frac{E_r}{E_p} = -\sqrt{\pi} \frac{a_0^2}{2} \frac{L_0 r}{\sigma^2} \exp\left(-\frac{k_p^2 L_0^2}{4}\right) \exp\left(-\frac{r^2}{\sigma^2}\right) \sin(k_p \xi) \tag{1.67}$$

and the expression of the density perturbation in the plasma for $\xi < 0$ is:

$$\frac{\delta n_e}{n_0} = \sqrt{\pi} a_0^2 \frac{k_p L_0}{4} \exp\left(-\frac{k_p^2 L_0^2}{4}\right) \exp\left(-\frac{r^2}{\sigma^2}\right) \sin(k_p \xi) \left[1 + \frac{4}{\sigma^2 k_p^2}\left(1 - \frac{r^2}{\sigma^2}\right)\right] \tag{1.68}$$

The linear wakefield is driven more efficiently (the maximal wakefield amplitude ϕ_{max} is obtained) when the pulse duration is approximately half the plasma period. More precisely, as shown in fig. 1.3, the optimal pulse length to achieve the resonant condition is $k_p L_0 = \sqrt{2}$ which can also be written $\omega_p \tau_0 = \sqrt{2}$. This means that plasma wave formation is optimal in low density plasmas for long pulses while higher-density plasmas are better suited for shorter pulses. For example, a density $n_e \approx 10^{18} cm^{-3}$ imposes to use a laser pulse with a duration FWHM $\approx 40 fs$ in order to optimally drive the wakefield.

The electrostatic accelerating structure resulting from the propagation of a Gaussian beam in an underdense plasma exercises two types of force on a relativistic electron traveling with the wakefield. The longitudinal component E_z can accelerate electrons while the radial component E_r can focus the electrons close to the $r = 0$ axis. According to the expression of E_r, the transverse resulting force $\boldsymbol{F}_\perp = -e(E_r - v_z B_\theta)\boldsymbol{e_r} = -eE_r\boldsymbol{e_r}$ is focusing in the first half wavelength ($-2\pi < k_p\xi < -\pi$) of the wakefield and defocusing in the second half- wavelength ($-\pi < k_p\xi < 0$). Whereas, the longitudinal force $\boldsymbol{F}_z = -eE_z\boldsymbol{e_z}$ is decelerating in the first quarter wavelength ($-2\pi < k_p\xi < -3\pi/2$) and accelerating in the second quarter-wavelength ($-3\pi/2 < k_p\xi < -\pi$).

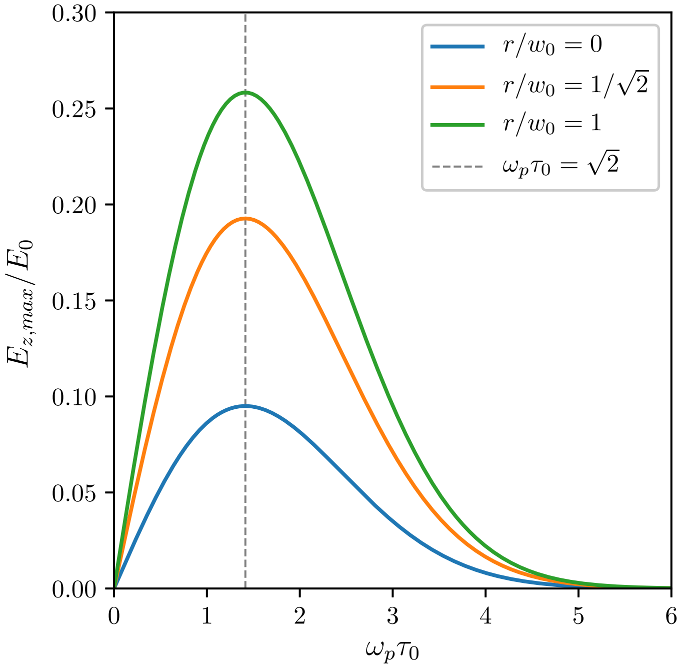

Figure 1.3: Normalized amplitude of the longitudinal field $E_{z,max}/E_0$ of the wakefield created by a Gaussian pulse with $a_0 = 0.5$ as a function of $\omega_p \tau_0$ for different values of r/w_0 where r is the distance from axis. All curves exhibits a resonance for $\omega_p \tau_0 = \sqrt{2}$

Over all, efficient electrons acceleration in a linear regime can only take place in the second quarter wavelength indicated by the delimited zone in fig. 1.4 which is both accelerating and focusing. If relativistic electrons traveled along in this region, they would be focused and accelerated over long distances and can result in high-quality beams.

1.4.2 Non-linear regime

The laser strength parameter a_0 is a key parameter to distinguish between the linear ($a_0^2 \ll 1$) and non-linear regime ($a_0^2 \gg 1$) of the laser wakefield excitation. In the nonlinear regime, the evolution of the laser includes non linear effects that deform the laser pulse spatially. Therefore the laser transverse size w_0 becomes also an important factor to take into account. In fact, for a broad pulse ($k_p w_0 \gg 1$), the plasma fluid model presented in section 1.3.2 can still be adapted to model the wakefield analytically but only in the 1D limit. Nevertheless, this is no longer valid when the laser pulse is radially bounded ($k_p w_0 \leq 1$) and the transverse ponderomotive force becomes sufficiently strong to dislodge the electrons and create electron-free cavities. This phenomena is referred to as the blowout or bubble regime. In this case, three dimensional effects in the wakefield become very important and must be modeled numerically, typically using particle-in-cell (PIC) codes.

One dimensional solution of the fluid model

The relativistic nonlinear theory of laser driven plasma waves can be solved analytically in the limit of 1D which is only valid in the case of a broad laser pulse ($k_p w_0 \gg 1$) [Akhiezer and

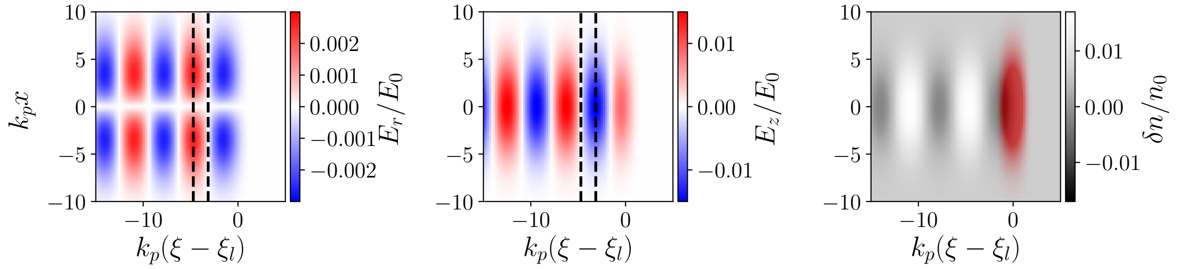

Figure 1.4: From left to right: colormaps of the radial electric field E_r/E_0, the longitudinal electric field E_z/E_0 and the density perturbation $\delta n/n_0$ in the linear regime for $a_0 = 0.2$ represented in the coordinates $(k_p(\xi-\xi_l), k_px)$ where ξ_l is the laser peak intensity position in the comoving coordinates $\xi = z - ct$. The laser pulse, represented here by its envelope, is the red spot in the density plot and propagates from left to right. The dashed lines delimit the second quarter-wavelength which is both the focusing and accelerating region.

Polovin, 1956; Dawson, 1959; Berezhiani and Murusidze, 1990] and can be a good starting point to understand the phenomena related to the non linear regime in the multidimensional case.

We consider that all quantities depend only on (z, t) where z is the axis along which a purely transverse non evolving laser pulse $\boldsymbol{a} = \boldsymbol{a}_\perp$ is propagating. This simplification implies that the following differential equation is verified by the normalized electric potential under the quasi-static approximation with the transformations $(\tau = t, \xi = z - v_gt)$ and $\partial\tau \ll c\partial\xi$ [Berezhiani and Murusidze, 1992; Esarey and Pilloff, 1995]:

$$\frac{\partial^2\phi}{\partial\xi^2} = k_p^2\gamma_g^2\left[\beta_g\left(1-\frac{1+a^2}{\gamma_g^2(1+\phi)^2}\right)^{-1/2}-1\right] \tag{1.69}$$

where $\beta_g = v_g/c$ and $\gamma_g = 1/\sqrt{1-(v_g/c)^2}$. In the case where $w_p \ll w_0$, the laser group velocity can be confused with the speed of light $v_g \sim c$, thus $\beta_g \approx 1$ and $\gamma_g \gg 1$. Therefore, the above equation can be simplified:

$$\frac{\partial^2\phi}{\partial\xi^2} = \frac{k_p^2}{2}\left[\frac{1+a^2}{(1+\phi)^2-1}\right] \tag{1.70}$$

In the limit of weak perturbations $\phi \ll 1$ corresponding to the case where $a_0 \ll 1$ we can retrieve the differential equation of the potential in the case of linear regime eq. (1.63) from eq. (1.70).

The expressions for the plasma potential, longitudinal electric field and plasma density in 1D can be calculated by integrating eq. (1.70) numerically. The generated plasma waves evaluated in both linear regime ($a_0 = 0.2$) and non-linear regime ($a_0 = 2$) using the 1D nonlinear plasma fluid theory are shown in fig. 1.5.

The density perturbation ($\delta n/n_0$) in the linear regime is small and plasma wake quantities evolve sinusoidally. However, it is no more the case in the nonlinear regime where the density

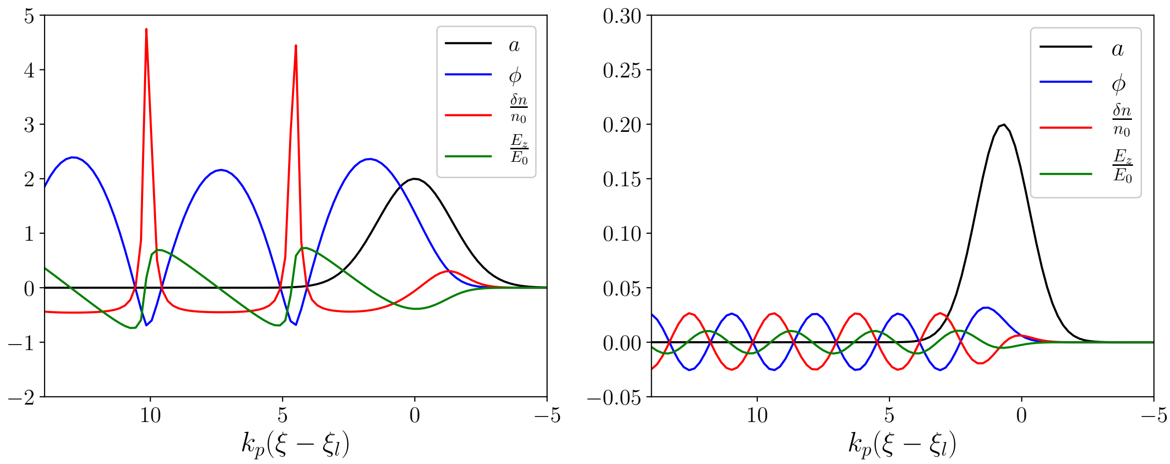

Figure 1.5: Normalized envelope of the laser vector a, plasma potential ϕ, the associated longitudinal electric field, $E_z/E0$ and density perturbation $\delta n_e/n_0$ on axis in the co-moving coordinate system for a Gaussian laser pulse with $a_0 = 0.2$ (linear regime) in the right panel and $a_0 = 2$ (non-linear regime) in the left panel.

exhibits sharp peaks that can reach several times the initial density value with a typical saw tooth shape and steep gradients. One can notice that the effective plasma period becomes non-linear $\lambda_{p,NL}$ and undergoes a lengthening when the laser amplitude increases and electrons velocity becomes relativistic. As a_0 increases, wakes become sharper and bent like a horse shoe shape and the wave front becomes curved due to the relativistic shift of the plasma frequency. The peaks in the density profile correspond to the points where the electric field switches its sign. It is where electrons have velocities close to the plasma wave velocity. If E_z is sufficiently important ($E_z > E_0$) electron self-trapping is susceptible to occur [10]. Trapped electrons can be efficiently accelerated up to relativistic energies over half a plasma wavelength, assuming transverse fields are focusing over this length.

Even though the one dimensional model is insightful for the phenomena that takes place in the non-linear regime, it is not sufficient to describe the non-linear effects that play an important role in defining the radial structure of the plasma wave. For instance, besides wave steepening and period lengthening, the wave front can exhibit severe curvature resulting in a nonlinear plasma wavelength that is greater on axis than off axis. Hence, the laser pulse acts as a snowplow for the electron density expelling electrons off axis which are pulled afterwards toward it creating thus a bare ion cavity surrounded by a thin sheath of expelled electrons. This is known as bubble regime, because the cavity usually has an approximately spherical shape [Sun et al., 1987; Rosenzweig et al., 1991b]. Since neither fluid nor one-dimensional theory applies in this case, a phenomenological description of the LWFA in the blowout regime has been established through numerical simulations [Mora and Antonsen, 1996; Lefebvre et al., 2003; Pukhov and

---

[10] E_z can be more important than E_0 while still being below the relativistic cold wave breaking-limit $E_{WB} = E_0\sqrt{2(\gamma_p - 1)}$(This limit is modified in the case of relativistic electrons due to thermal effects in the plasma [Rosenzweig et al., 1988; Katsouleas and Mori, 1988] which suggests that additional laser plasma instabilities such as the coupling of Raman backscatter (RBS) and Raman sidescatter (RSS) may play a role in lowering the effective amplitude for electron self-trapping.

Meyer-ter Vehn, 2002; Lu et al., 2006b,a]. The core of the work established in this thesis is based on the results in the bubble regime. Therefore PIC simulations has been extensively used throughout this manuscript.

Bubble regime

In 2002, the pioneering theoretical work of [Pukhov and Meyer-ter Vehn, 2002] has predicted the possibility of generating quasi-monoenergetic accelerated electron distribution based on three-dimensional PIC simulations with the code VLPL [Pukhov, 1999]. In this acceleration mechanism, called the bubble regime, the dimensions of the focused laser in both longitudinal and transverse directions are shorter than the plasma wavelength. The laser ponderomotive force varies as the laser energy gradient, therefore when the energy contained in the laser spherical volume is important enough, it expels the electrons radially from the plasma. This results in the formation of a bubble-like cavity, free from the electrons and surrounded by a thin sheath of higher electrons density, behind the laser. Behind this cavity, the electrons density increases gradually until some electrons are trapped and injected at the back of the cavity and thereby accelerated along the propagation axis. A schematic representation of the bubble is shown in fig. 1.7.

The accelerating field, limited to the wave breaking limit for a non-relativistic cold plasma $E_0 = m_e c\omega_p/e$, can exceed it in the bubble regime which leads to large electron oscillations. As a result, some electrons can escape the collective motion and trajectories intersections may occur. This is the origin of electron injection in the bubble regime. Contrarily, in the linear regime, the relativistic electrons need to be produced by an external source and injected into the linear plasma wave in order to be accelerated.

The signature of this regime is quasi-monoenergetic electron spectra resulting from the localization of the injection at the back of the cavity where interaction between the trapped electrons and the electric field of the laser is negligible and gives similar initial properties in the phase space to injected electrons, hence creating an electron beam with a transverse dimension smaller than the initial laser waist and a duration shorter than that of the laser pulse. This is of a major interest for a number of applications, because it is possible to transport it and then refocus the resulting beam. Since most of LWFA experiments generating self-injected electrons take place in the blowout regime, it was necessary to develop a model that describes the characteristics of the accelerating cavity and specify the plasma parameters in this regime.

Firstly, Gordienko and Puhkov have proposed a model based on a single similarity parameter $S = n_0/n_c a_0$ determined via simulations which states that for laser-plasma interactions with different a_0 and n_0/n_c scale in the same way as soon as the similarity parameter is constant [Gordienko and Pukhov, 2005]. However, this model is not very useful, because it is restricted to the case where $a_0 \gg 1$, while in most of the lasers used in experiments up to date do not have an $a_0 \gg 1$ but rather an $a_0 \gtrsim 1$. Therefore, [Lu et al., 2007b] established a phenomenological description of three-dimensional plasma waves in the blowout regime driven by an extremely intense laser with $a_0 \gtrsim 1$. In their semantic paper, they presented several useful scaling laws for the ideal laser spot size in terms of self-guiding. They also provided an expression to estimate the expected accelerated particle energies for fixed LWFA parameters. Their scaling laws help identifying key characteristics of the physics such as wake excitation, pump depletion, dephasing and beam loading in order to design future LWFA experiments and predict simulations.

For a given plasma density n_0 and a Gaussian laser pulse with a fixed power P_L, Lu's model presumes that a laser with a size matched to the condition $k_p w_0 = 2\sqrt{a_0}$ [Lu et al., 2007b] (where the factor of 2 is deduced from full PIC simulations) and a duration resonant with the

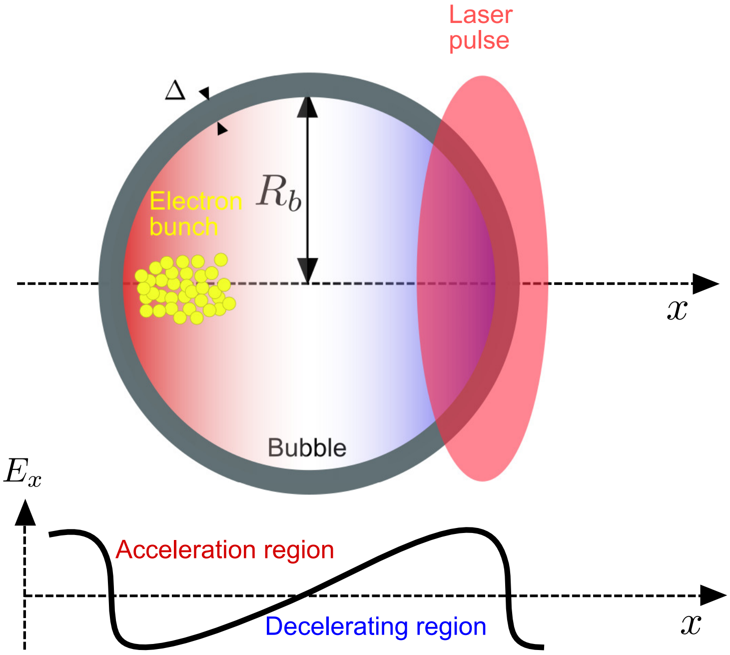

Figure 1.6: Representation of the blowout regime: an intense laser pulse propagating in the x-direction drives a strong wakefield with an accelerating field (red gradient) and a decelerating field (blue gradient). All background electrons within a blow-out radius R_b are totally expelled outward from the axis, creating a spherical ion cavity just behind the pulse. The expelled electrons form a thin sheath around the cavity of a width Δ. They are then pulled towards the axis because of the transverse force produced by the ion cavity. Electron trajectories cross behind the cavity and close it. Some of the electrons are trapped and injected at the back of the bubble (yellow dots) in the accelerating region.

plasma period $\omega_p \tau_{0,res} = 2$, triggers a transverse ponderomotive force sufficiently strong to expel all the electrons from the first bucket of the wakefield. Under this condition, the cavity takes a quasi-spherical shape and the optical guiding of the laser is optimal. Once this requirement is fulfilled, the acceleration can last over a significant distance.

The blowout regime provides a three dimensional spherical accelerating and focusing structure for self-guided electrons with a maximum blowout radius $R_b = 2\sqrt{a_0}/k_p$ (since $k_p w_0 \sim k_p R_b$) [Lu et al., 2007b] that is determined by the balance of two forces: the space-charge force of electrons and the ponderomotive force of the laser. If the waist is larger than the matched laser spot size, a_0 would not be strong enough to reach the blowout regime. Inversely, if the laser's waist is smaller than the matched laser spot size, the ponderomotive force will expel the electrons to the edge of the laser from the beginning resulting in wide bubble and only a small fraction, if any, of them would feel the impact of the ponderomotive force to be injected in the back of the cavity. Additionally, the laser would be too small to be guided and will diffract very early.

Considering the quasi-static approximation inside the bubble, the plasma wave can be described entirely in terms of the cavity radius $r_b(\xi)$. In the case of a sufficiently intense laser ($a_0 > 4$), the cavity has a perfectly spherical shape of a maximal radius R_b and one can derive the expressions for the normalized potential and the longitudinal and transverse electromagnetic fields inside the bubble in cylindrical coordinates (r, θ, z) [Lu et al., 2006a; Xie et al., 2007] for $r \leq r_b(\xi)$:

$$\phi = -\frac{k_p^2 r^2}{4} + \phi_0(\xi) \tag{1.71}$$

$$E_z \simeq \frac{k_p \xi}{2} E_0 \tag{1.72}$$

$$\frac{E_r}{E_0} \simeq \frac{k_p r}{4} E_0 \tag{1.73}$$

$$B_\theta \simeq -\frac{k_p r}{4c} E_0 \tag{1.74}$$

with $\phi_0(\xi) = \phi_0(r = 0, \xi)$, where $(r = 0, \xi = 0)$ is the center of the bubble, and $E_0 = m_e c \omega_p / e$ is the cold wavebreaking maximum field.

This regime is particularly interesting in the design of an accelerator because it conserves the transverse emittance of the electrons all along their acceleration. In fact, the transverse force associated with the fields above $F_\perp = -m_e \omega_p^2 r/2$ is always focusing, linear in r and independent of ξ, contrarily to the linear regime. Hence, it is uniform for all the phases and it compensates the natural diffraction of the electrons bunch. The accelerating force $F_z = -m_e \omega_p^2 \xi/2$ experienced by an electron in the cavity is independent of the transverse position with respect to the cavity axis. Its expression shows that it is zero near the maximum of the cavity $(r_b(\xi = 0) = R_b)$, decelerating in the first half of the cavity $(\xi > 0)$ and accelerating in the second half $(\xi < 0)$. The order of magnitude of the longitudinal accelerating field inside the cavity can be evaluated by considering the typical length of the bubble $L_b = 4\sqrt{a_0} c/w_p$ [Lu et al., 2007b] as

$$|E_z| \simeq \frac{m_e c \omega_p}{e} \sqrt{a_0} \simeq 96 \sqrt{a_0 n_0 [10^{18} \mathrm{cm}^{-3}]} \mathrm{GeV.m}^{-1}$$

In this regime, the cavity shape and thus the associated transverse and longitudinal fields can be controlled by adjusting the focal spot transverse size and the pulse duration and tuning the plasma electron density. Hence, electron injection can be somehow controlled. Moreover, the electron energy distribution exhibits peaked distributions and the accelerating structure prevents emittance growth.

Experimental demonstration

With the increase in laser power and the development of short pulse durations in laser facilities worldwide, nonlinear plasma waves in the blowout regime became experimentally achievable. The first experimental demonstrations of self-injection resulted in a large energy distribution of the accelerated bunch with most of the electrons at low energy ($<$ 10 MeV) [Modena et al., 1995a; Umstadter et al., 1996a; Leemans et al., 2002; Malka et al., 2002]. Subsequently, a major breakthrough has been made and in 2004: several laboratories succeeded in accelerating quasi-monoenergetic electrons up to $\sim$ 100 MeV. This has been achieved using a laser energy $E_{laser} \sim$ 1J and a plasma density $n_0 \sim 10^{19} cm^{-3}$ in France [Faure et al., 2004b] with a laser pulse shorter than the plasma period, but also with pulses slightly longer than the plasma period in the U.K [Mangles et al., 2004b] and in the United States [Geddes et al., 2004b]. Despite their quasi-monoenergetic spectra, the produced bunches were not sufficiently stable and better beam quality with improved stability and tunability has been achieved thereafter through better control of self- injection and dephasing length [Faure et al., 2006a; Geddes et al., 2008; Gonsalves et al., 2011]. Electrons in the GeV level were firstly observed in this regime in 2006

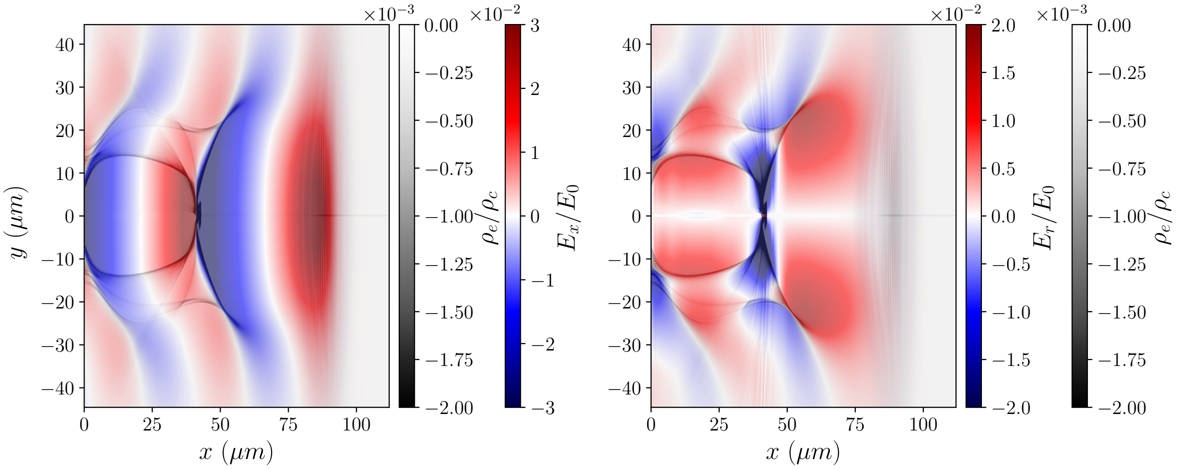

Figure 1.7: Representation of a typical normalized electron charge density map along with the associated normalized electromagnetic fields in the blowout regime from PIC simulation. An intense and short laser pulse of an $a_0 = 2.9$ and a duration of FWHM$\simeq$ 28 fs propagating in the x-direction, expels all the electrons from the optical axis creating an ionic cavity. These electrons then form a dense sheath surrounding the cavity, before crossing the axis and closing the cavity where some of the electrons are trapped and accelerated to high energies. A superposition of the normalized electronic density map with the longitudinal field is presented in the *left-hand panel*, and with the transverse field in the *right-hand panel*. The bubble provides an ideal structure for accelerating electrons because beyond the sheath there is a linear response region with fields that are both accelerating and focusing over nearly half a plasma wavelength.

using preformed plasma channel from capillary discharge to guide the 40 TW peak power laser pulse over a 3 cm acceleration distance [Leemans et al., 2006] in a low density $n_0 \sim 10^{18} cm^{-3}$. With the development of PW class lasers with femtosecond pulses, multi-GeV electron beam has been reported in 2013 using uniform plasma and with considerably higher laser energy reaching $E_{laser} = 30$ J in the case of 2 GeV [Kim et al., 2013] and $E_{laser} = 150$ J in the case of 3 GeV. Afterwards, in 2014 a 4.2 GeV electron beam using 16 J of laser energy has been achieved in a 9 cm-long preformed plasma channel waveguide. The latest record in this race is the production of 7.8 GeV by guiding a 0.85 PW peak power laser with an energy of $E_{laser} = 31$ J over 20 cm-long capillary of $n_0 = 3.410^{17} \times cm^{-3}$ [Gonsalves et al., 2019].

1.5 Laser-wakefield acceleration

In order to be accelerated, electrons with sufficient initial velocity should be placed in the accelerating and focusing phase of the wakefield as mentioned earlier. Otherwise, they would slip back experiencing defocusing and will leave the plasma wave without any energy gain. The first requirement to the electrons acceleration is then trapping. In the following section, first the theoretical conditions for trapping and the different injection schemes will be presented, then key physics of the acceleration and its limits will be summarized. Finally, the properties of the accelerated electron bunch will be detailed.

1.5.1 Electrons trapping

The study of electron trapping can be carried out using a one-dimensional Hamiltonian model which describes the total energy of a single electron in the wakefield. We assume a Gaussian laser vector potential, polarized in the y-direction and propagating in the z-direction. The Hamiltonian for an electron with Lorentz factor γ interacting with a laser and a plasma wave represented by the normalized potential ϕ [Esarey and Pilloff, 1995] writes:

$$H = \gamma_p - \phi(z - v_g t) = \sqrt{1 + u_\perp^2 + u_z^2} - \phi(z - v_g t) \tag{1.75}$$

where $u_\perp^2 = p_\perp / m_e c$ and $u_z^2 = p_z / m_e c$ are respectively the transverse and longitudinal normalized momenta.

Using a canonical transformation $(z, u_z) \to (\xi, u_z)$ with $\xi = z - v_g t$ and supposing f a function verifying : $f(z, u) = u(z - v_g t) = u\xi$, the transformation satisfies $\xi = \partial f / \partial u_z = z - v_g t$ and $u_z = \partial f / \partial z$. The new Hamiltonian H' [Esirkepov et al., 2006], hence reads:

$$H' = H - \frac{v_g u_z}{c} \tag{1.76}$$

$$= \sqrt{1 + u_\perp^2 + u_z^2} - \phi(\xi) - \beta_p u_z \tag{1.77}$$

Where $\phi(\xi)$ is the potential of the wakefield, oscillating between ϕ_{min} and ϕ_{max}. Since in 1D the laser field has only a transverse component, from Hamilton's equation we can see that the transverse canonical momentum $\tilde{u}_\perp = u_\perp - a$ is conserved ($\dot{u}_\perp = -\partial H / \partial r_\perp = 0$). Therefore, $u_\perp(\xi) - a(\xi) = u_0$, with u_0 is a constant of motion representing the initial perpendicular momentum of the electron. For an electron initially at rest in front of the laser pulse ($\xi_i = +\infty$, where index i denotes initial), $u_\perp = a(\xi)$. In eq. (1.76), H' does not depend explicitly on time, so $dH'/dt = 0$ and hence $H' = constant$, which means that the energy of the system is conserved along an electron orbit. By solving the Hamiltonian for u_z, one can derive the trajectory of an electron with initial energy H_0 in phase space :

$$u_z = \beta_p \gamma_p^2 (H_0' + \phi) \pm \gamma_p \sqrt{\gamma_p^2 (H_0' + \phi^2) - \gamma_\perp^2} \tag{1.78}$$

The trajectory of particles in phase space (ξ, u_z) can be understood thanks to the study of the Hamiltonian once $a(\xi)$ and $\phi(\xi)$ are known. We can distinguish a particular trajectory that separates the closed orbits of trapped electrons and the open orbits of untrapped electrons that flow from the right to the left of the phase portrait depicted in fig. 1.8. This special trajectory is denominated *the separatrix* and defined by electrons initially located at a minimum potential $\phi(\xi_{min}) = \phi_{min} < 0$ and moving with $u_z(\xi_{min}) = \gamma_p \beta_p$. It can be obtained when the conservation of canonical momentum verifies $u_z(\xi_{min}) = a(\xi_{min})$

$$H_{sep} = \frac{\sqrt{1 + a(\xi_{min})}}{\gamma_p} - \phi_{min} \tag{1.79}$$

From figure 1.8, two types of trajectories partitioned by the separatrix (red line) [Teychenné et al., 1994; Esarey and Pilloff, 1995] can be distinguished: fluid orbits (blue lines) where electrons are not trapped, they correspond to the trajectory of plasma background electrons that contribute to the formation of the plasma wakefield by just oscillating in the plasma wakefield with low energies. They correspond to electrons initially at rest in front of the laser pulse, $\xi = +\infty$ and $u_z(\xi) = u_\perp(\xi) = 0$ and a Hamiltonian $H_0' = 1$. The second trajectory refers to orbits of

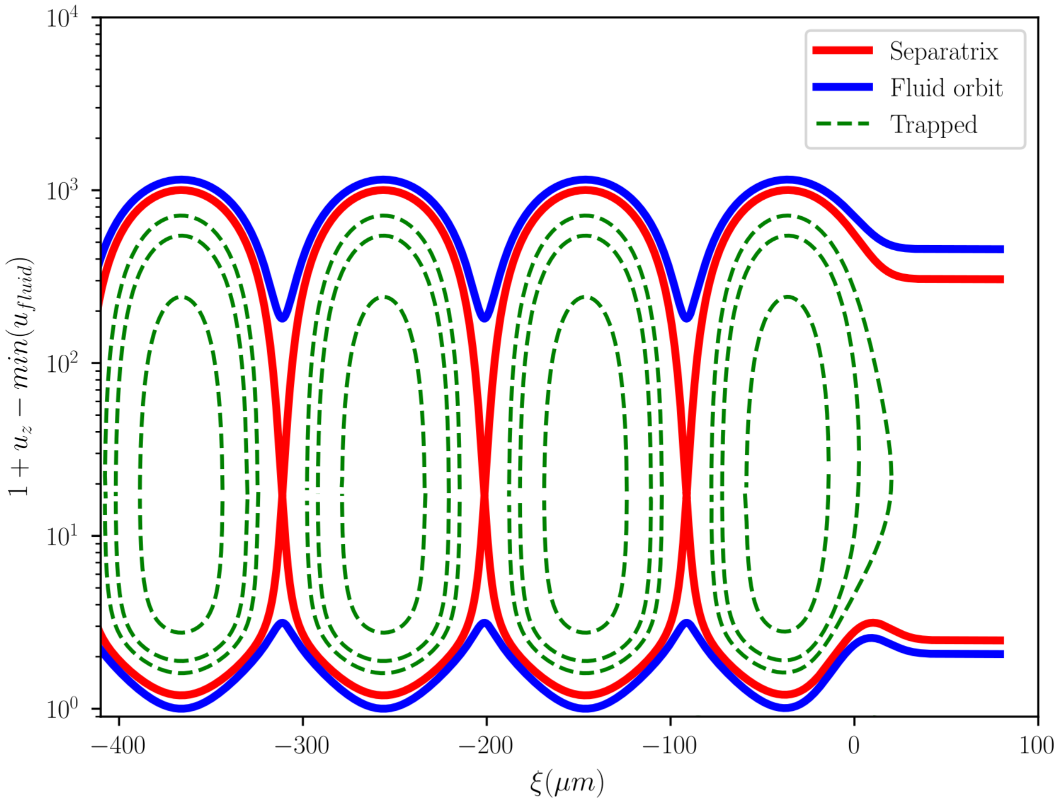

Figure 1.8: Phase space of a plasma wave in the co-moving coordinates driven by a laser pulse with $a_0 = 2$, $\tau_0 = 44$ fs in a plasma with a background electron density $n_0/n_c = 0.44 \times 10^{-2}$. The blue lines represents the trajectory of non-trapped electrons called fluid orbits, they contribute to the plasma wakefield formation. The red line represents the separatrix, which separates the trapping and non- trapping orbits. The green lines represent the trajectory of trapped electrons.

trapped electrons (green lines) corresponding to $H_{trapped} \leq H_{sep}$. The plasma wave potential of a trapped electron behind the laser pulse with a phase $\xi_{trapped}$ and $u_z(\xi_{trapped}) = \gamma_p\beta_p$ is $\phi(\xi_{trapped}) = \phi_{trapped} \geq \phi_{min}$.

From eq. (1.76) the Hamiltonian for a trapped electron can be written as

$$H_{trapped} = \sqrt{1 + \gamma_p^2\beta_p^2} - \phi_{trapped} - \gamma_p^2\beta_p^2 = \frac{1}{\gamma_p} - \phi_{trapped} \tag{1.80}$$

The necessary and sufficient condition for trapping can therefore be found: $H_{trapped} \leq H_{sep}$. For an electron initially located in the front of the laser pulse to be trapped and accelerated in the bubble regime, it must have an initial longitudinal momentum greater than the initial momentum of the separatrix $u_z(+\infty) > u_{z,sep}(+\infty) = \beta_p\gamma_p^2 H_{sep} - \gamma_p\sqrt{\gamma_p^2 H_{sep}^2 - 1}$ and a sufficient initial kinetic energy $E > E_{trapped} = m_e c^2(\sqrt{1 + u_{z,sep}(+\infty)} - 1)$, once it finds itself in the rear part of the bubble where fields are both accelerating and focusing.

The presented 1D model gives insight into the electrons dynamics and how they can be trapped. However, transverse effects and laser evolution which play a very important role during the interaction are neglected. The multi-dimensional study of self-trapping cannot be carried out analytically and need 3D numerical simulations using PIC codes in order to describe kinetic non-linear effects [Kostyukov et al., 2004; Kalmykov et al., 2011]. 3D simulations show that in order to reach the trapping threshold, the laser pulse should be shorter than λ_p.

1.5.2 Electrons injection schemes

Plasma densities typically used in laser driven acceleration in the non linear regime are in the range of $10^{18} - 10^{19}$ cm^{-3} corresponding to plasma wavelengths of $10 - 40\ \mu m$. Generated cavities in such wakefields have dimensions on the order of the plasma wavelength. Successful injection of electrons in these cavities requires fine tuning of the injection phase, the energy of the electrons and the strength of the plasma wakefield in order to place them in the closed orbits. In order to be efficiently accelerated, the electrons should be injected in the back of the cavity where the field is both focusing and accelerating. This makes the injection in such cavities very challenging. Several physical mechanisms leading to electrons riding on the wake have been demonstrated and further studied. The most important techniques are summarized below.

self-injection

A relatively simple and convenient way to inject electrons in the plasma wave is to directly trap and accelerate the electrons from the plasma itself when the plasma wave amplitude is close to the wave-breaking threshold. This technique is referred to as the *self-injection* scheme [Modena et al., 1995b; Umstadter et al., 1996a; Faure et al., 2004b; Benedetti et al., 2013]. Two distinct sub-categories can be distinguished: longitudinal and transverse self-injection.

Longitudinal injection

In longitudinal self-injection, the transverse motion is negligible and the process is similar to longitudinal wavebreaking in 1D. It is the result of the relativistic lengthening of the plasma wake that follows strong relativistic self-focusing effects. The only electrons that are trapped are those that were initially close to the propagation axis ($r_0 < R_b$) where the laser intensity and the wakefield amplitude are the highest and where the ponderomotive force is small. The injected electrons pass through the laser pulse without being strongly deviated, so they remain in the region of largest accelerating field E_z and gain energy while crossing the first period of the plasma wave. When they reach its rear, their longitudinal velocity exceeds the wake phase velocity and the electrons are eventually injected. Longitudinal self-injection is possible when the pulse self-focuses at the beginning of the propagation: a_0 steadily increases thus the plasma wavelength increases and the wake phase velocity decreases resulting in a sudden expansion of the bubble where electrons near the axis are trapped [Corde et al., 2013].

Longitudinal injection produces electron beams with low charge ($\sim 2 - 10$ pC) but also a relatively low divergence (quasi-monoenergetic spectrum). It ensures a good shot-to-shot stability since longitudinal injection happens at the beginning of the self-focusing process, which is less fluctuating than the intensity oscillations during the propagation.

Transverse injection

Contrarily to the longitudinal injection, transverse self-injection is a multi-dimensional effect that occurs in the bubble regime when electrons inside the sheath cross the axis to contribute to close the cavity in the bubble regime [Lu et al., 2007b]. It is usually triggered when the cavity frontier abruptly changes [Kalmykov et al., 2009; Kostyukov et al., 2010] due to the strong self-focusing of the laser. The injected electrons in this case, are initially located at approximately one laser waist from the axis ($r_0 \sim w_0$), where w_0 is the laser waist in vacuum [Kalmykov et al., 2011; Benedetti et al., 2013].

Transverse injection can be easily achieved with currently available setups and results in higher charge bunches ($> 50 - 100$ pC) but lower quality than the longitudinal one. The process lacks stability as it is triggered by self-focusing which is highly non linear and it is very sensitive to the shot-to-shot fluctuations of the laser intensity profile. Since injected electrons are far from the axis, the betatron oscillations are important leading to large beam divergence. Besides, the process can last for a long propagation distance leading to electron beams with large energy spread.

Both longitudinal and transverse injection were experimentally demonstrated by [Corde et al., 2013]. It was shown that it is possible to achieve transverse injection with the same experimental parameters as longitudinal injection but after a longer propagation of the laser in the plasma: electrons in the first bunch come from regions close to the axis and were injected in the beginning of the self-focus when the normalized laser amplitude is still low and the radial ponderomotive force close to the axis is small. Electrons in the second bunch originate from positions close to the laser waist, hence they were triggered by transverse injection. Usually, longitudinal self-injection is dominant at low electron plasma densities ($n_0 < 10^{19}$ cm $^-3$), while transverse self-injection is predominant at higher densities [Corde et al., 2013].

The self-injection scheme is unstable due to non-linear effects of the laser such as relativistic self-focusing and self-compression. In order to improve the electron bunch quality, more control over the injection process is desirable. In the following, several controlled injection techniques to overcome this shortcoming, are presented.

Ionization injection

Ionization injection is a technique based on the use of a mixture of low-Z gaz (hydrogen or helium) with a smaller percentage of high-Z gas (oxygen, nitrogen, or argon) [McGuffey et al., 2010; Pak et al., 2010; Pollock et al., 2011] or a pure high-Z gas [Singh and Sajal, 2009; Mori et al., 2009; Guillaume et al., 2015a] to control the injection process into the wakefield by ionizing deeply bound electrons from the high-Z gas at a proper phase inside the wakefield. Thanks to the difference in ionization potentials between successive ionization thresholds in large Z gas, some electrons are released later than others. On one hand, electrons from the low-Z atoms together with the electrons from the outer shells of the high-Z atoms are stripped from their atoms earlier by the edge of the laser, where the laser intensity is still relatively low. On the other hand, the electrons from the inner shell of the high-Z atoms are ionized near the peak of the pulse. They may be easily trapped directly in the bubble as they are born inside an optimal location of the wake and thus can be accelerated.

The advantage of using this method is that the energy required to trap electrons is reduced compared to the self-injection scheme, which allows to produce electron beams with a important charge at moderate laser energy. Due to the relativistic self-focusing effect, the laser is guided through a long distance where the peak intensity variations can trigger inhomogeneous continuous electrons injections, thus leading to electron beams with high charge but also large relative energy spread [Pak et al., 2010]. One way to overcome his limitation is to use two stages accelerators, with the first stage based on ionization injection technique followed by a second stage with only low-Z gas [Bourgeois et al., 2013].

Optical injection

Another way to trigger electron injection in the wakefield is optical or ponderomotive injection using a secondary laser pulse (injection pulse) that injects electrons precisely and locally in the wakefield driven by a primary intense laser (pump or excitation pulse). In fact, the interaction between the two laser pulses creates a beat wave that can provoke electrons injection. The first proposed configuration was based on two perpendicular pulses [Umstadter et al., 1996b]. The transverse ponderomotive force of the injection pulse provides some electrons with the necessary momentum to cross the wakefield separatrix and be trapped. An other scheme known as the colliding pulse optical injection scheme was suggested in [Esarey et al., 1997] and experimentally demonstrated by [Faure et al., 2006b] using two counter-propagating pulses . This technique has demonstrated a good control over the injected charge and energy gain, thus producing high quality electron beams. It was shown that the beam energy and charge of the accelerated particles were controlled by tuning the intensity and delay between the two pulses in order to adjust the injection phase and therefore the acceleration length which defines the final energy [Rechatin et al., 2009b].

Another colliding laser pulse scheme, where the the lasers are in circular polarization and the second pulse has a very low-energy, called cold optical injection was proposed by [Davoine et al., 2009]. In this scheme the longitudinal motion of electrons remains frozen during the interaction between the pulses by the injection pulse and the electrons can enter into the propagating plasma wave, at a phase-space position across the separatrix allowing their injection.

In the previous method the electrons were injected longitudinally. [Lehe et al., 2013b] have proposed a scheme where the pulses collision occuring in low densities results in a fast expansion of the bubble to control transverse injection. This scheme, known as the optical transverse injection demonstrated a generation of low emittance electron beam with relatively high charge. The two last schemes have been studied through PIC simulations but have not been experimentally demonstrated so far.

Although optical injection can provide extremely stable, quasi-monoenergetic bunches of electrons, the system is quite complicated to implement since it requires femtosecond level synchronization and micrometer level alignment.

Density transition injection

Another method of controlling the injection process is by using a downward density ramp. The inhomogeneities in the plasma can trigger local particles injection. The downward density transition causes slowing of the plasma wave phase velocity v_ϕ at the density ramp when the density downramp length is long compared to the plasma wavelength λ_p which lowers the threshold for trapping the plasma background electrons and causes wave-breaking of the wakefield in a localized manner. This idea was first demonstrated theoretically [Bulanov et al., 1998] the studied experimentally [Geddes et al., 2008; Gonsalves et al., 2011]. The change in the plasma phase velocity triggers an expansion of the bubble resulting in electrons injection at the back of the bubble. Nevertheless, a long downramp leads to continuous injection along the density ramp and thus a large energy spread. When using a sharper density transition with a length smaller than the plasma wavelength λ_p, the injection method is more commonly known as shock-front injection. This scheme has been both studied numerically [Kim et al., 2004; Brantov et al., 2008] and demonstrated experimentally by forming the density transition either with a second laser pulse propagating transversely to the main interaction pulse [Faure et al., 2010] or by a shock in a supersonic gas flow [Schmid et al., 2010; Burza et al., 2013]. By correctly tailoring the density transition, the injection process is controlled. Particularly, injection in sharper gradients leads to better beam quality.

Controlled injection techniques offer better regulation over the quality of the beam. However, they are usually hard to implement experimentally. With the increase in the laser power, self-injection which usually requires a high laser strength a_0 has become more accessible. Hence, we have chosen this scheme to study the properties of the produced electron bunches via PIC simulations with realistic laser profiles in chapter 4.

In figure 1.9, a summary of main but not exclusive achievements in LWFA experiments with the different injection techniques is presented [A. Ghaith, 2020]

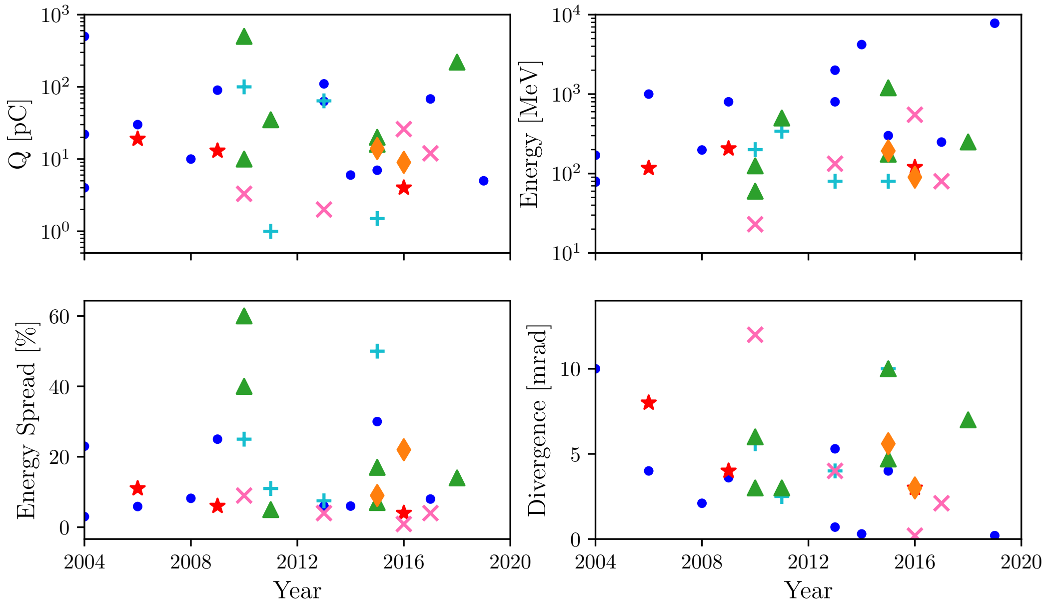

Figure 1.9: Beam charge (top left), energy (top right), energy spread (bottom left) and divergence (bottom right) reported in LWFA experiments obtained through different injection techniques. (●) Self-Injection [Mangles et al., 2004b; Geddes et al., 2004b; Faure et al., 2004a; Leemans et al., 2006; Osterhoff et al., 2008; Kneip et al., 2009; Kim et al., 2013; Wang et al., 2013; Leemans et al., 2014; Guillaume et al., 2015b; Gonsalves et al., 2019], (★) Colliding Pulse Injection [Faure et al., 2006b; Rechatin et al., 2009a; Hansson et al., 2016], (▲) Ionization Injection [McGuffey et al., 2010; Pak et al., 2010; Pollock et al., 2011; Golovin et al., 2015; Mirzaie et al., 2015; Couperus et al., 2017; Irman et al., 2018], (+) Downramp Injection [Faure et al., 2010; Gonsalves et al., 2011; Burza et al., 2013; Hansson et al., 2015], (×)Density Transition (/ Shock) Injection [Schmid et al., 2010; Buck et al., 2013; Wang et al., 2016; Swanson et al., 2017], (♦) Downramp / Shock + Ionization Injection [Thaury et al., 2015; Hansson et al., 2016]. The definition of the beam parameters in the given references may vary.

1.5.3 Laser propagation and modulation in plasma

At high intensities, electrons become relativistic and local properties of the medium are altered due to the effective relativistic mass increase of electrons in the plasma. In particular, the dispersion relation of the laser electromagnetic wave becomes

$$\omega_0^2 = c^2 k_0^2 + \omega_p(r)^2 \tag{1.81}$$

where $\omega_p(r)^2 = (\omega_{p0}^2/\gamma(r))(n_e(r)/n_0)$ is the effective plasma frequency.

The corresponding refractive index in the equation of propagation varies as a function of the laser intensity.

$$\eta(r) = \frac{ck_0}{\omega_0} = \sqrt{\frac{\omega_0^2 - \omega_p(r)^2}{\omega_0^2}} = \sqrt{1 - \frac{\omega_{p0}^2}{\omega_0^2}\frac{n_e(r)}{\gamma(r) n_0}} \tag{1.82}$$

we assume that $\omega_{p0}^2/\omega_0^2 \ll 1$ and $\gamma \simeq \gamma_\perp \simeq (1+a^2)^{1/2}$ since the leading-order motion of the electrons in the laser field is the quiver motion $\boldsymbol{p}_\perp = m_e c \boldsymbol{a}$. In the weakly relativistic case ($a^2 \ll 1$ and $\delta n_e \ll n_0$), the local group velocity of the drive laser can be written

$$\eta \simeq \frac{v_g}{c} \simeq \frac{c}{v_\phi} \simeq 1 - \frac{\omega_{p0}^2}{2\omega_0^2}\left(1 - \frac{a^2}{2} + \frac{\delta n_e}{n_0}\right) \tag{1.83}$$

Self-focus

In the standard theory of self-focusing of laser beams by relativistic effects [Sprangle et al., 1987], only the effects of the transverse quiver motion of the electrons are included in the expression1.83, while the density response has been neglected $n_e = n_0$:

$$\eta \simeq 1 - \frac{\omega_{p0}^2}{2\omega_0^2}\left(1 - \frac{a^2}{2}\right) \tag{1.84}$$

For a laser where the intensity is peaked on axis, typically a Gaussian pulse, $\partial a^2(r)/\partial r < 0$. This implies $\partial \eta/\partial r < 0$ and $\partial v_\phi/\partial r > 0$ ($\eta = c/v_\phi$) which satisfies the condition for refractive guiding. Hence, the on-axis phase velocity is less than the off-axis velocity, making the laser wavefront curved. Therefore, the plasma medium acts as a focusing lens in optics terminology, for the electromagnetic field of the laser. This mechanism is known as self-focusing, and plays an important role in laser guiding during its propagation to balance laser diffraction.

self-compression

Besides its evolution in the transverse direction, the beam size is also modulated in the longitudinal direction. The variation of plasma density along the propagation axis $\delta n_e(\xi)$ makes the laser pulse undergo different local refraction indices that will either compress or relax the laser in the temporal domain.

From equation eq. (1.83), the laser group velocity decreases $v_g < v_{g0}$ when $\delta n_e > 0$ while it increases $v_g > v_{g0}$ when $\delta n_e < 0$ where v_{g0} corresponds to the laser group velocity in the background plasma ($\delta n_e = 0$). As a consequence of this variations, the rear of the laser pulse moves faster than its front edge and the spectral bandwidth of the short laser pulse will increase. While most of the laser is redshifted the back is blueshifted specially when it comes to pulses longer than the plasma period [Schreiber et al., 2010]. This mechanism is called temporal compression or pulse shortening and it contributes to matching the laser pulse duration and plasma wave period when the initial laser pulse duration is long.

It can also lead to a piston shaped laser pulse sometimes responsible for continuous self-injection [Kalmykov et al., 2011].

1.5.4 Limits of acceleration

The maximum of energy that an electron accelerated in a plasma wave can gain ΔE can be estimated as the the product of the accelerating longitudinal field E_z and the acceleration length L_{acc} over which the electron undergoes the effect of the acceleration field.

$$\Delta E = eE_z L_{acc} \tag{1.85}$$

Both the amplitude of the accelerating field and the acceleration length depend on the regime of the laser wakefield. The acceleration distance is typically bounded with three main constraints: if not couter-balanced by a focusing mechanism, laser diffraction restricts acceleration to a length of the order of the Rayleigh length, pump depletion determines the length over which half of the laser energy is transferred to the plasma wave and dephasing length defines the distance in which accelerated electrons outrun the plasma wave and enter a decelerating phase. These three shortcomings are described next.

Laser diffraction

If the laser is not properly guided, its spot size expands progressively decreasing the intensity until the laser is not able to drive efficiently a substantial accelerating wakefield anymore. However this shortcoming can be mitigated in the non-linear regime by self-focusing which extends the acceleration length over few Rayleigh lengths by shaping the transverse density profile to act as a transient focusing lens. For a given beam divergence, there is a minimum threshold for laser intensity to compensate diffraction by self-focusing which will occur when the laser power P exceeds a critical power [Sprangle et al., 1992]

$$\mathrm{P}_c = \frac{8\pi\epsilon_0 m_e^2 c^5 \omega_0^2}{e^2\omega_p^2} \simeq 17\frac{\omega_0^2}{\omega_p^2}[\mathrm{GW}] \tag{1.86}$$

Practically, the refractive index is modified by other phenomena such as the plasma wave and the ponderomotive channelling [Hafizi et al., 2000]. For example, the plasma wave tends to defocus the laser pulse, which might block the pulse from self-focusing at P_c [Ting et al., 1990]. Meanwhile, ponderomotive channelling slightly relaxes the critical power for self-guiding to $\mathrm{P}_c = 16.8(\omega_0^2/\omega_p^2)[\mathrm{GW}]$.

However, in the linear regime the self-focusing is negligible and external guiding is requisite. Various methods of optical guiding can be applied to maintain the laser-plasma interaction for a longer propagation distance among which we mention using preformed plasma density channels [Steinhauer and Ahlstrom, 1971; Johnson and Chu, 1974; Leemans et al., 2006; Karsch et al., 2007; Walker et al., 2013] or dielectric capillaries [Cros et al., 2002; Desforges et al., 2014].

Laser pump depletion

Another common limit to the acceleration is the so-called pump depletion, denoted by L_{pd}, over which the driving laser has lost a substantial amount of energy. In fact, as the laser pulse propagates in the plasma, it transfers its energy to the plasma wave. This energy transfer progressively damps the amplitude of the laser and hence that of the wakefield resulting in the termination of the acceleration. The pump depletion length [Bulanov et al., 1992; Shadwick et al., 2009] can be estimated by equating the energy contained in the laser pulse to that transferred to the wakefield $E_{z,max}^2 L_{pd} \approx \int_\xi E_L^2 d\xi$ where E_L is the laser field and $E_{z,max}$ is the maximum of the longitudinal electric field of the plasma wave. For linearly polarized laser pulses, the depletion length [Esarey et al., 2004] can be estimated according to the following relations:

$$L_{pd} \propto \begin{cases} \frac{\lambda_p^3}{\lambda_0^2} a_0^{-2} & \text{if} \quad a_0 \ll 1 \\ \frac{\lambda_p^3}{\lambda_0^2} a_0 & \text{if} \quad a_0 > 1 \end{cases}$$

Pump depletion is bound to happen, but its consequences can be delayed by increasing the initial energy contained in the driver pulse and decreasing the plasma density or staging with a fresh pump pulse.

Electron dephasing

Another underlying cause that may cease the acceleration is electron dephasing, which is due to the fact that the group velocity of the laser pulse v_g is slightly lower than c. While relativistic electrons can reach velocities extremely close to the speed of light c, the plasma wave is bound to the group velocity of the laser pulse v_g. Therefore, electrons will eventually outrun the accelerating phase of the wakefield and slip into the decelerating phase over a length referred to as the electron dephasing length L_d [Tajima and Dawson, 1979; Esarey et al., 1996; Geddes et al., 2005].

In the linear regime, the maximum length over which the field is accelerating during one period is a quarter-wavelength distance from the laser pulse. In this case and supposing that electrons travel at the speed of light c, L_d can be evaluated as $\Delta v L_d / c = \lambda_p/4$ with $\Delta v = c - v_g$ and $v_g/c = 1 - \omega_p^2/2\omega_0^2$. Therefore:

$$L_d = \frac{\lambda_p^3}{2\lambda_0^2} \tag{1.87}$$

In the 3D bubble regime, the dephasing occurs once the electrons reach the center of the cavity where the accelerating field is zero. Beyond that point, they enter the decelerating zone and therefore do not gain energy anymore. The phase velocity of the plasma wave in 3D non-linear wakefield is modified and accordingly the dephasing length yields:

$$L_d \simeq \frac{2}{3}\frac{\omega_0^2}{\omega_p^2} R_b = \frac{4}{3}\frac{\omega_0^2}{\omega_p^2}\frac{\sqrt{a_0}}{k_p} = \frac{2}{3\pi}\frac{\lambda_p^3}{\lambda_0^2}\sqrt{a_0} \tag{1.88}$$

Although electron dephasing cannot be avoided, it can be delayed. Since the 3D non-linear dephasing length depends on both the plasma electron density and the laser intensity, it can be increased either by decreasing the plasma density (the laser propagates faster) or by increasing the laser intensity. Among acceleration limitations dephasing remains probably the most serious challenge for applications of LWFA. Several solutions to overcome this problem can be suggested such as staging with a second laser- plasma accelerator, where the electron bunch is re- injected into a new plasma wave at the appropriate phase before reaching the decelerating region. Another solution proposed theoretically by [Sprangle et al., 2001], suggests to spatially tailor the plasma density so that the accelerated bunch of electrons would see an accelerating field whose phase velocity is c. Later, this idea has been experimentally demonstrated at LOA by [Guillaume et al., 2015b] where a density step was introduced to reduce suddenly the plasma wavelength and therefore guarantee that the bunch would stay in an accelerating region for a longer time.

Beamloading effect

When the injected charge accumulated in the rear region becomes very important, the electron bunch can exert a space charge force that repels plasma electrons with a lighter relativistic mass away and distort the local wakefield. This effect is called beam loading [Katsouleas et al., 1987; Tzoufras et al., 2008] and can place severe limitations on the efficiency of the plasma-based accelerator by altering the bubble shape and the accelerating field to the point that it prevents further injection. The trapping process stops when the charge contained in the cavity compensates the ionic charge.

The loaded charge can be estimated in both linear and nonlinear plasma waves based on the following formulas:

$$Q = \begin{cases} \frac{\epsilon_0 m_e c^2}{2 r_e E_l} \left(\frac{n_l}{n_0}\right)^2 \left(1 - \frac{E_l^2}{E_0^2}\right) \\ \frac{\pi \epsilon_0 m_e c^2}{4^2 r_e E_{nl}} (k_p r_b)^4 \end{cases}$$

where E is the accelerating field, the subscript l represents quantities in the linear regime and nl those in the non-linear regime.

Scaling laws

Scaling laws play a crucial role in understanding and designing laser plasma accelerators, since they give an approximation of the optimal key parameters in LWFA. They have been established based on phenomenological considerations and 3D PIC simulations by [Lu et al., 2007a] and have been verified in the experiments. The table 1.1 summarizes the main scaling laws to find the limits leading to the termination of electrons acceleration and their corresponding energy gain in the different regimes.

	a_0	w_0	L_d	L_{pd}	γ_p	$\Delta E/m_e c^2$
Linear	< 1	λ_p	$\frac{w_0^2}{w_p^2}\lambda_p$	$\frac{w_0^2}{w_p^2}\frac{c\tau_0}{a_0}$	$\frac{w_0}{w_p}$	$a_0^2\frac{w_0^2}{w_p^2}$
1D non-linear	> 1	λ_p	$4a_0^2\frac{w_0^2}{w_p^2}\lambda_p$	$\frac{w_0^2}{w_p^2}\frac{c\tau_0}{3}$	$\sqrt{a_0}\frac{w_0}{w_p}$	$4a_0^2\frac{w_0^2}{w_p^2}$
3D non-linear	> 2	$\frac{\sqrt{a_0}}{\pi}\lambda_p$	$\frac{4}{3}\frac{w_0^2}{w_p^2}\frac{\sqrt{a_0}}{k_p}$	$\frac{w_0^2}{w_p^2}c\tau_0$	$\frac{1}{3}\frac{w_0}{w_p}$	$\frac{2}{3}a_0\frac{w_0^2}{w_p^2}$

Table 1.1: Summary of the scaling laws with w_0 is the matched laser waist, L_d the dephasing length [11], L_{pd} the depletion length, γ_p the relativistic factor of the plasma wave and ΔE the energy gain of an electron accelerated over the dephasing length.

1.5.5 Properties of the accelerated electron bunch

Electron beams generated from LWFA can be accelerated to high energies over a very short distance compared to conventional accelerators. This attractive feature that made them a potential candidate for multiple applications such as Free-Electron Lasers (FEL) [Nakajima, 2008;

---

[10] τ_0 here denotes directly the FWHM and not the laser duration as defined previously.

[11] τ_0 here denotes directly the FWHM and not the laser duration as defined previously.

Schlenvoigt et al., 2008], compact high-energy colliders [Schroeder et al., 2010; Humphries, 1990] or X-rays source (for instance using betatron radiation) for single-shot phase-contrast imaging [Fourmaux et al., 2011]. Nevertheless, accelerated electron beams from LWFA are still far from being monoenergetic. In fact, their energy spread presently of the order of a few percents [Pollock et al., 2011; Wiggins et al., 2010] is still very large compared to the one achieved conventional accelerators reaching 10^{-4} percent energy spread. Besides, they suffer from large divergence that reaches ~ 1 mrad [Plateau et al., 2012]. However, there have been some progress recently to make high-quality bunches foreseeable using different plasma sources such as capillary waveguides [Leemans et al., 2014] and tailored density profiles [Gonsalves et al., 2011]. In this section, the main electron bunch parameters to quantify its quality are presented. These definitions hold for the rest of the manuscript unless stated otherwise.

Bunch definition

Energy distribution dQ/dE of the accelerated bunch is one of the main properties in the beam quality study. It expresses the charge of electrons dQ in the interval between E and $E + dE$ as a function of the energy E. In order to reach capabilities of conventional accelerators, the peak energy must be increased and the energy spread strongly reduced.

In order to introduce the bunch parameters, one should define what is considered as a bunch. Among the various approaches to define the bunch, the root-mean-square (rms) and the full-width at half-maximum (FWHM) are the most commonly used estimators to define the bunch and thus its charge Q. In both ways, the definition is closely related to the peak energy of the beam Epeak which is defined as the energy where the charge per MeV is maximum.

FWHM bunch definition

In this approach, the bunch is defined as the part of the energy distribution between 2 full-width at half-maximum (FWHM) around the Energy peak. The FWHM corresponds to the width of the energy spectrum curve measured between the two abscissa corresponding to half of the maximum amplitude. The charge of the bunch Q is therefore defined as the charge contained in the delimited area by 2 FWHM around Epeak. Even though this definition suppose that the distribution of the electron bunch can be fitted with the Gaussian distribution, in reality it is not the case. Hence, the bunch is not necessarily centered on Epeak.

Nrms bunch definition

The definition of Nrms bunch is a more sophisticated one. It is based on the root-mean square of the energy part corresponding to the FWHM bunch definition. It can be calculated according to:

$$\Delta_{rms} = \sqrt{\langle(\Delta E_{FWHM} - \langle\Delta E_{FWHM}\rangle)^2\rangle} \tag{1.89}$$

where $\langle.\rangle$ defines the average over the macro-particles and within ΔE_{FWHM} as defined previously by 2 FWHM around the energy peak.

The charge of the bunch Q in this case is the fraction between $E_{\text{peak}} - N_{rms}\Delta_{rms}$ and $E_{\text{peak}} + N_{rms}\Delta_{rms}$ where N_{rms} can be chosen arbitrarily.

Energy spread

The energy spread, ΔE_{rms} is given by the following expression:

$$\Delta E_{rms} = \sqrt{\langle(E - \langle E\rangle)^2\rangle} \tag{1.90}$$

where $\langle.\rangle$ is the average over the bunch macro-particles.

It is usually more practical to define the energy spread in percentage by normalizing to the energy peak E$_{\text{peak}}$. In fig. 1.10, a typical energy spectrum of an electron bunch in the bubble regime from a PIC simulation is presented. The delimited area by the blue dashed lines indicates the bunch defined with FWHM estimator which gives an energy spread $\Delta E/E_{\text{peak}} = 4.7\%$. On the other hand, the area between the red dashed lines indicates the bunch estimation with Nrms definition using $N_{rms} = 3$. The latter gives $\Delta E/E_{\text{peak}} = 3.7\%$.

The properties of the bunch may then vary with the chosen bunch estimator. This makes the comparison between different simulations not straightforward.

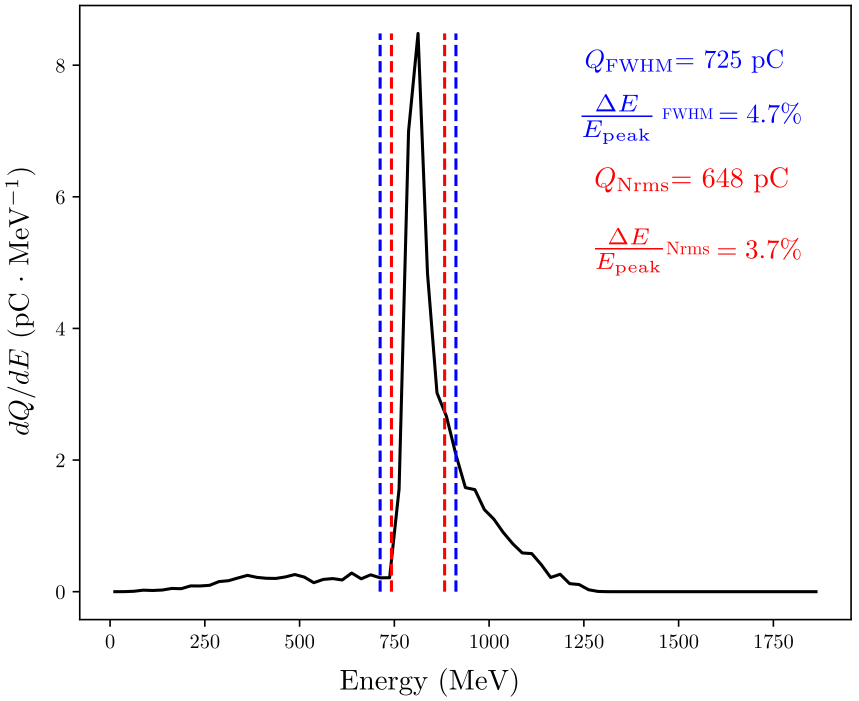

Figure 1.10: Energy spectrum dQ/dE from simulation of laser-accelerated electron beam in the non-linear regime. The bunch defined with $\Delta FWHM$ is delimited with the dashed blue lines while the bunch defined with $3\Delta_{rms}$ is delimited with dashed red lines.

Sources of energy spread increase There are several sources of energy spread increase in the electron injector. The following is not an exhaustive list.

Degradation due to long injected bunch: electrons in elongated bunch might not all be injected at the same phase in the wakefields. Due to the difference between the accelerating field experienced by the front and the back of the bunch, the energy spread tends to increase when electrons located at higher accelerating field region already have a larger energy.

Degradation by continuous injection: when the injection lasts for a relatively long duration, electrons injected later are not accelerated for as long as earliest ones, hence it creates a bulk of low energy electrons, often referred to as dark current [Schroeder et al., 2006]. This phenomenon results in a large energy spread.

Emittance

For a large variety of potential applications of laser-wakefield accelerators, producing high quality beams with high luminosity, i.e large numbers of particles and with very small bunch sizes, is crucial. This requirements can be translated in a low divergence and a low transverse beam size. However, these quantities evolve during the acceleration and can further be manipulated after the acceleration, by the use of drift spaces and focusing devices. A figure of merit and an intrinsic quantitative measurement of the transverse quality is the transverse emittance that will be presented in this paragraph along with a discussion regarding the sources of emittance growth, that degrade the beam quality.

The beam transverse emittance ϵ is a measure that combines the bunch energy spread as well as its transverse size and divergence. In the case of a beam propagating in the z direction, the transverse emittance is usually represented by the volume occupied by the beam in the transverse trace space (x, y, x', y') where $x' = p_x/p_z$ and $y' = p_y/p_z$ are the measures of angular deviation from straight motion along the propagation axis (velocity spread), thus related directly to the beam divergence [Floettmann, 2003] in the paraxial approximation where $p_x, p_y \ll p_z$ which is the case for relativistic electrons. Projecting this volume V onto the orthogonal planes $(x, x'), (y, y')$ results in the same expression for ϵ_x and ϵ_y. Therefore, for simplicity we limit the discussion to the x-dimension. It is convenient to describe the beam distribution in trace space as an ellipse (as shown in fig. 1.11) that best fits the electrons distribution with equation:

$$\gamma x^2 + 2\alpha x x' + \beta x'^2 = \epsilon_x \tag{1.91}$$

where α, β and γ are the Twiss parameters related through $\gamma\beta - \alpha^2 = 1$ [Ferrario, 2016]. From figure 1.11 we can see that β and γ quantify respectively the projected bunch size $X = \sqrt{\beta\epsilon}$ and its divergence $X' = \sqrt{\gamma\epsilon}$ while $\varphi = 1/2 \arctan(2\alpha/(\gamma - \beta))$ measures the bunch rotation during a drift in free space where α defines whether the bunch is converging towards the waist ($\alpha > 0$) or diverging away from it ($\alpha < 0$, as it is the case presented in the figure 1.11). As the beam propagates, the orientation and size of the trace-space ellipse change and hence the Twiss parameters vary accordingly. However, according to Liouville's theorem [Goldstein et al., 1980; C. Lejeune, 1980] the phase space volume V remains constant for a conservative system which means that the emittance is conserved under ideal accelerating conditions like propagation of the bunch in vacuum or through linear focusing systems. The geometrical emittance is calculated from the area occupied by the ellipse A in the trace space that best fits the beam distribution:

$$\epsilon_x = \frac{1}{\pi} \int_A dx dx' \tag{1.92}$$

Nevertheless, in practice electron beams do not have a well-defined shape and sometimes it is hard to fit well the electrons distribution with an ellipse in order to calculate its value. In addition to its geometrical definition, emittance can also be evaluated statistically based on the root mean square (rms) values for the first and second momenta of the distribution.

$$\epsilon_{x,rms} = \sqrt{\langle x^2 \rangle \langle x'^2 \rangle - \langle x x' \rangle^2} \tag{1.93}$$

where $\langle . \rangle$ defines the average value over all the particles in the bunch. The last term $\langle x x' \rangle$ indicates the correlation in trace-space between the bunch size x and the divergence x'. This definition is more general than the geometrical one since it is not limited by a specific shape and it is the one usually used in simulations analysis. From the definition in eq. (1.93), we can see that the emittance will decrease when the beam energy increases which is the case for the accelerated electrons in LWFA. In fact, while being accelerated, the longitudinal momentum of electrons increases drastically compared to the transverse momenta, resulting in a divergence reduction and thus a rms emittance decrease. It is more convenient when studying the evolution of the beam emittance throughout its propagation to take into account the energy dependence

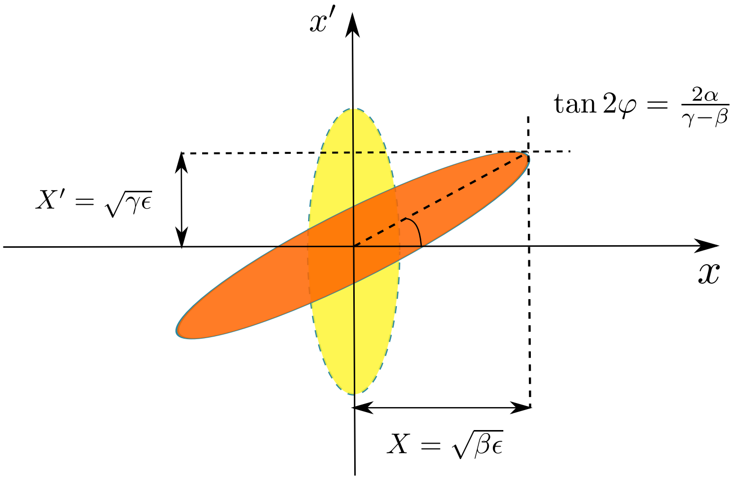

Figure 1.11: Electrons distribution represented by an ellipse in the transverse trace space (x, x_0). The geometrical emittance is the area of the ellipse multiplied by π. The yellow ellipse represents a bunch at waist while the orange one represents a bunch drifting in free space, diverging from the waist (adapted from **??**).

and define a normalized rms emittance which is invariant during acceleration. In this definition the transverse momentum $p_x = p_z x' = m_e c\beta\gamma x'$ is used instead of the divergence, the equation is written as:

$$\epsilon_{x,n,rms} = \frac{1}{m_e c}\sqrt{\langle\tilde{x}^2\rangle\langle\tilde{p_x}^2\rangle - \langle\tilde{x}\tilde{p_x}\rangle^2} \tag{1.94}$$

$$= \sqrt{\langle\tilde{x}^2\rangle\langle\beta^2\gamma^2\tilde{x}'^2\rangle - \langle\tilde{x}\beta^2\gamma\tilde{x}'\rangle^2} \tag{1.95}$$

where $\tilde{x} = x - \langle x\rangle$. Assuming that the correlation between the energy and transverse divergence is negligible, the normalized emittance can be approximated by:

$$\epsilon^2_{x,n,rms} = \langle\tilde{x}^2\rangle\langle\beta^2\gamma^2\rangle\langle\tilde{x}'^2\rangle - \langle\beta\gamma\rangle^2\langle\tilde{x}\tilde{x}'\rangle^2 \tag{1.96}$$

Introducing the definition of the energy spread as :

$$\sigma^2_E = \langle\beta^2\gamma^2\rangle - \langle\beta\gamma\rangle^2 \tag{1.97}$$

Equation (1.98) can be rearranged to be:

$$\epsilon^2_{x,n,rms} = \sigma^2_E\langle\tilde{x}^2\rangle\langle\tilde{x}'^2\rangle + \langle\beta\gamma\rangle^2(\langle\tilde{x}^2\rangle\langle\tilde{x}'^2\rangle - \langle\tilde{x}\tilde{x}'\rangle^2) \tag{1.98}$$

$$= \sigma^2_E\langle\tilde{x}^2\rangle\langle\tilde{x}'^2\rangle + \langle\beta\gamma\rangle^2\epsilon^2 \tag{1.99}$$

Assuming relativistic electrons ($\beta = 1$), the energy spread defined in eq. (1.97) is related to our definition of energy spread in eq. (1.90) by $\Delta E = m_e c^2\sigma_E$, and hence the normalized emittance reads:

$$\epsilon^2_{x,n,rms} = \frac{\Delta E^2}{m_e^2 c^4}\langle\tilde{x}^2\rangle\langle\tilde{x}'^2\rangle + \langle\gamma\rangle^2\epsilon^2 \tag{1.100}$$

To simplify the notations, $\sigma_x = \sqrt{\langle \tilde{x}^2 \rangle}$ is used to denote the bunch size and $\sigma'_x = \sqrt{\langle \tilde{x}'^2 \rangle}$ is used to denote its divergence. Equation (1.100) rewritten with new notations reads:

$$\epsilon^2_{x,n,rms} = \frac{\Delta E^2}{m_e^2 c^4} \sigma_x^2 \sigma_x'^2 + \langle \gamma \rangle^2 \epsilon^2 \tag{1.101}$$

We recover the expression of the un-normalized emittance in the second right-hand term. The resulting projected normalized emittance then becomes a function position σ_x, divergence σ'_x and energy spread ΔE. The main advantage of using the definition of the normalized rms emittance is the concatenation of all transverse properties in a single quantity. Thanks to small energy spread values in conventional accelerators beams, the first term is negligible and $\epsilon^2_{x,n,rms} \approx \langle \gamma \rangle^2 \epsilon^2$. However, the same does not apply to LWFA beams due to the large value of the energy spread as well as the big angular divergence which make the first term the leading one. Moreover, since the energy spread varies with the propagation distance, the normalized emittance is not constant in this scenario. The relation between normalized and un-normalized emittance is adressed in details in [Antici et al., 2012].

sources of emittance growth Theoretically and under ideal acceleration conditions, the emittance should remain constant throughout acceleration and further beam manipulation, thereby determined at injection. Small emittance is a major requirement for most of LWFA applications. It implies high focusability and the potential of generating high quality radiation sources. In order to lower the initial beam emittance, one should consider optimizing the conditions during the generation process of the particle beam by mitigating all possible sources of emittance growth. The degradation of the transverse quality of the beam can have several origins [Reiser, 2008] such as experiencing nonlinear forces or chromatic aberration of the focusing magnetic optics or transport line misalignment The most common ones for LWFA are the following.

Degradation by betatron oscillations: Electrons undergoing betatron oscillations rotate around the origin of (x, p_x) phase space with a frequency $\omega_\beta = \omega_p/\sqrt{2\gamma}$. Since γ varies across the bunch, each electron will rotate with its own frequency. In particular, low-energy electrons will rotate faster than high- energy electrons in phase space spreading out the area occupied by the whole bunch and increasing emittance. This phenomenon is known as decoherence [Michel et al., 2006b] and depicted in fig. 1.12.

Degradation by ξ-dependent linear focusing forces:

focusing forces can be linearly dependent on the longitudinal variable ξ (in the direction of their propagation) besides being transversely linear (i.e $F_x = -K_1(\xi)x$, $F_y = -K_2(\xi)y$). This phenomenon can happen for instance in the linear regime where the focusing forces close to the axis rotate the electrons at different ξ with different frequencies in the phase space which results also in decoherence [Mehrling et al., 2012] that distorts the beam ellipse in trace space. However, in this case the emittance is preserved per thin slice at a given ξ in time, for electrons close to the axis.

Degradation by nonlinear focusing forces: non-linear transverse focusing forces can be a source of emittance growth specially when the transverse size of the bunche in the laser wakefield is large. In the linear regime, electrons traveling very far from the axis experience much stronger focusing force $\boldsymbol{F}_\perp = -e\boldsymbol{E}_r$(eq. (1.67)) than the ones close to the axis due to the non-linear term $\exp(-2r^2/w_0^2)$. Therefore, outer particles phase in trace-space can evolve faster. Electrons initially distributed along a straight line will rotate at different frequencies depending on their transverse coordinate. Thus, their distribution in phase space later becomes distorted. However, this does not happen in the blow-out regime, because the focusing forces are perfectly linear in r and independent of ξ due to the ion cavity.

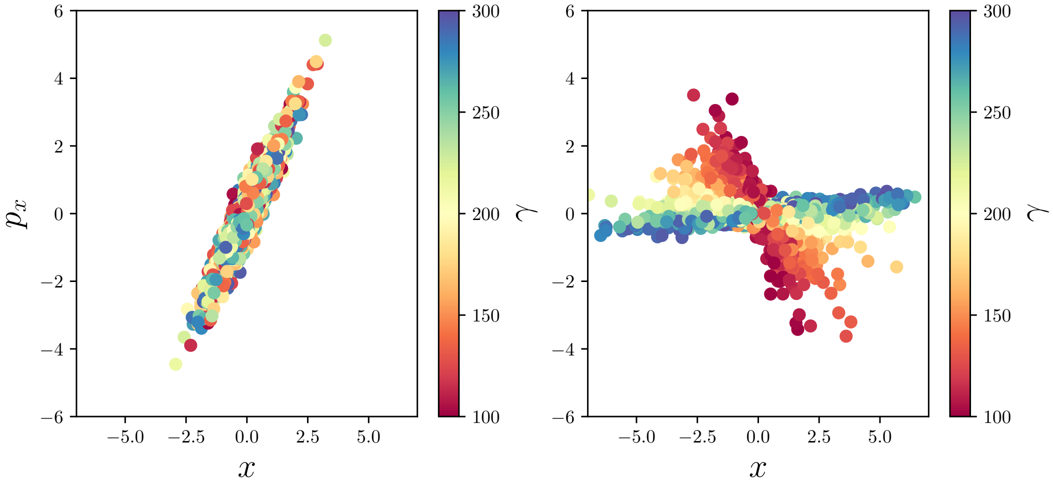

Figure 1.12: Schematic representation of the decoherence phenomenon: the initial distribution of the beam electrons in the phase space (x, p_x) presented in the left-hand panel encounters betatron oscillations and low-energy electrons rotate faster than the high-energy electrons in phase space resulting in the emittance growth and a final distribution presented in the right-hand panel.

Another type of non-linear forces are the space charge forces that the beam exerts on itself. However, the emittance increase due to them is significant only for low-energy, wide bunches. In LWFA, the bunches are usually narrow with high energies, which makes the degradation of emittance due to space-charge forces usually negligible in this case.

Degradation by direct interaction with the laser pulse: in [Shaw et al., 2017], it has been demonstrated that electrons being accelerated in a laser wakefield accelerator operating in the forced or blowout regimes gain significant energy from both the direct laser acceleration (DLA) and the laser wakefield acceleration mechanisms. DLA is the process by which electrons that undergo betatron oscillations in the transverse plane gain energy directly from the laser field itself when the betatron frequency coincides with the laser frequency [Pukhov et al., 1999]. Electrons are thus accelerated at the betatron resonance when the laser power overcomes significantly the critical power for self-focusing. In spite of the energy gain, the transverse momentum of the electrons increases from the DLA. This results in emittance growth of the electron bunch.

Chapter 2

Numerical modeling and simulation tools for laser-wakefield acceleration

With the fast-paced development of both computational resources and algorithmic methods, numerical simulations has become a reliable and cost-effective tool to corroborate theoretical predictions, complete experimental studies and investigate unexplored interaction regimes in the Laser WakeField Acceleration (LWFA).

In this context, the Particle-In-Cell (PIC) is the method of choice for LWFA community to study numerically the plasma dynamics at the kinetic level, since the full set of Maxwell's equations and the relativistic equations of motion are self-consistently evolved. Within the validity of classical physics and numerical accuracy, they provide a very detailed and accurate description on the processes occurring in the plasma.

This chapter is dedicated to the introduction of the standard PIC algorithm and the specific features of the open-source PIC code Smilei which has been extensively used in this thesis.

Contents

2.1 Numerical resolution of Maxwell-Vlasov system 44
  2.1.1 Overview of numerical methods 44
  2.1.2 Particle-In-Cell method 44
2.2 Overview of the Particle-In-Cell algorithm 46
  2.2.1 Particle dynamics 46
  2.2.2 Yee method 48
  2.2.3 The PIC cycle 50
2.3 The PIC code Smilei 55
  2.3.1 Parallelization strategy of the PIC algorithm with the FDTD scheme . 55

2.1 Numerical resolution of Maxwell-Vlasov system

2.1.1 Overview of numerical methods

Maxwell-Vlasov system eqs. (1.1) to (1.4) and eq. (1.41) can be numerically solved with an Eulerian approach [1] in the so-called Vlasov simulation. In this case, the phase space $(\boldsymbol{x}, \boldsymbol{p})$ is discretized along all directions and each particle distribution function $f_p(\boldsymbol{x}, \boldsymbol{p}, t)$ is evaluated on computation axes at each time step. However this approach, while very accurate, is extremely computationally expensive. In fact, discretizing the phase space in 3D geometry (3 space dimensions and 3 momentum dimensions) would require thousands of billions of cells.

Another shortcoming in Vlasov simulations is that one has to process many empty regions and maintain them as parts of the numerical arrays leading to an enormous waste of computational time and computer memory. This is depicted in fig. 2.1 (a). It shows a grid of the phase space (x, p_x) in 1D (one spatial coordinate and one momentum/velocity coordinate). The colored area represents the region occupied by plasma, where the associated two-dimensional distribution function $f_p(x, p_x)$ is non-zero whereas the rest of the area is void of particles. This burden becomes more significant with a higher dimensionality, yet crucial for a correct LWFA modelling.

Another more popular choice to solve the Maxwell-Vlasov system, is the **Particle-In-Cell (PIC)** algorithm which is a particle-mesh method. This numerical approach is based on a Lagrangian description [2] of the density distribution functions in the phase space. This description relies on the introduction of numerical macro-particles that represent a small volume of the phase space.

On the one hand, the electromagnetic quantities, obeying to Maxwell's equations are discretized using an Eulerian description on a fixed simulation grid. On the other hand, macro-particles are free to move in the simulation domain under the effect of Lorentz forces.

In this context, it represents a good numerical strategy to substantially reduce the computational complexity of the Maxwell-Vlasov system while still keeping an accurate kinetic description of the physics at play.

The PIC method, extensively used in this work, is presented hereafter with more details.

2.1.2 Particle-In-Cell method

The Particle-In-Cell (PIC) method [Hockney and Eastwood, 1988; Birdsall and Langdon, 2004] is the most frequently used approach to study numerically the plasma dynamics at the kinetic level. It assumes that the distribution function of each species is given by the superposition of several elements called macro-particles. Each macro-particle regroups physical particles close to each other in phase space fig. 2.1 (b). Thus, the distribution function of each species s can be written as a sum of N elementary functions assigned to each macro-particle p of this species.

$$f_s(\boldsymbol{x}, \boldsymbol{p}, t) = \sum_{p=1}^{N_s} f_p(\boldsymbol{x}, \boldsymbol{p}, t) \tag{2.1}$$

where N_s is the total number of macro-particles of the species s in the domain.

The specific functional form of each macro-particle describes the distribution in the phase space $(\boldsymbol{x}, \boldsymbol{p})$ of the actual particles. This is performed by assigning a weight w_p and a shape function S to the macro-particles.

---

[1] The Eulerian description is often described with an analogy of watching the flow of the river from the bridge

[2] In the Lagrangian description, we follow the behavior of the particle. It is compared to sitting in a boat carried by the water

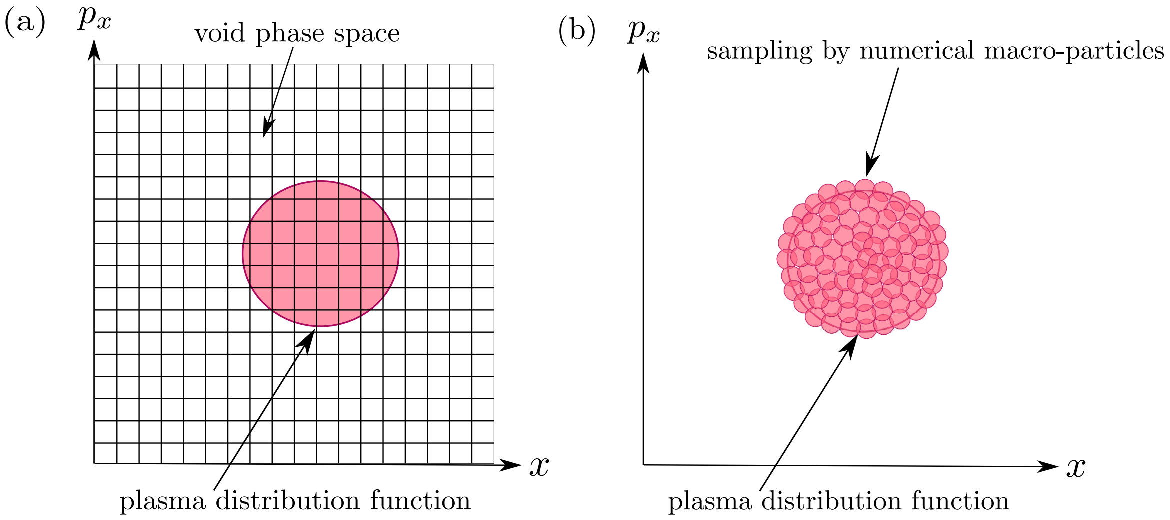

Figure 2.1: Kinetic plasma simulations: (a) Vlasov method, using an Eulerian grid in the phase space. (b) PIC method, where numerical macro-particles describe the distribution function.

$$f_p(\boldsymbol{x}, \boldsymbol{p}, t) = w_p S_x(\boldsymbol{x} - \boldsymbol{x_p}) S_p(\boldsymbol{p} - \boldsymbol{p_p}) \tag{2.2}$$

In this equation, S_x and S_p are the shape functions of the macro-particles respectively in space and momentum.

To simplify the calculation, the shape function is a fixed function verifying $\int S = 1$, which is identical for all macro-particles of all species. The macro-particle is supposed to have a certain finite spatial extent around its average position $\boldsymbol{x_p}$ with a definite momentum $\boldsymbol{p_p}$ at all times. This means that $S_p(\boldsymbol{p} - \boldsymbol{p_p})$ is chosen to be a Dirac impulse $\delta_p(\boldsymbol{p} - \boldsymbol{p_p})$ in order to ensure that there is no deformation of $S_x(\boldsymbol{x} - \boldsymbol{x_p})$. The latter is the support function centered at the position of the macro-particle. It represents the spatial extent of one macro-particle. This choice has the fundamental advantage that if all particles within the element of phase space described by one computational particle have the same speed, they remain close to each other in phase space during the subsequent evolution. Since each macro-particle usually stands for a large number of physical particles of the same species, its spatial shape function shows a non-Dirac shape function.

In PIC simulation, the plasma involves displacements of charges that modify the electric and magnetic fields discretized on a spatial grid and calculated by solving Maxwell's equations. Meanwhile, particles are moving freely in space and their contributions to the local charge and current densities are calculated on the neighboring grid nodes. Therefore, interpolations between particle variables $(\boldsymbol{x_p}, \boldsymbol{p_p})$ and grid variables $(\boldsymbol{E}, \boldsymbol{B}, \rho, \boldsymbol{J})$ are required. Because the shape factor has a bounded support that spans few grid cells, its contribution is zero for most of the cells and only the grid cells that are in the immediate neighborhood of the macro-particles contribute to the interpolation.

The simplest method consists in depositing the particle current to the Nearest Grid Point (NGP method). Yet, when a particle travels through the grid, its contribution suddenly shifts from one grid point to its neighbor, provoking a statistical fluctuation both in the charge and the current densities. This introduces, in its turn, a fluctuation in electromagnetic fields and thus in the force acting on the particles and results in numerical noise. Even though this noise can be smoothed by increasing the number of particles, it is not sufficient since the noise scales only as the inverse of the square root of the number of particles. Hence, the NGP method is seldom used. Instead, it is substituted with higher-order shape functions that involve one or more grid cells of the immediate neighborhood of the particles contributing to the interpolation.

Choice of particle shape functions

The canonical expressions for the shape functions are the so called b-splines through which the particle contribution is assigned to several neighbors [Lapenta, 2015]. The b-spline functions are a series of consecutively higher-order functions obtained from each other by convolution. The first b-spline is the flat-top function corresponding to the NGP method, also known as the zero-order weighting. Below, we present its expression for the 1D case for simplicity reasons.

$$b_0(\xi) = \begin{cases} 1 & \text{if } |\xi| < 1/2 \\ 0 & \text{otherwise} \end{cases} \quad \text{for NGP} \tag{2.3}$$

The subsequent b-splines b_l are obtained by successive integration via the following generating formula:

$$b_l(\xi) = \int_{-\infty}^{\infty} b_0(\xi - \xi') b_{l-1}(\xi - \xi') \tag{2.4}$$

The Cloud-In-Cell (CIC) method, also known as the first-order area weighting, corresponds to $l = 1$ and involves non-zero contribution to two neighbors which allows for an accuracy improvement at the cost of increasing the number of arithmetic operations per macro-particle for each time step. The Triangular-Shaped density Cloud (TSC) method further improves the accuracy of interpolation of field quantities to particles. It involves the contribution of three grid-points and corresponds to the third b-spline $l = 2$, implying even a higher computational cost than the CIC method.

$$b_1(\xi) = \begin{cases} 1 - |\xi| & \text{if } |\xi| < 1 \\ 0 & \text{otherwise} \end{cases} \quad \text{for CIC} \tag{2.5}$$

$$b_2(\xi) = \begin{cases} \frac{3}{4} - \xi^2 & \text{if } |\xi| < 1/2 \\ \frac{1}{2}\left(\frac{3}{2} - |\xi|\right)^2 & \text{if } 1/2 < |\xi| < 3/2 \\ 0 & \text{otherwise} \end{cases} \quad \text{for TSC} \tag{2.6}$$

Based on the b-splines, the spatial shape function of PIC methods is chosen as:

$$S_x(\boldsymbol{x} - \boldsymbol{x_p}) = b_l\left(\frac{\boldsymbol{x} - \boldsymbol{x_p}}{\Delta_x}\right) \tag{2.7}$$

where Δx is the cell size.

The choice of the interpolation method is a trade-off between numerical noise and computational cost. An interpolation involving many neighbors (such as TSC) typically reduces the noise, but requires of course more operations. The three commonly used shape functions corresponding to the three first b-splines are depicted in fig. 2.2.

2.2 Overview of the Particle-In-Cell algorithm

2.2.1 Particle dynamics

The macro-particles can be seen as collisionless solid bodies driven by electromagnetic forces. For each macro-particle p, $(\boldsymbol{x}_p(t), \boldsymbol{p}_p(t))$ follow a well determined Vlasov characteristic line in

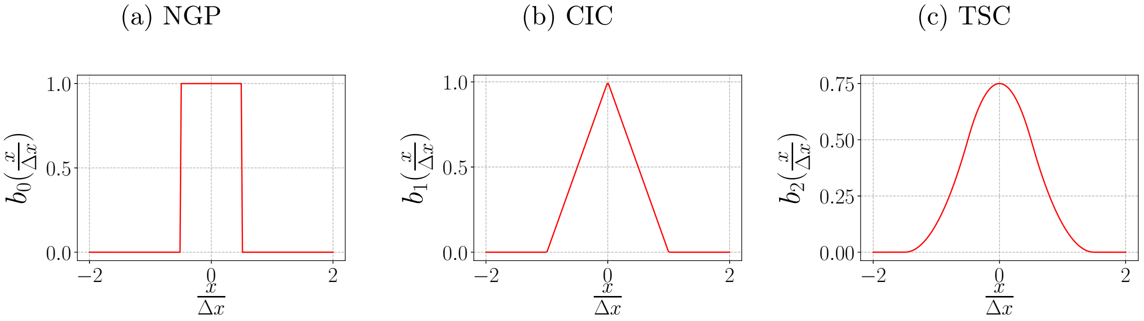

Figure 2.2: Particle shape functions in the x-direction, in units of grid cells. a) is the b-spline of order 0 corresponding to the Nearest Grid Point method. b) is the b-spline of order 1 corresponding to the Cloud-In-Cell method. c) is the b-spline of order 2 corresponding to the convolution of the Triangular-Shaped density Cloud method.

the phase space, specified by eq. (1.42). Macro-particles have a finite size in space due to their shape functions. Therefore, $\boldsymbol{E}$ and $\boldsymbol{B}$ are averaged over the spatial extent of the macro-particle.

We note each macro-particle with an index p, its mass with m_p, charge with q_p [3], position with $\boldsymbol{x}_p$ and momentum with $\boldsymbol{p}_p = \boldsymbol{v}_p\sqrt{m_p^2 + \boldsymbol{p}_p^2/c^2}$. The Lorentz force acting on the particles is computed from the electric and magnetic fields evaluated at the particle position by :

$$\boldsymbol{F}_p = q_p(\bar{\boldsymbol{E}}(\boldsymbol{x}_p) + \boldsymbol{v}_p \times \bar{\boldsymbol{B}}_p(\boldsymbol{x}_p)) \tag{2.8}$$

where $\bar{\boldsymbol{E}}$ and $\bar{\boldsymbol{B}}$ are the averages of the electromagnetic fields $\boldsymbol{E}$ and $\boldsymbol{B}$ over the macro-particle spatial extent.

The evolution of the particle dynamics is described by the following equations:

$$\frac{d\boldsymbol{x}_p}{dt} = \boldsymbol{v}_p = \frac{\boldsymbol{p}_p}{\sqrt{m_p^2 + \boldsymbol{p}_p^2/c^2}} \qquad \frac{d\boldsymbol{p}_p}{dt} = q_p[\ \bar{\boldsymbol{E}}(\boldsymbol{x}_p) + \boldsymbol{v}_p \times \bar{\boldsymbol{B}}(\boldsymbol{x}_p)\ ] \tag{2.9}$$

$$\text{where} \qquad \bar{\boldsymbol{E}} = \int S_x(\boldsymbol{x'} - \boldsymbol{x}_p)\boldsymbol{E}(\boldsymbol{x'})\, d\boldsymbol{x'} \qquad \bar{\boldsymbol{B}} = \int S_x(\boldsymbol{x'} - \boldsymbol{x}_p)\boldsymbol{B}(\boldsymbol{x'})\, d\boldsymbol{x'} \tag{2.10}$$

The evolution of the fields on the grid is tightly coupled with the motion of the charged macro-particles through this grid. This coupling requires some kind of weighting procedure between the macro-particles and the grid to build the charge and current densities on the grid, and for interpolating forces that are found on the grid back to the particles.

Since the particles are weighted to the grid points, their charge is effectively a charge smoothed over the grid cell, hence the name of the method. The charge density ρ and current density $\boldsymbol{J}$ evaluated at the grid are:

$$\rho = \sum_s q_s \int f_s\ d\boldsymbol{p} \qquad \boldsymbol{J} = \sum_s q_s \int \frac{\boldsymbol{p}_p}{\sqrt{1 + \boldsymbol{p}_p^2}} f_s\ d\boldsymbol{p} \tag{2.11}$$

---

[3] All the real particles represented by a given macro-particle have the same mass and charge

More precisely and taking into account the definition of f_s eq. (2.2), ρ and $\boldsymbol{J}$ are expressed as the following

$$\rho = \sum_s q_s \sum_p w_p \, S_x(\boldsymbol{x} - \boldsymbol{x}_p) \qquad \boldsymbol{J} = \sum_s q_s \sum_p w_p \, \boldsymbol{v}_p S_x(\boldsymbol{x} - \boldsymbol{x}_p) \tag{2.12}$$

After initializing the plasma macro-particles and initial fields in the simulation domain, the fields are interpolated to macro-particles whose positions and momenta are updated under the effect of Lorentz force modifying as a consequence the charge densities and currents. Those charge and currents are projected onto the simulation grid nodes then used to update the electromagnetic fields over one time step on the simulation domain.

2.2.2 Yee method

Conversely to macro-particles which move freely across the grid and are therefore only discretized in time, fields and densities have to be discretized in both space and time.

In 3D cartesian coordinates, Maxwell's equations read:

$$\begin{aligned}
\frac{1}{c^2}\frac{\partial E_x}{\partial t} &= \frac{\partial B_z}{\partial y} - \frac{\partial B_y}{\partial z} - \mu_0 J_x & \qquad \frac{\partial B_x}{\partial t} &= -\frac{\partial E_z}{\partial y} + \frac{E_y}{\partial z} \\
\frac{1}{c^2}\frac{\partial E_y}{\partial t} &= \frac{\partial B_x}{\partial z} - \frac{\partial B_z}{\partial x} - \mu_0 J_y & \qquad \frac{\partial B_y}{\partial t} &= -\frac{\partial E_x}{\partial z} + \frac{E_z}{\partial x} \\
\frac{1}{c^2}\frac{\partial E_z}{\partial t} &= \frac{\partial B_y}{\partial x} - \frac{\partial B_x}{\partial y} - \mu_0 J_z & \qquad \frac{\partial B_z}{\partial t} &= -\frac{\partial E_y}{\partial x} + \frac{E_x}{\partial y}
\end{aligned} \tag{2.13}$$

Thanks to its simplicity, the Yee method [Yee, 1966] also referred to as the Finite-Difference Time-Domain (FDTD) method, is the most popular technique to solve Maxwell's equations by introducing a numerical spatial grid. The time-dependent Maxwell's equations are discretized using central-difference approximations to the space and time partial derivatives.

Spatial discretization: The spatial numerical grid for field discretization used in this method is known as the Yee lattice. This space grid defines two spatially staggered meshes (i.e shifted by a half-cell) along each axis, usually referred to as primal and dual grids, where the electric and magnetic fields $\boldsymbol{E}$ and$\boldsymbol{B}$, the currents $\boldsymbol{J}$ and the charge densities ρ are discretized.

One can distinguish the standard Finite-Difference scheme from the Non-Standard finite-difference (NSFD) schemes where both use the Yee lattice [Yee, 1966], but the computational stencil to discretize Maxwell's equations is altered. In fact, in NSFD schemes such as *Cole-Karkkainen* [Gjonaj et al., 2006], *Cowan* [Cowan et al., 2013] and *Lehe* [Lehe et al., 2013a], the fields are still defined at the same position as in the Yee lattice, but the discretization of the space derivatives in the Maxwell-Faraday equation is modified. However, the NSFD solvers are not presented in this manuscript and the study case is limited to standard finite differences when the Finite Difference Time Domain solver is used.

The Yee lattice is captured in fig. 2.3 along with the field notations which will be used in section 2.2.3.

Time discretization: The Maxwell equations are also discretized in time using a centered scheme, where the electromagnetic fields $\boldsymbol{E}$ and $\boldsymbol{B}$ are staggered by a half time step: $\boldsymbol{E}$ is defined at integer time steps $n\Delta t$ and $\boldsymbol{B}$ is defined at half-integer time steps $(n+1/2)\Delta t$.

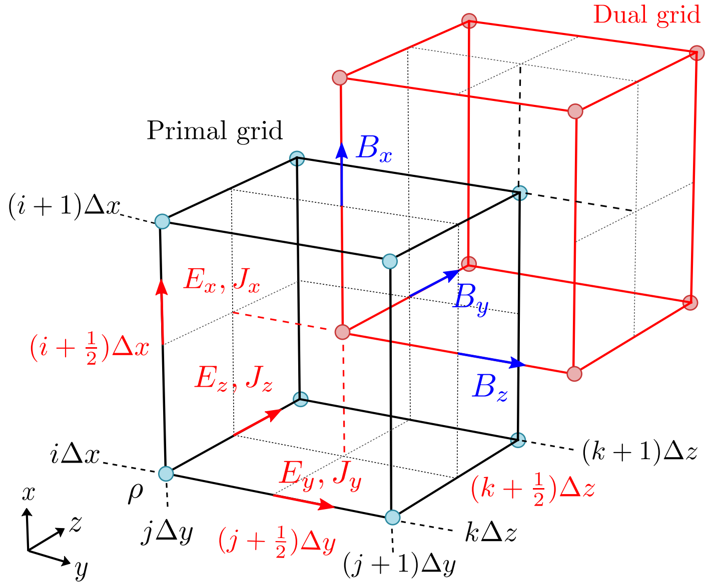

Field	Position in space and time				Notation
	x	y	z	t	
E_x	$(i+\frac{1}{2})\Delta x$	$j\Delta y$	$k\Delta z$	$n\Delta t$	${E_x}^{n}_{i+\frac{1}{2},j,k}$
E_y	$i\Delta x$	$(j+\frac{1}{2})\Delta y$	$k\Delta z$	$n\Delta t$	${E_y}^{n}_{i,j+\frac{1}{2},k}$
E_z	$i\Delta x$	$j\Delta y$	$(k+\frac{1}{2})\Delta z$	$n\Delta t$	${E_z}^{n}_{i,j,k+\frac{1}{2}}$
B_x	$i\Delta x$	$(j+\frac{1}{2})\Delta y$	$(k+\frac{1}{2})\Delta z$	$(n+\frac{1}{2})\Delta t$	${B_x}^{n+\frac{1}{2}}_{i,j+\frac{1}{2},k+\frac{1}{2}}$
B_y	$(i+\frac{1}{2})\Delta x$	$j\Delta y$	$(k+\frac{1}{2})\Delta z$	$(n+\frac{1}{2})\Delta t$	${B_y}^{n+\frac{1}{2}}_{i+\frac{1}{2},j,k+\frac{1}{2}}$
B_z	$(i+\frac{1}{2})\Delta x$	$(j+\frac{1}{2})\Delta y$	$k\Delta z$	$(n+\frac{1}{2})\Delta t$	${B_z}^{n+\frac{1}{2}}_{i+\frac{1}{2},j+\frac{1}{2},k}$
ρ	$i\Delta x$	$j\Delta y$	$k\Delta z$	$n\Delta t$	$\rho^{n}_{i,j,k}$
J_x	$(i+\frac{1}{2})\Delta x$	$j\Delta y$	$k\Delta z$	$(n+\frac{1}{2})\Delta t$	${J_x}^{n+\frac{1}{2}}_{i+\frac{1}{2},j,k}$
J_y	$i\Delta x$	$(j+\frac{1}{2})\Delta y$	$k\Delta z$	$(n+\frac{1}{2})\Delta t$	${J_y}^{n+\frac{1}{2}}_{i,j+\frac{1}{2},k}$
J_z	$i\Delta x$	$j\Delta y$	$(k+\frac{1}{2})\Delta z$	$(n+\frac{1}{2})\Delta t$	${J_z}^{n+\frac{1}{2}}_{i,j,k+\frac{1}{2}}$

Figure 2.3: Schematic representation of fields staggering on the Yee lattice in 3D: i,j,k are integers corresponding to the primal grid (Black) and $i+\frac{1}{2}$, $j+\frac{1}{2}$, $k+\frac{1}{2}$ are half-integers corresponding to the dual grid (red). The table shows at which position and time each component of the fields is defined where Δx, Δy, Δz are the spatial steps of the grid.

In the FDTD method, the Maxwell's equations are solved on the numerical grid with a second-order accurate explicit solver. This second- order convergence is ensured by centering the differentiation both in time and in space without increasing the computational cost significantly provided that both the fields and the charge and current densities are evaluated at specific times, and positions that allow for a spatio-temporal leap-frog integration of Maxwell's equations.

The coupling with the macro-particles via the source term $\boldsymbol{J}$ has to be dealt with. We deduce from the equations (2.13) that current density and the magnetic field should be calculated at the same time step which is half time steps $(n + 1/2)\Delta t$. From the continuity equation,

$$\frac{\partial \rho(\boldsymbol{x}, t)}{\partial t} = -\nabla \boldsymbol{J}(\boldsymbol{x}, t) \tag{2.14}$$

it is deduced that the charge density should be evaluated at the same time as the electric field $n\Delta t$.

Even though macro-particles are free to move across the grid and thus their momenta/positions are not discretized spatially, they are discretized in time. Their discretization relies on temporal staggering between position and momentum, in order to enable leap-frog integrations of macro-particles dynamics as well.

2.2.3 The PIC cycle

After introducing the basics of the PIC method, we present here in details the different steps involved in this process and their ordering in time starting from a given configuration.

Let us assume that at a given time step $n\Delta t$, the following quantities $\boldsymbol{B}^{n-1/2}$, $\boldsymbol{E}^{n}$ and $\boldsymbol{B}^{n+1/2}$ as well as $\boldsymbol{x}_p^n$ and $\boldsymbol{p}_p^{n-1/2}$ corresponding to the Yee lattice in fig. 2.3 are known. One single update of these quantities over one time step is known as a PIC *cycle* or PIC *loop*, illustrated in fig. 2.4. This section describes the operations that allow us to obtain the unknown quantities $\boldsymbol{E}^{n+1}$, $\boldsymbol{B}^{n+3/2}$, $\boldsymbol{x}_p^{n+1}$ and $\boldsymbol{p}_p^{n+1/2}$ at the next iteration $(n + 1)\Delta t$ from the previous known quantities.

Interpolation

To solve the macro-particles dynamics, the evaluation of Lorentz force on their positions is required. Hence, the knowledge of $\bar{\boldsymbol{E}}(\boldsymbol{x}_p)$ and $\bar{\boldsymbol{B}}(\boldsymbol{x}_p)$ defined by eq. (2.10) on the grid is also needed. For this, the electromagnetic fields initially defined on the mesh are interpolated on the macro-particles positions employing shape functions. Therefore, eq. (2.10) is discretized on the Yee grid with respect to the staggering of $\boldsymbol{E}$ and $\boldsymbol{B}$ in time and space:

$$\begin{aligned}
\bar{\boldsymbol{E}}^n(\boldsymbol{x}_p^n) = \sum_{i,j,k} \Big[& P_{i+\frac{1}{2},j,k}(\boldsymbol{x}_p^n) {E_x}^{n}_{i+\frac{1}{2},j,k} \boldsymbol{e}_x \\
& + P_{i,j+\frac{1}{2},k}(\boldsymbol{x}_p^n) {E_y}^{n}_{i,j+\frac{1}{2},k} \boldsymbol{e}_y \\
& + P_{i,j,k+\frac{1}{2}}(\boldsymbol{x}_p^n) {E_z}^{n}_{i,j,k+\frac{1}{2}} \boldsymbol{e}_z \Big]
\end{aligned} \tag{2.15}$$

$$\begin{aligned}
\bar{\boldsymbol{B}}^n(\boldsymbol{x}_p^n) = \sum_{i,j,k} \Big[& P_{i,j+\frac{1}{2},k+\frac{1}{2}}(\boldsymbol{x}_p^n) \frac{1}{2} \left({B_x}^{n+\frac{1}{2}}_{i,j+\frac{1}{2},k+\frac{1}{2}} + {B_x}^{n-\frac{1}{2}}_{i,j+\frac{1}{2},k+\frac{1}{2}} \right) \boldsymbol{e}_x \\
& + P_{i+\frac{1}{2},j,k+\frac{1}{2}}(\boldsymbol{x}_p^n) \frac{1}{2} \left({B_y}^{n+\frac{1}{2}}_{i+\frac{1}{2},j,k+\frac{1}{2}} + {B_y}^{n-\frac{1}{2}}_{i+\frac{1}{2},j,k+\frac{1}{2}} \right) \boldsymbol{e}_y \\
& + P_{i+\frac{1}{2},j+\frac{1}{2},k}(\boldsymbol{x}_p^n) \frac{1}{2} \left({B_z}^{n+\frac{1}{2}}_{i+\frac{1}{2},j+\frac{1}{2},k} + {B_z}^{n-\frac{1}{2}}_{i+\frac{1}{2},j+\frac{1}{2},k} \right) \boldsymbol{e}_z \Big]
\end{aligned} \tag{2.16}$$

A straightforward solution to determine the interpolation factors $P_{i',j',k'}$ is by integrating the *shape function* $S_x(\boldsymbol{x} - \boldsymbol{x}_p)$ between two grid-points over a length given by the cell size

$$P_{i',j',k'}(\boldsymbol{x}_p^n) \equiv \int_{(i'-\frac{1}{2})\Delta x}^{(i'+\frac{1}{2})\Delta x} dx \int_{(j'-\frac{1}{2})\Delta y}^{(j'+\frac{1}{2})\Delta y} dy \int_{(k'-\frac{1}{2})\Delta z}^{(k'+\frac{1}{2})\Delta z} dz \; S(\boldsymbol{x} - \boldsymbol{x}_p^n) \tag{2.17}$$

$$\text{where} \quad P_{i',j',k'}(\boldsymbol{x}_p^n) = P_{i'}(x_p^n)P_{j'}(y_p^n)P_{k'}(z_p^n) \quad \text{and} \quad \sum_{i',j',k'} P_{i',j',k'}(\boldsymbol{x}_p^n) = 1 \tag{2.18}$$

i',j',k' can be integers or half-integers. Equations (2.15) and (2.16) are the discretized version of eq. (2.10) and can be derived from it by considering that the fields $\boldsymbol{E}$ and $\boldsymbol{B}$ are piecewise constant in between the grid points.

Since the shape factors have a bounded support that cover few grid cells as shown in fig. 2.2, the sums in eq. (2.15) and eq. (2.16) over i, j, k are restricted only to the few immediate neighboring cells of the macro-particles which contribute to the interpolation. They depend on the order of the interpolation according to the choice of the shape factors [Hockney and Eastwood, 1988].

To use the leap-frog algorithm for the equations of motion, one needs to know the value of $\bar{\boldsymbol{B}}$ at the integer time $n\Delta t$ in eq. (2.16), whereas $\boldsymbol{B}$ is known at half-integer times on the grid. For this reason, we use the average in time value of $\boldsymbol{B}^n = (\boldsymbol{B}^{n-1/2} + \boldsymbol{B}^{n+1/2})/2$.

Particle pusher

Once the fields $\bar{\boldsymbol{E}}^n$ and $\bar{\boldsymbol{B}}^n$ are determined according to the previous step, the discretized equations of motion eq. (2.19) are used to obtain $(\boldsymbol{p}_p^{n+1/2}, \boldsymbol{x}_p^{n+1})$ from $(\boldsymbol{p}_p^{n-1/2}, \boldsymbol{x}_p^n)$.

$$\frac{\boldsymbol{p}_p^{n+1/2} - \boldsymbol{p}_p^{n-1/2}}{\Delta t} = q_p \left[\bar{\boldsymbol{E}}^n + \left(\frac{\boldsymbol{p}_p^{n+1/2} + \boldsymbol{p}_p^{n-1/2}}{2\gamma^n} \right) \times \bar{\boldsymbol{B}}^n \right] \quad \gamma^n \equiv \sqrt{1 + \left(\frac{\boldsymbol{p}_p^{n-1/2} + \boldsymbol{p}_p^{n+1/2}}{2m_p c} \right)^2} \tag{2.19}$$

At first glance, eq. (2.19) may seem to imply that this scheme is implicit. However, the dependence on $\boldsymbol{p}_p^{n+1/2}$ is linear and $\boldsymbol{p}_p^{n+1/2}$ can be found analytically in terms of $\boldsymbol{p}_p^{n-1/2}$. There are several equivalent numerical approaches to do so. The most commonly employed method in PIC codes is the well-known Boris pusher [Boris, 1970]. It combines speed and accuracy to update the macro-particles momenta $\boldsymbol{p}_p^{n-1/2}$ and positions $\boldsymbol{x}_p^n$ through a leap-frog integration. It shows that this integration can be performed explicitly by splitting the Lorentz force and separating the electric and magnetic force as follows:

$$\boldsymbol{p}_p^- = \boldsymbol{p}_p^{n-1/2} + q_p \, \frac{\Delta t}{2} \, \bar{\boldsymbol{E}}^n \tag{2.20}$$

$$\frac{\boldsymbol{p}_p^+ - \boldsymbol{p}_p^-}{\Delta t} = \frac{q_p}{2\gamma^n} \, \left(\boldsymbol{p}_p^+ - \boldsymbol{p}_p^- \right) \times \bar{\boldsymbol{B}}^n \tag{2.21}$$

$$\boldsymbol{p}_p^{n+1/2} = \boldsymbol{p}_p^+ + q_p \, \frac{\Delta t}{2} \, \bar{\boldsymbol{E}}^n \tag{2.22}$$

This scheme can be summarized in the following three steps:

1. First, half of the electric field contribution is added to calculate $\boldsymbol{p}_p^-$ from $\boldsymbol{p}_p^{n-1/2}$ according to eq. (2.20) to perform a half-step acceleration by the electric field.

2. $\boldsymbol{p}_p^+$ is calculated from eq. (2.21) by performing a full rotation to $\boldsymbol{p}_p^-$ due to the magnetic field.

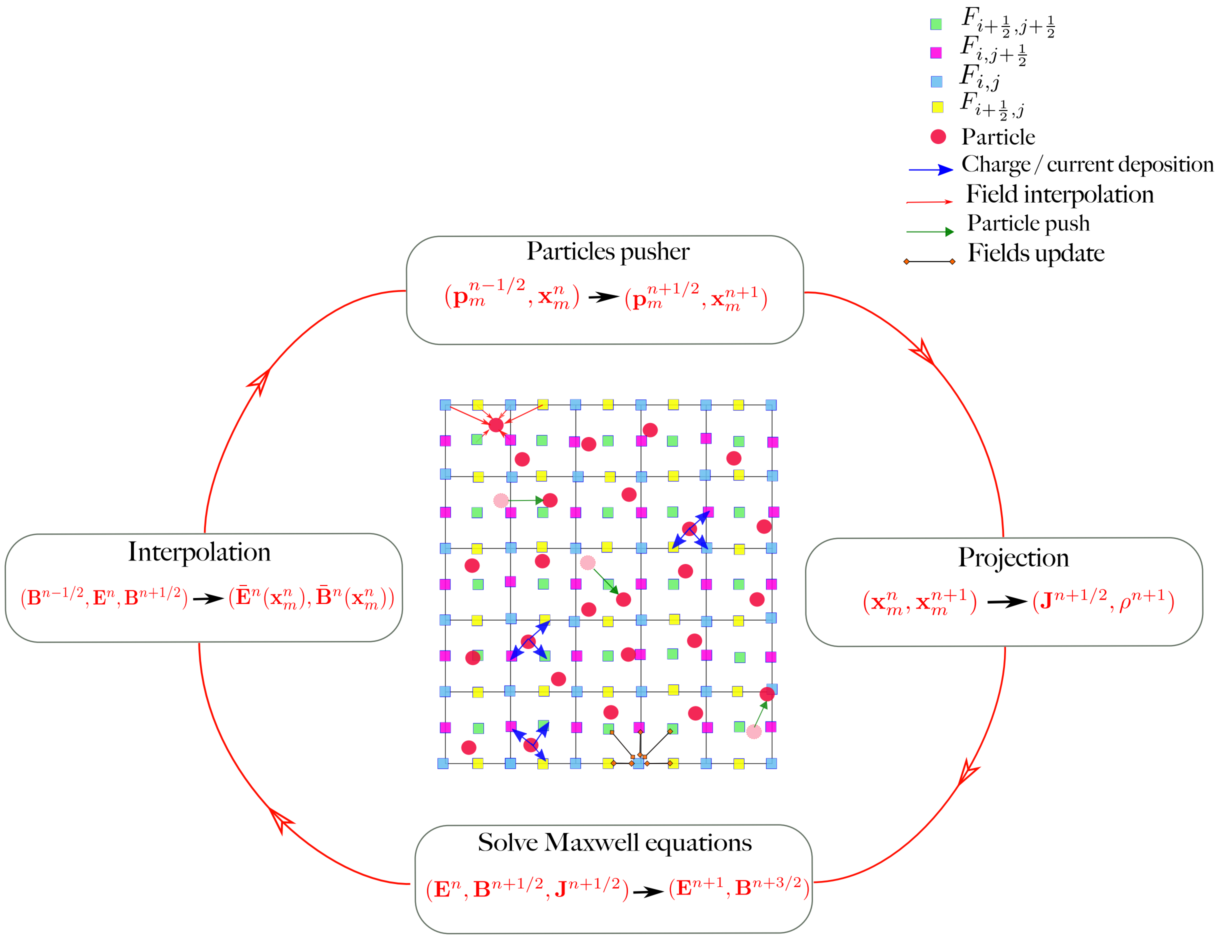

Figure 2.4: Sketch of the PIC cycle steps in a $2D$ Yee grid (x, y): Starting from the initial fields, charge and current density deposited on the grid at iteration n. The successive four steps are executed at each iteration: (i) Maxwell's equations are solved to update the electric and magnetic fields. (ii) Field values are gathered from the mesh to each particle position using interpolation (iii) Particles are advanced using equations of motion (particle push) knowing the values of the electromagnetic fields at their position to determine the position and momentum at iteration $n+1$. (iv) Current/charge contribution of each particle on the grid is deposited on the neighboring grid points.

3. Finally, $\boldsymbol{p}_p^{n+1/2}$ is obtained by adding the remaining half of the electric field to $\boldsymbol{p}_p^{+}$ using eq. (2.22).

Once $\boldsymbol{p}_p^{n+1/2}$ is known, $\boldsymbol{x}_p^{n+1}$ can be directly calculated from $\boldsymbol{x}_p^{n}$, through the following discretized equation:

$$\frac{\boldsymbol{x}_p^{n+1} - \boldsymbol{x}_p^{n}}{\Delta t} = \frac{\boldsymbol{p}_p^{n+1/2}}{\sqrt{m_p^2 + (\boldsymbol{p}_p^{n+1/2})^2/c^2}} \tag{2.23}$$

The Boris pusher intrinsically ensures that the kinetic energy of the particle remains constant when no electric field is present (i.e. when $\boldsymbol{E} = \boldsymbol{0}$ and $\boldsymbol{B} \neq \boldsymbol{0}$). However, an issue occurs with Boris pusher if we apply a constant non-zero $\boldsymbol{E}$ and $\boldsymbol{B}$ in such a way that their mutual contributions cancel the Lorentz force $\boldsymbol{E} + \boldsymbol{v} \times \boldsymbol{B} = 0$. For instance, in the relativistic regime, when particles travel near the speed of light with Lorentz factor close to 1 and the force from their own magnetic field compensates the electric field repulsion i.e $\boldsymbol{E} + \boldsymbol{v} \times \boldsymbol{B} = 0$, the particle velocity should remain unchanged as long as the electric field cancels the magnetic rotation. Nevertheless, if we suppose $\boldsymbol{p}^{n+1/2} = \boldsymbol{p}^{n-1/2}$ in Boris scheme eq. (2.19) the system has a solution only if $\boldsymbol{E} = \boldsymbol{B} = 0$. Consequently, this results in particles undergoing a spurious force. In this context, another leap-frog pusher has been proposed by Vay [Vay, 2008a], in order to mitigate this effect when the electric and magnetic fields compensate. It reads

$$\frac{\boldsymbol{p}_p^{n+1/2} - \boldsymbol{p}_p^{n-1/2}}{\Delta t} = q_p \left[\bar{\boldsymbol{E}}^n + \frac{1}{2} \left(\frac{\boldsymbol{p}_p^{n+1/2}}{\gamma^{n+1/2}} + \frac{\boldsymbol{p}_p^{n-1/2}}{\gamma^{n-1/2}} \right) \times \bar{\boldsymbol{B}}^n \right] \quad \gamma^{n\pm1/2} \equiv \sqrt{1 + \left(\frac{\boldsymbol{p}_p^{n\pm1/2}}{m_p c} \right)^2} \tag{2.24}$$

A comparison between the two pushers can be found in [Lobet, 2015].

Projection

In order to solve Maxwell's equations and after updating the particles positions and momenta, each particle contribution to the current and charge density has to be known on the grid, at time $(n + 1/2)\Delta t$ and $(n + 1)\Delta t$ respectively through eq. (2.11). Numerically, retrieving the charge density from the macro-particles distribution consists in averaging ρ over each grid cell:

$$\rho_{i,j,k}^{n+1} = \frac{1}{\Delta x \Delta y \Delta z} \int_{(i-\frac{1}{2})\Delta x}^{(i+\frac{1}{2})\Delta x} dx \int_{(j-\frac{1}{2})\Delta y}^{(j+\frac{1}{2})\Delta y} dy \int_{(k-\frac{1}{2})\Delta z}^{(k+\frac{1}{2})\Delta z} dz\ \rho(\boldsymbol{x}) = \frac{1}{\Delta x \Delta y \Delta z} \sum_p N_p q_p S_{i,j,k}(\boldsymbol{x}_p^{n+1}) \tag{2.25}$$

where the projection factor $S_{i,j,k} = P_{i,j,k}$ is again given by eq. (2.17). Depending on the spatial extension of shape functions, each macro-particles inducts a charge density on an arbitrary number of grid points. Note that the shape functions used for both the fields interpolation eq. (2.15) and eq. (2.16) and the current and charge deposition need to be the same to avoid an asymmetry that will introduce unphysical self-exerted fields [Innocenti et al., 2016].

In principle, the same computational method described to compute ρ^{n+1} can be used to compute $\boldsymbol{J}^{n+1/2}$. However, such an expression would not guarantee that the discretized continuity equation eq. (2.26) is verified and in this case, the scheme is not charge conserving, leading to error accumulation during the interaction process.

$$\frac{\rho_{i,j,k}^{n+1} - \rho_{i,j,k}^{n}}{\Delta t} + \frac{{J_x}_{i+\frac{1}{2},j,k}^{n+\frac{1}{2}} - {J_x}_{i-\frac{1}{2},j,k}^{n+\frac{1}{2}}}{\Delta x} + \frac{{J_y}_{i,j+\frac{1}{2},k}^{n+\frac{1}{2}} - {J_y}_{i,j-\frac{1}{2},k}^{n+\frac{1}{2}}}{\Delta y} + \frac{{J_z}_{i,j,k+\frac{1}{2}}^{n+\frac{1}{2}} - {J_z}_{i,j,k-\frac{1}{2}}^{n+\frac{1}{2}}}{\Delta z} = 0 \tag{2.26}$$

For this reason, several solutions have been proposed to ensure a better charge conservation with the Yee solver among which we mention Boris correction [Boris, 1970] in which the electric field $\boldsymbol{E}$ is corrected by adding an electrostatic term at every time step after solving the Ampere equation. Marder has introduced a "pseudo-current" $\boldsymbol{F}$ [Marder, 1993] in the Maxwell-Ampere equation to correct the error buildup. However, they are not the most efficient way due to their high computational cost. For this reason, $\boldsymbol{J}^{n+1/2}$ is instead commonly obtained using a modified version of the current deposition, known as the Esirkepov current deposition algorithm [Esirkepov, 2001]. It is the generalization of the method developed by Villasenor and Buneman [Villasenor and Buneman, 1992]. In Villasenor and Buneman, only the first and second order of B-spline particle shape factor are used whereas in the Esirkepov method, it is extended to particle shape factor of an arbitrary order assuming that the particle trajectory over one time-step is linear. Esirkepov algorithm intrinsically satisfies the discretized continuity equation eq. (2.26), considering second order spatial and temporal derivative operators and hence ensures the charge conservation.

Maxwell solver

In the FDTD scheme, $\boldsymbol{E}^{n+1}$ and $\boldsymbol{B}^{n+3/2}$ are determined from respectively $\boldsymbol{E}^{n}$ and $\boldsymbol{B}^{n+1/2}$ knowing $\boldsymbol{J}^{n+1/2}$ on the grid nodes and using a finite difference scheme to discretize Maxwell-Ampere and Maxwell-Faraday equations in both time and space using a low order stencil according to Yee grid and a leap frog integration previously described in section 2.2.2. The discretized equations read:

$$\frac{{E_x}^{n+1}_{i+\frac{1}{2},j,k} - {E_x}^{n}_{i+\frac{1}{2},j,k}}{c^2\Delta t} = (D_y B_z^{n+\frac{1}{2}})_{i+\frac{1}{2},j,k} - (D_z B_y^{n+\frac{1}{2}})_{i+\frac{1}{2},j,k} - \mu_0 {J_x}^{n+\frac{1}{2}}_{i+\frac{1}{2},j,k} \tag{2.27}$$

$$\frac{{E_y}^{n+1}_{i,j+\frac{1}{2},k} - {E_y}^{n}_{i,j+\frac{1}{2},k}}{c^2\Delta t} = (D_z B_x^{n+\frac{1}{2}})_{i,j+\frac{1}{2},k} - (D_x B_z^{n+\frac{1}{2}})_{i,j+\frac{1}{2},k} - \mu_0 {J_y}^{n+\frac{1}{2}}_{i,j+\frac{1}{2},k} \tag{2.28}$$

$$\frac{{E_z}^{n+1}_{i,j,k+\frac{1}{2}} - {E_z}^{n}_{i,j,k+\frac{1}{2}}}{c^2\Delta t} = (D_x B_y^{n+\frac{1}{2}})_{i,j,k+\frac{1}{2}} - (D_y B_x^{n+\frac{1}{2}})_{i,j,k+\frac{1}{2}} - \mu_0 {J_z}^{n+\frac{1}{2}}_{i,j,k+\frac{1}{2}} \tag{2.29}$$

$$\frac{{B_x}^{n+\frac{1}{2}}_{i,j+\frac{1}{2},k+\frac{1}{2}} - {B_x}^{n-\frac{1}{2}}_{i,j+\frac{1}{2},k+\frac{1}{2}}}{\Delta t} = -(D_y E_z^{n})_{i,j+\frac{1}{2},k+\frac{1}{2}} + (D_z E_y^{n})_{i,j+\frac{1}{2},k+\frac{1}{2}} \tag{2.30}$$

$$\frac{{B_y}^{n+\frac{1}{2}}_{i+\frac{1}{2},j,k+\frac{1}{2}} - {B_y}^{n-\frac{1}{2}}_{i+\frac{1}{2},j,k+\frac{1}{2}}}{\Delta t} = -(D_z E_x^{n})_{i+\frac{1}{2},j,k+\frac{1}{2}} + (D_x E_z^{n})_{i+\frac{1}{2},j,k+\frac{1}{2}} \tag{2.31}$$

$$\frac{{B_z}^{n+\frac{1}{2}}_{i+\frac{1}{2},j+\frac{1}{2},k} - {B_z}^{n-\frac{1}{2}}_{i+\frac{1}{2},j+\frac{1}{2},k}}{\Delta t} = -(D_x E_y^{n})_{i+\frac{1}{2},j+\frac{1}{2},k} + (D_y E_x^{n})_{i+\frac{1}{2},j+\frac{1}{2},k} \tag{2.32}$$

The numerical operators D_x, D_y, D_z are defined (for any field F) by

$$(D_x F)_{i',j',k'} = \frac{F_{i'+\frac{1}{2},j',k'} - F_{i'-\frac{1}{2},j',k'}}{\Delta x} \tag{2.33}$$

$$(D_y F)_{i',j',k'} = \frac{F_{i',j'+\frac{1}{2},k'} - F_{i',j'-\frac{1}{2},k'}}{\Delta y} \tag{2.34}$$

$$(D_z F)_{i',j',k'} = \frac{F_{i',j',k'+\frac{1}{2}} - F_{i',j',k'-\frac{1}{2}}}{\Delta z} \tag{2.35}$$

where i', j' and k' can be integers or half-integers. When replacing n by $n+1$, eqs. (2.30) to (2.32) can be used to obtain $\boldsymbol{B}^{n+3/2}$ from $\boldsymbol{B}^{n+1/2}$ and $\boldsymbol{E}^{n+1}$.

By staggering the electric and magnetic fields both spatially and temporally as defined in the Yee lattice, all the numerical derivatives are time-centered and space-centered, and therefore they are second-order accurate i.e the numerical error induced by the spatial and temporal derivatives over a single time step is of order two in both time and space.

Notice that when updating the electromagnetic fields, only two of Maxwell's equations are used: Maxwell Fraday eq. (1.1) and Maxwell Ampere eq. (1.2). Using the FDTD scheme with

Yee discretization on the grid and provided that the numerical divergence of $\boldsymbol{B}$ is initially verified to be zero, the discretized Maxwell Thomson corresponding to eq. (1.4) is automatically satisfied throughout the simulation.

$$(D_x B_x^{n+\frac{1}{2}})_{i+\frac{1}{2},j+\frac{1}{2},k+\frac{1}{2}} + (D_y B_y^{n+\frac{1}{2}})_{i+\frac{1}{2},j+\frac{1}{2},k+\frac{1}{2}} + (D_z B_z^{n+\frac{1}{2}})_{i+\frac{1}{2},j+\frac{1}{2},k+\frac{1}{2}} = 0$$

One can apply the operator $\boldsymbol{\nabla}\cdot$ to the Faraday equation eq. (1.1) and use the Gauss equation eq. (1.3) to obtain the continuity equation eq. (2.14). The opposite is true as well: if the charge density always satisfies the continuity equation, then the discretized Gauss law is satisfied automatically during the evolution of the system, if it was initially satisfied.

$$(D_x E_x^n)_{i,j,k} + (D_y E_y^n)_{i,j,k} + (D_z E_z^n)_{i,j,k} - \frac{\rho^n_{i,j,k}}{\epsilon_0} = 0$$

Consequently, using a charge conserving algorithm for the current deposition such as Esirkepov algorithm along FDTD scheme as mentioned previously in section 2.2.3, guarantees that the Maxwell-Gauss equation is verified at each time step, provided that the initial electric field verifies it. When other algorithms are used to calculate $\boldsymbol{J}^{n+1/2}$, additional corrections (known as *Poisson correctors*) have to be applied to $\boldsymbol{E}$ in order to ensure eq. (1.3).

The FDTD scheme is the most common implementation for Maxwell solver in PIC codes because it is a "local" algorithm (provided that no Poisson correction is done) i.e. at each time step information is exchanged between neighbouring grid cells only and no global information exchange is necessary. Therefore, it is very scalable and well-suited to be parallelized at arbitrary scale on distributed memory architectures. In the next section, the features of FDTD parallelization in SMILEI are presented.

2.3 The PIC code SMILEI

Turning the prevailing promising technology of plasma based accelerators into an evolved scientific tool depends tightly on the advent of high-performance, high-fidelity simulation tools. These tools will harness the power of future exascale supercomputers for the exploration of outstanding questions in the physics of plasma based acceleration. In this context, efforts were put together to meet the growing needs in terms of accurate and scalable simulations by developing the PIC code SMILEI.

SMILEI is a collaborative open-source project, developed by both physicists and High Performance Computing (HPC) experts and written based on object-oriented programming in C++. It is designed for high performances on massively parallel computers thanks to hybrid MPI/OpenMP parallelization, dynamic load balancing and SIMD operations. It also offers a user-friendly Python interface for inputs and post-processing besides a whole set of run-time diagnostics based on HDF5.

SMILEI is a multi-purpose Particle-In-Cell code providing the scientific community in plasma physics with a wide variety of simulation-related applications ranging from relativistic laser-plasma interaction to astrophysics owing to a large choice of additional physics modules such as: ionization, binary collisions and QED processes ...

A detailed account of the code's structures, capabilities, parallelization strategy and performances can be found in [Derouillat et al., 2018]. In this section, the focus will be mainly on HPC features of the code.

2.3.1 Parallelization strategy of the PIC algorithm with the FDTD scheme

The number of cores available on massively parallel hybrid supercomputers relying on both shared and distributed memory has skyrocketed. As high-performance computing (HPC) systems are evolving towards the exascale, software development has to meet the emerging needs of parallelism in order not to be lagged by the technologies evolution. This can be achieved by implementing an efficient parallelization strategy that allows for conserving data locality and minimizing load imbalance. In this section, first the overall parallelization strategy chosen for SMILEI is presented, followed by the descriptions of some of its features.

Standard domain decomposition

In this section, we present the overall parallelization strategy chosen for SMILEI within the FDTD discretization scheme for the fields.

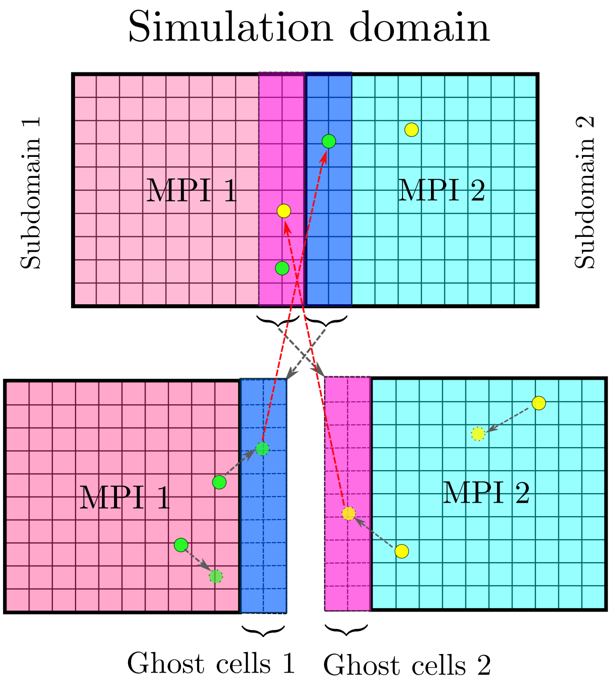

Figure 2.5: Domain decomposition and parallelization strategy in the PIC algorithm. The simulation domain is divided in subdomains, each of whom is juxtaposed with ghost cells. Each MPI task handles the computations associated to a unique subdomain with its ghost cells. Macro-particles deposit current and charge in the whole combo subdomain+ghost cells. Then contributions to densities and currents within ghost-cells are summed to the overlapping neighbouring subdomains and Maxwell's equations are solved. Updated values of the electromagnetic field from neighbours are then communicated to update the field quantities of the local ghost cells. Macro-particles are pushed after fields interpolation. If their new positions is in the ghost cells, they are sent to the neighboring corresponding subdomain(figure adapted from [Kallala, 2020]).

The FDTD scheme is a relatively simple numerical approach to implement Maxwell's solver. Besides, it is straightforward to parallelize at arbitrary scale on distributed memory architectures since the electric/magnetic field values on each node are only correlated with values located on the adjacent nodes. Therefore, the computational domain can be simply divided into several subdomains by employing a standard domain decomposition technique illustrated in fig. 2.5 and where each subdomain can execute independently. Each subdomain is handled by an independant Message Passing Interface (MPI) process. There is no correlation between the grid points in the subdomain and other subdomains except over a small region of few cells called ghost-region where neighboring subdomains overlap. At each time step, the data from the ghost region is used to advance electromagnetic fields near the subdomains borders. Reciprocally, data from neighboring subdomains intervenes to update the electromagnetic quantities inside the ghost regions of adjacent subdomains.

The same principle is also applied to the computations pertaining to the macro-particles since no intra-particles communications are required because particles only interact with fields and are independent from each other. However, particles are volatile objects traveling throughout the entire domain. That is why, macro-particles are exchanged between neighboring subdomains when they cross the boundaries. Note that the number of ghost-cells depends on the differentiation order in the FDTD scheme used but also on the shape function used for the particles: extended shape functions with larger support implies that macro-particles laying near subdomains borders are handled differently when it comes to the computation of their contributions in current/charge densities to the next subdomain.

This standard parallelization strategy based on pure MPI communication between distinct nodes of the distributed-memory architecture is implemented in many PIC softwares. However, it limits the scalability of the code and a better performance can be achieved by using a second layer of parallelization in the shared memory level with Open Multi-Processing (openMP) interface to harmonize the computational load within each node with a reduced programming complexity.

A hybrid MPI+Open MP parallelization

In SMILEI, each MPI region (the grid portion pertaining to one MPI task and where communication between two portions is handled by MPI library) is divided in many sub-subdomains called "patches". Each MPI process handles many small patches with the same content as the global subdomain that regroups those patches: computations related to particles and fields belonging to that portion of the grid are performed at the patch level before being merged with synchronization on the MPI region level. Patches being independent, the work load associated to each patch is distributed among different threads belonging to each MPI task using the shared memory parallelization API OpenMP which offers more local parallelism within the MPI region. As a result, this hybrid MPI + OpenMP implementation of a patch-based decomposition illustrated in fig. 2.6 naturally extends the pure MPI one.

The computational load related to each patch may be different from one to another due to the imbalance in the particles distribution between them. Hence, the use of the openMP dynamic scheduler which shares the computational load between threads grants a local load balancing and an optimized cache reuse at a reasonable cost as synchronization between patches belonging to the same MPI process is cheaper than the one between patches belonging to different MPI processes. This cost is minimized in SMILEI by grouping patches in compact clusters that reduce the interface between MPI sub-domains as much as possible using patches ordering along a Hilbert space-filling curve fig. 2.7 divided into as many segments of similar length as there are MPI processes.

Dynamic load balancing

Besides the local load balance that is done between threads thanks to the dynamic scheduler of OpenMP at the node level, SMILEI offers the chance to perfom a dynamic load balancing

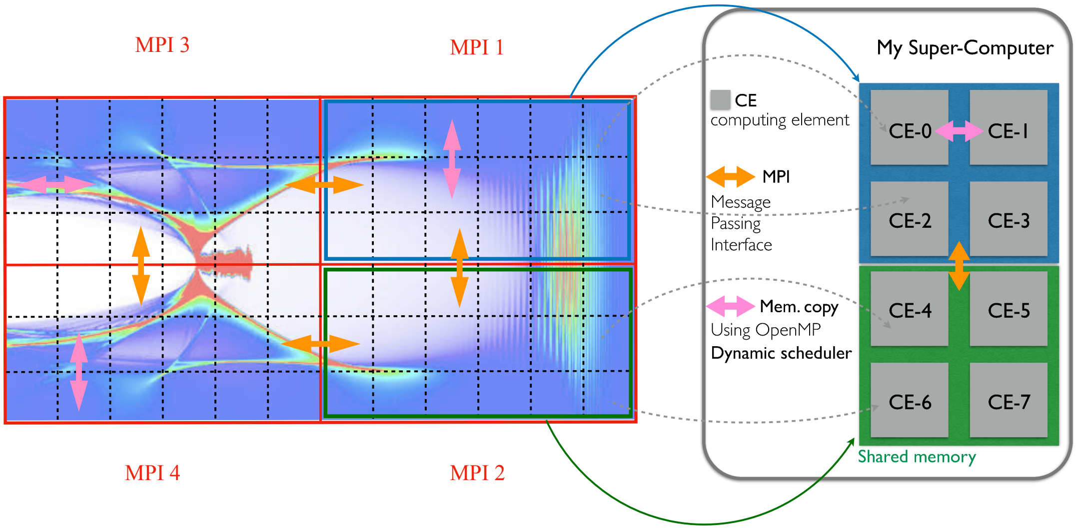

Figure 2.6: The simulation box is divided into sub-domains. Each one of them is handled by an MPI process and subdivided in smaller domains called "patches". Each patch being independent, they can be easily treated in parallel by the threads owned by the MPI process.

between MPI tasks by exchanging patches from two neighbour MPI regions along the Hilbert space-filling curve. An overloaded MPI process sends patches to its neighbours along the Hilbert curve. Inversely, an underloaded process will receive patches from its neighbours. Thus, its segment shortens or lengthens depending whether he sends or receives patches. The number of OpenMP threads is restricted to the number of physical cores accessible on the shared memory system.

The best performances are obtained when a single MPI process is affected to each processor and when all cores of the processor are managed by the OpenMP scheduler. Hence, the best configuration of the load balancing via the OpenMP dynamic scheduler strictly depends on the size (in number of cores) of the processors composing the nodes.

The patch size defines the balance grain: the smaller the patches the smoother the balance. Yet, the patch size minimization is limited by the number of ghost cells used which are dictated, as mentioned before, by the order of Maxwell's equations discretization scheme, and by the shape function of the macro-particles: the number of cells in a patch should be greater than the number of ghost cells. Typically, with a standard second-order Yee scheme, 4 ghost cells per dimension (2 on each side) are used. Therefore, the patch in this case should include at least 6 cells per dimension. This condition also insures that ghost cells from non-neighbour patches do not overlap, which is necessary for a synchronization limited to neighbor patches only.

SIMD

Particles are volatile objects traveling through the grid from one domain to another which triggers randomness in the memory access whenever they interact with the grid throughout the different operations pertaining to particles. This randomness affects negatively the code performances

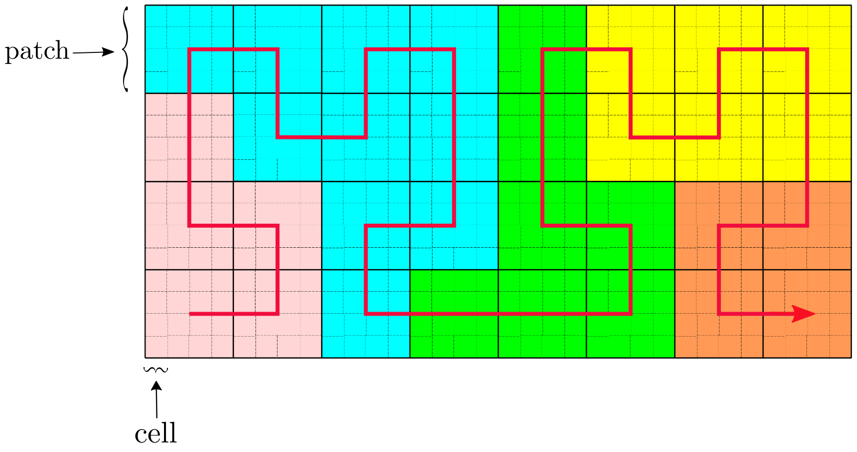

Figure 2.7: Example of 8 × 4patches domain decomposition, shared between 5 MPI processes. MPI domains are delimited by different colors. Patches are organized along a one dimensional Hilbert space-filling curve (red line). MPI processes can exchange their patches to balance their load along the space-filling curve.

especially that in most cases, PIC simulations are becoming increasingly memory bound as memory performance is not developing as fast as the computation capabilities. In order to enhance the performance, this randomness should thereby be mitigated for an optimized memory usage.

```
for(int i = 0 ; i < n ; i++) {
  if (condition dependent of i) {
    d[i] = a[i] + b[i]*c[i]
  }
}
```

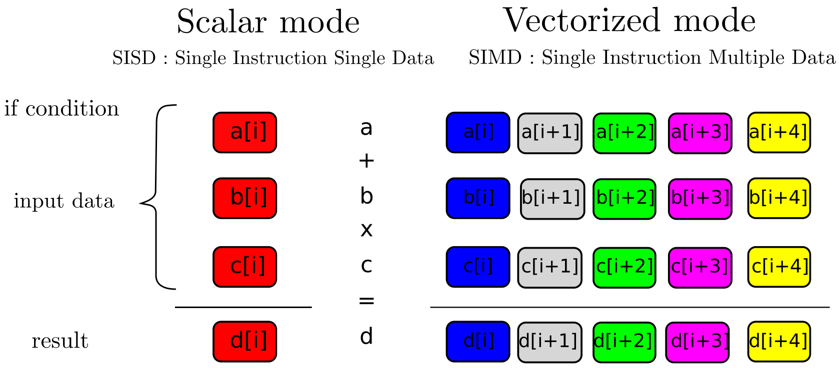

Figure 2.8: Scalar mode: one instruction produces one result versus SIMD processing: one instruction produces multiple results.

A first method to avoid this randomness is the use of fine domain decomposition so that the size of data laying within each patch can fit into the fastest cache memory layer to enable an efficient cache reuse and optimized computations. This method enables a kind of sorting since particles of each patch all access the same grid region which is limited by the patch extension. An other approach to mitigate this randomness is to perform particles sorting by organizing the particles in memory according to their location. Once particles are sorted, not only the cache use is improved but also computations within each patch are significantly accelerated by allowing the use of vectorized implementations of different PIC steps via Single Instructions Multiple Data instruction set, which are very efficient at speeding up memory-bound operations yet restricted to very regular memory access patterns [Vincenti et al., 2017]. Nevertheless, the vectorized operators are faster than the scalar ones only when the number of particles per cell is larger than the vector register length. On top of that, the sorting procedure implies a significant computation overhead because of potentially heavy data movements. Therefore, using vectorized operators combined with sorting becomes more beneficial than their scalar counterparts only when the number of Particle-Per-Cell (PPC) is above the inversion point where sorting can actually overcome its cost, which depends on the architecture.

Since, the number of PPC in many application of PIC such as laser-plasma interaction may drastically vary between patches and in time for the same patch, this shortcoming is addressed in SMILEI by suggesting an adaptive vectorization mode. It can locally (each patch, each species) and dynamically (same patch in time) switch between the scalar and vectorized operators at run time, choosing the most efficient one in the region of interest.

More details about the implementation strategy of the adaptive SIMD optimizations with fine-grain particle sorting in SMILEI as well as its impact on the performances can be found in [Beck et al., 2019].

Chapter 3

Azimuthal Fourier decomposition in cylindrical geometry

Particle-In-Cell (PIC) algorithms are extensively used in several areas of nonlinear laser-plasma interactions including astrophysics [Hughes and Bregman, 2006], plasma based accelerators [Qiang et al., 2000], and advanced radiation sources [Thaury and Quéré, 2010]. A PIC code self-consistently calculates the positions and momenta of a large number of particles and the fields they generate. Although full PIC codes are powerful tools which capture a wide range of physical phenomena, they also require large computational resources. This problem becomes particularly acute with regard to laser–plasma interactions because of the large disparity between the scales involved in this process: resolving the high-frequency laser field requires the use of fine space and time resolution. This task becomes very challenging in three-dimensions where it requires hundreds of nodes on super computers.

Despite the extensive work on maximizing the code parallelism and efficiency on today's supercomputer, high-resolution simulations in 3D can only be run on costly large-scale computer facilities which are not accessible to everyone. In order to reduce the computational cost of such simulations, we need to resort to reduced numerical models which simplify the problem while retaining a high fidelity.

While the two dimensional simulations in Cartesian coordinates can be very useful for carrying out parametric scans and to have physical insight, they can not be relied on as a reference. There are some physics problems in which three dimensional effects lead to both qualitative or quantitative differences. Unlike 2D simulations in Cartesian geometry, the ones carried in cylindrical geometry preserve the representation of the geometric scaling factors for the wake excitation in the nonlinear blowout regime, when there is cylindrical symmetry. In Particle WakeField Acceleration (PWFA)[1], 2D cylindrical simulations can be used successfully except in modeling effects of hosing or asymmetric transverse envelope of both the driving and trailing particle beams. Unfortunately, it is not the case for LWFA. The reason is that even with an azimuthally symmetric laser spot, the high frequency in the laser plays in important role and its polarization breaks this symmetry. Therefore, a linearly or any linear combination of linearly polarized lasers: such as circularly or elliptically polarized laser with an azimuthally symmetric transverse envelope is not azimuthally symmetric in cylindrical geometry [Davidson, 2016].

In 2009, an algorithm based on azimuthal Fourier decomposition of the electromagnetic fields was proposed by [Lifschitz et al., 2009] and implemented in the PIC code Calder-Circ. It enables

---

[1] PWFA is a plasma-based particle accelerator where an intense, relativistic charged-particle bunch is the wakefield driver with analogy to the laser in LWFA.

an accurate modeling of close-to-cylindrical physical systems and captures physical effects that are intrinsically 3D in laser propagation like self-focusing [Esarey et al., 2009]. Besides, it has a similar computational load to that of a cylindrical code.

This geometry has been implemented with Finite Difference Time Domain (FDTD) discretization scheme for the Maxwell solver in Smilei and with Pseudo Spectral Analytical Time Domain (PSATD) solver in PICSAR library as part of the work undertaken during my PhD. The PSATD solver is then coupled with Smilei to benefit from its parallelization technique.

In this Chapter, first the theory and mathematical derivation of this reduced model is described in section 3.1. The FDTD implementation of the algorithm in Yee grid is detailed in section 3.2 while its PSATD implementation is detailed in section 3.3. The parallelization technique that enabled the coupling of PICSAR with Smilei is presented in section 3.4. Finally, the advantages of the PSATD solver over its FDTD counter part are summarized in section 3.5.

Contents

3.1 Theory and mathematical derivation of azimuthal Fourier field decomposition 63
  3.1.1 Maxwell's equations in azimuthal geometry 65
3.2 FDTD scheme 65
  3.2.1 Discretized Maxwell equations in the Yee grid 66
  3.2.2 On axis condition 66
  3.2.3 Boundary conditions 71
  3.2.4 Esirkepov algorithm for charge conserving current deposition 75
  3.2.5 Interpolation 77
  3.2.6 Numerical dispersion relation and stability condition for FDTD 78
  3.2.7 limits of the FDTD 81
3.3 Pseudo Spectral Analytical Time Domain scheme 82
  3.3.1 Spectral Cartesian representation 83
  3.3.2 Spectral quasi-cylindrical representation 84
  3.3.3 Overview of the quasi-cylindrical spectral algorithm 85
3.4 Parallelization strategy of the PIC algorithm with the PSATD scheme 91
  3.4.1 Domain decomposition and parallelization of the PSATD solver 91
  3.4.2 Single domain multiple decompositions (SDMD) 92
3.5 Advantages of PSATD 93
  3.5.1 Comparison between FDTD and PSATD schemes 94
  3.5.2 Discussion 95

3.1 Theory and mathematical derivation of azimuthal Fourier field decomposition

In this algorithm the fields and currents are expanded into azimuthal modes resulting in a set of fields and currents that only depend on r and z. They are then substituted into Maxwell's equations to generate a series of equations where each mode is evolving independently from the others. However, the particles are still pushed in 3D Cartesian geometry.

We begin by detailing the mathematical derivation of the equations describing this method. In this algorithm, the fields $\mathbf{E}, \mathbf{B}, \mathbf{J}, \rho$ in cylindrical coordinates (r, z, θ) are 2π-periodic and thus can be decomposed in Fourier series in θ direction according to (3.1) and (3.3).

$$F(r,z,\theta) = \sum_{m=-\infty}^{\infty} \hat{F}_m(r,z) e^{-im\theta} \qquad \text{with} \qquad \hat{F}_m(r,z) = \frac{1}{2\pi}\int_0^{2\pi} d\theta\, F(r,z,\theta) e^{im\theta} \tag{3.1}$$

where F denotes any of the cylindrical components $E_{r,z,\theta}, B_{r,z,\theta}, J_{r,z,\theta}$ or ρ and $\hat{F}_m$ is the associated Fourier components with m is the azimuthal mode index.

When taking into consideration the fact that all the physical fields F are real ($\bar{F} = F$) and that $\hat{F}_{-m} = \bar{\hat{F}}_m$ where the bar denotes the complex conjugate, the above sum on both negative and positive modes can be rewritten to include only positive ones. We therefore define the quantities calculated in the code $\tilde{F}_m$ as:

$$\tilde{F}_0 = \hat{F}_0 \quad \text{and} \quad \tilde{F}_m = 2\hat{F}_m \quad \text{for} \quad m \geq 1$$

Using the definition of $\tilde{F}_m$, the field F can be written as the following:

$$\begin{aligned} F(r,z,\theta) &= \Re\left(\sum_{m=0}^{\infty} \tilde{F}_m(r,z) e^{-im\theta}\right) && (3.2)\\ &= \tilde{F}_0(r,z) + \sum_{m=1}^{\infty} \Re\left(\tilde{F}_m(r,z)\right)\cos(m\theta) + \Im\left(\tilde{F}_m(r,z)\right)\sin(m\theta) && (3.3) \end{aligned}$$

where $\Re$ is the real part and $\Im$ is the imaginary one. The fields modes $\tilde{F}_m$ are complex for $m \geq 1$ and real for $m = 0$, whereas the corresponding physical fields are real.

Because the algorithm is able to take into account modes $m > 0$ and not only fields that are independent of θ (mode 0) in contrast with cylindrical codes, it is referred to as quasi-3D algorithm [Davidson et al., 2014], or as quasi-cylindrical algorithm. For simplicity, quasi-cylindrical is used in the following to refer to this algorithm.

At first glance, the method does not simplify the complexity of the problem since an infinity of modes should be included to calculate the fields. However, in practice the Fourier series in equations 3.1 and 3.3 is usually truncated up to very first modes in the case of low dependence on θ. In fact, any linearly polarized laser or any linear combination of linearly polarized lasers such as circularly or elliptically polarized lasers[2] with a cylindrically-symmetric envelope can be modeled exclusively by the mode $m = 1$.

---

[2] Circularly and elliptically polarized lasers can be obtained by combining two linearly polarized lasers with equal or different amplitudes and phase and polarization offset by $\pi/2$

For a cylindrically symmetric pulse (for example a Gaussian one) propagating in z and polarized linearly along $\boldsymbol{e_\alpha} = \cos(\alpha)\boldsymbol{e_x} + \sin(\alpha)\boldsymbol{e_y}$, the field component $\boldsymbol{E}$ can be transformed to the cylindrical frame, depicted in fig. 3.1, according to:

$$\begin{aligned}
\boldsymbol{E} &= E_0(r,z)\boldsymbol{e}_\alpha \\
&= E_0(r,z)[\ \cos(\alpha)(\cos(\theta)\boldsymbol{e}_r - \sin(\theta)\boldsymbol{e}_\theta)\ +\ \sin(\alpha)(\sin(\theta)\boldsymbol{e}_r + \cos(\theta)\boldsymbol{e}_\theta)\ ] \\
&= \mathrm{Re}[\ E_0(r,z)e^{i\alpha}e^{-i\theta}\ ]\boldsymbol{e}_r\ +\ \mathrm{Re}[\ -iE_0(r,z)e^{i\alpha}e^{-i\theta}\ ]\boldsymbol{e}_\theta \\
&=\ E_r\boldsymbol{e_r}\ +\ E_\theta\boldsymbol{e_\theta}
\end{aligned} \tag{3.4}$$

Here the amplitude E_0 does not depend on θ because the pulse envelope was assumed to be cylindrically symmetric. By equating the fields in eq. (3.4) to the modes expansion in eq. (3.3), one can identify the fields E_r and E_θ of the laser as the first order term in Fourier expansion of the electric field $\boldsymbol{E}$. Hence, they are represented exclusively by the mode $m = 1$ and the same stands for B_r and B_θ.

$$\begin{aligned}
\tilde{E}_{r,1} &= E_0(r,z)e^{i\alpha} & \tilde{B}_{r,1} &= iE_0(r,z)e^{i\alpha} \\
\tilde{E}_{\theta,1} &= -iE_0(r,z)e^{i\alpha} & \tilde{B}_{\theta,1} &= E_0(r,z)e^{i\alpha}
\end{aligned} \tag{3.5}$$

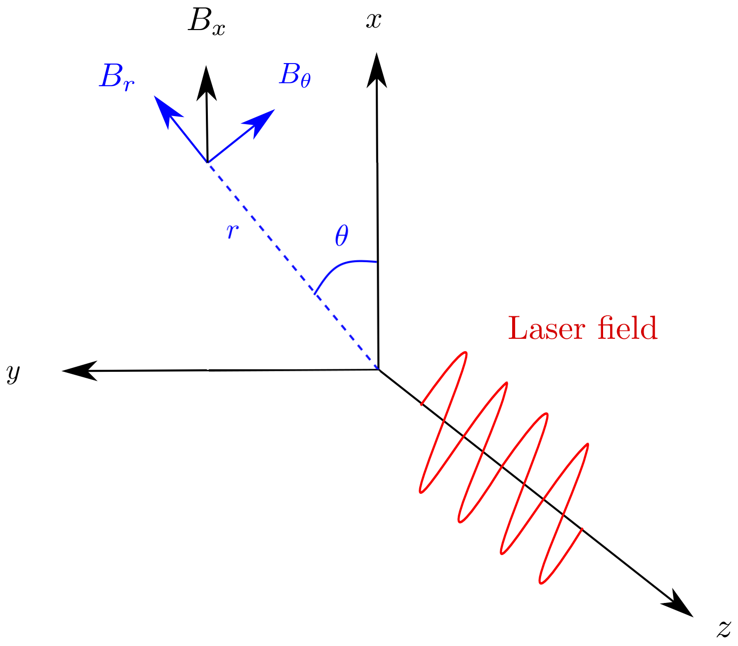

Figure 3.1: Definition of the cylindrical frame.

Thus, any laser pulse with a symmetric envelope can be thoroughly described by the mode $m = 1$. On the other hand, the pondoromotive force that drives the wakefield in LWFA has the same symmetry as the laser envelope. Therefore, for an axis-symmetric laser envelope, the wakefield and his associated fields do not depend on θ and can be mostly represented by the mode $m = 0$.

As a consequence, the infinite sum of modes can be truncated at the first two modes since only the modes $m = 0$ and $m = 1$ are necessary to model laser wakefield acceleration with linearly polarized lasers with axis-symmetric envelope such as Gaussian ones.

3.1.1 Maxwell's equations in azimuthal geometry

Maxwell's equations in cylindrical geometry are given by:

$$
\begin{aligned}
\frac{\partial B_r}{\partial t} &= -\frac{1}{r}\frac{\partial E_z}{\partial \theta} + \frac{\partial E_\theta}{\partial z} & \frac{1}{c^2}\frac{\partial E_r}{\partial t} &= -\frac{1}{r}B_z - \frac{\partial B_\theta}{\partial z} - \mu_0 J_r \\
\frac{\partial B_\theta}{\partial t} &= -\frac{\partial E_r}{\partial z} + \frac{\partial E_z}{\partial r} & \frac{1}{c^2}\frac{\partial E_\theta}{\partial t} &= \frac{\partial B_r}{\partial z} - \frac{\partial B_z}{\partial r} - \mu_0 J_\theta \\
\frac{\partial B_z}{\partial t} &= -\frac{1}{r}\frac{\partial (rE_\theta)}{\partial r} + \frac{1}{r}\frac{\partial E_r}{\partial \theta} & \frac{1}{c^2}\frac{\partial E_z}{\partial t} &= \frac{1}{r}\frac{\partial (rB_\theta)}{\partial r} + \frac{1}{r}\frac{\partial B_r}{\partial \theta} - \mu_0 J_z
\end{aligned}
\tag{3.6}
$$

Once the electromagnetic fields, $\boldsymbol{E}$ and $\boldsymbol{B}$ are properly defined, their Fourier expansion presented in (3.3) is replaced in Maxwell's equations (3.6).

$$
\frac{\partial\left(\tilde{F}_m(r,z)e^{-im\theta}\right)}{\partial \theta} = -im\tilde{F}_m(r,z)e^{-im\theta} \tag{3.7}
$$

Owing to the linearity of Maxwell's equations and using the relation (3.7), it generates a set of equations (3.8) where each mode m evolves independently in vacuum and different modes can be coupled in the presence of the plasma through the source term $\boldsymbol{J}$.

$$
\begin{aligned}
\frac{\partial \tilde{B}_{r,m}}{\partial t} &= \frac{im}{r}\tilde{E}_{z,m} + \frac{\partial \tilde{E}_{\theta,m}}{\partial z} & \frac{1}{c^2}\frac{\partial \tilde{E}_{r,m}}{\partial t} &= -\frac{im}{r}\tilde{B}_{z,m} - \frac{\partial \tilde{B}_{\theta,m}}{\partial z} - \mu_0 \tilde{J}_{r,m} \\
\frac{\partial \tilde{B}_{\theta,m}}{\partial t} &= -\frac{\partial \tilde{E}_{r,m}}{\partial z} + \frac{\partial \tilde{E}_{z,m}}{\partial r} & \frac{1}{c^2}\frac{\partial \tilde{E}_{\theta,m}}{\partial t} &= \frac{\partial \tilde{B}_{r,m}}{\partial z} - \frac{\partial \tilde{B}_{z,m}}{\partial r} - \mu_0 \tilde{J}_{\theta,m} \\
\frac{\partial \tilde{B}_{z,m}}{\partial t} &= -\frac{1}{r}\frac{\partial (r\tilde{E}_{\theta,m})}{\partial r} - \frac{im}{r}\tilde{E}_{r,m} & \frac{1}{c^2}\frac{\partial \tilde{E}_{z,m}}{\partial t} &= \frac{1}{r}\frac{\partial (r\tilde{B}_{\theta,m})}{\partial r} + \frac{im}{r}\tilde{B}_{r,m} - \mu_0 \tilde{J}_{z,m}
\end{aligned}
\tag{3.8}
$$

When the plasma response is linear, each mode for the current is driven by the same mode for the fields. The electromagnetic modes coupling occurs due to the nonlinearities in the plasma excitation. But even with a high level of nonlinearity, the symmetry of the wakefield is still approximately conserved since nonlinearities are independent of the polarization direction and depend mainly on the field modules and hence remain mainly axis-symmetric. Therefore, this coupling is assumed to take place mainly between mode 0 and mode 1. However, the maximal number of modes used m_{max} is kept as a free parameter in the implementation of the method, in order to allow for less-symmetric configurations.

The major advantage of using this method is that even with the inclusion of few higher Fourier modes, if modes up to m_{max} are retained, the cost of such a simulation would be roughly equivalent to performing $(m_{max}+1)$ bi-dimensional calculations.

3.2 FDTD scheme

In this section, first the finite difference discretization of Maxwell's equations modes eq. (3.8) on the Yee grid is presented. Then, specificities related to its numerical implementation like the associated complications near the $r = 0$ axis and the suitable boundary conditions are addressed. The adaptation of the different steps in the PIC loop to this method are presented. Finally, the limits of using FDTD scheme are discussed.

3.2.1 Discretized Maxwell equations in the Yee grid

Just like in cylindrical coordinates, each field mode in eq. (3.8) is discretized on a two-dimensional Yee grid (r,z) with respect to the fields duality according to the layout in fig. 3.2. We define the numerical differentiation operators (D_rF) and (D_zF) :

$$
\begin{aligned}
(D_rF)_{j',k'} &= \frac{F_{j'+\frac{1}{2},k'} - F_{j'-\frac{1}{2},k'}}{\Delta r} \\
(D_zF)_{j',k'} &= \frac{F_{j',k'+\frac{1}{2}} - F_{j',k'-\frac{1}{2}}}{\Delta z}
\end{aligned}
$$

where j' and k' can be integers or half-integer. Using these notations, the discretized Maxwell modes in cylindrical coordinates are written:

$$
\begin{aligned}
\frac{\tilde{B}_{r\,j,k+\frac{1}{2},m}^{\,n+\frac{1}{2}} - \tilde{B}_{r\,j,k+\frac{1}{2},m}^{\,n-\frac{1}{2}}}{\Delta t} &= \frac{i\,m}{j\Delta r}\tilde{E}_{z\,j,k+\frac{1}{2},m}^{\,n} + (D_z\tilde{E}_\theta^n)_{j,k+\frac{1}{2},m} \\
\frac{\tilde{B}_{\theta\,j+\frac{1}{2},k+\frac{1}{2},m}^{\,n+\frac{1}{2}} - \tilde{B}_{\theta\,j+\frac{1}{2},k+\frac{1}{2},m}^{\,n-\frac{1}{2}}}{\Delta t} &= -\,(D_z\tilde{E}_r^n)_{j+\frac{1}{2},k+\frac{1}{2},m} + (D_r\tilde{E}_z^n)_{j+\frac{1}{2},k+\frac{1}{2},m} \\
\frac{\tilde{B}_{z\,j+\frac{1}{2},k,m}^{\,n+\frac{1}{2}} - \tilde{B}_{z\,j+\frac{1}{2},k,m}^{\,n-\frac{1}{2}}}{\Delta t} &= -\,\frac{(j+1)\tilde{E}_{\theta\,j+1,k,m}^{\,n} - j\tilde{E}_{\theta\,j,k,m}^{\,n}}{(j+\frac{1}{2})\Delta r} - \frac{i\,m}{(j+\frac{1}{2})\Delta r}\tilde{E}_{r\,j+\frac{1}{2},k,m}^{\,n} \\
\frac{\tilde{E}_{r\,j+\frac{1}{2},k,m}^{\,n+1} - \tilde{E}_{r\,j+\frac{1}{2},k,m}^{\,n}}{c^2\Delta t} &= -\,\frac{i\,m}{(j+\frac{1}{2})\Delta r}\tilde{B}_{z\,j+\frac{1}{2},k,m}^{\,n+\frac{1}{2}} - (D_z\tilde{B}_\theta^{n+\frac{1}{2}})_{j+\frac{1}{2},k,m} - \mu_0\tilde{J}_{r\,j+\frac{1}{2},k,m}^{\,n+\frac{1}{2}} \\
\frac{\tilde{E}_{\theta\,j,k,m}^{\,n+1} - \tilde{E}_{\theta\,j,k,m}^{\,n}}{c^2\Delta t} &= (D_z\tilde{B}_r^{n+\frac{1}{2}})_{j,k,m} - (D_r\tilde{B}_z^{n+\frac{1}{2}})_{j,k,m} - \mu_0\tilde{J}_{\theta\,j,k,m}^{\,n+\frac{1}{2}} \\
\frac{\tilde{E}_{z\,j,k+\frac{1}{2},m}^{\,n+1} - \tilde{E}_{z\,j,k+\frac{1}{2},m}^{\,n}}{c^2\Delta t} &= \frac{\left(j+\frac{1}{2}\right)\tilde{B}_{\theta\,j+\frac{1}{2},k+\frac{1}{2},m}^{\,n+\frac{1}{2}} - \left(j-\frac{1}{2}\right)\tilde{B}_{\theta\,j-\frac{1}{2},k+\frac{1}{2},m}^{\,n+\frac{1}{2}}}{j\Delta r} \\
&\quad + \frac{i\,m}{j\Delta r}\tilde{B}_{r\,j,k+\frac{1}{2},m}^{\,n+\frac{1}{2}} - \mu_0\tilde{J}_{z\,j,k+\frac{1}{2},m}^{\,n+\frac{1}{2}}
\end{aligned}
\tag{3.9}
$$

Note that the above expressions are no more valid on axis $r = 0$ (ie. $j = 0$) due to the arising singularities in some terms from the division by r. Therefore, a special boundary condition should be applied for these quantities based on their symmetry properties [Lifschitz et al., 2009; Davidson, 2016] before using them in the equations of dynamics.

3.2.2 On axis condition

Due to singularities at $r = 0$ in the cylindrical coordinates, a special treatment for the fields on axis is required. In this section, specific on-axis conditions are derived for the FDTD solver of the quasi-cylindrical algorithm in a Yee lattice. The conditions on axis, implemented in SMILEI are based on the original paper [Lifschitz et al., 2009]. However, only the conditions for the $m = 0$ mode of the longitudinal electric field and the $m = 1$ mode of the radial magnetic field are given in the paper. The current implementation has improved those specific boundary conditions and extended them to all the fields and to greater modes. It is based on contributions from Davoine in Calder-Circ and the SMILEI team.

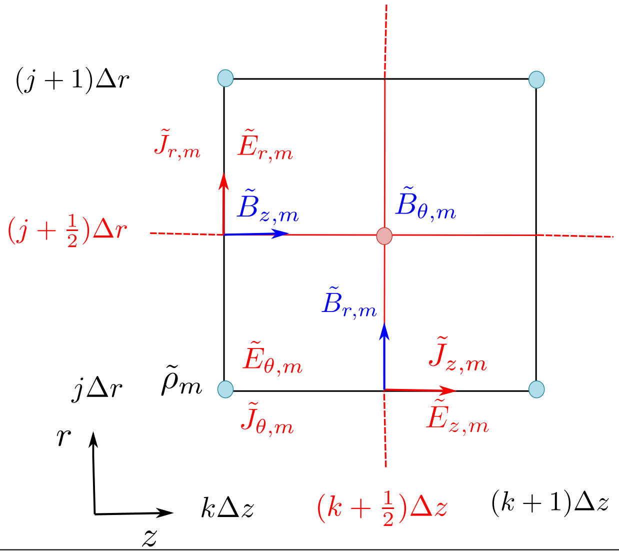

Field	Position in space and time			Notation
	r	z	t	
$\tilde{E}_{r,m}$	$(j+\frac{1}{2})\Delta r$	$k\Delta z$	$n\Delta t$	${\tilde{E}_r}^{n}_{j+\frac{1}{2},k,m}$
$\tilde{E}_{\theta,m}$	$j\Delta r$	$k\Delta z$	$n\Delta t$	${\tilde{E}_\theta}^{n}_{j,k,m}$
$\tilde{E}_{z,m}$	$j\Delta r$	$(k+\frac{1}{2})\Delta z$	$n\Delta t$	${\tilde{E}_z}^{n}_{j,k+\frac{1}{2},m}$
$\tilde{B}_{r,m}$	$j\Delta r$	$(k+\frac{1}{2})\Delta z$	$(n+\frac{1}{2})\Delta t$	${\tilde{B}_r}^{n+\frac{1}{2}}_{j,k+\frac{1}{2},m}$
$\tilde{B}_{\theta,m}$	$(j+\frac{1}{2})\Delta r$	$(k+\frac{1}{2})\Delta z$	$(n+\frac{1}{2})\Delta t$	${\tilde{B}_\theta}^{n+\frac{1}{2}}_{j+\frac{1}{2},k+\frac{1}{2},m}$
$\tilde{B}_{z,m}$	$(j+\frac{1}{2})\Delta r$	$k\Delta z$	$(n+\frac{1}{2})\Delta t$	${\tilde{B}_z}^{n+\frac{1}{2}}_{j+\frac{1}{2},k,m}$
$\tilde{\rho}_m$	$j\Delta r$	$k\Delta z$	$n\Delta t$	$\tilde{\rho}^{n}_{j,k,m}$
$\tilde{J}_{r,m}$	$(j+\frac{1}{2})\Delta r$	$k\Delta z$	$(n+\frac{1}{2})\Delta t$	${\tilde{J}_r}^{n+\frac{1}{2}}_{j+\frac{1}{2},k,m}$
$\tilde{J}_{\theta,m}$	$j\Delta r$	$k\Delta z$	$(n+\frac{1}{2})\Delta t$	${\tilde{J}_\theta}^{n+\frac{1}{2}}_{j,k,m}$
$\tilde{J}_{z,m}$	$j\Delta r$	$(k+\frac{1}{2})\Delta z$	$(n+\frac{1}{2})\Delta t$	${\tilde{J}_z}^{n+\frac{1}{2}}_{j,k+\frac{1}{2},m}$

Figure 3.2: Schematic representation of fields modes staggering on the Yee lattice where j,k are integers corresponding to the primal grid (blue) and $j+\frac{1}{2}$, $k+\frac{1}{2}$ are half-integers corresponding to the dual grid (red). The table shows at which positions and time each component of the fields modes is defined where Δr, Δz are the spatial grid cell sizes.

The primality/duality of the fields plays an important role in the definition of this condition, therefore an illustrative scheme of the ghost cells representation with the primal and dual points next to the axis is shown in fig. 3.3 in the case of $N_{ghost} = 2$. In Smilei, ghost cells in the radial direction (light blue) are located "below" the axis and the number of ghost cells N_{ghost} equals the number of the primal points (blue) before reaching the physical domain (light red) separated by the actual geometric axis $r = 0$. If Δr is a radial cell size, the dual points (red) on the radial axis are shifted by $-\Delta r/2$ from primal ones.

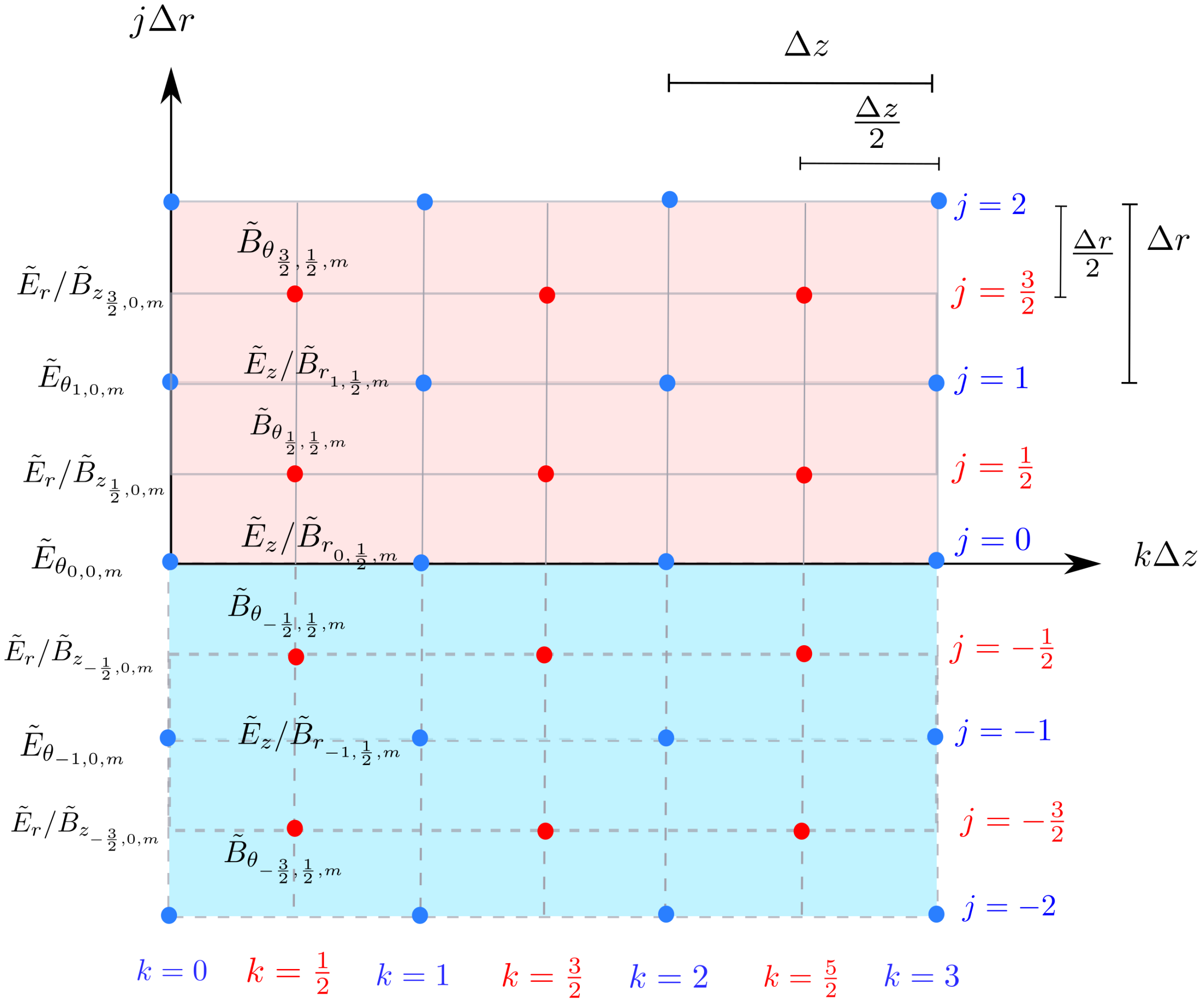

Figure 3.3: Scheme of the electric and magnetic fields representation in the ghost region (light blue) and physical domain (light red) for a few primal (blue) and dual (red) nodes next to the geometrical axis $r = 0$ on Yee-grid.

Transverse fields on axis

The first basic principle is that a mode 0 field defined on axis can only be longitudinal otherwise it would be ill defined. From this we can already state that $\tilde{E}_{r,m=0}$, $\tilde{E}_{\theta,m=0}$, $\tilde{B}_{r,m=0}$ and $\tilde{B}_{\theta,m=0}$ are zero on axis. This condition is straightforward for primal fields in r which are defined exactly on axis, hence their values are simply set to zero. For dual fields in r the value is set using a linear interpolation between nearest grid points $F(r = 0) = (F_{j=-\frac{1}{2}} + F_{j=\frac{1}{2}})/2 = 0$. Therefore, the discretized transverse fields on axis for the mode $m = 0$ are given by:

$$\begin{aligned} \tilde{E}_{\theta j=0,k,m=0} &= 0 & \tilde{E}_{r j=-\frac{1}{2},k,m=0} &= -\tilde{E}_{r j=\frac{1}{2},k,m=0} \\ \tilde{B}_{r j=0,k,m=0} &= 0 & \tilde{B}_{\theta j=-\frac{1}{2},k,m=0} &= -\tilde{B}_{\theta j=\frac{1}{2},k,m=0} \end{aligned} \tag{3.10}$$

The transverse electric field can be described by the two components E_r and E_θ

$$\boldsymbol{E}_\perp = \boldsymbol{E}_y + \boldsymbol{E}_z = (E_r \cos\theta - E_\theta \sin\theta)\boldsymbol{e_y} + (E_r \sin\theta + E_\theta \cos\theta)\boldsymbol{e_z} \tag{3.11}$$

It can not depend on θ otherwise it would be ill defined, i.e

$$\frac{\partial \boldsymbol{E}_{\perp}}{\partial\theta}(r=0)=0 \qquad \forall\theta \tag{3.12}$$

Thus

$$\cos\theta\left(\frac{\partial E_r}{\partial\theta}-E_\theta\right)+\sin\theta\left(\frac{\partial E_\theta}{\partial\theta}+E_r\right)=0 \quad \text{for} \quad r=0 \quad \forall\theta \tag{3.13}$$

This leads to the two following conditions:

$$\frac{\partial E_r}{\partial\theta}-E_\theta=0 \qquad \forall\theta \tag{3.14}$$

$$\frac{\partial E_\theta}{\partial\theta}+E_r=0 \qquad \forall\theta \tag{3.15}$$

Using the definition of the azimuthal decomposition of a given field F in θ (3.2), we can write the previous equations for each mode m as follows:

$$\tilde{E}_{r,m}=\frac{i\tilde{E}_{\theta,m}}{m} \qquad\qquad \tilde{E}_{r,m}=im\tilde{E}_{\theta,m} \tag{3.16}$$

Since we have already established earlier that the mode $m=0$ must cancel on axis, we are concerned only about $m>0$. The system of equations 3.16 can have a non-zero solution only for $m=1$. We therefore conclude that all modes must cancel on axis except for $m=1$. The same principle applies also for the magnetic field.

$$\tilde{E}_{\theta\, j=0,k,m>1}=0 \qquad\qquad \tilde{E}_{r\, j=-\frac{1}{2},k,m>1}=-\tilde{E}_{r\, j=\frac{1}{2},k,m>1} \tag{3.17}$$

$$\tilde{B}_{r\, j=0,k,m>1}=0 \qquad\qquad \tilde{B}_{\theta\, j=-\frac{1}{2},k,m>1}=-\tilde{B}_{\theta\, j=\frac{1}{2},k,m>1} \tag{3.18}$$

To calculate the transverse electric fields on axis for $m=1$, we use Maxwell-Gauss equation (1.3):

$$\nabla\cdot\tilde{\boldsymbol{E}}_{m=1}=\frac{\tilde{\rho}_{m=1}}{\epsilon_0} \tag{3.19}$$

The charge density being a scalar field, it takes zero for a value on axis. Since the longitudinal fields are zero on axis for all modes $m>0$, the previous equation can be rewritten as:

$$\frac{\tilde{E}_{r,m=1}-im\tilde{E}_{\theta,m=1}}{r}+\frac{\partial\tilde{E}_{r,m=1}}{\partial r}=0 \tag{3.20}$$

The second equation in (3.16) already establishes that the first term is zero. It is only necessary to cancel the second term. In order to do so, we build an uncentered finite difference scheme of the second order. Simple Taylor developments for any quantity u give:

$$u(r+\frac{dr}{2})=u(r)+\frac{dr}{2}u'(r)+\frac{dr^2}{8}u''(r)+\mathcal{O}(dr^3)$$

and

$$u(r+\frac{3dr}{2})=u(r)+\frac{3dr}{2}u'(r)+\frac{9dr^2}{8}u''(r)+\mathcal{O}(dr^3)$$

By combining them, we obtain the scheme we are looking for:

$$u'(r) = \frac{9u(r+\frac{dr}{2}) - u(r+\frac{3dr}{2}) - 8u(r)}{3dr}$$

We can therefore write:

$$\frac{\partial \tilde{E}_{r\,m=1}}{\partial r}(r=0) = \frac{9\tilde{E}_{r\,m=1}(r=\frac{\Delta r}{2}) - \tilde{E}_{r\,m=1}(r=\frac{3\Delta r}{2}) - 8\tilde{E}_{r\,m=1}(r=0)}{3\Delta r} \tag{3.21}$$

Since $(\partial \tilde{E}_{r\,m=1}/\partial r)(r=0) = 0$, the previous equation results in :

$$\tilde{E}_{r\,m=1}(r=0) = \frac{1}{8}\left(9\tilde{E}_{r\,m=1}(r=\frac{\Delta r}{2}) - \tilde{E}_{r\,m=1}(r=\frac{3\Delta r}{2})\right) \tag{3.22}$$

And from eq. (3.16) this turns into:

$$\tilde{E}_{\theta\,m=1}(r=0) = -\frac{i}{8}\left(9\tilde{E}_{r\,m=1}(r=\frac{\Delta r}{2}) - \tilde{E}_{r\,m=1}(r=\frac{3\Delta r}{2})\right) \tag{3.23}$$

giving the corresponding boundary condition for $\tilde{E}_{\theta\,m=1}$:

$$\tilde{E}_{\theta\,j=0,k,m=1} = -\frac{i}{8}\left(9\tilde{E}_{r\,j=\frac{1}{2},k,m=1} - \tilde{E}_{r\,j=\frac{3}{2},k,m=1}\right) \tag{3.24}$$

Once $\tilde{E}_{\theta\,m=1}$ is defined on axis, we need to pick $\tilde{E}_{r\,m=1}$ so that the condition in eq. (3.16) is matched. With a linear interpolation we obtain:

$$\tilde{E}_{r\,j=-\frac{1}{2},k,m=1} = 2i\tilde{E}_{\theta\,j=0,k,m=1} - \tilde{E}_{r\,j=\frac{1}{2},k,m=1} \tag{3.25}$$

Although the same principle also applies to the magnetic field, a different treatment should be accorded due to the difference in the duality. The expression of $\tilde{B}_{r\,m}$ in (3.6) has a $\tilde{E}_{z\,m}/r$ term which makes it undefined on axis. This term can be evaluated for the mode $m=1$ using the fact that $\tilde{E}_{z\,m=1}$ vanishes at the axis.

$$\lim_{r\to 0} \frac{\tilde{E}_{z\,m=1}(r)}{r} = \lim_{r\to 0} \frac{\tilde{E}_{z\,m=1}(r) - \tilde{E}_{z\,m=1}(r=0)}{r} \tag{3.26}$$

Since $\tilde{E}_{z\,m=1}(r=0) = 0$ and by definition of a derivative, we have:

$$\lim_{r\to 0} \frac{\tilde{E}_{z\,m=1}(r) - \tilde{E}_{z\,m=1}(r=0)}{r} = \frac{\partial \tilde{E}_{z\,m=1}}{\partial r}(r=0) \tag{3.27}$$

This derivative can be evaluated by a simple finite difference scheme. We get the following result:

$$\lim_{r\to 0} \frac{\tilde{E}_{z\,m=1}(r)}{r} = \frac{\tilde{E}_{z\,m=1}(\Delta r)}{\Delta r} \tag{3.28}$$

Plugging this result in the standard FDTD scheme for $\tilde{B}_{r\,m=1}$, we get the on-axis boundary condition:

$$\tilde{B}^{\,n+1}_{r\,j=0,k,m=1} = \tilde{B}^{\,n}_{r\,j=0,k,m=1} + \Delta t\left(\frac{i}{\Delta r}\tilde{E}^{\,n}_{z\,j=1,k,m=1} + \frac{\tilde{E}^{\,n}_{\theta\,j=0,k+1,m=1} - \tilde{E}^{\,n}_{\theta\,j=0,k,m=1}}{\Delta z}\right) \tag{3.29}$$

Exactly as for the electric field, we need to have $B_r^{m=1} = iB_\theta^{m=1}$. With a similar interpolation, we obtain the boundary condition on axis for $\tilde{B}_{\theta\,m=1}$:

$$\tilde{B}_{\theta\,j=-\frac{1}{2},k,m=1} = -2i\tilde{B}_{r\,j=0,k,m=1} - \tilde{B}_{\theta\,j=\frac{1}{2},k,m=1} \tag{3.30}$$

Longitudinal fields on axis

Longitudinal fields on axis can only be of mode 0, since they do not depend on θ. Therefore, the discretized longitudinal fields on axis for modes $m > 0$ are given by:

$$\tilde{E}_{z\,j=0,k,m>0} = 0 \qquad \tilde{B}_{z\,j=-\frac{1}{2},k,m>0} = -\tilde{B}_{z\,j=\frac{1}{2},k,m>0} \tag{3.31}$$

In order to get an evaluation of $\tilde{E}_{z\,m=0}$ on axis, one can use the same approach as for $\tilde{B}_{r\,m=1}$. Since $\tilde{E}_{\theta\,m=0}$ is zero on axis, the following relation can be derived using similar arguments as eq. (3.28):

$$\lim_{r\to 0} \frac{1}{r}\frac{\partial r\tilde{B}_{\theta\,m=0}}{\partial r} = \frac{4\tilde{B}_{\theta\,m=0}(\Delta r/2)}{\Delta r} \tag{3.32}$$

Introducing this result in the discretized Maxwell's equation for $\tilde{E}_{z\,m=0}$, we get:

$$\tilde{E}_{z\,j=0,k,m=0}^{\;n+1} = \tilde{E}_{z\,j=0,k,m=0}^{\;n} + \Delta t\left(\frac{4}{\Delta r}\tilde{B}_{\theta\,k=\frac{1}{2},k,m=0}^{\;n+\frac{1}{2}} - \tilde{J}_{z\,j=-\frac{1}{2},k,m=0}^{\;n+\frac{1}{2}}\right) \tag{3.33}$$

To calculate $\tilde{B}_{z\,m=0}$ which is independant of θ, we assume it is differentiable at $r = 0$ then its derivative along r is zero on axis (derivative of a pair function is zero at $r = 0$). From this, we get:

$$\tilde{B}_{z\,j=-\frac{1}{2},k,m=0} = \tilde{B}_{z\,j=\frac{1}{2},k,m=0} \tag{3.34}$$

3.2.3 Boundary conditions

In this part, the specific longitudinal and transverse boundary conditions implemented in SMILEI for the FDTD quasi-cylindrical scheme are presented.

Silver-Muller

Silver-Müller is a boundary condition (BC) that has a double function. On the one hand, it allows the injection of the laser at the entry of the simulation box. On the other hand, it enables the absorption of the reflected waves by determining the magnetic field components in the perpendicular direction to the boundary wall. In our case, Silver-Müller BCs are implemented in the left Z_{min} and right Z_{max} boundaries in the propagation direction z.

Any electromagnetic wave can be represented as a sum of linearly polarized plane waves, therefore we consider a monochromatic plane wave propagating in the z-direction $\boldsymbol{E} = \boldsymbol{E_0}e^{i(\boldsymbol{k}\cdot\boldsymbol{z}-\omega t)}$ and $\boldsymbol{B} = \boldsymbol{B_0}e^{i(\boldsymbol{k}\cdot\boldsymbol{z}-\omega t)}$ where $\boldsymbol{k}$ is the wave vector and $\boldsymbol{k}\cdot\boldsymbol{z} = k_z z$.

The fields are considered as a sum of forward and backward moving plane waves with a given frequency and wave number, therefore $\boldsymbol{E} = \boldsymbol{E}^+ + \boldsymbol{E}^-$ and $\boldsymbol{B} = \boldsymbol{B}^+ + \boldsymbol{B}^-$. We start by writing the Maxwell-Ampère equation in vacuum:

$$\partial_t \boldsymbol{E} = \boldsymbol{\nabla}\times\boldsymbol{B} \qquad \text{where} \quad \boldsymbol{\nabla} = (0, 0, \partial_z)^T$$

We then obtain for each mode m:

$$\begin{cases} \partial_t \tilde{E}_{z\,m} = 0 \\ \partial_t \tilde{E}_{r\,m} = -\partial_z \tilde{B}_{\theta\,m} \\ \partial \tilde{E}_{\theta\,m} = \partial_z \tilde{B}_{r\,m} \end{cases}$$

Using the fact that $\partial_t \equiv -i\omega t$, $\partial_z \equiv ik_z$ and that $|\boldsymbol{k}|/\omega = k_z/\omega = 1$ in vacuum, the transverse fields corresponding to the last two equations are rewritten in the following way:

$$\begin{aligned}\tilde{E}_{rm} &= \tilde{B}_{\theta m}^{+} - \tilde{B}_{\theta m}^{-}\\ \tilde{E}_{\theta m} &= -\tilde{B}_{rm}^{+} + \tilde{B}_{rm}^{-}\end{aligned}$$

Left boundary Z_{min}:

At the left boundary, the known fields are the incoming ones $\tilde{B}_{\theta m}^{+}$ and $\tilde{B}_{rm}^{+}$. Hence, we can write:

$$\tilde{E}_{rm} = 2\tilde{B}_{\theta m}^{+} - \tilde{B}_{\theta m} \tag{3.35}$$

$$\tilde{E}_{\theta m} = -2\tilde{B}_{rm}^{+} + \tilde{B}_{rm} \tag{3.36}$$

We start by discretizing the first equation (3.35) while centering all the fields in the first equation (3.35) on the same point $r = (j+\frac{1}{2})\Delta r$ and time $t = (n+\frac{1}{2})\Delta t$

$$\frac{1}{2}\left(\tilde{E}_{r\,j+\frac{1}{2},k,m}^{\,n+1} + \tilde{E}_{r\,j+\frac{1}{2},k,m}^{\,n}\right) = 2\tilde{B}_{\theta\,j+\frac{1}{2},k-\frac{1}{2},m}^{\,+,n+\frac{1}{2}} - \frac{1}{2}\left(\tilde{B}_{\theta\,j+\frac{1}{2},j-\frac{1}{2},m}^{\,n+\frac{1}{2}} + \tilde{B}_{\theta\,j+\frac{1}{2},k+\frac{1}{2},m}^{\,n+\frac{1}{2}}\right) \tag{3.37}$$

The discretized Maxwell-Ampère equations for $\tilde{E}_{rm}$ and $\tilde{E}_{\theta m}$ read:

$$\tilde{E}_{r\,j+\frac{1}{2},k,m}^{\,n+1} - \tilde{E}_{r\,j+\frac{1}{2},k,m}^{\,n} = -\frac{c^2\Delta t}{\Delta z}\left(\tilde{B}_{\theta\,j+\frac{1}{2},k+\frac{1}{2},m}^{\,n+\frac{1}{2}} - \tilde{B}_{\theta\,j+\frac{1}{2},k-\frac{1}{2},m}^{\,n+\frac{1}{2}}\right) - \frac{im}{(j+\frac{1}{2})\Delta r}\tilde{B}_{z\,j+\frac{1}{2},k,m}^{\,n+\frac{1}{2}} \tag{3.38}$$

$$\tilde{E}_{\theta\,j,k,m}^{\,n+1} - \tilde{E}_{\theta\,j,k,m}^{\,n} = \frac{c^2\Delta t}{\Delta z}\left(\tilde{B}_{r\,j,k+\frac{1}{2},m}^{\,n+\frac{1}{2}} - \tilde{B}_{r\,j,k-\frac{1}{2},m}^{\,n+\frac{1}{2}}\right) - \frac{c^2\Delta t}{\Delta r}\left(\tilde{B}_{z\,j+\frac{1}{2},k,m}^{\,n+\frac{1}{2}} - \tilde{B}_{z\,j-\frac{1}{2},k,m}^{\,n+\frac{1}{2}}\right) \tag{3.39}$$

Using the given quantities by eq. (3.38) and eq. (3.37), we obtain the unknown quantity $\tilde{B}_{\theta\,j+\frac{1}{2},k-\frac{1}{2},m}^{\,n+\frac{1}{2}}$ for the left boundary given by:

$$\begin{aligned}\left(1+\frac{c^2\Delta t}{\Delta z}\right)\tilde{B}_{\theta\,j+\frac{1}{2},k-\frac{1}{2},m}^{\,n+\frac{1}{2}} = &-\left(1-\frac{c^2\Delta t}{\Delta z}\right)\tilde{B}_{\theta\,j+\frac{1}{2},k+\frac{1}{2},m}^{\,n+\frac{1}{2}} + 4\tilde{B}_{\theta\,j+\frac{1}{2},k-\frac{1}{2},m}^{\,+,n+\frac{1}{2}}\\ &+ \frac{im}{(j+\frac{1}{2})\Delta r}\tilde{B}_{z\,j+\frac{1}{2},k,m}^{\,n+\frac{1}{2}} - 2\tilde{E}_{r\,j+\frac{1}{2},k,m}^{\,n}\end{aligned} \tag{3.40}$$

The discretized version of eq. (3.36) after centering all fields at the same position $r = j\Delta r$ and time $t = (n+\frac{1}{2})\Delta t$ reads:

$$\frac{1}{2}\left(\tilde{E}_{\theta\,j,k,m}^{\,n+1} + \tilde{E}_{\theta\,j,k,m}^{\,n}\right) = -2\tilde{B}_{r\,j,k-\frac{1}{2},m}^{\,+,n+\frac{1}{2}} + \frac{1}{2}\left(\tilde{B}_{r\,j,k-\frac{1}{2},m}^{\,n+\frac{1}{2}} + \tilde{B}_{r\,j,k+\frac{1}{2},m}^{\,n+\frac{1}{2}}\right) \tag{3.41}$$

Using eq. (3.39) and eq. (3.41), the unknown field $\tilde{B}_{r\,j,k-\frac{1}{2},m}^{\,n+\frac{1}{2}}$ for the left boundary can be determined according to:

$$\begin{aligned}\left(1+\frac{c^2\Delta t}{\Delta z}\right)\tilde{B}_{r\,j,k-\frac{1}{2},m}^{\,n+\frac{1}{2}} = &-\left(1-\frac{c^2\Delta t}{\Delta z}\right)\tilde{B}_{r\,j,k+\frac{1}{2},m}^{\,n+\frac{1}{2}} + 4\tilde{B}_{r\,j,k-\frac{1}{2},m}^{\,+,n+\frac{1}{2}}\\ &+ 2\tilde{E}_{\theta\,j,k,m}^{\,n} - \frac{c^2\Delta t}{\Delta r}\left(\tilde{B}_{z\,j+\frac{1}{2},k,m}^{\,n+\frac{1}{2}} - \tilde{B}_{z\,j-\frac{1}{2},k,m}^{\,n+\frac{1}{2}}\right)\end{aligned} \tag{3.42}$$

Right boundary Z_{max}:

In the case of right boundary, the known fields are the incoming ones $\tilde{B}_{\theta m}^{-}$ and $\tilde{B}_{rm}^{-}$ and therefore

$$\tilde{E}_{rm} = \tilde{B}_{\theta m} - 2\tilde{B}_{\theta m}^{-} \tag{3.43}$$

$$\tilde{E}_{\theta m} = -\tilde{B}_{rm} + 2\tilde{B}_{rm}^{-} \tag{3.44}$$

Applying the same previous procedure, one can determine the fields $\tilde{B}_{\theta}{}_{j+\frac{1}{2},k+\frac{1}{2},m}^{n+\frac{1}{2}}$ and $\tilde{B}_{r}{}_{j,k+\frac{1}{2},m}^{n+\frac{1}{2}}$ at the right boundary which are given by the following equations:

$$\begin{aligned}\left(1+\frac{c^2\Delta t}{\Delta z}\right)\tilde{B}_{\theta}{}_{j+\frac{1}{2},k+\frac{1}{2},m}^{n+\frac{1}{2}} =& -\left(1-\frac{\Delta t}{\Delta z}\right)\tilde{B}_{\theta}{}_{j+\frac{1}{2},k-\frac{1}{2},m}^{n+\frac{1}{2}} + \tilde{B}_{\theta}{}_{j+\frac{1}{2},k+\frac{1}{2},m}^{-,n+\frac{1}{2}} \\ &+ 2\tilde{E}_{r}{}_{j+\frac{1}{2},k,m}^{n} + \frac{im}{(j+\frac{1}{2})\Delta r}\tilde{B}_{z}{}_{j+\frac{1}{2},k,m}^{n+\frac{1}{2}}\end{aligned} \tag{3.45}$$

$$\begin{aligned}\left(1+\frac{c^2\Delta t}{\Delta z}\right)\tilde{B}_{r}{}_{j,k+\frac{1}{2},m}^{n+\frac{1}{2}} =& -\left(1-\frac{c^2\Delta t}{\Delta z}\right)\tilde{B}_{r}{}_{j,k-\frac{1}{2},m}^{n+\frac{1}{2}} + 4\tilde{B}_{r}{}_{j,k+\frac{1}{2},m}^{-,n+\frac{1}{2}} \\ &- 2\tilde{E}_{\theta}{}_{j,k,m}^{n} - \frac{c^2\Delta t}{\Delta r}\left(\tilde{B}_{z}{}_{j+\frac{1}{2},k,m}^{n+\frac{1}{2}} - \tilde{B}_{z}{}_{j-\frac{1}{2},k,m}^{n+\frac{1}{2}}\right)\end{aligned} \tag{3.46}$$

Buneman

Buneman's absorbing boundary condition [Buneman, 1993] is a good alternative to reflecting or open boundary conditions. In the context of this PhD, this boundary condition is implemented and adapted to the architecture of SMILEI. We start by the general case in a Cartesian 3D frame $(O, \boldsymbol{e_1}, \boldsymbol{e_2}, \boldsymbol{e_3})$, where an incoming electromagnetic wave is propagating towards the plane $S = (\boldsymbol{e_2}, \boldsymbol{e_3})$ with the normal vector $\boldsymbol{n} = \boldsymbol{e_1}$ as illustrated in fig. 3.4.

The projection of the outgoing wave vector $\boldsymbol{k}$ in the frame $(O, \boldsymbol{e}_1, \boldsymbol{e}_2, \boldsymbol{e}_3)$ in terms of the angles θ_s and φ_s represented in fig. 3.4, reads:

$$\begin{aligned}\boldsymbol{k}\cdot\boldsymbol{e}_1 &= k\cos\theta\cos\varphi \\ \boldsymbol{k}\cdot\boldsymbol{e}_2 &= k\sin\theta \\ \boldsymbol{k}\cdot\boldsymbol{e}_3 &= k\cos\theta\sin\varphi\end{aligned} \tag{3.47}$$

Based on the previous representation of the wave vector in spherical coordinates (3.47) and using the notations $\boldsymbol{B}_n = (\boldsymbol{B}\cdot\boldsymbol{n})\cdot\boldsymbol{n} = \boldsymbol{B_{e1}}$ and $\boldsymbol{B}_S = (\boldsymbol{B_{e2}}, \boldsymbol{B_{e3}})$, the absorption condition at the boundaries can be found from Maxwell's equations. It is given by the general formula [Buneman, 1993]

$$(\partial_t + \partial_n)\boldsymbol{B}_S = c_B\nabla_S\boldsymbol{B}_n - c_E\nabla_S\times\boldsymbol{E}_n \tag{3.48}$$

where ∂_t is the time derivative, ∂_n is the normal spatial derivative, $c_B = \frac{\cos\theta_s\cos\varphi_s}{1+\cos\theta_s\cos\varphi_s}$ and $c_E = 1 - c_B$.

The application of this condition to the upper border R_{max} in the case of azimuthal geometry is equivalent to apply an absorbing boundary condition in $Y_{min}, Y_{max}, X_{min}, X_{max}$ in the

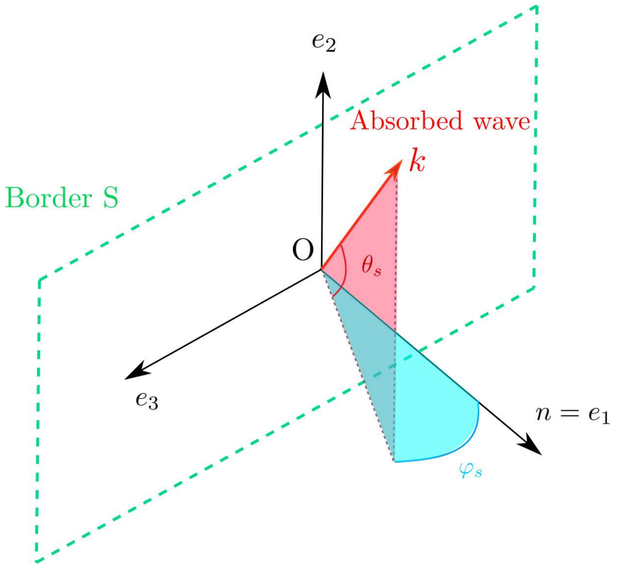

Figure 3.4: Representation of the absorbed wave propagating toward the border S in the Cartesian frame $(O, \boldsymbol{e}_1, \boldsymbol{e}_2, \boldsymbol{e}_3)$.

Cartesian geometry. It results in two constraints on $\tilde{B}_{\theta m}$ and $\tilde{B}_{zm}$ fields. Thus, eq. (3.48) in the azimuthal cylindrical coordinates (r, z, θ) reads:

$$(\partial_t + \partial_r)\tilde{B}_{\theta,m} = -\frac{imc_B}{r}\tilde{B}_{r,m} - c_E\partial_z\tilde{E}_{r,m} - \frac{c_B}{r}\tilde{B}_{\theta,m}$$

$$(\partial_t + \partial_r)\tilde{B}_{z,m} = c_B\partial_z\tilde{B}_{r,m} - \frac{imc_E}{r}\tilde{E}_{r,m} - \frac{c_E}{r}\tilde{E}_{\theta,m}$$

Discretizing the above equations on the grid with respect to the duality of the fields in time and space and after centering all the quantities on the position $r = j\Delta r$ and on the time $t = n\Delta t$, results in:

$$\begin{aligned}\tilde{B}_{\theta\, j+\frac{1}{2},k+\frac{1}{2},m}^{\ n+\frac{1}{2}} = \frac{1}{\alpha_\theta}\Bigg(&\beta_\theta\tilde{B}_{\theta\, j-\frac{1}{2},k+\frac{1}{2},m}^{\ n+\frac{1}{2}} + \gamma_\theta\tilde{B}_{\theta\, j+\frac{1}{2},k+\frac{1}{2},m}^{\ n-\frac{1}{2}} + \kappa_\theta\tilde{B}_{\theta\, j-\frac{1}{2},k+\frac{1}{2},m}^{\ n-\frac{1}{2}}\\ &- \frac{imc_B}{j\Delta r}\left(\tilde{B}_{r\, j,k+\frac{1}{2},m}^{\ n+\frac{1}{2}} + \tilde{B}_{r\, j,k+\frac{1}{2},m}^{\ n-\frac{1}{2}}\right)\\ &-\frac{c_E}{\Delta z}\left(\tilde{E}_{r\, j+\frac{1}{2},k+1,m}^{\ n} + \tilde{E}_{r\, j-\frac{1}{2},k+1,m}^{\ n} - \tilde{E}_{r\, j+\frac{1}{2},k,m}^{\ n} - \tilde{E}_{r\, j-\frac{1}{2},k}^{\ n}\right)\Bigg)\end{aligned} \tag{3.49}$$

$$\begin{aligned}\tilde{B}_{z\, j+\frac{1}{2},k,m}^{\ n+\frac{1}{2}} =&\tilde{B}_{z\, j-\frac{1}{2},k,m}^{\ n-\frac{1}{2}} + \alpha_z\left(\tilde{B}_{z\, j+\frac{1}{2},k,m}^{\ n-\frac{1}{2}} - \tilde{B}_{z\, j-\frac{1}{2},k,m}^{\ n+\frac{1}{2}}\right)\\ &+ \frac{c_B\beta_z}{\Delta z}\left(\tilde{B}_{r\, j,k+\frac{1}{2},m}^{\ n+\frac{1}{2}} + \tilde{B}_{r\, j,k+\frac{1}{2},m}^{\ n-\frac{1}{2}} - \tilde{B}_{r\, j,k-\frac{1}{2},m}^{\ n+\frac{1}{2}} - \tilde{B}_{r\, j,k-\frac{1}{2},m}^{\ n-\frac{1}{2}}\right)\\ &- \frac{imc_E\beta_z}{j\Delta r}\left(\tilde{E}_{r\, j+\frac{1}{2},k,m}^{\ n} + \tilde{E}_{r\, j-\frac{1}{2},k,m}^{\ n}\right) - 2\frac{c_E\beta_z}{j\Delta r}\tilde{E}_{\theta\, j,k,m}^{\ n}\end{aligned} \tag{3.50}$$

where

$$\alpha_\theta = \frac{1}{\Delta t} + \frac{1}{\Delta r} + \frac{c_B}{2\Delta r} \qquad \beta_\theta = -\frac{1}{\Delta t} + \frac{1}{\Delta r} - \frac{c_B}{2\Delta r} \qquad \gamma_\theta = \frac{1}{\Delta t} - \frac{1}{\Delta r} - \frac{c_B}{2\Delta r}$$

$$\kappa_\theta = \frac{1}{\Delta t} + \frac{1}{\Delta r} - \frac{c_B}{2\Delta r} \qquad \alpha_z = \frac{\Delta r - \Delta t}{\Delta r + \Delta t} \qquad \beta_z = \frac{\Delta r \Delta t}{\Delta r + \Delta t}$$

3.2.4 Esirkepov algorithm for charge conserving current deposition

In the original paper suggesting the quasi-cylindrical algorithm [Lifschitz et al., 2009], the current deposition did not conserve the charge therefore a Marder's correction[Marder, 1987] was used to maintain the validity of Gauss's law. This correction is obtained by solving the Poisson equation where a field $\boldsymbol{E}_c$ is added to the uncorrected electric field $\boldsymbol{E}$ so that $\nabla \cdot (\boldsymbol{E} + \boldsymbol{E}_c) = \rho$. The correction term is defined as $\boldsymbol{E}_c = -\nabla\Phi_c$ with $\nabla^2\Phi_c = \nabla \cdot \boldsymbol{E} - \rho$.

In order to maintain the accuracy of Gauss's law without resorting to a correction of the electric field at each time step, an implementation of a charge conserving current deposition in the quasi-cylindrical algorithm was proposed in [Davidson et al., 2014]. It is the adaptation of Esirkepov charge conserving current deposition scheme to the azimuthal Fourier field decomposition algorithm for an arbitrary number of modes. This method, also implemented in Smilei is detailed in this paragraph.

Esirkepov is a charge conserving current deposition method valid for arbitrary particle shape functions. In this method, when a particle moves from (x_i, y_i) to (x_f, y_f) during one time step, its current contribution is averaged over its path by decomposing its motion into segments orthogonal to cell faces. If the particle crosses the cell boundary, then the particle current contribution in each cell is calculated by splitting its motion path into segments lying entirely inside each cell then the same principle is applied to these segments.

Even though the fields modes are solved on a 2D cylindrical grid (r, z) in the quasi-cylindrical algorithm, the particles are still freely moving in a 3D Cartesian frame. Therefore, particles depositing their charges and currents into a rectangular cell of the 2D (r, z) grid located between r_g and $r_g + \Delta r$, are actually lying in a 3D volume defined by the revolution of this rectangle around the z axis (fig. 3.5). Since this 3D volume is proportional to r_g, the weight of macro-particles with a fixed charge is scaled with a factor $1/r_g$ in order to correctly estimate their charge density and currents contributions.

In cylindrical geometry, particles have the shape function $S = S_r(r - r_p(t))S_\theta(\theta - \theta_p(t))S_z(z - z_p(t))$. The corresponding electrons charge density reads:

$$\rho = \sum_p q_p w_p S_r(r - r_p(t))S_\theta(\theta - \theta_p(t))S_z(z - z_p(t)) \tag{3.51}$$

where q_p is the charge of the particle p and w_p is its associated weight. For simplicity, we suppose $q_p = 1$ for the rest of this derivation.

In the quasi-cylindrical geometry, charge and currents are only defined on the (r, z) grid and there is no grid in θ, therefore it is not straightforward to define J_θ using the standard method of Esirkepov for current deposition . In order to determine the expression of J_θ, the current density vector $\boldsymbol{J}$ is decomposed into two components J_θ and $\boldsymbol{J}_\perp$ where $\perp$ refers to the vector in $r - z$ plane. Hence, the continuity equation can be written

$$\frac{\partial}{\partial t}\rho + \boldsymbol{\nabla}_\perp \cdot \boldsymbol{J}_\perp + \frac{1}{r}\frac{\partial}{\partial \theta} J_\theta = 0 \tag{3.52}$$

The shape function S_θ is expanded in azimuthal modes by proceeding with a Fourier decom-

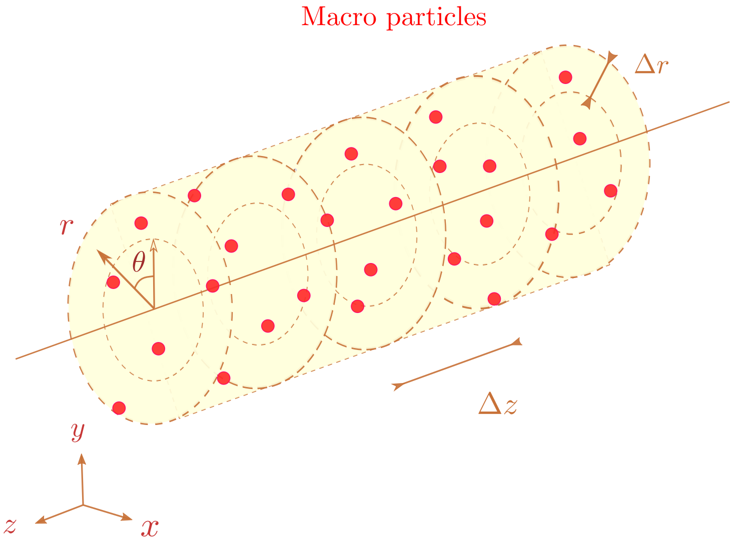

Figure 3.5: Representation of the cylindrical and Cartesian frames in quasi-cylindrical algorithm: the macroparticles (red dots) are defined by their position and momenta in 3D Cartesian coordinates. Particles depositing their charges and currents in the portion of the 2D (r, z) grid located between r_g and $r_g + \Delta r$ (dashed brown lines), are actually lying in a 3D volume defined by the revolution of this rectangle around the z axis.

position in θ:

$$S_\theta(\theta - \theta_p) = \sum_{m=-\infty}^{+\infty} S_{\theta,m}(\theta_p)e^{-im\theta} \tag{3.53}$$

where

$$S_{\theta,m} = \frac{1}{2\pi}\int_0^{2\pi} S_\theta(\theta' - \theta_p)e^{im\theta}d\theta'$$

We consider that particles have a punctual shape function in θ, $S_\theta = \delta(\theta - \theta_p)$ then $S_{\theta,m} = \frac{1}{2\pi}e^{im\theta_p}$. For each particle, the charge density modes $\hat{\rho}_m$ and the transverse current density $\hat{\boldsymbol{J}}_{\perp,m}$ for $m > 0$ can be obtained from $\hat{\rho}_0$ and $\hat{\boldsymbol{J}}_{\perp,0}$ $(S_{\theta,0} = 1)$. The total charge density ρ and current density $\boldsymbol{J}$ are calculated by summing over the modes:

$$\rho = \sum_{m=-\infty}^{+\infty} \hat{\rho}_m e^{-im\theta} \qquad \text{where} \qquad \hat{\rho}_m = \hat{\rho}_0 S_{\theta,m} \tag{3.54}$$

$$\boldsymbol{J}_\perp = \sum_{m=-\infty}^{+\infty} \hat{\boldsymbol{J}}_{\perp,m} e^{-im\theta} \qquad \text{where} \qquad \hat{\boldsymbol{J}}_{\perp,m} = \hat{\boldsymbol{J}}_{\perp,0} S_{\theta,m} \tag{3.55}$$

$$\boldsymbol{J}_\theta = \sum_{m=-\infty}^{+\infty} \hat{\boldsymbol{J}}_{\theta,m} e^{-im\theta} \tag{3.56}$$

We are looking for solutions of $\boldsymbol{J}$ that satisfy the continuity equation:

$$\begin{aligned}\frac{\partial}{\partial t}\rho^{n+\frac{1}{2}} =&\sum_p \frac{w_p}{\Delta t}\left[S_r(r-r_p^{n+1})S_\theta(\theta-\theta_p^{n+1})S_z(z-z_p^{n+1})-S_r(r-r_p^{n})S_\theta(\theta-\theta_p^{n})S_z(z-z_p^{n})\right]\\ =&-\nabla\cdot\boldsymbol{J}^{n+\frac{1}{2}}\end{aligned} \tag{3.57}$$

Substituting eq. (3.54), eq. (3.55) and eq. (3.56) in the Yee-FDTD version of eq. (3.52) and using S_θ expansion in azimuthal modes gives:

$$\begin{aligned}\sum_{m=-\infty}^{+\infty} e^{-im\theta}\Bigg(\sum_p\Bigg\{\frac{w_p}{\Delta t}&\left[S_r(r-r_p^{n+1})S_{\theta,m}(\theta_p^{n+1})S_z(z-z_p^{n+1})-S_r(r-r_p^{n})S_{\theta,m}(\theta_p^{n})S_z(z-z_p^{n})\right]\\ &+\boldsymbol{\nabla}_\perp\cdot\hat{\boldsymbol{J}}_{\perp,m}^{n+\frac{1}{2}}-\frac{im}{r_g}\hat{J}_{\theta,m}^{n+\frac{1}{2}}\Bigg\}\Bigg)=0\end{aligned} \tag{3.58}$$

Substituting the expression of $\hat{\boldsymbol{J}}_{\perp,m}$ into eq. (3.58) gives for each m and p in the sum

$$\begin{aligned}&\frac{w_p}{\Delta t}\left[S_r(r-r_p^{n+1})S_{\theta,m}(\theta_p^{n+1})S_z(z-z_p^{n+1})-S_r(r-r_p^{n})S_{\theta,m}(\theta_p^{n})S_z(z-z_p^{n})\right]\\ &\quad+S_{\theta,m}(\theta_p^{n+\frac{1}{2}})\boldsymbol{\nabla}_\perp\cdot\hat{\boldsymbol{J}}_{\perp,0}^{n+\frac{1}{2}}-\frac{im}{r_g}\hat{J}_{\theta,m}^{n+\frac{1}{2}}=0\end{aligned} \tag{3.59}$$

Using a charge conserving definition for $\hat{\boldsymbol{J}}_{\perp,0}$ similar to the current deposition in 2D Cartesian geometry guarantees that $\frac{\partial}{\partial t}\hat{\rho}_0+\boldsymbol{\nabla}_\perp\cdot\hat{\boldsymbol{J}}_{\perp,0}=0$ and thus leads to an expression for $\hat{\boldsymbol{J}}_{\theta,m}$:

$$\begin{aligned}\hat{J}_{\theta,m}^{n+\frac{1}{2}}=-i\frac{w_p r_g}{m\Delta t}\Bigg(&S_r(r_g-r_p^{n+1})S_z(z_g-z_p^{n+1})\left[S_{\theta,m}(\theta_p^{n+1})-S_{\theta,m}(\theta_p^{n+\frac{1}{2}})\right]\\ &-S_r(r_g-r_p^{n})S_z(z_g-z_p^{n})\left[S_{\theta,m}(\theta_p^{n})-S_{\theta,m}(\theta_p^{n+\frac{1}{2}})\right]\Bigg)\end{aligned} \tag{3.60}$$

Using the relation $S_{\theta,m}=\frac{1}{2\pi}e^{im\theta_p}$ and defining the following quantities $\bar{\theta}_p=\frac{\theta_p^{n+1}+\theta_p^n}{2}$ and $\Delta\theta_p=\frac{\theta_p^{n+1}-\theta_p^n}{2}$, we obtain the result for each particle,

$$\begin{aligned}\hat{J}_{\theta,m}^{n+\frac{1}{2}}=-i\frac{w_p r_g}{m\Delta t}\frac{e^{im\bar{\theta}_p}}{2\pi}\Bigg(&S_r(r_g-r_p^{n+1})S_z(z_g-z_p^{n+1})\left[e^{-im\Delta\theta_p}-1\right]\\ &-S_r(r_g-r_p^{n})S_z(z_g-z_p^{n})\left[e^{im\Delta\theta_p}-1\right]\Bigg)\end{aligned} \tag{3.61}$$

where the particle shapes in r and z are still general. The complex exponentials $e^{im\theta}$ used in the previous equations are evaluated by the the recurrence relation $e^{i(m+1)\theta}=e^{i\theta}\times e^{im\theta}$ where $e^{i\theta}=\frac{y+iz}{r}$ and $e^{-i\theta}=\frac{y-iz}{r}$.

3.2.5 Interpolation

Since, the interpolation step involves interactions with macro-particles that move freely in Cartesian 3D coordiantes while the fields modes are defined on 2D cylindrical grid (r,z), this step requires a special treatment to take into account this specific representation just like in the charge and current deposition.

Therefore, the Fourier fields are summed over the azimuthal modes to obtain the real fields besides summing over the grid points.

$$\begin{aligned}\bar{\boldsymbol{E}}^n(\boldsymbol{x}_p^n) = \mathrm{Re}\Bigg(\sum_{m=0}^{m_{max}} \sum_{j,k} e^{-im\theta_p} \,[\, & P_{j+\frac{1}{2},k}(r_p, z_p) \tilde{E}^{\,n}_{r\,j+\frac{1}{2},k,m}\, \boldsymbol{e}_r \\ & + P_{j,k}(r_p, z_p) \tilde{E}^{\,n}_{\theta\,j,k,m}\, \boldsymbol{e}_\theta \\ & + P_{j,k+\frac{1}{2}}(r_p, z_p) \tilde{E}^{\,n}_{z\,j,k+\frac{1}{2},m} \boldsymbol{e}_z \,]\Bigg) \end{aligned} \tag{3.62}$$

$$\begin{aligned}\bar{\boldsymbol{B}}^n(\boldsymbol{x}_p^n) = \mathrm{Re}\Bigg(\sum_{m=0}^{m_{max}} \sum_{j,k} e^{-im\theta_p} \,[\, & P_{j,k+\frac{1}{2}}(r_p, z_p) \frac{1}{2} \left(\tilde{B}^{\,n+\frac{1}{2}}_{r\,j+\frac{1}{2},k,m} + \tilde{B}^{\,n-\frac{1}{2}}_{r\,j+\frac{1}{2},k,m} \right) \boldsymbol{e}_r \\ & + P_{j+\frac{1}{2},k+\frac{1}{2}}(r_p, z_p) \frac{1}{2} \left(\tilde{B}^{\,n+\frac{1}{2}}_{\theta\,j,k,m} + \tilde{B}^{\,n-\frac{1}{2}}_{\theta\,j,k,m} \right) \boldsymbol{e}_\theta \\ & + P_{j+\frac{1}{2},k}(r_p, z_p) \frac{1}{2} \left(\tilde{B}^{\,n+\frac{1}{2}}_{z\,j,k+\frac{1}{2},m} + \tilde{B}^{\,n-\frac{1}{2}}_{z\,j,k+\frac{1}{2},m} \right) \boldsymbol{e}_z \,]\Bigg) \end{aligned} \tag{3.63}$$

where the general expression of $P_{i',j',k'}$ is determined by integrating the shape function $S(\boldsymbol{x}-\boldsymbol{x}_p)$ around the grid-points and given by the same relation as in eq. (2.17). $S(\boldsymbol{x}-\boldsymbol{x}_p)$ is the same as the one used for charge and current deposition with $S_\theta(\theta-\theta_p) = \delta(\theta-\theta_p)$.

Once the fields are gathered onto the particles, the motion of the particles is integrated in Cartesian coordinates using the usual discretized equations of motion eqs. (2.19) and (2.23)

3.2.6 Numerical dispersion relation and stability condition for FDTD

The discretization in FDTD scheme introduces numerical artifacts arising from the unphysical behaviour of the electromagnetic field when propagated via this scheme. It is insightful to proceed with a numerical dispersion analysis in order to study the accuracy and stability of the FDTD solver used in the PIC simulation. To do so, plane monochromatic waves are injected into the discretized wave propagation equation which combines Maxwell's equations in vacuum ($\boldsymbol{J} = 0$ and $\rho = 0$).

$$\Delta E = \frac{1}{c^2} \frac{\partial^2 E}{\partial t^2} \tag{3.64}$$

In cylindrical coordinates, the wave equation (3.64) leads to the following 3 equations:

$$(\Delta E)_r = \Delta E_r - \frac{2}{r^2}\frac{\partial E_\theta}{\partial \theta} - \frac{E_r}{r^2} = \frac{1}{r}\frac{\partial}{\partial r}\left(r \frac{\partial E_r}{\partial r} \right) + \frac{1}{r^2}\frac{\partial^2 E_r}{\partial \theta^2} + \frac{\partial^2 E_r}{\partial z^2} - \frac{2}{r^2}\frac{\partial E_\theta}{\partial \theta} - \frac{E_r}{r^2}$$

$$(\Delta E)_\theta = \Delta E_\theta + \frac{2}{r^2}\frac{\partial E_r}{\partial \theta} - \frac{E_\theta}{r^2} = \frac{1}{r}\frac{\partial}{\partial r}\left(r \frac{\partial E_\theta}{\partial r} \right) + \frac{1}{r^2}\frac{\partial^2 E_\theta}{\partial \theta^2} + \frac{\partial^2 E_\theta}{\partial z^2} + \frac{2}{r^2}\frac{\partial E_r}{\partial \theta} - \frac{E_\theta}{r^2}$$

$$(\Delta E)_z = \Delta E_z = \frac{1}{r}\frac{\partial}{\partial r}\left(r \frac{\partial E_z}{\partial r} \right) + \frac{1}{r^2}\frac{\partial^2 E_z}{\partial \theta^2} + \frac{\partial^2 E_z}{\partial z^2}$$

By performing a Fourier modes expansion in the previous equations, we obtain:

$$(\Delta E)_{r,m} = \frac{1}{r}\frac{\partial}{\partial r}\left(r\frac{\partial E_{r,m}}{\partial r}\right) - \frac{m^2}{r^2}E_{r,m} + \frac{\partial^2 E_{r,m}}{\partial z^2} + \frac{2im}{r^2}E_{\theta,m} - \frac{E_{r,m}}{r^2}$$

$$(\Delta E)_{\theta,m} = \frac{1}{r}\frac{\partial}{\partial r}\left(r\frac{\partial E_{\theta,m}}{\partial r}\right) - \frac{m^2}{r^2}E_{\theta,m} + \frac{\partial^2 E_{\theta,m}}{\partial z^2} - \frac{2im}{r^2}E_{r,m} - \frac{E_{\theta,m}}{r^2}$$

$$\Delta E_{z,m} = \frac{1}{r}\frac{\partial}{\partial r}\left(r\frac{\partial E_{z,m}}{\partial r}\right) - \frac{m^2}{r^2}E_{z,m} + \frac{\partial^2 E_{z,m}}{\partial z^2}$$

The dispersion relation for each mode can be readily obtained by injecting plane monochromatic waves modes propagating in the z direction of the form $\boldsymbol{E}_m(r,z,t) = \boldsymbol{E}_0 e^{i\omega t - k_z z}$ in the discretized wave equation for each Fourier mode m. According to Gauss's law in vacuum, $\boldsymbol{k}\cdot\boldsymbol{E}_m = 0$ thus $E_{z,m} = 0$ and $E_{r,m}, E_{\theta,m} \propto e^{i\omega t - k_z z}$ with $k_z \in [-\pi/\Delta z, \pi/\Delta z]$.

We define the following numerical differentiation operations

$$\frac{\partial^2 F_m}{\partial z^2} = \frac{F_m(r,z+\Delta z,t) - 2F_m(r,z,t) + F_m(r,z-\Delta z,t)}{\Delta z^2} \tag{3.65}$$

$$\frac{\partial^2 F_m}{\partial t^2} = \frac{F_m(r,z,t+\Delta t) - 2F_m(r,z,t) + F_m(r,z,t-\Delta t)}{\Delta t^2} \tag{3.66}$$

Using eq. (3.65) and eq. (3.66), the discretized wave equation for $E_{r,m}$ and $E_{\theta,m}$ components read:

$$\left(-\frac{m^2}{r^2} - \frac{4}{\Delta z^2}\sin^2(\frac{k_z\Delta z}{2}) - \frac{1}{r^2}\right)E_{r,m} + \frac{2im}{r^2}E_{\theta,m} = -\frac{4}{c^2\Delta t^2}\sin^2(\frac{\omega\Delta t}{2})E_{r,m} \tag{3.67}$$

$$\left(-\frac{m^2}{r^2} - \frac{4}{\Delta z^2}\sin^2(\frac{k_z\Delta z}{2}) - \frac{1}{r^2}\right)E_{\theta,m} - \frac{2im}{r^2}E_{r,m} = -\frac{4}{c^2\Delta t^2}\sin^2(\frac{\omega\Delta t}{2})E_{\theta,m} \tag{3.68}$$

The above two relations can be written as a matrix multiplication by the vector $(E_{r,m}, E_{\theta,m})^T$.

$$\begin{pmatrix}\alpha & \beta\\ -\beta & \alpha\end{pmatrix}\begin{pmatrix}E_{r,m}\\ E_{\theta,m}\end{pmatrix} = -\frac{4}{(c\Delta t)^2}\sin^2(\frac{\omega\Delta t}{2})\begin{pmatrix}E_{r,m}\\ E_{\theta,m}\end{pmatrix} \tag{3.69}$$

where $\alpha = -\frac{(m^2+1)}{r^2} - \frac{4}{\Delta z^2}\sin^2(\frac{k_z\Delta z}{2})$ and $\beta = \frac{2im}{r^2}$

This formulation is of the from $A\boldsymbol{v} = \lambda\boldsymbol{v}$ where $\boldsymbol{v}$ is an eigenvector of A. It can be equivalently written as $(\lambda I - A)\boldsymbol{v} = 0$. The vector v can be non zero, only if the matrix $(\lambda I - A)$ has a non zero kernel. Thus this matrix is not invertible, and its determinant is zero. The eigenvalues of A are the roots of the characteristic polynomial $p_A(\lambda) = \det(\lambda I - A)$.

$$\begin{aligned} p_A(\lambda) =& (\lambda-\alpha)^2 + \beta^2 \\ =& \left(\lambda + \frac{m^2+1}{r^2} + \frac{4}{\Delta z^2}\sin^2(\frac{k_z\Delta z}{2})\right)^2 - \left(\frac{2m}{r^2}\right)^2 \end{aligned} \tag{3.70}$$

The solutions of the $p_A(\lambda) = 0$ are:

$$\lambda_1 = -\left(\frac{m^2+1}{r^2} + \frac{4}{\Delta z^2}\sin^2(\frac{k_z\Delta z}{2})\right) - \left(\frac{2m}{r^2}\right) \qquad \lambda_2 = -\left(\frac{m^2+1}{r^2} + \frac{4}{\Delta z^2}\sin^2(\frac{k_z\Delta z}{2})\right) + \left(\frac{2m}{r^2}\right) \tag{3.71}$$

λ_1 and λ_2 are the eigenvalues of A. On the other hand, we have:

$$\lambda_1 = -\frac{4}{(c\Delta t)^2}\sin^2(\frac{\omega\Delta t}{2}) \qquad \text{or} \qquad \lambda_2 = -\frac{4}{(c\Delta t)^2}\sin^2(\frac{\omega\Delta t}{2})$$

The *numerical dispersion relation* satisfied by the waves modes in the leap-frog scheme is found for λ_1. It relates the numerical wave vector k_z, the wave frequency ω and the time and space steps, Δt and Δz and it reads:

$$\left(\sin(\frac{\omega\Delta t}{2})\right)^2 = \left(\frac{c\Delta t}{\Delta z}\sin(\frac{k_z\Delta z}{2})\right)^2 + \left(\frac{(m+1)c\Delta t}{2r}\right)^2 \tag{3.72}$$

A direct consequence of the numerical dispersion relation (3.72) is the existence of a stability constraint that restricts the time step Δt with an upper limit. In fact, due to the projection of the particles momentum onto the grid, the source terms of Maxwell's equations is subject to noise. The artifact induced by the noise should propagate without any further amplification, otherwise the time integration scheme is no longer stable. Therefore, ω should have a real value for any values of the wavenumber, because complex roots entails an exponential growth of its corresponding solution in time. For instance, at the Nyquist frequency $k_z = \pm\pi/\Delta z$ eq. (3.72) becomes:

$$\left(\sin(\frac{\omega\Delta t}{2})\right)^2 = \left(\frac{c\Delta t}{\Delta z}\right)^2 + \left(\frac{(m+1)c\Delta t}{2r}\right)^2 \tag{3.73}$$

which requires that

$$\left(\frac{c\Delta t}{\Delta z}\right)^2 + \left(\frac{(m_{max}+1)c\Delta t}{2r}\right)^2 \leq 1 \tag{3.74}$$

where $m_{max} = N_m - 1$ is the maximal non zero mode and N_m is the total number of modes. To ensure the stability of the scheme, Δt must satisfy the following condition:

$$\Delta t \leq \frac{1}{c}\sqrt{\frac{1}{\frac{1}{\Delta z^2} + \frac{(m_{max}+1)^2}{4r^2}}} \tag{3.75}$$

This condition is known as the Courant-Friedrichs-Lewy (CFL) condition [Courant et al., 1967]. In our case, the condition becomes more restrictive close to the axis when $r = \Delta r$ for primal fields and $r = \Delta r/2$ for dual ones. Consequently, the condition at its minimum reads

$$\Delta t \leq \frac{1}{c}\sqrt{\frac{1}{\frac{1}{\Delta z^2} + \frac{(m_{max}+1)^2}{\Delta r^2}}} \tag{3.76}$$

However, this relation is only true for the specific case of plane waves that propagate purely along the longitudinal z axis ($k_x = 0$ and $k_y = 0$).

Functions of the form $\boldsymbol{E}(r,z,t) = \boldsymbol{E}_0 e^{i(\omega t - k_x x - k_y y - k_z)}$ are not eigenmodes of the propagation equations in the general case of the quasi-cylindrical algorithm and the complete set of solutions of the discretized equations of propagation has to be found numerically and not analytically.

However, the above relation can give us a good insight about the role of the number of modes in the CFL condition: the more modes we use, the smaller the time step Δt should be. Accordingly, the code is more performant when we use less number of modes.

3.2.7 limits of the FDTD

Another important consequence of the numerical dispersion relation (3.72) is the introduction of a numerical vacuum phase velocity of the electromagnetic waves v_{ϕ}^{sim} that depends on the discretization. In quasi-cylindrical geometry and under the previous assumption ($k_x = k_y = 0$) the latter reads for each mode m

$$v_{\phi,m}^{sim} = \frac{\omega}{k} = \frac{2}{k_z \Delta t} \arcsin\left(\sqrt{\left[\frac{c\Delta t}{\Delta z}\sin(\frac{k_z \Delta z}{2})\right]^2 + \left[\frac{(m+1)c\Delta t}{2r}\right]^2}\right) \tag{3.77}$$

Thus in the simulations, the electromagnetic waves propagate with a phase velocity lower than c in vacuum. Besides, the electromagnetic wave modes have different different phase velocities depending on their mode $v_{\phi,m}^{sim}$ which gives rise to numerical artifacts that can in some cases have a substantial impact on the simulation results especially for long propagation distances. To reduce this impact, the following condition should be fulfilled $\Delta z \ll \Delta r/(m+1)$. In particular, when $v_{\phi,m}^{sim} < c$, relativistic particles may travel at $v > v_{\phi,m}^{sim}$ and generate a nonphysical radiation known as numerical Cherenkov radiation.

Numerical Cherenkov radiation in LWFA simulations

Numerical Cherenkov radiation (NCR) is associated to the well-known Cherenkov effect. This effect occurs when a relativistic charged particle travels with a velocity $v > v_{\phi}$ through a medium in which the phase velocity of light v_{ϕ} is lower than c. This will lead to the emission of a characteristic radiation, known as the Cherenkov emission [Jackson, 1998]. This effect can occur in dielectric media, such as air or water, yet not in vacuum ($v_{\phi} = c$) nor in plasma ($v_{\phi} > c$). In the case of LWFA, the relativistic accelerated bunch is either surrounded by the plasma (linear regime) or by the vacuum (in the blow-out regime neglecting the impact of the ion cavity on the light propagation). Therefore, the Cherenkov emission can not take place in any configuration during LWFA. Nevertheless, in simulations with FDTD solvers, the unphysical numerical Cherenkov effect can occur due to the numerical dispersion relation ($v_{\phi}^{sim} \leq c$). In this case, accelerated particles traveling at a velocity larger or equal to the numerical phase velocity emit radiations that stay in phase with the accelerated particles leading to a resonant numerical instability that can impact the quality of the simulations [Boris and Lee, 1973; Godfrey, 1974].

In order to reduce the impact of the numerical Cherenkov effect and its related instabilities, $c - v_{\phi}^{sim}$ should be reduced to its minimum which is reached when the time step is fixed almost at its CFL limit. Besides, in most of the LWFA simulations the spatial step in the propagation direction z is chosen to be much smaller than the ones in the transverse direction ($\Delta z \ll \Delta r$) in order to resolve the laser wavelength λ_0, thus the optimal time step should satisfy $\Delta t = \Delta z/c - \epsilon$ with $0 < \epsilon \ll 1$.

Impact of FDTD solver on the accuracy of LWFA simulations

The FDTD scheme has several advantages specially when it comes to the optimization of the simulation cost. In fact, the differentiation operator in standard FDTD scheme is discretized to the second order which means that the information on a grid node is only correlated to the juxtaposed ones. Thus, the number of ghost cells is usually restricted to two which reduces the overlapping region between two domains. This allows an efficient parallelization based on a fine-grain domain decomposition particularly in Smilei where there are two layers of parallelism: each sub-domain is divided itself into smaller portions called "patches" (chapter 2). Besides, most of the required calculations for the FDTD solver are basic operations over large tables which motivates the use of Single Instruction Multiple Data (SIMD) capibility, known also as vectorization.

Despite its scalability and cost efficiency, the FDTD method suffers from some limitations that hinder its accuracy. In order to guarantee the stability of the second-order finite-difference solver the choice of the time step Δt is constrained with an upper limit fixed by the CFL condition. The latter becomes more restrictive in the case of quasi-cylindrical algorithm, when many modes are used. However, the most important limitation remains the NCR which was proven to cause spurious unphysical emittance growth specially in the case of high charge density bunches. The accuracy of the numerical simulation results is strongly affected by the instabilities originating from the NCR that alters the particle dynamics and results in wrong estimation of the maximum attained energy and angular divergence of the particles [Lehe et al., 2013a]. Therefore, several methods have been proposed in order to alleviate this deficiency.

These methods include lowpass spectral filters to attenuate the waves caused by the NCR. However, this method is not specifically selective to frequency bands related to NCR as a high number of passes would inevitably damp some of the lower-frequency fields as well. In the case of LWFA simulations, the low-frequency fields include for instance the laser pulse, and thus digital filtering can alter the physics of interest at stake. A more physically accurate choice is the use of modified computational stencils to approximate the curl operator in FDTD discretization of Maxwell-Faraday equation [Vay et al., 2011; Cowan et al., 2013; Pukhov, 1999]. These extended computational stencils allow to suppress NCR along the grid axes under some conditions by increasing the numerical phase velocity in this direction. A comparison between these schemes can be found in [Nuter et al., 2014]. However, they are still dispersive off the main axes. Besides, it is hard to quantify how much these added corrections could impact the underlying physics.

3.3 Pseudo Spectral Analytical Time Domain scheme

A more sophisticated alternative to the finite difference based methods is the class of pseudo-spectral time-domain (PSTD) solvers [Liu, 1997; Dawson, 1983] which represents the spatial derivatives in the frequency domain. They are typically less prone to numerical artifacts. In particular, [I. Haber and Boris, 1973] presented a pseudo-spectral solver that integrates analytically Maxwell's equations over a finite time step, under the assumption of constant source (currents) over that time step. It is therefore more robust than the PSTD scheme that still relies on finite difference for temporal integration. This formulation, usually referred to as the Pseudo-Spectral Analytical Time-Domain (PSATD) method offers various advantages over the FDTD scheme which advances electromagnetic fields in the Yee lattice. This type of solvers provides a higher level of numerical accuracy since the derivatives are correctly evaluated. Thereby, it correctly models the dispersion of electromagnetic waves and mitigates the problem of NCR in simulations of relativistic beams [Vay et al., 2013]. Besides, it is not subject to a CFL time step limit in vacuum as long as the assumption of constant current source over that time step is verified. Furthermore, pseudo-spectral methods allow the centering of all fields in time [3], eliminating stag-

---

[3] We note that the electric and magnetic field components can also be expressed at staggered times in the context of PSATD solver.

gering errors which lead to inexact cancellation of relativistic beams' self electric and magnetic components in the calculation of the Lorentz force $\boldsymbol{E} + \boldsymbol{v} \wedge \boldsymbol{B}$ [Vay, 2008b].

Until recently, the pseudo-spectral solvers were exclusively implemented in Cartesian system coordinates employing Fourier transforms which are incompatible with the radial coordinate in cylindrical geometry. In [Lehe et al., 2016], a formalism that combines the speed of the quasi-cylindrical algorithm with the accuracy of dispersion-free PSATD algorithms, is proposed.

These advantages motivated the implementation of this spectral quasi-cylindrical algorithm in the open-source library PICSAR during my PhD. It is then coupled and adapted to the parallelization startegy of the PIC code Smilei. Besides, it also opens up the way to other PIC codes to benefit from this contribution.

The following section describes the concept behind this formalism and explains the derivation and implementation of the algorithm in PICSAR library coupled with Smilei PIC code.

3.3.1 Spectral Cartesian representation

Before presenting the algorithm in the quasi-cylindrical geometry, the formulation of Maxwell's equations in 3D Cartesian Fourier space is reminded here.

The equations are obtained by employing Fourier transform:

$$\mathcal{F}_u(\mathbf{k}) = \int_{-\infty}^{\infty} dx \int_{-\infty}^{\infty} dy \int_{-\infty}^{\infty} dz F_u(\mathbf{r}) e^{-i(k_x x + k_y y + k_z z)} \tag{3.78}$$

with

$$F_u(\mathbf{r}) = \frac{1}{(2\pi)^3} \int_{-\infty}^{\infty} dk_x \int_{-\infty}^{\infty} dk_y \int_{-\infty}^{\infty} dk_z \mathcal{F}_u(\mathbf{k}) e^{i(k_x x + k_y y + k_z z)} \tag{3.79}$$

where F is any of the fields E, B or J, and u is either x, y or z. $\mathcal{F}$ represents the Fourier components of F denoted by $\mathcal{E}$ for E, $\mathcal{B}$ for B and $\mathcal{J}$ for J.

Replacing the fields in Maxwell's equations (2.13) by their Fourier representation eq. (3.78) in the spectral space (k_x, k_y, k_z) gives:

$$\frac{1}{c^2}\frac{\partial \mathcal{E}_x}{\partial t} = ik_y\mathcal{B}_z - ik_z\mathcal{B}_y - \mu_0\mathcal{J}_x \qquad \partial_t\mathcal{B}_x = -ik_y\mathcal{E}_z + ik_z\mathcal{E}_y \tag{3.80}$$

$$\frac{1}{c^2}\frac{\partial \mathcal{E}_y}{\partial t} = ik_z\mathcal{B}_x - ik_x\mathcal{B}_z - \mu_0\mathcal{J}_y \qquad \partial_t\mathcal{B}_y = -ik_z\mathcal{E}_x + ik_x\mathcal{E}_z \tag{3.81}$$

$$\frac{1}{c^2}\frac{\partial \mathcal{E}_z}{\partial t} = ik_x\mathcal{B}_y - ik_y\mathcal{B}_x - \mu_0\mathcal{J}_z \qquad \partial_t\mathcal{B}_z = -ik_x\mathcal{E}_y + ik_y\mathcal{E}_x \tag{3.82}$$

These equations can then be analytically integrated in time and then advanced for an interval of Δt assuming constant source term over that interval. This analytical integration in time allows to get rid of the temporal staggering between the electric and magnetic fields usually necessary in other solvers.

The *pseudo* in PSATD algorithm refers to the use of an intermediate interpolation grid in real space where the current deposition and field gathering steps are performed. Therefore, at each time step of the PIC loop we make use of the Fourier transform (3.78) to solve Maxwell's equations in the spectral space then we proceed with the inverse Fourier transform (3.79) to bring back the calculated fields to real space before interpolating them onto the particles.

3.3.2 Spectral quasi-cylindrical representation

The Fourier transform is incompatible with Maxwell's equations written in cylindrical coordinates. In fact, if we apply the Fourier transform in eq. (3.78) to equations (3.6), the Fourier modes do not decouple. For close to cylindrical geometry, a popular alternative that enables the decoupling between r and θ in the spectral space is the Fourier-Hankel transform, also called Fourrier-Bessel transform, because it makes use of Bessel functions denoted by J_m for the order m. The transformed fields in the spectral space $\hat{\mathcal{F}}_{z,m}$, $\hat{\mathcal{F}}_{+,m}$ and $\hat{\mathcal{F}}_{-,m}$ are related to the real ones F_r, F_θ and F_z by the following relations:

$$\hat{\mathcal{F}}_{z,m}(k_z,k_\perp) = \int_{-\infty}^{\infty} dz \int_{-\infty}^{\infty} rdr \int_{-\infty}^{\infty} d\theta \times F_z(\mathbf{r}) J_m(k_\perp r) e^{im\theta - ik_z z} \tag{3.83}$$

$$\hat{\mathcal{F}}_{+,m}(k_z,k_\perp) = \int_{-\infty}^{\infty} dz \int_{-\infty}^{\infty} rdr \int_{-\infty}^{\infty} d\theta \times \frac{F_r(\mathbf{r}) - iF_\theta(\mathbf{r})}{2} J_{m+1}(k_\perp r) e^{im\theta - ik_z z} \tag{3.84}$$

$$\hat{\mathcal{F}}_{-,m}(k_z,k_\perp) = \int_{-\infty}^{\infty} dz \int_{-\infty}^{\infty} rdr \int_{-\infty}^{\infty} d\theta \times \frac{F_r(\mathbf{r}) + iF_\theta(\mathbf{r})}{2} J_{m-1}(k_\perp r) e^{im\theta - ik_z z} \tag{3.85}$$

where $\hat{\mathcal{F}}_{z,m}$, $\hat{\mathcal{F}}_{+,m}$ and $\hat{\mathcal{F}}_{-,m}$ represent the spectral components of F with F is either E, B or J. The last-mentioned ones can be found by operating the inverse Fourier Bessel transform using the following relations:

$$F_z(\mathbf{r}) = \frac{1}{(2\pi)^2} \sum_{m=-\infty}^{\infty} \int_{-\infty}^{\infty} dk_z \int_{-\infty}^{\infty} k_\perp dk_\perp \times \hat{\mathcal{F}}_{z,m}(k_z,k_\perp) J_m(k_\perp r) e^{-im\theta + ik_z z} \tag{3.86}$$

$$\begin{aligned} F_r(\mathbf{r}) =& \frac{1}{(2\pi)^2} \sum_{m=-\infty}^{\infty} \int_{-\infty}^{\infty} dk_z \int_{-\infty}^{\infty} k_\perp dk_\perp \\ & \times (\hat{\mathcal{F}}_{+,m}(k_z,k_\perp) J_{m+1}(k_\perp r) + \hat{\mathcal{F}}_{-,m}(k_z,k_\perp) J_{m-1}(k_\perp r)) e^{-im\theta + ik_z z} \end{aligned} \tag{3.87}$$

$$\begin{aligned} F_\theta(\mathbf{r}) =& \frac{1}{(2\pi)^2} \sum_{m=-\infty}^{\infty} \int_{-\infty}^{\infty} dk_z \int_{-\infty}^{\infty} k_\perp dk_\perp \\ & \times i(\hat{\mathcal{F}}_{+,m}(k_z,k_\perp) J_{m+1}(k_\perp r) - \hat{\mathcal{F}}_{-,m}(k_z,k_\perp) J_{m-1}(k_\perp r)) e^{-im\theta + ik_z z} \end{aligned} \tag{3.88}$$

Injecting eqs. (3.86) to (3.88) into Maxwell's equations in cylindrical coordinates (3.6) leads to modes decoupling and the equations in the spectral space $(k_\perp, k_z)$ become:

$$\frac{1}{c^2}\partial_t \hat{\mathcal{E}}_{+,m} = -i\frac{k_\perp}{2}\hat{\mathcal{B}}_{z,m} + k_z \hat{\mathcal{B}}_{+,m} - \mu_0 \hat{\mathcal{J}}_{+,m} \qquad \partial_t \hat{\mathcal{B}}_{+,m} = i\frac{k_\perp}{2}\hat{\mathcal{E}}_{z,m} - k_z \hat{\mathcal{E}}_{+,m} \tag{3.89}$$

$$\frac{1}{c^2}\partial_t \hat{\mathcal{E}}_{-,m} = -i\frac{k_\perp}{2}\hat{\mathcal{B}}_{z,m} - k_z \hat{\mathcal{B}}_{-,m} - \mu_0 \hat{\mathcal{J}}_{-,m} \qquad \partial_t \hat{\mathcal{B}}_{-,m} = i\frac{k_\perp}{2}\hat{\mathcal{E}}_{z,m} + k_z \hat{\mathcal{E}}_{-,m} \tag{3.90}$$

$$\frac{1}{c^2}\partial_t\hat{\mathcal{E}}_{z,m} = i\frac{k_\perp}{2}\hat{\mathcal{B}}_{+,m} + ik_\perp\hat{\mathcal{B}}_{-,m} - \mu_0\hat{\mathcal{J}}_{z,m} \qquad \partial_t\hat{\mathcal{B}}_{z,m} = -ik_\perp\hat{\mathcal{E}}_{+,m} - ik_\perp\hat{\mathcal{E}}_{-,m} \tag{3.91}$$

These equations are the core of the quasi-cylindrical PSATD solver.
In this formalism, the conservation equations $\nabla \cdot \boldsymbol{E} = \rho/\epsilon_0$ and $\nabla \cdot \boldsymbol{B} = 0$ read:

$$k_\perp\left(\hat{\mathcal{E}}_{+,m} - \hat{\mathcal{E}}_{-,m}\right) + ik_z\hat{\mathcal{E}}_{z,m} = \frac{\hat{\rho}_m}{\epsilon_0} \qquad k_\perp\left(\hat{\mathcal{B}}_{+,m} - \hat{\mathcal{B}}_{-,m}\right) + ik_z\hat{\mathcal{B}}_{z,m} = 0 \tag{3.92}$$

These equations are verified by the Maxwell's equations eqs. (3.89) to (3.91), provided that the charge density continuity equation in spectral space is satisfied i.e $\partial_t\hat{\rho}_m + k_\perp\left(\hat{\mathcal{J}}_{+,m} - \hat{\mathcal{J}}_{-,m}\right) + ik_z\hat{\mathcal{J}}_{z,m} = 0$.

The Maxwell's equations in spectral space eqs. (3.89) to (3.91) are combined with the spectral conservation equations eq. (3.92) to obtain the propagation equations for $\mathcal{E}$ and $\mathcal{B}$. The propagation equations are then integrated analytically between $n\Delta t$ and $(n+1)\Delta t$ supposing that the currents are constant over one time step, and that the charge density is linear in time.

3.3.3 Overview of the quasi-cylindrical spectral algorithm

In Cartesian PSATD formalism once the electromagnetic fields are advanced in the spectral space, they are transformed to real space where operations pertaining to macro particles are performed. The reason why those operations are kept in the real grid is that only the few cells neighboring the particle (depending on the order of the deposition) are used for the deposition and hence for the gathering. In fact, they are rather local operations in real space. Contrarily, they become global operations that effects all the spectral modes simultaneously in spectral space.

With regard to quasi-cylindrical PSATD formalism, a similar approach is also applied to guarantee the locality of the current deposition and field gathering operations. In this context, the spectral fields are transformed into an "intermediate" grid where only the Fourier transform in the θ direction is preserved. The latter coincides with the grid used in the FDTD quasi cylindrical formalism. Therefore, the current deposition and field gathering steps in this case are the same as the ones used for the FDTD where the particles are still distributed in 3D and their motion is integrated in 3D Cartesian coordinates.

Hereafter, the transformations from the intermediate grid to the spectral one and vice versa, in the context of quasi-cylindrical PSATD solver, are presented.

Transformations between spectral and intermediate grid

At each time step, transformations between spectral and intermediate grid are operated. The fields representation in the intermediate grid is recalled here:

$$F(r,z,\theta) = \sum_{m=-\infty}^{\infty} \hat{F}_m(r,z)e^{-im\theta} \tag{3.93}$$

with

$$\hat{F}_m(r,z) = \frac{1}{2\pi}\int_0^{2\pi} d\theta F(r,z,\theta)e^{im\theta} \tag{3.94}$$

where F denotes any cylindrical component of $\boldsymbol{E}, \boldsymbol{B}, \boldsymbol{J}$ or ρ and $\hat{F}_m$ is the associated Fourier components where m is the azimuthal mode index.

From intermediate to spectral

The transformation from intermediate grid $\hat{F}_m(r,z)$ to spectral one $\hat{\mathcal{F}}(k_\perp, k_z)$ is done in two interchangeable steps: Fourier transform along propagation direction z and Hankel transform in the radial direction r.

$$\hat{\mathcal{F}}_{z,m}(k_\perp, k_z) = \mathrm{HT}_m[\mathrm{FT}[\hat{F}_{z,m}(r,z)]] \tag{3.95}$$

$$\hat{\mathcal{F}}_{+,m}(k_\perp, k_z) = \mathrm{HT}_{m+1}[\mathrm{FT}[\frac{\hat{F}_{r,m}(r,z) - i\hat{F}_{\theta,m}(r,z)}{2}]] \tag{3.96}$$

$$\hat{\mathcal{F}}_{-,m}(k_\perp, k_z) = \mathrm{HT}_{m-1}[\mathrm{FT}[\frac{\hat{F}_{r,m}(r,z) + i\hat{F}_{\theta,m}(r,z)}{2}]] \tag{3.97}$$

where FT denotes the Fourier transform and HT_m the Hankel transform of order m. Their respective expressions are the following:

$$\mathrm{FT}[f](kz) = \int_{-\infty}^{\infty} f(z) e^{-ik_z z} dz \tag{3.98}$$

and

$$\mathrm{HT}_m[f](k_\perp) = 2\pi \int_0^{\infty} f(r) J_m(k_\perp r) r dr dz \tag{3.99}$$

where J_m denotes the Bessel function of order m.

From spectral to intermediate

The transformation from the spectral grid $\hat{\mathcal{F}}(k_\perp, k_z)$ to the intermediate one $\hat{F}_m(r,z)$ is done using the corresponding inverse transforms:

$$\hat{F}_{z,m}(r,z) = \mathrm{IFT}[\mathrm{IHT}_m[\hat{\mathcal{F}}_{z,m}(k_\perp, k_z)]] \tag{3.100}$$

$$\hat{F}_{r,m}(r,z) = \mathrm{IFT}[\mathrm{IHT}_{m+1}[\hat{\mathcal{F}}_{+,m}(k_\perp, k_z)] + \mathrm{IHT}_{m-1}[\hat{\mathcal{F}}_{-,m}(k_\perp, k_z)]] \tag{3.101}$$

$$\hat{F}_{\theta,m}(r,z) = i\,\mathrm{IFT}[\mathrm{IHT}_{m+1}[\hat{\mathcal{F}}_{+,m}(k_\perp, k_z)] - \mathrm{IHT}_{m-1}[\hat{\mathcal{F}}_{-,m}(k_\perp, k_z)]] \tag{3.102}$$

where IFT denotes the inverse Fourier transform and IHT_m the inverse Hankel transform of order m. Their expressions are give by:

$$\mathrm{IFT}[f](z) = \frac{1}{2\pi} \int_{-\infty}^{\infty} f(k_z) e^{ik_z z} dk_z \tag{3.103}$$

and

$$\mathrm{IHT}_m[f](r) = \frac{1}{2\pi} \int_0^{\infty} f(k_\perp) J_m(k_\perp r) k_\perp dk_\perp \tag{3.104}$$

where J_m denotes the Bessel function of order m.

Numerical implementation of the transforms

The fourier transform is carried out with a 1D Discrete Fourier Transform (DFT) along the longitudinal axis z. This transform requires a regular discretization in intermediate and spectral space respectively denoted by z and k_z:

$$z_j = j\Delta z \quad j \in 0, .., N_z - 1 \text{ where } \Delta z = \tfrac{z_{max}}{Nz}$$

and

$$k_{z_j} = j\Delta k_z \quad j \in 0, .., N_z - 1 \text{ where } \Delta z = \tfrac{z_{max}}{Nz}$$

However, the discretization of the transverse radial direction is different between the intermediate space and the spectral one.

In the intermediate grid, a regular discretization in r is kept but with a shift of a half cell. In contrast with z that is discretized on a the primal grid, r is discretized on a dual grid.

$$r_j = \left(j + \tfrac{1}{2}\right) \Delta r \quad j \in 0, .., N_r - 1 \text{ where } \Delta r = \tfrac{r_{max}}{Nr}$$

On the other hand, in the spectral grid the $k_\perp$ vector is discretized on an irregular grid corresponding to the zeros of Bessel functions following this expression:

$$k^m_{\perp,j} = \tfrac{\alpha^m_j}{r_{max}} \text{ where } j \in 0, .., N_r - 1$$

with α^m_j is the j^{th} zeros of Bessel function of order m where m corresponds to the considered azimuthal mode index. As a consequence, we have a different discretization for each mode in the spectral grid. Nevertheless, it's not a problem since the spectral modes are decoupled and each one evolves separately in Maxwell's equations. Actually, we can see each mode as being operated on a separate grid.

Once the m-grid is discretized in $k^m_\perp$, the Discrete Hankel Transform (DHT) for each mode is evaluated on the correspooding grid nodes by performing a set of linear operations. Thus, it can be represented by a matrix multiplication of the field. The inverse of the DHT (IDHT) is obtained by inversion of the DHT matrix. The inverse matrix is found by proceeding with an algorithm based on pseudo-inversion. Thereby, the DHT and IDHT of a field F are calculated as:

$$\mathrm{DHT}^m_n[F](k^m_{\perp,j}) = \sum_{p=0}^{N_r-1} (M_{n,m})_{j,p} F(r_p) \tag{3.105}$$

$$\mathrm{IDHT}^m_n[F](r_j) = \sum_{p=0}^{N_r-1} (M'_{n,m})_{j,p} F(k^m_{\perp,p}) \tag{3.106}$$

The square matrices $M_{n,m}$ and $M'_{n,m}$ of size $(N_r \times N_r)$ depend on both the order n of the Bessel function J_n and m the index of the mode where $n \in \{m-1, m, m+1\}$ as it can be seen in eqs. (3.95) to (3.97) and eqs. (3.100) to (3.102). Note that the computation of the matrices $M_{n,m}$ and $M'_{n,m}$ need to be performed only once at the beginning of the simulation and then used at each time step. Despite the cost of the matrix multiplication ($\propto N_r^2$), the quasi-cylindrical PSATD solver cost ($\propto N_r^2 N_z \log(N_z)$) is still less important than the one in 3D Cartesian ($NzN_yN_x(\log(N_xN_yN_z))$).

PSATD Maxwell solver in quasi-cylindrical geometry

Assuming constant currents and a linear time dependence for the charge density over one time step $t \in [n\Delta t, (n+1)\Delta t]$ and following a similar scheme as the one described in [I. Haber and Boris, 1973], the integration of eqs. (3.89) to (3.91) between $n\Delta t$ and $(n+1)\Delta t$ gives:

$$\begin{aligned}\hat{\mathcal{E}}^{n+1}_{+,m} = C\hat{\mathcal{E}}^{n}_{+,m} &+ c^2\frac{S}{\omega}\left(-\frac{ik_\perp}{2}\hat{\mathcal{B}}^n_{z,m} + k_z\hat{\mathcal{B}}^n_{+,m} - \mu_0\hat{\mathcal{J}}^{n+\frac{1}{2}}_{+,m}\right)\\ &+ \frac{c^2}{\epsilon_0}\frac{k_\perp}{2}\left[\frac{\hat{\rho}^{n+1}_m}{\omega^2}\left(1-\frac{S}{\omega\Delta t}\right) - \frac{\hat{\rho}^n_m}{\omega^2}\left(C-\frac{S}{\omega\Delta t}\right)\right]\end{aligned} \tag{3.107}$$

$$\begin{aligned}\hat{\mathcal{E}}^{n+1}_{-,m} = C\hat{\mathcal{E}}^{n}_{-,m} &+ c^2\frac{S}{\omega}\left(-\frac{ik_\perp}{2}\hat{\mathcal{B}}^n_{z,m} - k_z\hat{\mathcal{B}}^n_{+,m} - \mu_0\hat{\mathcal{J}}^{n+\frac{1}{2}}_{-,m}\right)\\ &- \frac{c^2}{\epsilon_0}\frac{k_\perp}{2}\left[\frac{\hat{\rho}^{n+1}_m}{\omega^2}\left(1-\frac{S}{\omega\Delta t}\right) - \frac{\hat{\rho}^n_m}{\omega^2}\left(C-\frac{S}{\omega\Delta t}\right)\right]\end{aligned} \tag{3.108}$$

$$\begin{aligned}\hat{\mathcal{E}}^{n+1}_{z,m} = C\hat{\mathcal{E}}^{n}_{z,m} &+ c^2\frac{S}{\omega}\left(ik_\perp\hat{\mathcal{B}}^n_{+,m} + ik_\perp\hat{\mathcal{B}}^n_{-,m} - \mu_0\hat{\mathcal{J}}^{n+\frac{1}{2}}_{z,m}\right)\\ &- \frac{c^2}{\epsilon_0}k_z\left[\frac{\hat{\rho}^{n+1}_m}{\omega^2}\left(1-\frac{S}{\omega\Delta t}\right) - \frac{\hat{\rho}^n_m}{\omega^2}\left(C-\frac{S}{\omega\Delta t}\right)\right]\end{aligned} \tag{3.109}$$

$$\hat{\mathcal{B}}^{n+1}_{+,m} = C\hat{\mathcal{B}}^{n}_{+,m} - \frac{S}{\omega}\left(-\frac{ik_\perp}{2}\hat{\mathcal{E}}^n_{z,m} + k_z\hat{\mathcal{E}}^n_{+,m}\right) + \mu_0 c^2\frac{1-C}{\omega^2}\left(-\frac{ik_\perp}{2}\hat{\mathcal{J}}^{n+\frac{1}{2}}_{z,m} + k_z\hat{\mathcal{J}}^{n+\frac{1}{2}}_{+,m}\right) \tag{3.110}$$

$$\hat{\mathcal{B}}^{n+1}_{-,m} = C\hat{\mathcal{B}}^{n}_{-,m} - \frac{S}{\omega}\left(-\frac{ik_\perp}{2}\hat{\mathcal{E}}^n_{z,m} - k_z\hat{\mathcal{E}}^n_{-,m}\right) + \mu_0 c^2\frac{1-C}{\omega^2}\left(-\frac{ik_\perp}{2}\hat{\mathcal{J}}^{n+\frac{1}{2}}_{z,m} - k_z\hat{\mathcal{J}}^{n+\frac{1}{2}}_{-,m}\right) \tag{3.111}$$

$$\hat{\mathcal{B}}^{n+1}_{z,m} = C\hat{\mathcal{B}}^{n}_{z,m} - \frac{S}{\omega}\left(ik_\perp\hat{\mathcal{E}}^n_{+,m} + k_z\hat{\mathcal{E}}^n_{-,m}\right) + \mu_0 c^2\frac{1-C}{\omega^2}\left(ik_\perp\hat{\mathcal{J}}^{n+\frac{1}{2}}_{+,m} + ik_\perp\hat{\mathcal{J}}^{n+\frac{1}{2}}_{-,m}\right) \tag{3.112}$$

where $\omega = c\sqrt{k_z^2 + k_\perp^2}$, $C = \cos(\omega\Delta t)$ and $S = \sin(\omega\Delta t)$. In the above equations, all the fields are centered at integer time steps except for the currents, which are defined at half time steps (particles momenta are calculated at half time steps). However, it does not preclude the accuracy of the integration since the currents are considered constant over this time step and equal to $\hat{\mathcal{J}}^{n+\frac{1}{2}}_m$ [4].

A full detailed derivation of the method and the implementation of the utilized transforms can be found in the original paper describing the algorithm [Lehe et al., 2016].

---

[4] Since the currents are considered constant over the integration time step, their derivatives drops in the propagation equations for $\hat{\mathcal{E}}$

Boundary conditions

In Cartesian spectral algorithms, periodic boundary conditions are arbitrarily adopted in the spectral grid for mathematical convenience, in order to be able to represent the fields with discrete Fourier sum. This periodic boundary conditions are also applied in the spectral quasi-cylindrical algorithm, along the longitudinal axis z where the FFT is applied. However, in order to ensure the correctness of the simulation, absorbing boundary conditions should be implemented to avoid instabilities coming from reflected or reinjected waves due to the periodicity of FFT. These absorbing boundary conditions should be applied in the real space and within the finite box before transforming the fields back to spectral space at each time step. For instance a widely adopted and efficient type of boundary conditions especially for spectral solvers are the PML (Perfectly Matched Layers) [Lee and Vay, 2016]. However, they are not straightforward to implement. Instead, we apply simple boundary conditions on z which consist in damping linearly the fields to zero over the first n_{damp} ghost cells laying next to the boundaries, where n_{damp} is a user-defined parameter.

On the other hand, Dirichlet boundary conditions are applied on the upper limit of the r axis ie. $\mathbf{E}(r_{max}) = 0$ and $\mathbf{B}(r_{max}) = 0$ which is compatible with the definition of Fourier-Bessel decomposition in this direction. Note that for the PSATD solver the complications related to the on axis non-defined fields in FDTD are avoided by the half-cell shift in the r axis.

Interaction with macro-particles

Even with the second-order Esirkepov charge/current deposition algorithm 3.2.4 like the one used with FDTD, the PSATD solver does not conserve Maxwell-Gauss equation due to the difference in the spatial derivative order between Maxwell's equations and the numerical continuity equation verified by Esirkepov scheme. In fact, Maxwell's equations are solved using exact spatial differentiation while the Esirkepov current/charge deposition verifies the continuity equation to the second order only and does not satisfy the discretized continuity equation in Fourier space $\hat{\rho}^{n+1} = \hat{\rho}^{n} - i\Delta t \boldsymbol{k}\hat{\mathcal{J}}^{n+\frac{1}{2}}$.

In order to prevent the accumulation of errors resulting from the violation of the discretized Gauss' Law, a Boris correction to the electric field [Birdsall and Langdon, 2004] or alternatively a current correction should be applied [Vay and Godfrey, 2014].

Following the implementation in [Lehe et al., 2016], the interpolation and current deposition are performed using linear shape functions for the particles and a current correction is applied to the currents after their deposition in the spectral space at each time step [Vay et al., 2013] with some similarity to the current deposition presented by Morse and Nielson in their potential-based model in [Morse and Nielson, 1971].

This is done by slightly modifying the currents without modifying their curl: $\boldsymbol{J}' = \boldsymbol{J} - \nabla \boldsymbol{G}$ where $\boldsymbol{G}$ satisfies the Poisson-like equation $\nabla^2 \boldsymbol{G} = \partial_t \rho + \nabla \cdot \boldsymbol{J}$.

In the spectral space the correction reads:

$$\hat{\mathcal{J}}'^{\,n+\frac{1}{2}}_{+,m} = \hat{\mathcal{J}}^{n+\frac{1}{2}}_{+,m} + \frac{k_\perp}{2}\hat{\mathcal{G}}^{n+\frac{1}{2}}_{m} \qquad \hat{\mathcal{J}}'^{\,n+\frac{1}{2}}_{-,m} = \hat{\mathcal{J}}^{n+\frac{1}{2}}_{-,m} - \frac{k_\perp}{2}\hat{\mathcal{G}}^{n+\frac{1}{2}}_{m} \qquad \hat{\mathcal{J}}'^{\,n+\frac{1}{2}}_{z,m} = \hat{\mathcal{J}}^{n+\frac{1}{2}}_{z,m} - k_z\hat{\mathcal{G}}^{n+\frac{1}{2}}_{m} \tag{3.113}$$

with

$$\hat{\mathcal{G}}^{n+\frac{1}{2}}_{m} = -\frac{1}{k_\perp^2 + k_z^2}\left(\frac{\hat{\rho}^{n+1}_{m} - \hat{\rho}^{n}_{m}}{\Delta t} + k_\perp\left(\hat{\mathcal{J}}^{n+\frac{1}{2}}_{+,m} - \hat{\mathcal{J}}^{n+\frac{1}{2}}_{-,m}\right) + ik_z\hat{\mathcal{J}}^{n+\frac{1}{2}}_{z,m}\right) \tag{3.114}$$

An overview of the successive steps of the PIC cycle, including the corresponding intermediate grid $\hat{F}_{u,m}$ or spectral grid $\hat{\mathcal{F}}_{u,m}$ involved in the step is summarized in fig. 3.6.

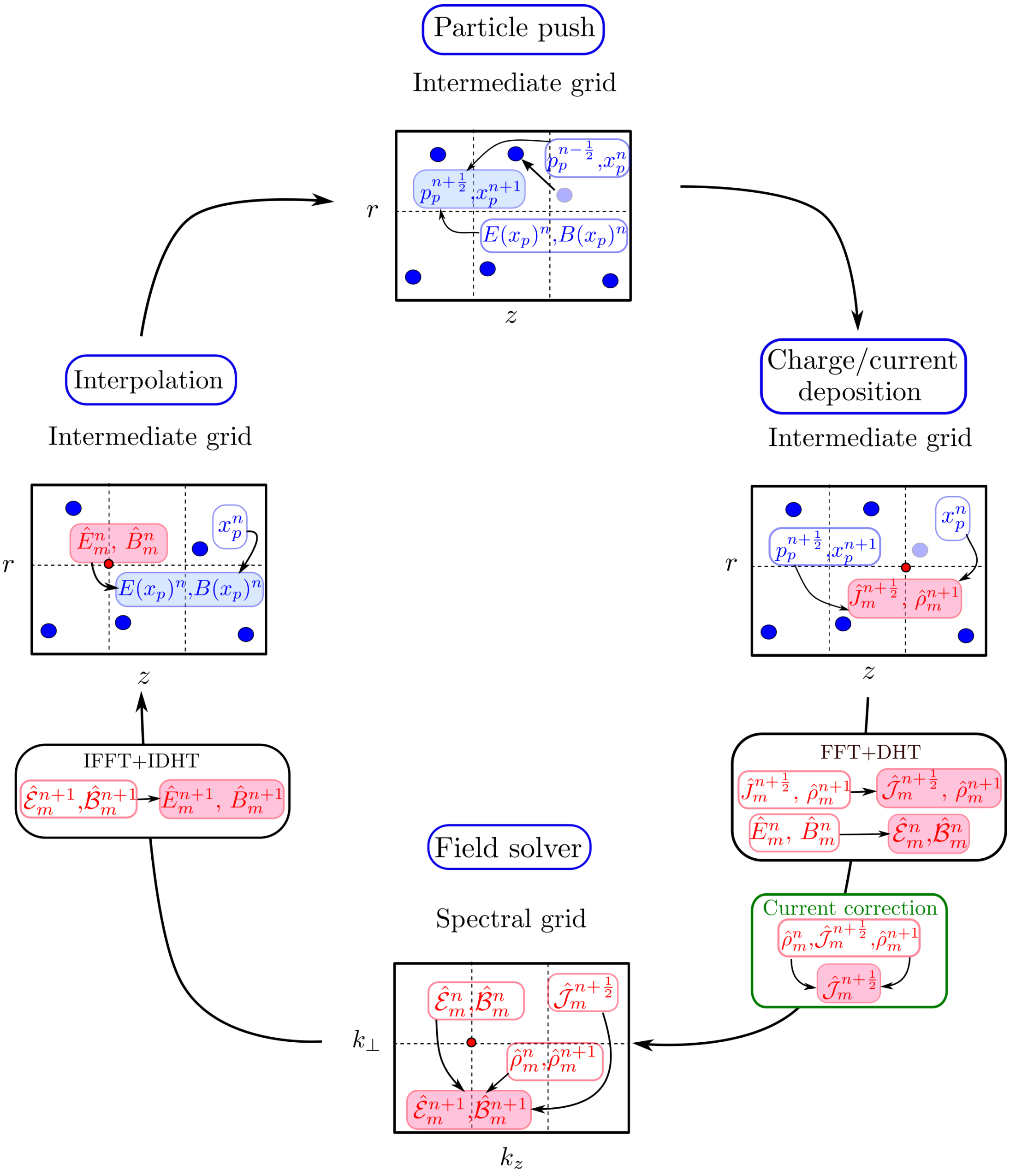

Figure 3.6: Schematic description of the 4 steps of a PIC cycle in the quasi-cylindrical spectral algorithm. At each time step, the fields are shown in red while quantities pertaining to particles in blue. The quantities that are being calculated at a given step are displayed with a colored background. The quantities that are used for this calculation, are displayed with a white background.

3.4 Parallelization strategy of the PIC algorithm with the PSATD scheme

3.4.1 Domain decomposition and parallelization of the PSATD solver

Pseudo-spectral electromagnetic solvers, integrating analytically the solution over a finite time step, have been firstly introduced by [I. Haber and Boris, 1973]. However, despite their extraordinary precision, they have not been widely adopted in PIC codes due to the difficulty of an efficient parallelization and their poor scalability beyond few thousands of cores. In fact, the use of Fast Fourier Transforms (FFTs) on a distributed data sets requires global communications that span the entire domain. Contrarily, the FDTD solvers require only local communications between neighboring subdomains, making them well suited for massively parallel super-computers based on distributed memory architectures scaling to hundreds of thousand of CPU cores.

In [Vay et al., 2013], an efficient method for the parallelization of the PSATD solver in Cartesian geometry has been proposed and demonstrated. This method is based on a standard domain decomposition, just like the one used in the case of FDTD solvers, where FFTs are computed locally. It exploits the properties of Discrete Fourier Transforms (DFTs), the linearity of Maxwell's equations and the finite speed of electromagnetic waves propagation to enable the parallelization and limit the data exchange within ghost cells between neighboring subdomains. Hence, the proposed method combines the efficiency of suppressing numerical instabilities and the scalability level of the FDTD scheme, provided that enough ghost cells are used.

One limitation of the use of the parallel PSATD algorithm is that the number of the ghost cells is relatively high compared to its FDTD counterpart, where usually 2 ghost cells are enough. This is due to the fact that the spatial derivative in the Fourier space does not correspond to the same local grid points in real space and it may involve data from arbitrarily distant grid points. Therefore, the truncation of the derivative operator in Fourier space by the domain decomposition results in numerical noise especially near the subdomains edges. However, a detailed analysis of the *truncation error* in [Vincenti and Vay, 2016] has shown that the noise is mainly localized near the subdomain boundaries and does not build up to affect the whole simulation domain and that it decreases significantly with the use of sufficiently large ghost regions.

This paper also suggests to employ a finite order derivative stencils instead of the exact computation of the derivative operator $i\boldsymbol{k}$ which corresponds to an infinite order with a stencil extending across the entire simulation grid. The purpose of reducing the order of the solver is to bring more locality, so that the truncation error is less important when decomposing the simulation grid since the required number of the ghost cells is governed by this order. However, this order reduction comes at the cost of slightly reducing the accuracy of the solver. A detailed study of the relation between the accuracy and the order of the solver as well as the required number of ghost cells for an arbitrary order can be found in [Jalas et al., 2017].

At each time step, the following steps are applied to the spectral grid:

- Local DFT followed by Hankel matrices multiplication of the fields is performed on each subdomain including ghost cells.
- Fields are advanced in time using eqs. (3.107) to (3.112).
- Local IDFTs of the fields are computed including the ghost cells to recover the fields in the corresponding real space.
- The fields in the guard regions are updated from data in the neighboring subdomains.

3.4.2 Single domain multiple decompositions (SDMD)

Regarding the quasi-cylindrical spectral algorithm, the solver is parallelized only along the z direction where the FFT is applied while a single domain in the r direction is kept. This is due to the non-locality in matrix-matrix multiplication, making the parallelization in r very complicated and incompatible with domain decomposition. This limits the scalability of the solver and the gain that can be achieved with the standard domain decomposition. Moreover, the large number of ghost cells associated to spectral solvers imposes a coarse-grain domain decomposition with large subdomains. Contrariwise, small subdomains allow for a better scalability and load balancing.

In order to circumvent this limitation, a two-level decomposition has been implemented in SMILEI [Derouillat and Beck, 2020]. This decomposition technique, referred to as "*Single Domain Multiple Decompositions*" uncouples the fields related grid from the one pertaining to macro-particles.

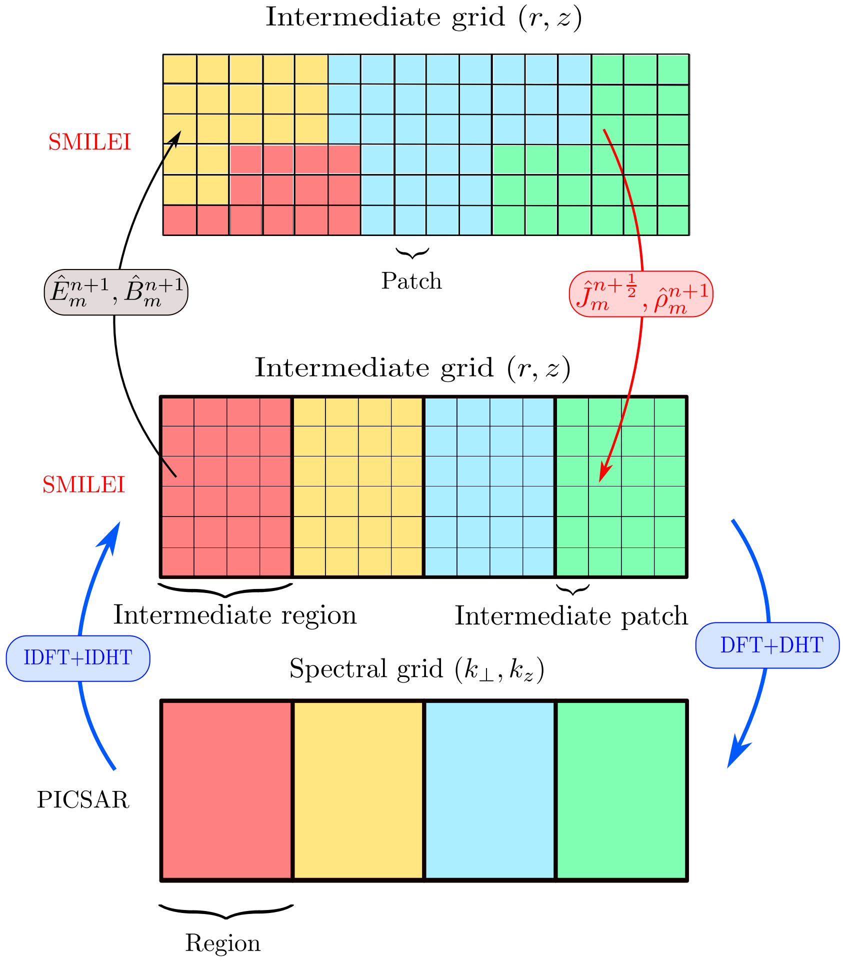

Figure 3.7: Schematic illustration of the decomposition involved in each type of grid with the associated transformations and its pertaining fields. MPI domains are delimited by different colors.

Therefore, it grants the use of large and static subdomains for the fields operations called *regions* on one hand and small dynamic subdomains for the macro-particles operations called *patches* on the other hand. In this configuration, the patch stores both the informations of the fields and macro-particles that belong to it while the region is totally unaware of macro-particles and only stores the fields information.

For each mode in the quasi-cylindrical pseudo-spectral solver, the spectral grid $(k_\perp, k_z)$ is decomposed only into regions while the intermediate grid (r, z) has the two decompositions: the one into regions and that into patches.

This decomposition technique slightly alters the PIC loop steps by introducing two additional steps illustrated in fig. 3.7 in order to ensure the communication between the two grids:

- After charge/current deposition on patches, charge and current densities must be communicated from patches to regions.
- Once the electromagnetic fields are updated after solving Maxwell's equations on regions, electromagnetic fields must be communicated from regions to patches.

This can improve the performances of the code since the simulation cost is dominated by the cost of particle-related operations. In fact, using small patches enables benefiting from the full capacity of the OpenMP dynamic scheduler by offering a better distribution of the particles between OpenMP threads. Contrarily, MPI processes with few patches may lead to load imbalance at the thread level.

In the case where the same decomposition is used for both the fields and for the particle operations, smaller patches usually lead to an increase of the fields synchronization cost. This fine grain decomposition overhead cost can also be mitigated using SDMD since the fields synchronization is handled between regions instead of patches.

Besides, the use of patches allows a radial decomposition for the particle-related operations, which enables a good strong scaling of the code. In fact, without the patches in the r direction, the code's performance is quickly limited once the number of cores reaches the number of patches. This is illustrated in fig. 3.8, where we can see that using the maximal number of patches in the longitudinal direction $n_{patch,z} = 256$ and just one radial patch does not scale beyond the point where the number of cores equals the number of patches. On the other hand, the use of more patches in the radial direction leads to a better strong scaling which allows a significant speed-up in the code's performance.

3.5 Advantages of PSATD

Thanks to their analytical integration over time and accurate spatial differentiation in Fourier space, spectral algorithms offer a multitude of advantages over the finite difference ones. For example, in finite difference simulations the group velocity of the laser v_g depends on the grid resolution and it is under-estimated compared to the analytical prediction even for a relatively high resolution, due to spurious numerical dispersion. Conversely, the PSATD algorithm estimates correctly the group velocity which is practically independent of the resolution in its framework.

Besides, contrarily to the FDTD method, the PSATD does not impose a CFL condition on the time step and offers an unconditional stability. However in the case of PIC codes, the time step is limited by the condition:

$$\Delta t \leq \frac{min(\Delta z, \Delta r)}{c} \tag{3.115}$$

This condition ensures that ultra-relativistic particles do not travel more than one mesh cell over a single time step. Therefore, the PSATD solver allows the use of larger time step compared

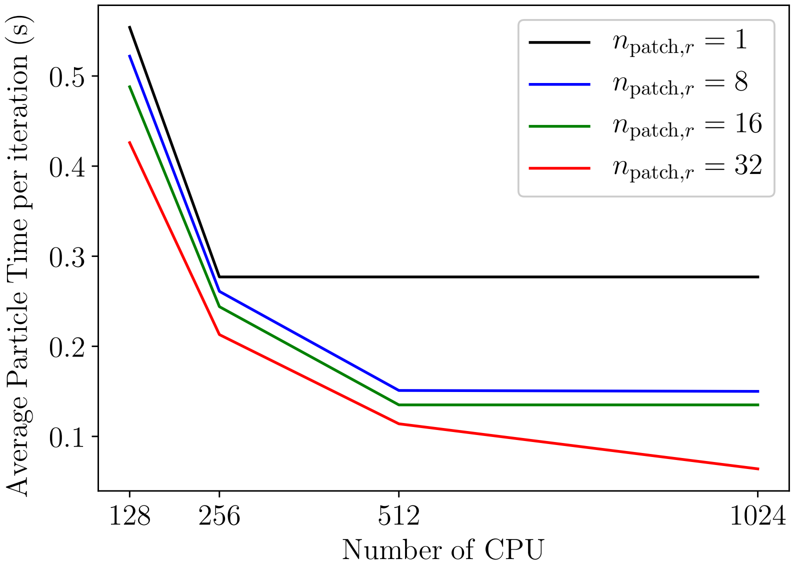

Figure 3.8: Scaling of the particles operation with the number of cores for different number of radial patches.

to the FDTD one especially in the case of quasi-cylindrical geometry where the CFL condition becomes more strict with the number of modes included.

Moreover, the centering in time in the PSATD solver allows an accurate estimation of the force felt by the electrons inside a copropagationg laser which is overestimated in the case of the standard finite-difference PIC solvers due to the staggering in time of their $\boldsymbol{E}$ and $\boldsymbol{B}$ fields [Lehe et al., 2016].

Most importantly, since the PSATD algorithm is dispersion-free, it allows the suppression of the zero-order numerical Cherenkov effect [5] caused by the spurious numerical dispersion. In order to illustrate this, a comparison is performed between two equivalent simulations of LWFA, one with the spectral and the other with the finite difference quasi-cylindrical algorithm, both implemented in the PIC code Smilei.

3.5.1 Comparison between FDTD and PSATD schemes

In order to benchmark the PSATD implementation and to test its accuracy and its ability to suppress the NCR, a comparison between two simulations run with the FDTD solver and the PSATD solver in the quasi-cylindrical geometry is presented next.

---

[5] The PSATD solver correctly models the dispersion of electromagnetic waves and thereby mitigates the problem of numerical Cherenkov radiation (NCR) also called zero-order numerical Cherenkov effect, in simulations of relativistic beams. Yet, it is not free of the numerical Cherenkov instability (NCI) also called high-order numerical Cherenkov effects [Pukhov, 2020; Kirchen et al., 2020]. However, the NCI are most likely to appear in boosted-frame simulations while they are negligible and usually do not have enough time to develop in the case of lab-frame simulations [Lehe et al., 2016].

Numerical parameters

The simulations are performed in a moving window of respectively longitudinal and transverse dimensions of 92 μm and 205 μm with $\Delta z = 0.032\ \mu m$ and $\Delta r = 0.32\ \mu m$ where a laser pulse linearly polarized along $\boldsymbol{e}_x$ with a waist $w_0 = 6.2\ \mu m$, a wavelength $\lambda_0 = 0.8\ \mu m$, a FWHM duration in intensity $\tau_0 = 25\ fs$ and a normalized peak vector potential $a_0 = 7$ is sent in a plasma target. The plasma target has a density up-ramp of 500 μm at its entry followed by a plateau of a density $n_e = 8.6 \times 10^{17}\ \mathrm{cm}^{-3} = 4.94 \times 10^{-4}\ n_c$ where $n_c = \omega_0^2 m_e \epsilon_0 / e^2$ is the critical density at this laser frequency ω_0. In both simulations, 54 regularly initialized particles per cell are used.

The PSATD solver is used with the finite order $n_{\mathrm{order}} = 32$ and $n_{\mathrm{ghost}} = 64$ as recommended in [Jalas et al., 2017]. In the boundaries of the domain, $n_{\mathrm{damp}} = 44$ cells were used to avoid the reflection of the waves inside the simulation domain.

In the finite-difference simulation a time step of $c\Delta t = 0.99\Delta z$ is used, while the spectral simulation was run with $c\Delta t = \Delta z$. These specific parameters have been selected to allow an important self-injected charge over a short propagation distance as well as to easily highlight the effects of numerical Cherenkov. In both simulations, the currents[6] are smoothed with a single-pass binomial filter in the longitudinal z and transverse r directions. In the case of the spectral algorithm, the smoothing is directly applied in the spectral space $k_z, k_\perp$.

Results

Figure 3.9 is a snapshot of both FDTD simulation (left panel) and PSATD simulation (right panel) after 885μm of propagation. The red colormap in the top panels represents the laser field $|E_y|$ while the superimposed shades of blue represent the charge density ρ . In the bottom panels, the quantity $E_y + cB_x$ is shown in blue and red along with bubble and the injected bunch in grey. The quantity $E_y + cB_x$ is chosen instead of E_y in order to cancel the strong space-charge field that would otherwise dominate the figure. In fact, both the laser and the self-generated field of a relativistic beam propagate at $v_\phi \sim c$ along z direction and their contributions cancel out leaving only the contribution from the cavity fields ($|E + c \times B| \ll |E|$) [Jackson, 1998]. The quantity $E_y + cB_x$ is particularly interesting because it is proportional to the y-component of the Lorentz force felt by a relativistic electron of a velocity $\boldsymbol{v} = c\boldsymbol{e_z}$. In the bubble regime, this transverse force component is linear in y i.e $F_y \propto y$. This can be seen in fig. 3.9 (bottom panels) where $E_y + cB_x$ is stronger off axis and decreases linearly to cancel on the axis of the bubble.

Despite the qualitative resemblance between the overall aspect of the bubble structure and the shape of the injected beam in the two simulations, the $E_y + cB_x$ color map reveals a high frequency radiation inside the ionic cavity around the accelerated bunch in the finite difference scheme. Zooming on the bunch and rescaling the field $|E_y + cB_x|$ in the top panels of fig. 3.10 shows clearly this high frequency radiation surrounding the electrons beam in the simulation with the FDTD solver. The amplitude of this unphysical radiation is comparable to that of $|E_y + cB_x|$ inside the bubble and hence can substantially alter the physics at stake.

3.5.2 Discussion

The high frequency radiation around the bunch is a typical signature of the zero-order NCR which modifies the electromagnetic fields inside the ionic cavity and may hence influence the transverse

---

[6] In spectral solver, the charges are also smoothed as they are also used in the source term to solve Maxwell's equations.

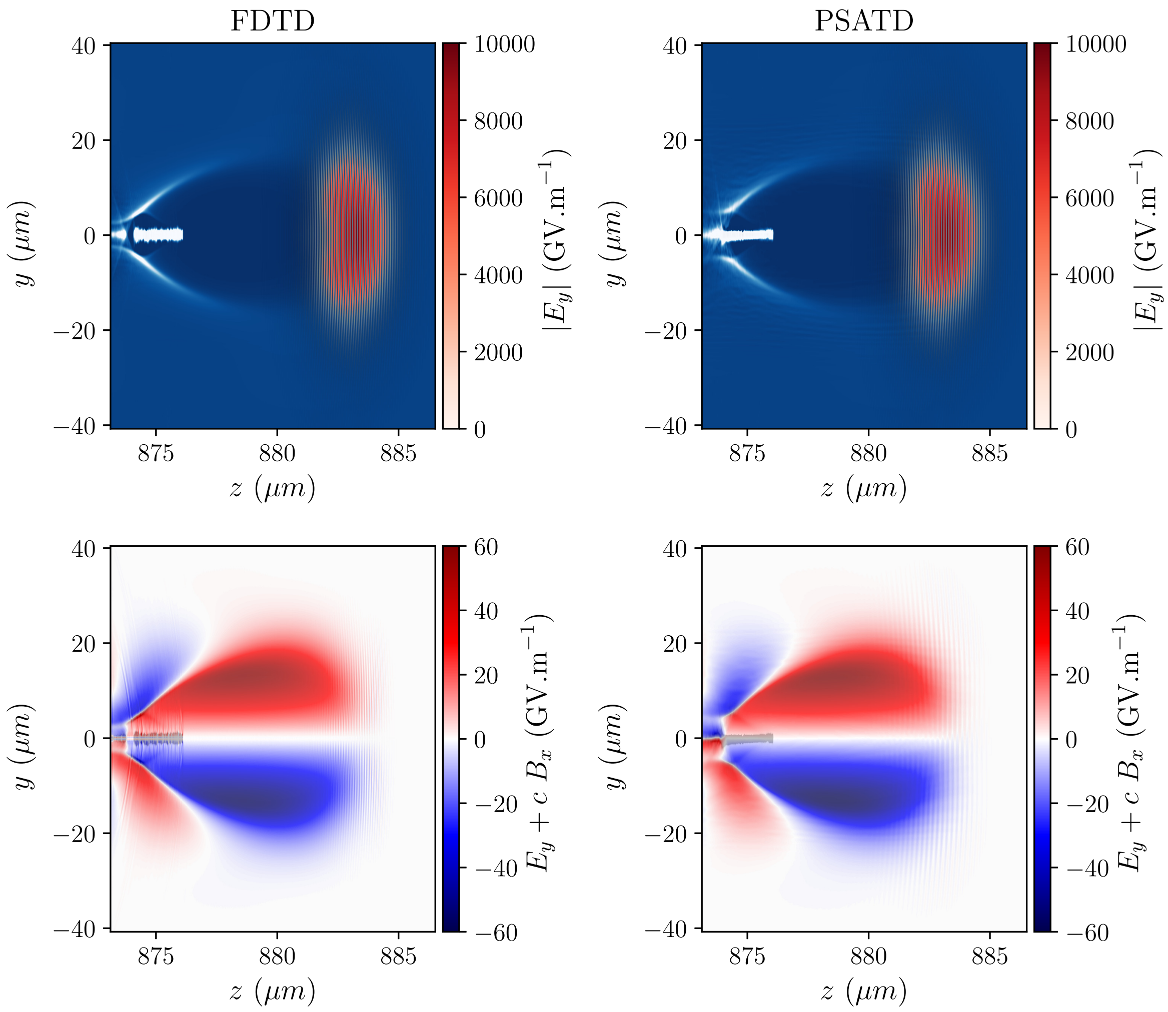

Figure 3.9: Comparison of simulations outputs between FDTD (left) and PSATD (right) after 885 μm of propagation. Upper panels: The laser field amplitude $|E_y|$ in red and superimposed with the charge density ρ in blue. Lower panels: representation of the bubble with the field $E_y + cB_x$ color map in red and blue and the injected bunch in grey.

motion of the electrons inside the bubble. This hypothesis is confirmed by the observation of the corresponding characteristic double-parabola in Fourier space [Lehe et al., 2013a, 2016; Bourgeois and Davoine, 2020] shown in the lower left panel of fig. 3.10. The physically relevant frequencies are confined in the center around $k_y = 0$ and $k_z = 0$ while the higher values covering a wide range of frequencies correspond to the unphysical radiation around the beam.

On the other hand, this radiation is absent in the case of the PSATD simulation in both real (top right) and Fourier space (lower right) in fig. 3.10 which confirms that the PSATD solver is free from the zero-order numerical Cherenkov radiation associated with the numerical dispersion [Godfrey, 1974].

A direct consequence of the Cherenkov radiation is the unphysical emittance growth of the bunch [Lehe et al., 2013a]. In order to confirm this, the energy spectrum of the previous simulations are plotted after a propagation distance of 885μm corresponding to the same time where

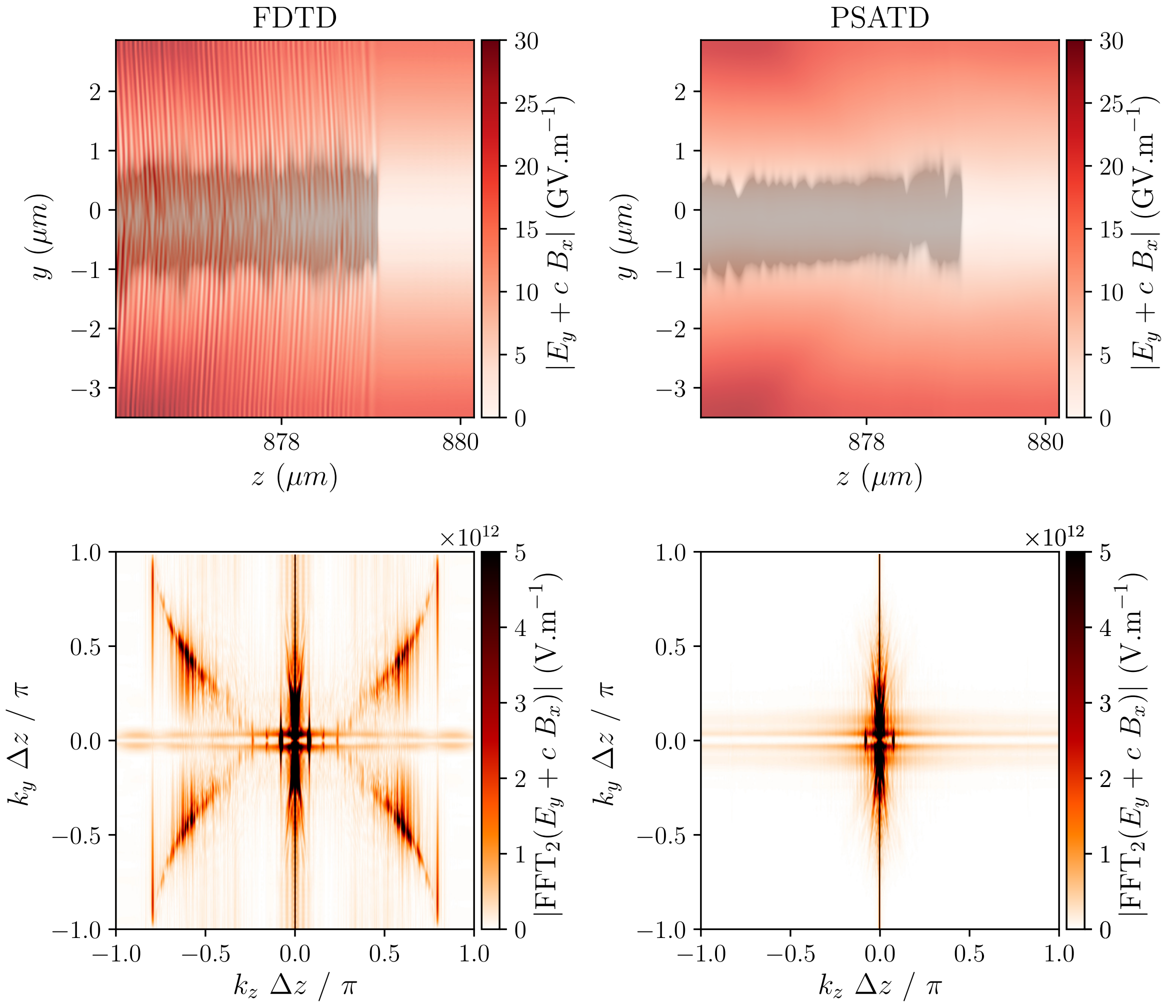

Figure 3.10: Comparison of simulations outputs between FDTD (left) and PSATD (right) after 885 μm of propagation. Upper panels: close-up look to the bunch and its surrounding $|E_y + cB_x|$ region shows a high frequency radiation. Lower panels: two-dimensional Fourier transform of the quantity $E_y + cB_x$.

the snapshots fig. 3.9 and fig. 3.10 were taken. The bunches (shaded area delimited by two vertical red dashed lines) were selected by energy interval = [29, 34] (MeV) with only electrons in the quasi-monoenergetic peak of the spectrum. They are presented in fig. 3.11. The bunch properties are summarized in table 3.1. The FDTD scheme overestimates the transverse emittance of the bunch which is 40% more than that of its PSATD counterpart. Here the accelerated electrons are in a fully evacuated cavity characterized by linear focusing fields and the space charge effects can be neglected, thus the emittance growth could be only caused by the energy spread. However, conversely the bunch's energy spread in the case of PSATD scheme is more important ($\sim 39\%$) than that in the case of FDTD and both bunches have almost the same divergence $\theta_\perp$. The main difference between the two bunches is the emittance in the y-direction which is correlated to the y-rms bunch size (1.101) and results in an important transverse emittance value in the case of the FDTD bunch compared to the one in PSATD scheme. Based on the previous observations,

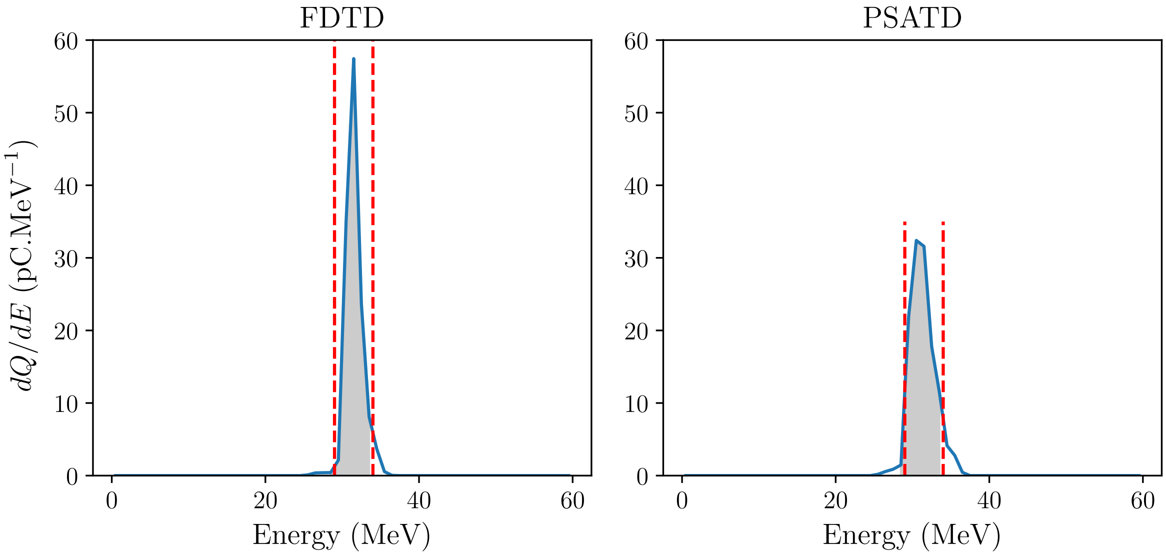

Figure 3.11: Energy spectrum of the electrons after a 885 μm of propagation. The shaded areas in grey correspond to the selected bunches for which the bunch-related quantities are evaluated and compared in table 3.1.

the difference in the transverse emittance can only be explained by the numerical-Cherenkov radiation.

This study puts forward the importance of suppressing this unphysical radiation in order to correctly estimate the bunch charge and its transverse properties. Therefore, it has been shown that the PSATD suppresses efficiently the NCR responsible of a non-physical growth of the transverse size, divergence and beam emittance and may also modify the physics which is not straightforwardly discerned in a finite-difference simulation especially in the cases where there is no exact analytical formula to predict them as it is the case for the dephasing length.

Bunch properties	FDTD	PSATD
Q (pC)	126	115
E_{peak} (MeV)	31.5	30.5
Δ E / E_{peak} (%)	2.8	3.9
$\theta_{\perp}$ (mrad)	14	13
x-rms size (μm)	0.98	1.14
y-rms size (μm)	1.47	0.8
z-rms size (μm)	4.62	4.44
$\varepsilon_{n,x}$ (mm $\cdot$ mrad)	0.25	0.36
$\varepsilon_{n,y}$ (mm $\cdot$ mrad)	0.54	0.22
$\varepsilon_{n,\perp}$ (mm $\cdot$ mrad)	0.59	0.42

Table 3.1: Summary of the bunch-related quantities in FDTD and PSATD schemes.

Chapter 4

High fidelity simulations using realistic Apollon laser profile

Laser WakeField Acceleration (LWFA)[Tajima and Dawson, 1979; Esarey et al., 2009; Malka et al., 2002] has been proven to be a promising efficient way to accelerate electrons up to few GeVs[Leemans et al., 2006, 2014; Gonsalves et al., 2019] within a short propagation of distance. Nevertheless, one important challenge that arouses an increasing interest in the community is the improvement of the shot-to-shot reproducibility for the beam charge and energy [Mangles et al., 2007], which is important for most of the applications of this technology. In fact, fluctuations of the laser intensity profile, can affect the quality of the electron beam: divergence, emittance, energy spread and maximum energy gain [Cummings and Thomas, 2011]. In particular, multi-GeV electrons which are generated by self-injection in the bubble regime, are very sensitive to the quality and the complicated structure of the laser spot in ultra-short TW to PW systems.

So far, the influence of the presence of non-Gaussian features and imperfections in the laser pulse have been little investigated in the case of PW systems. Most theoretical and numerical studies on LWFA suppose an ideal Gaussian intensity profile. There were only few studies that dealt with realistic laser features and their impact on the beam quality and on the production of the betatron oscillations. However, they were carried with much lower power and energy than the one Apollon is aiming to produce. It is a particularly interesting feature because the self-focusing process depends to the first order on the pulse power thus, different results should be expected. Furthermore, it was found that in addition to the transverse intensity distribution, the electron beam distribution is sensitive to the laser wave front distortions [Beaurepaire et al., 2015].

The use of ideal laser profiles in the simulations may explain the gap between their results and the ones found in experiments. Hence it urges the use of realistic pulses as input in the simulations to retrieve some trends found in the LWFA experiments.

The aim of this chapter is to study the influence of both realistic laser intensity and wave front profiles from measurements in Apollon installation. As a first step, the algorithm of propagation using Fresnel integration is presented in section 4.1. It is used throughout the chapter to recover the laser intensity and wave front at the border of the simulation box close to the focal plan. The experimental set-up of laser focusing results in the presence of a hole in the near field, which is the region close to the laser output aperture before the focus. A study on the impact of this hole using a simplified case of a theoretical super-Gaussian fit to the intensity profile is presented in section 4.2. Finally, the results of a computational investigation into the influence of experimental intensity distribution and wave front on the electrons beam quality are presented and discussed in section 4.3.

Contents

4.1 Propagation using Fresnel integration 101
4.2 Study on the presence of a hole in the laser's near-field with a theoretical fit 103
4.2.1 Laser profile fitting with super-Gaussians in the near-field 105
4.2.2 Choice of the laser profiles 107
4.2.3 Results and discussion 109
4.2.4 Conclusions 119
4.3 Influence of experimental laser imperfections on laser wakefield acceleration 119
4.3.1 Motivation 119
4.3.2 Effect of realistic laser profiles on 3D Cartesian simulations 120
4.3.3 Effect of realistic laser profiles on quasi-cylindrical simulations 128

4.1 Propagation using Fresnel integration

In optics, the propagation of the field is usually addressed as a diffraction problem. In order to solve this problem, diffraction integrals need to be invoked. However, it is rare to find rigorous solutions to diffraction integrals and in most cases of practical interest, approximate methods are used [Welford, 1975; Azmayesh-Fard, 2013].

The propagation of waves far from the source can be efficiently estimated using the Huygens and Fresnel integral approaches. According to Huygens principle [Huygens, 1962]: "Every unobstructed point of a propagating wave front at a given instant, serves as a source of spherical secondary wavelets (with the same frequency as that of the primary wave) such that later the wave front is the superposition of all these wavelets (considering their respective amplitudes and phases)."

In other words, the amplitude of the electric field $U(x, y, z)$ at any plane (x, y) far from the source $U(X, Y) = U(X, Y, z = 0)$ in the plane (X, Y) by a distance z is the sum of all these wavelets. This leads to Fresnel diffraction integral:

$$U(x,y,z) = \frac{-i}{\lambda_0}\int_{-\infty}^{+\infty}\int_{-\infty}^{+\infty} U(X,Y)\frac{e^{ikr}}{r}\cos\theta dXdY \tag{4.1}$$

where $r = \sqrt{z^2 + (x-X)^2 + (y-Y)^2}$ and k is the wavenumber $2\pi/\lambda$. The term $\cos\theta$ is an "obliquity factor" defined by the angle θ between the line r and the normal to the plane (X, Y) $\equiv$ the propagation axis z in our case (fig. 4.1).

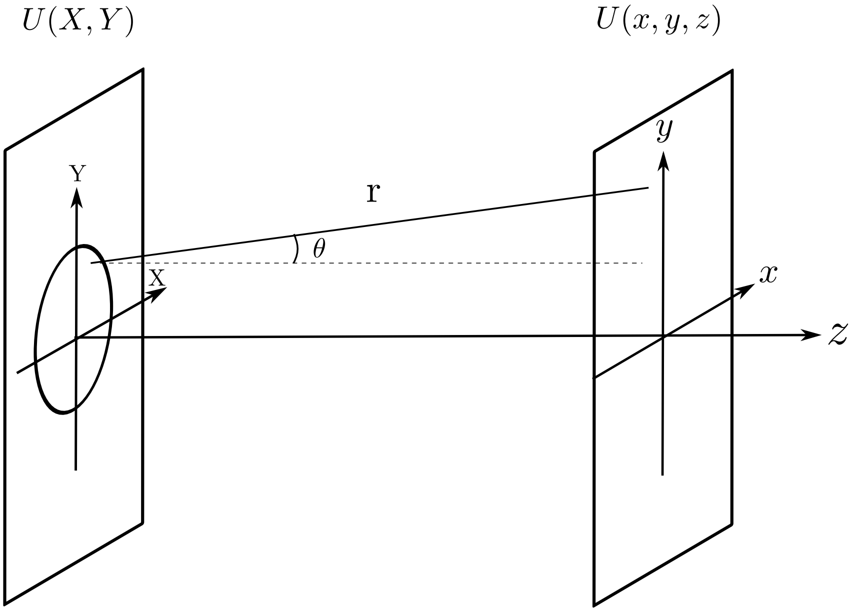

Figure 4.1: Diffraction geometry, showing aperture (or diffracting object) plane $U(X, Y)$ and image plane $U(x, y, z)$ after a propagation distance z, with the corresponding coordinate system.

Far from the source, the *paraxial approximation* is well verified, i.e. $z \gg (x - X)$ and $z \gg (y - Y)$, hence $r \simeq z$ and $\cos\theta = r/z \simeq 1$. We can Taylor-expand r and we can retrieve the Fresnel approximation valid under the previous inequality:

$$r \simeq z + \frac{(x-X)^2}{2z} + \frac{(y-Y)^2}{2z} = z + \frac{x^2+y^2}{2z} - \frac{xX+yY}{z} + \frac{X^2+Y^2}{2z} \tag{4.2}$$

Therefore, under Fresnel approximation, the field at (x, y, z) reads:

$$U(x,y,z) = \frac{e^{ikz}}{i\lambda_0 z} e^{i\frac{k}{2z}(x^2+y^2)} \int_{-\infty}^{+\infty}\int_{-\infty}^{+\infty} U(X,Y) e^{i\frac{k}{2z}(X^2+Y^2)} e^{-i\frac{k}{z}(xX+yY)} dXdY \qquad (4.3)$$

Assuming that the source U is the result of the focalization of a source U' through a lens of focal length f, we can write: $U(X,Y) = U'(X,Y)e^{-i\frac{k}{2f}(X^2+Y^2)}$ (we extract the phase introduced by the lens from U), we can rewrite the previous integral as

$$U(x,y,z) = \frac{e^{ikz}}{i\lambda_0 z} e^{i\frac{k}{2z}(x^2+y^2)} \int_{-\infty}^{+\infty}\int_{-\infty}^{+\infty} \left(U'(X,Y) e^{i\frac{k}{2}(X^2+Y^2)(\frac{1}{z}-\frac{1}{f})}\right) e^{-i\frac{k}{z}(xX+yY)} dXdY \qquad (4.4)$$

Hence, if the distance z from the lens is sufficiently large so that the *paraxial approximation* is valid, the field $U(x,y,z)$ is a rescaled Fourier transform of $U'(X,Y)e^{i\frac{k}{2}(X^2+Y^2)(\frac{1}{z}-\frac{1}{f})}$ evaluated at $k_x = \frac{k}{z}x$ and $k_y = \frac{k}{z}y$, where $U'(X,Y)$ is the field (amplitude and phase) just before the lens.

In practice, the input $U'(X,Y)$ is a digitized measurement provided by a CCD camera far from focus, thus it is a discrete signal with a given number of pixels n and a definite pixel size that only depends on the properties of the camera.

Therefore, the output field distribution at $U(x,y,z)$ after the lens is retrieved algorithmically using the following steps:

1. Applying a Discrete Fourier transform (DFT) algorithm to decompose the term $U'(X,Y)e^{i\frac{k}{2}(X^2+Y^2)(\frac{1}{z}-\frac{1}{f})}$.
2. Multiplying the obtained result with the multiplicative factor $\frac{e^{ikz}}{i\lambda_0 z}e^{i\frac{k}{2z}(x^2+y^2)}$ where the terms in the exponential are evaluated in the target plane z by computing the new pixel size from the source pixel size as:

$$\text{NewPixelSize} = \frac{2\pi z}{n \times \text{PixelSize} \times k}$$

When using the DFT, the signal has to be recentered at 0 first in order to obtain the correct phase. Otherwise, the resulting phase would be punctuated with additional minus signs every two pixels. In order to understand this, the DFT of a signal centered in 0 and that of a signal centered on the middle of the grid are compared.

The DFT of a signal centered in 0 on a $n_x \times n_y$ grid is written

$$u(k_x,k_y) = \frac{1}{n_x \times n_y} \sum_{x=0}^{n_x-1}\sum_{y=0}^{n_y-1} u(x,y) \exp\left(-2\pi i \left(\frac{k_x}{n_x}x + \frac{k_y}{n_y}y\right)\right) \qquad (4.5)$$

Whereas, the DFT of the same signal, but centered on the middle of a $n_x \times n_y$ grid, is written:

$$\begin{aligned} u(k_x,k_y) =& \frac{1}{n_x \times n_y} \sum_{x=0}^{n_x-1}\sum_{y=0}^{n_y-1} u(x,y) \exp\left(-2\pi i \left(\frac{k_x}{n_x}(x-n_x/2) + \frac{k_y}{n_y}(y-n_y/2)\right)\right) && (4.6)\\ =& \frac{1}{n_x \times n_y} \sum_{x=0}^{n_x-1}\sum_{y=0}^{n_y-1} u(x,y) \exp\left(-2\pi i \left(\frac{k_x}{n_x}x + \frac{k_y}{n_y}y\right)\right) \exp(ik_x\pi)\exp(ik_y\pi) && (4.7)\\ =& \frac{1}{n_x \times n_y} \sum_{x=0}^{n_x-1}\sum_{y=0}^{n_y-1} u(x,y) \exp\left(-2\pi i \left(\frac{k_x}{n_x}x + \frac{k_y}{n_y}y\right)\right) (-1)^{k_x}(-1)^{k_y} && (4.8) \end{aligned}$$

In the last case when the signal is centered on the middle of the grid, there is an extra multiplicative factor $(-1)^{k_x}(-1)^{k_y}$, leading to alternating signs in the DFT compared to the first case where the signal is centered on 0. Hence, the signal should be centered to 0 in order to obtain the correct results.

The implemented algorithm was benchmarked and validated (not presented here). It was proven to yield the desired phase and intensity as long as the paraxial approximation assumption is valid.

4.2 Study on the presence of a hole in the laser's near-field with a theoretical fit

Before focusing, the intensity distribution delivered by laser systems usually exhibits an imperfect, nearly flat-top distribution in the transverse plane. Therefore, the corresponding intensity profile in the focal plane is not purely Gaussian and exhibits a profile close to an Airy pattern. An example of the intensity distribution delivered by the Apollon laser in the near-field before the focusing mirror, is presented in fig. 4.2. The corresponding intensity profile in the focal plane, computed with the Fresnel diffraction is presented in fig. 4.3.

In the chosen design for the Apollon laser, the near field exhibits a hole of a radius $r_{hole} = 16\ mm$ at approximately but not exactly, the center of the distribution. A simplified schematic representation of the experimental set-up for the laser beam propagation and focusing is shown in fig. 4.4: a laser beam of $1/e^2$ diameter $\sim 2\sigma \simeq 130\ mm$ propagates until a reflecting drilled mirror positioned at 45° where a small fraction of the laser beam is lost. The rest of the laser beam is then reflected and focused with spherical mirror. The focused beam passes through the same hole and propagates in the plasma target.

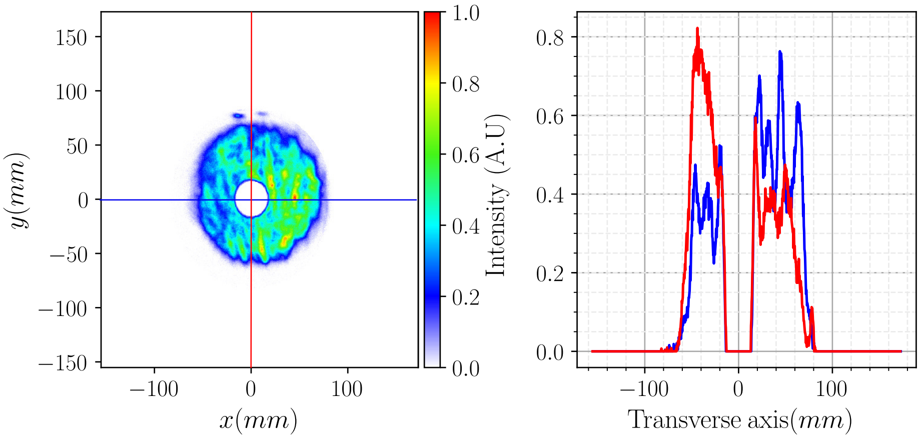

Figure 4.2: *Left panel*: typical 2D intensity profile delivered by the Apollon laser in the near-field. *Right panel*: 1D lineouts corresponding to the red and blue lines in the 2D colormap.

The center of the laser beam in near-field is determined as the barycenter of the area where the intensity is above 5% of the maximum intensity. The center of the hole is calculated as the barycenter of the area around the beam center within a radius $r = 1.5 \times r_{hole}$ where the intensity is below 5%. To obtain a symmetrical spot with a finite size, the intensity at a distance larger than R_{max} is set to zero. R_{max} is the radius after which the radial profile, obtained by averaging

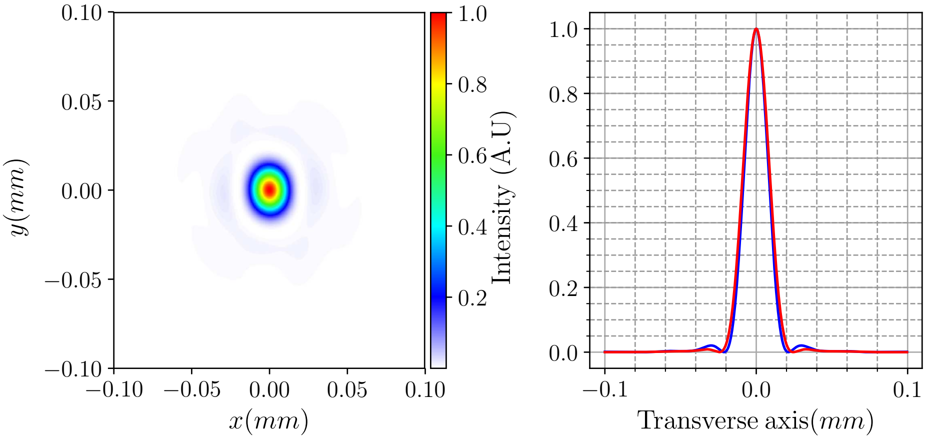

Figure 4.3: *Left panel*: 2D intensity profile in the focal plane for $f = 9\ m$ obtained by a Fresnel integration of the near field. *Right panel*: 1D lineouts corresponding to the ones in fig. 4.2.

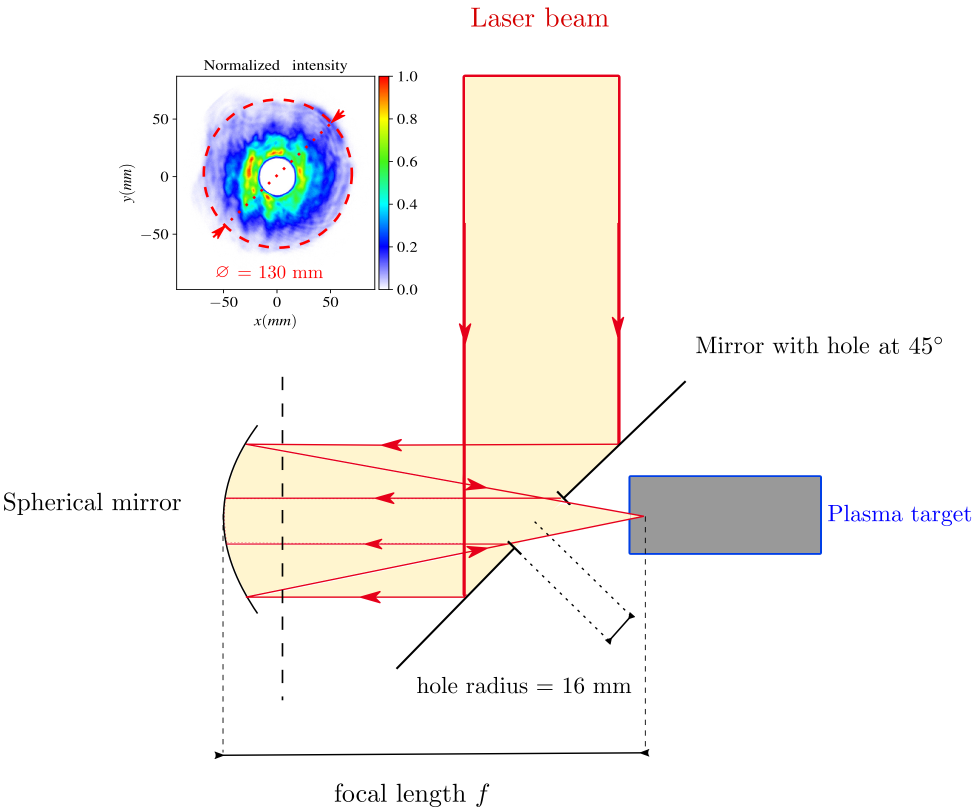

Figure 4.4: Schematic representation of the experimental set-up for the laser beam propagation and focusing in Apollon installation: a laser beam of a $1/e^2$ diameter $\simeq 130\ mm$ is sent and reflected by a mirror at 45° presenting a hole of a radius $= 16\ mm$ where a small fraction from the center of the laser is lost (estimated to be around $\sim 12\%$). The beam is focused by a spherical mirror of a focal length f.

the distribution over the azimuthal variable θ, is lower than 1% of the maximum.

The intensity profile is retrieved from the experimental data supposing a total energy U= 15 J and a Gaussian envelope in time with a duration $\tau_0 = 25\ fs$ corresponding to a power P $\sim \frac{U}{\tau_0} = 600$ TW. To do so, each "count" measured by the camera is multiplied by the quantity $\mathrm{I}_{\mathrm{count}} = U/(N_{\mathrm{counts}} \times \tau_0 \times \mathrm{PixelSize}^2)$ where N_{counts} is the sum of all the data counts.

The Apollon installation offers the possibility of two focal lengths $f = 3m$ or $f = 9m$. In both cases, the laser's radius in near-field $\sigma \simeq 65\ mm$ is small enough compared to the focal length $\sigma \ll f$. Therefore, the paraxial approximation is verified and the use of Fresnel integral to calculate the intensity and phase of the propagated field around the focal plane is justified.

4.2.1 Laser profile fitting with super-Gaussians in the near-field

2D curve fitting

In order to study the effect of the hole presence in the laser's transverse distribution, the intensity profile is fitted to a smooth theoretical function that can best describe the experimental measurement. The method of non-linear least squares is therefore used to determine the best fit. This method is based on minimizing the sum of the residuals squares where the residuals denote the offsets of the points from the curve. The approach is based on iterative refinement of the solution until convergence is achieved.

Firstly, we are looking to the best fitting function among super-Gaussian profiles defined by:

$$\begin{aligned} I^n(x,y) &= I_0^n \exp\left(-2\left(\frac{(r-r_0)}{\sigma}\right)^n\right) \\ &= I_0^n \exp\left(-2\left(\frac{(x-x_0)^2+(y-y_0)^2}{\sigma^2}\right)^{n/2}\right) \end{aligned} \tag{4.9}$$

with

$$I_0^n = \frac{P}{\int_x \int_y \exp\left(-2\left(\frac{(x-x_0)^2+(y-y_0)^2}{\sigma^2}\right)^{n/2}\right) dxdy}$$

where n denotes the order of the super-Gaussian, x_0 and y_0 are the coordinates of its center and σ is the radius.

The goal consists in adjusting the parameters σ, x_0 and y_0 of the model function while varying the order n to best fit the data set for a fixed laser power of P= 600 TW corresponding to a total energy of 15 J and a duration of 25 fs. Due to the presence of the hole in the experimental profile, the fitting functions in eq. (4.9) are multiplied by the indicator function $\mathbb{1}_A$ in order to estimate correctly the fit.

$$\mathbb{1}_A = \begin{cases} 0 & \text{if } r - r_0 < r_{hole} \\ 1 & \text{else.} \end{cases}$$

The order of the super-Gaussian n is varied from 2, corresponding to a Gaussian profile, to 16. The lineouts of these fitting functions are presented in fig. 4.5. For each order n, the normalized root-mean-square error (NRMSE) is calculated from the residuals $\hat{y}_i - y_i$ which are the differences between the actual observed values y_i and the predicted values $\hat{y}_i$.

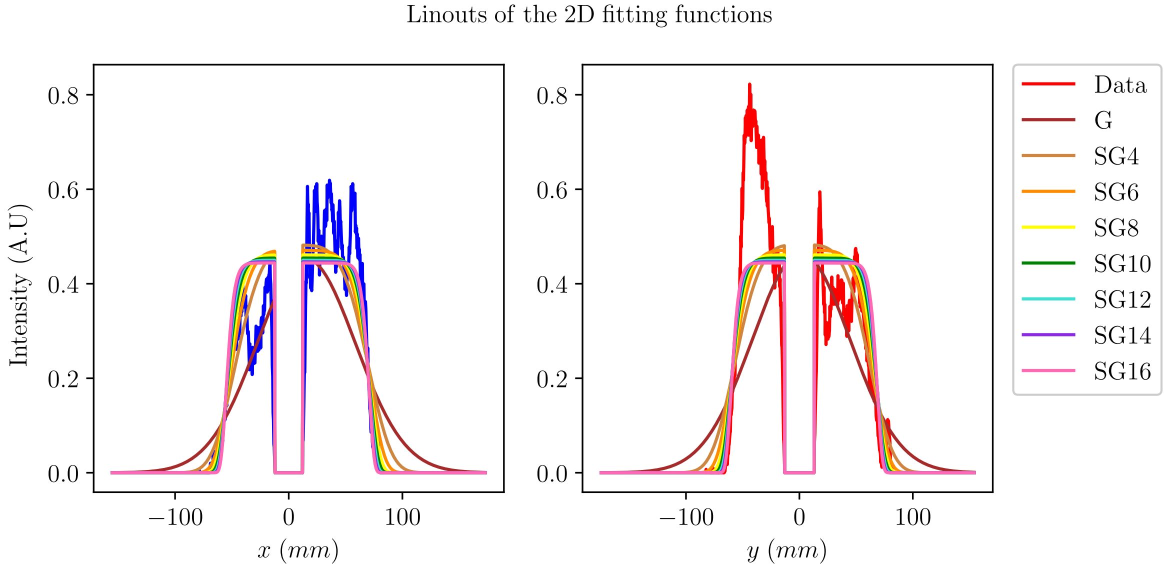

Figure 4.5: Lineouts of the super-Gaussians fitting functions superposed with the experimental intensity lineouts in the x and y directions.

$$\mathrm{NRMSE} = \sqrt{\frac{\sum_{i=1}^{N}(\hat{y}_i - y_i)^2}{N}} \tag{4.10}$$

The choice of the best fit is based on the criterion of minimizing the NRMSE. The evolution of the NRMSE as a function of the order n is depicted in fig. 4.6. For this experimental data, even though the NRMSE starts to converge starting from the order 10 as it barely changes for the following orders, the super-Gaussian of order 14 is found to be the best fit because it corresponds to the inversion point i.e the error starts to increase slightly for the order 16.

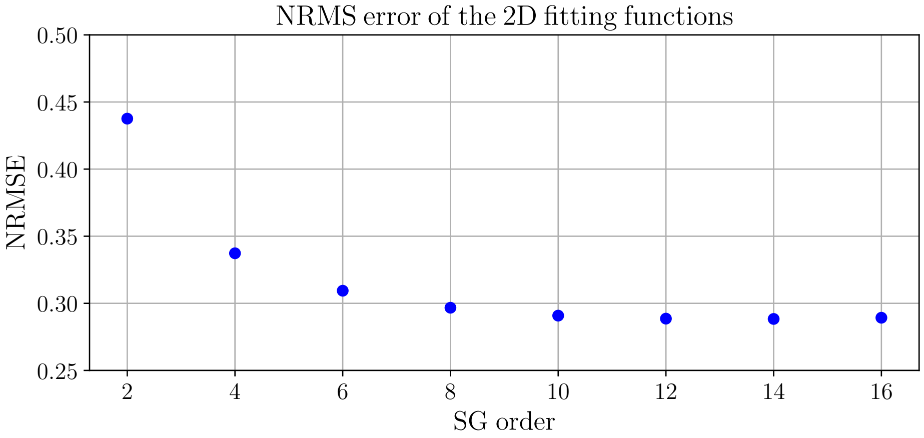

Figure 4.6: Normalized root-mean-square error of the 2D fitting super-Gaussians as a function of the order n.

Radial curve fitting

The provided experimental intensity profile is not symmetric and it exhibits a very complicated pattern in near field fig. 4.2. Thus, it is hard to find a smooth symmetric function in general and a super-Gaussian in particular to fit correctly the data. This is why, the values of the NRMSE are still high even for the best super-Gaussian fit.

In order to smooth a little bit the experimental intensity profile, it is integrated in θ to obtain the radial profile. However, we can see in fig. 4.2 that the hole is not centered in the data due to the fluctuations of shot-to-shot in laser. So basically, there are two centers that we can distinguish, the hole center and the global center which is defined as the barycenter of the intensity here. The purpose of the fitting with a super-Gaussian is to better describe the steep slope at the edges of the intensity distribution, so it is better to integrate with respect to the global center and not with the center of the hole.

In this case the hole in the radial profile is concealed as shown in fig. 4.7. We thereafter apply a filter to estimate the fitting only beyond the hole radius. Finally, the error curve of the radial fitting has a resembling pace as the one with the 2D fitting with a minimum also reached for the order 14. Thus, the choice of order 14 for the super-Gaussian is justified with a double check.

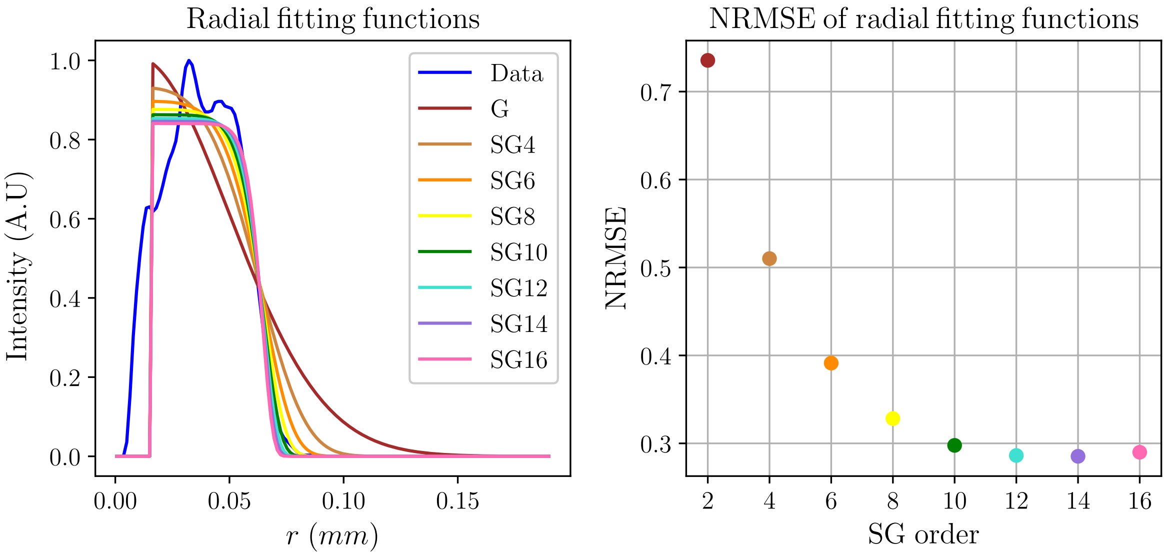

Figure 4.7: *Left panel*: Radial fitting functions with super-Gaussians superposed with the radial profile of the measured intensity. *Right panel*: the normalized root-mean-square error of the radial fitting super-Gaussians as a function of the order n.

4.2.2 Choice of the laser profiles

According to the previous study, it is found that the best super-Gaussian fit is of order 14. In order to study the impact of the hole in the laser near field on the future LWFA experiments, we perform a numerical study with super-Gaussians with and without the hole. In particular, we are interested in the effect of the hole presence from a geometrical point of view. Therefore, in the case of super-Gaussians with hole, the profile is rescaled either to have the same power or the same laser strength parameter a_0 as the one without the hole. It is also insightful to study the effect of non-Gaussian features by comparing the results with the ones of an "equivalent" Gaussian.

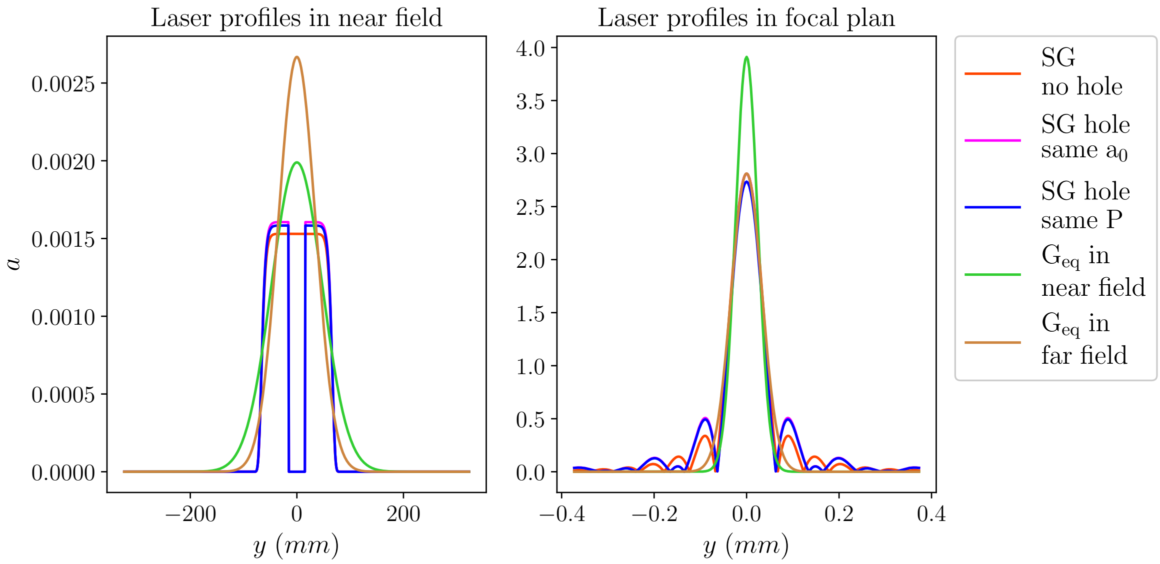

Figure 4.8: Normalized vector potential of the input laser profiles used in simulations.

The used input laser profiles presented in fig. 4.8 are detailed in the following.

1. **SG no hole**: theoretical fit of the measured laser intensity with a super-Gaussian of order 14 using non-linear least squares method. The hole presence as well as the resulting power loss is neglected.

2. **SG hole same a_0**: theoretical fit of the measured laser intensity with a drilled super-Gaussian of order 14. In this case, the lost power due to the presence of the hole is taken into account in the fitting function, then the profile is rescaled so that it has the same laser strength parameter a_0 as the profile without the hole.

3. **SG hole same P**: theoretical fit of the measured laser intensity with a super-Gaussian of order 14 presenting a hole of the same power as the one with no hole.

4. **G_{eq} in near field**: theoretical fit of the measured laser intensity with a Gaussian that has the same radius σ as the super-Gaussians as well as the same power P in the near field.

5. **G_{eq} in far field**: theoretical fit of the **SG no hole** intensity profile with a Gaussian of the same maximal intensity I_0 in the far field.

The main parameters of the input laser profiles are summarized in table 4.1 where the radius σ is calculated in the near field and the waist is estimated from the intensity profile in the focal plan.

The laser profiles described in table 4.1 are then used to run a set of simulations with the quasi-cylindrical algorithm in Smilei using only the first two azimuthal modes (m=0 and m=1). All the

---

[1] The waist was estimated to be the radius of the laser beam $d/2$ at the first intersection from the center where the intensity is $1/e^2$ of I_0 (note that it is possible that there are multiple intersection in the case of super-Gaussians).

Profiles	radius σ (mm)	waist w_0 (mm)[1]	Power P (TW)	a_0	hole
SG no hole	67.1	4.5×10^{-2}	600	2.81	no
SG hole same a_0	67.1	4.3×10^{-2}	628	2.81	yes
SG hole same P	67.1	4.3×10^{-2}	600	2.735	yes
G_{eq} in near field	67.1	3.4×10^{-2}	600	3.9	no
G_{eq} in far field	49.1	4.66×10^{-2}	577	2.81	no

Table 4.1: Summary of the laser profiles parameters.

simulations are run in a 6400×1280 moving window with a resolution defined by $\Delta z = 0.0127\ \mu m$, $\Delta r = 0.19\ \mu m$ and $c\Delta t = 0.99\times\Delta z$. All the lasers have a wavelength $\lambda_0 = 0.8\ \mu m$ and a Gaussian time envelope of a duration $\tau_0 = 25\ fs$. Using Fresnel integration, the laser profiles are evaluated at $z = f - 5\times10^{-4}$ m where the focal length is $f = 9$ m. This position corresponds to the beginning of the plasma target that has a 500 μm-long rising density gradient at its entrance, followed by a plateau of an electronic density $n_e = 8.6\times10^{23}$ cm^{-3}.

4.2.3 Results and discussion

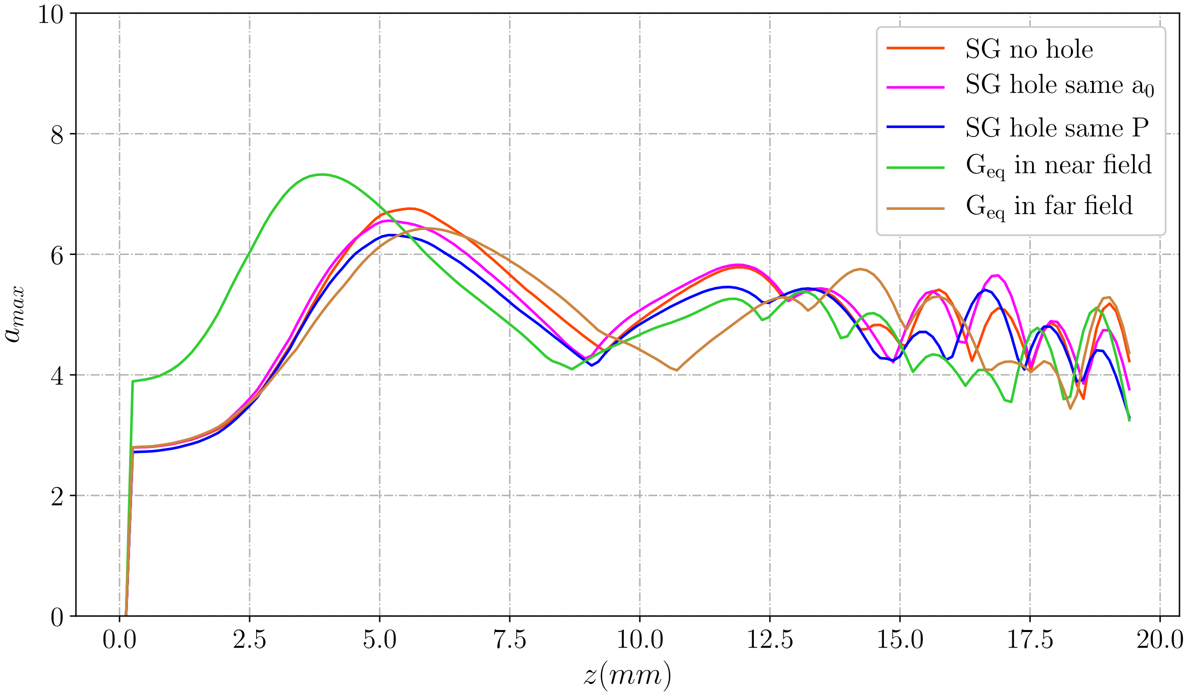

Figure 4.9: Evolution of the peak normalized laser field strength as a function of the propagation distance z.

The evolution of the peak normalized laser field strength as a function of the propagation distance z is depicted in fig. 4.9 for the different simulations. In all the cases, there is a main peak corresponding to a first important self-focusing of the laser at the entrance of the plasma. Then the maximal intensity starts to modulate corresponding to an alternation of focusing and defocusing which is a common behavior in self-guided propagation. The laser in the simulation

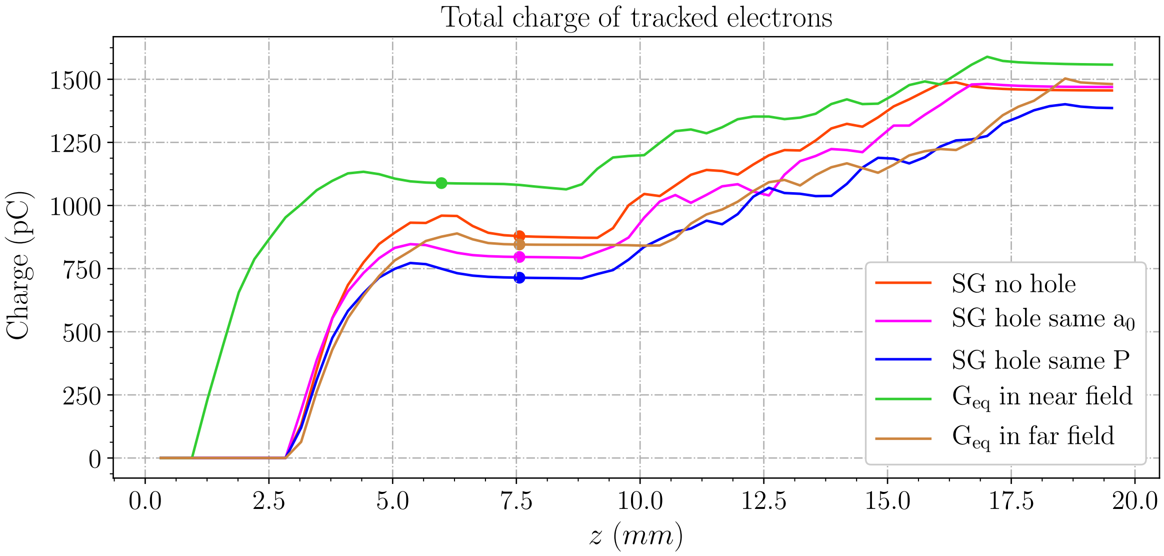

Figure 4.10: Evolution of total charge of tracked particles.

with G$_{eq}$ in near field (green) starts focusing earlier than the others and exhibits a higher main peak due to its higher initial a_0. All the super-Gaussian lasers self-focus almost at the same time in the beginning. Yet, the super-Gaussians with a hole defocus earlier than the SG no hole. On the other hand, the G$_{eq}$ in far field (brown) self-focuses a bit later than them and takes longer to defocus and thus to refocus afterwards. However, the self-modulation of all the lasers becomes comparable beyond 12.5 mm of propagation.

The same initial a_0 for the SG no hole (red) and the G$_{eq}$ in far field (brown) with comparable waists indicate that they have approximately the same power contained in the central part of the laser while the additional power in the case of the SG no hole is contained in the wings. Nevertheless, the SG no hole has a higher maximal intensity in the first self-focusing. Therefore, one can conclude that the energy in the wings of the super-Gaussian contributes to the self-focusing process. It has been previously reported in [Vieira et al., 2012] that super-Gaussian profiles may lead to a more effective self-guiding in the blowout regime. The SG hole (pink) has the same a_0 as the SG no hole (red) and even a higher total power. Yet, with the same radius in the near field, it has a slightly smaller waist. This means that the hole leads to less energy in the central part of the laser and to more energy diffracted in the wings as it can be seen in fig. 4.8. Therefore, the SG hole same a_0 leads to a less important maximal intensity in the first self-focusing phase. This suggests that even though the energy in the wings may contribute to the self-focusing, a high ratio of the maximal intensity in the wings to the main peak intensity may lead to a less intense self-focusing. This is the case for example for the SG hole same a_0 and SG hole same P, where the hole leads to an increase of the energy portion in the wings.

In fig. 4.10, the evolution of the total charge of tracked electrons is plotted. A tracked particle is a particle whose position and momentum are saved and updated for the rest of the simulation once its normalized longitudinal momentum verifies the condition $p_z/m_ec > 50$. Figure 4.11 reports the evolution of the energy spectrum of the tracked electrons as a function of the propagation distance.

The charge of the tracked electrons depends intrinsically on the self-focusing process during the propagation of the self-guided laser. The early self-focusing and the high peak in the normalized laser field strength, in the case of G_{eq} in near field, results in an earlier (around 0.75 mm) but also a more important injection in the beginning of the propagation that can be seen in both fig. 4.10 and in fig. 4.11. The injection in the super-Gaussian cases starts almost at the same time which is 2 mm later than the G_{eq} in near field. The G_{eq} in far field is the last to start the injection, due to the small delay in its self-focusing. All the curves reach a plateau afterwards which means that the injection has temporarily stopped. A second and longer injection in time starts due to the refocusing and modulation of the self-guided lasers, until reaching a second plateau at the end of the propagation towards 20 mm of propagation. However, these three phases do not start at the same time for all the cases. For example, the first injection in the cases where there is a hole stops slightly before the SG no hole because they have a shorter self-focusing duration. Also, the second injection starts first for the G_{eq} in near field then for the super-Gaussians and finally for the G_{eq} in far field.

From fig. 4.11, we can see that the bunch starts to be well established (dQ/dE has an important value and has a narrow extent meaning a low energy spread) around 7.5 mm of propagation for all the simulations except for the one with G_{eq} in near field where the bunch is well established at around a propagation distance of 6.25 mm. These distances, designed by bullets in fig. 4.10, also correspond to the beginning of the first plateau in the total charge of the tracked particles. In order to make sense of the comparison of the bunch characteristics between the different cases, it is essential to consider the bunch-related quantities only after these points when the bunches are properly defined.

Bunch-related quantities

For this set of simulations, the comparison between the bunch-related quantities starts from 6.25 mm of propagation where the bunch is determined using the FWHM bunch definition introduced in chapter 1.

Bunch charge

By comparing the total charge in fig. 4.10 and the bunch charge in fig. 4.13, one can notice that a lot of particles that were tracked are not actually part of the bunch but rather of the dark current [Schroeder et al., 2006]. This is particularly true for the $\mathrm{G_{eq}}$ in near field (green). Despite the fact that it has the highest value of the total charge of tracked electrons, a large part of that charge is outside of the bunch definition. This can be seen in fig. 4.12 which shows the energy spectra of the electrons after 8.5 mm of propagation. The bunches are delimited by the vertical lines corresponding to 2 FWHM around the peak. In the case of the $\mathrm{G_{eq}}$ in near field, the high energy part of the distribution has a low charge that is not included in the defined bunch. On the other hand, the SG no hole (red) has the least dark current and most of the electrons distribution sits inside the delimiting area of the bunch definition.

The injected quantity of charge depends on the evolution of the maximal laser intensity inside the plasma resulting from the self-focusing process which is conditioned to the first order by the power contained in the center of the laser. However, as mentioned before, the power in the wings can also contribute to the self-focusing. For instance, the SG no hole (red) reaches a more important maximal intensity in the first self-focusing phase than the other super-Gaussians with a hole. Therefore, it has a higher bunch charge. This has been also observed in [Michel et al., 2006a] where the authors report that laser profiles exhibiting higher Laguerre-Gauss modes, and thus have a portion of their energy outside the central part, may result in a higher injected charge when they are properly tailored.

The presence of the hole in both cases, where the SG profiles have either the same a_0 or

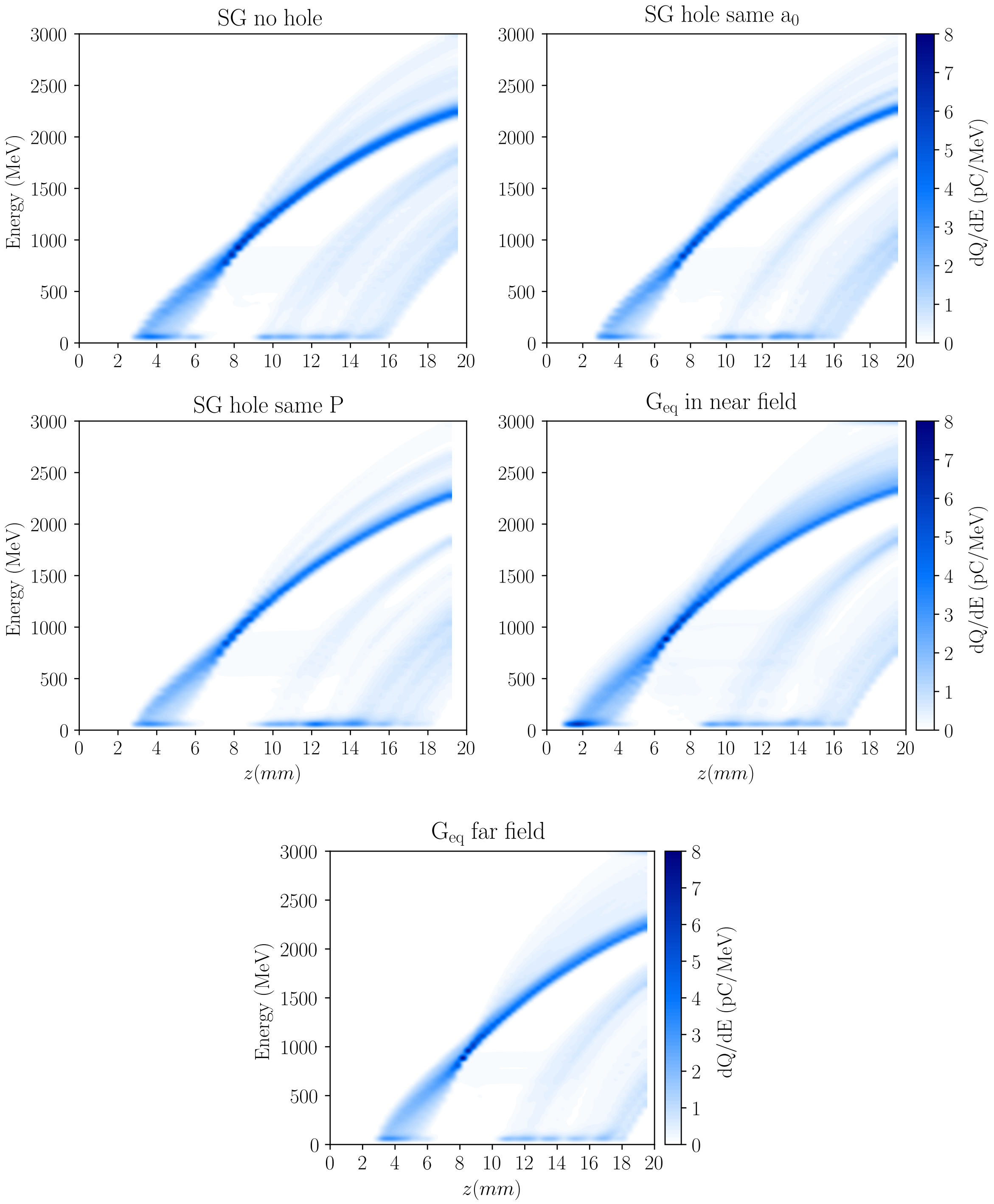
SG no hole

SG hole same a_0

SG hole same P

G_{eq} in near field

G_{eq} far field

Figure 4.11: Evolution of dQ/dE as a function of the acceleration distance z and the energy.

the same power P as the SG no hole, results in a lower bunch charge. Precisely, with the same focusing duration, the SG hole same P (blue) has a lower maximal intensity and thus a lower bunch charge compared to the other SG with hole (pink).

By comparing SG no hole (red) and SG hole same a_0 (pink), one can remark that with almost

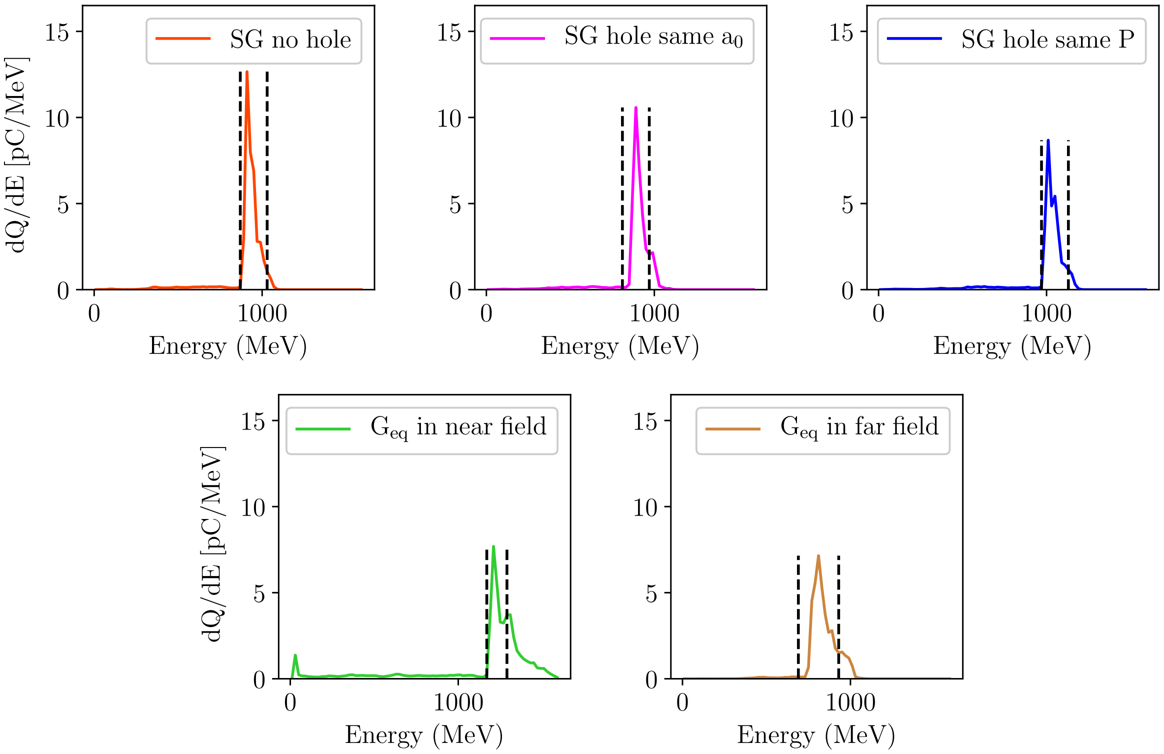

Figure 4.12: Energy spectra of the electron bunches, after 8.5 mm of propagation.

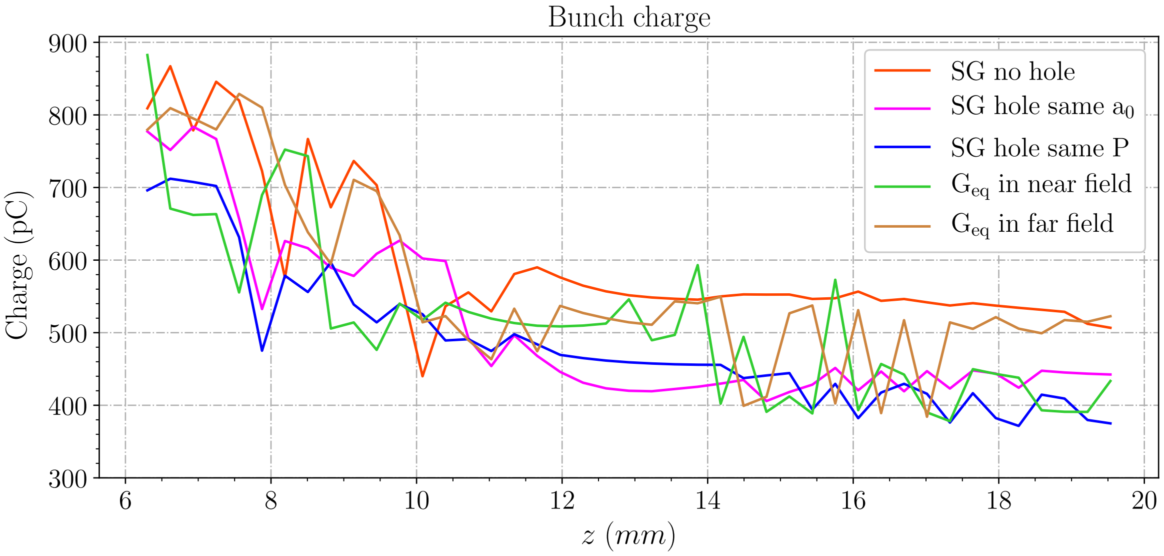

Figure 4.13: Evolution of the bunch charge Q as a function of the acceleration distance z.

the same power contained in the central peak but a higher energy in the wings, the maximal intensity reached with the self-focusing is less important and thus leads to less injected charge. Now, by comparing SG no hole (red) and SG hole same P (blue), one can see that with the same

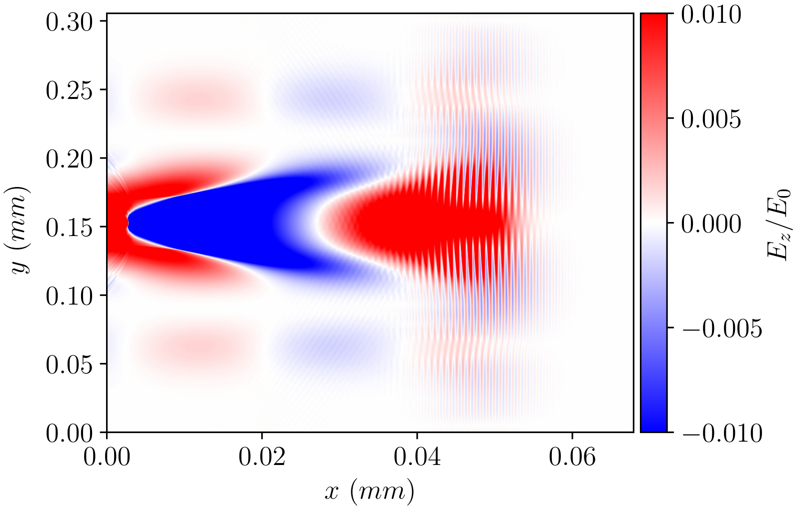

Figure 4.14: Normalized longitudinal electric field colormap of the SG hole same a_0 laser pulse after 3 mm of propagation.

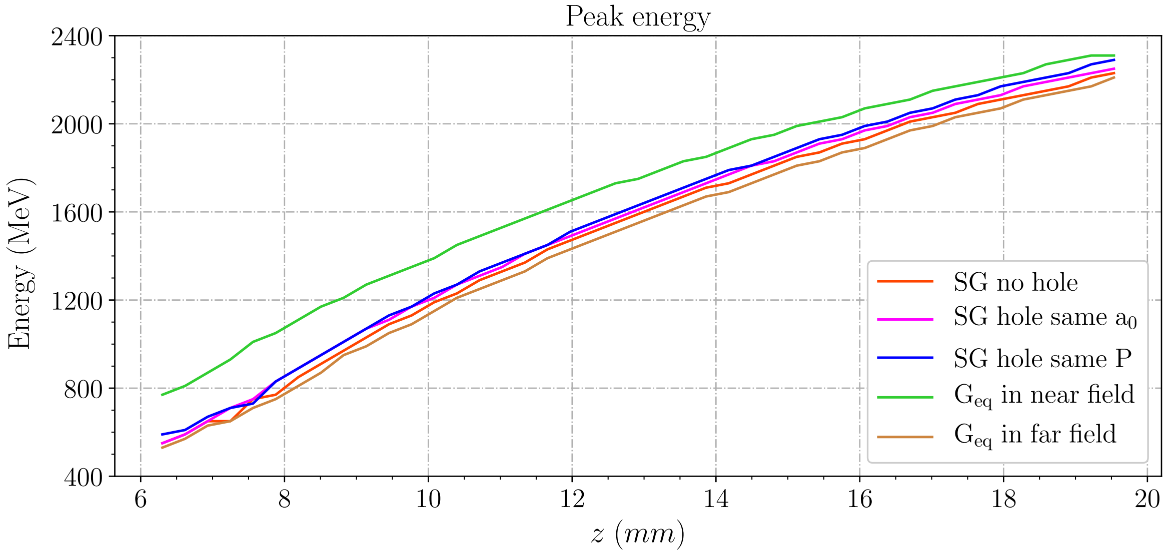

Figure 4.15: Evolution of the bunch's peak energy as a function of the acceleration distance z

total power in the overall laser but with less power in the center and more power in the wings also leads to less efficient self-focusing and thus less injected charge. Since the self-focusing is related to the ratio of the initial maximal intensity in the wings to the initial maximal intensity in the central in the case of super-Gaussians, a high ratio may lead to a less efficient injection. Thus, increasing the fraction of pulse energy contained within the central part of the focal spot while keeping the total energy and central spot size constant, can increase the amount of energy transferred to the wakefield and thus enables a more important injected charge [Genoud et al., 2013]. In fact, when the fraction of energy in the wings is sufficiently important, it can self-focus

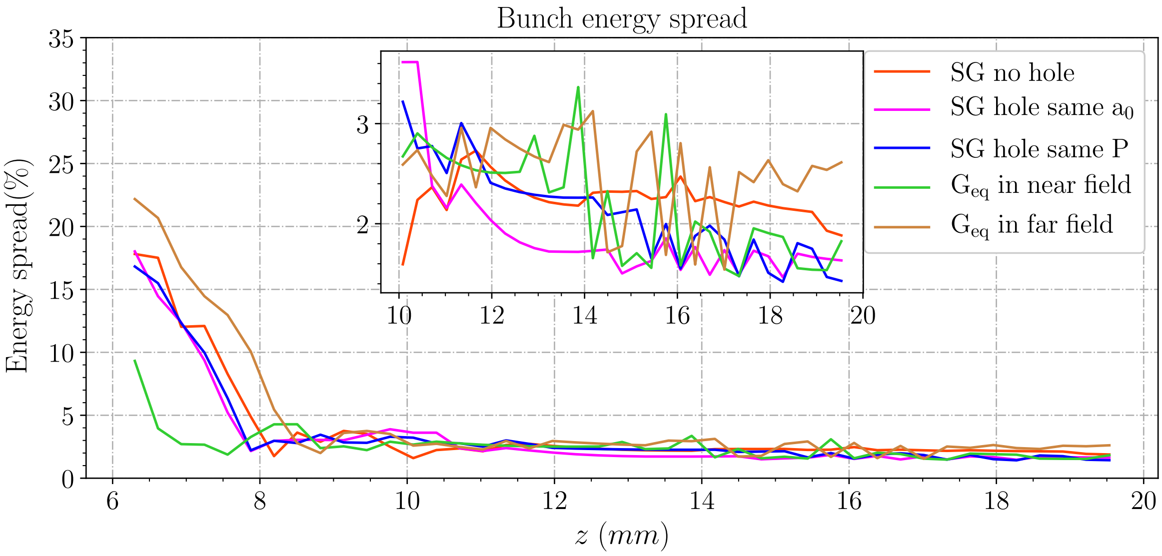

Figure 4.16: Evolution of the bunch's relative energy spread as a function of the acceleration distance z.

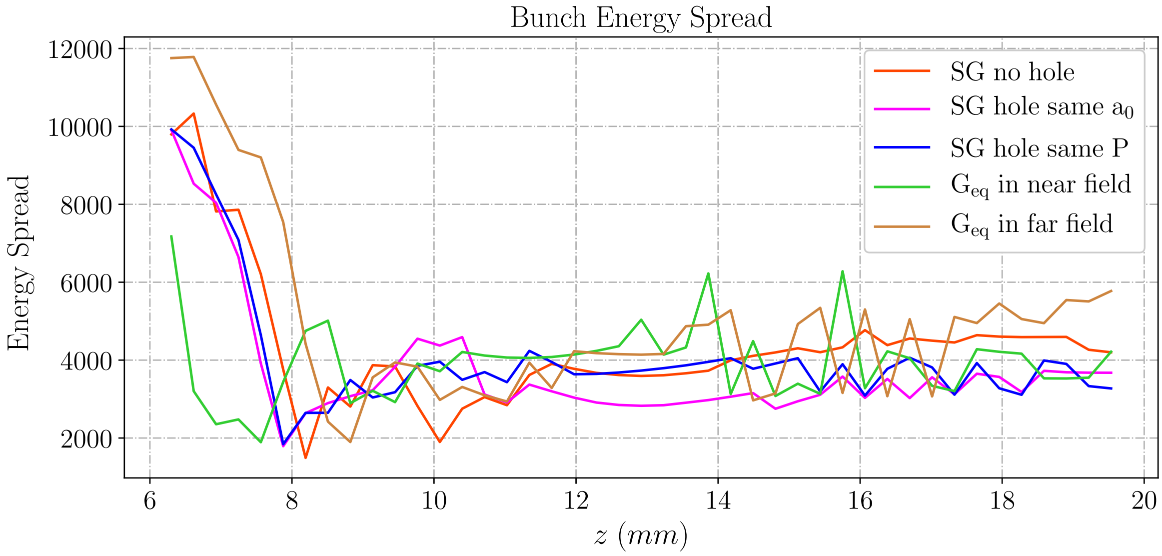

Figure 4.17: Evolution of the bunch's absolute energy spread as a function of the acceleration distance z.

and act like a secondary laser pulse which drives its own wakefield [Nakanii et al., 2016]. This can be seen in fig. 4.14 which displays the colormap of the normalized longitudinal electric field in the case of SG hole same a_0 (pink) around 3 mm of propagation. In this case, the interaction between the wakefield of the main pulse and the wakefield driven by the wings interact together and may lead to instabilities that can lead to a less efficient self-focusing and therefore a lower amount of injected charge.

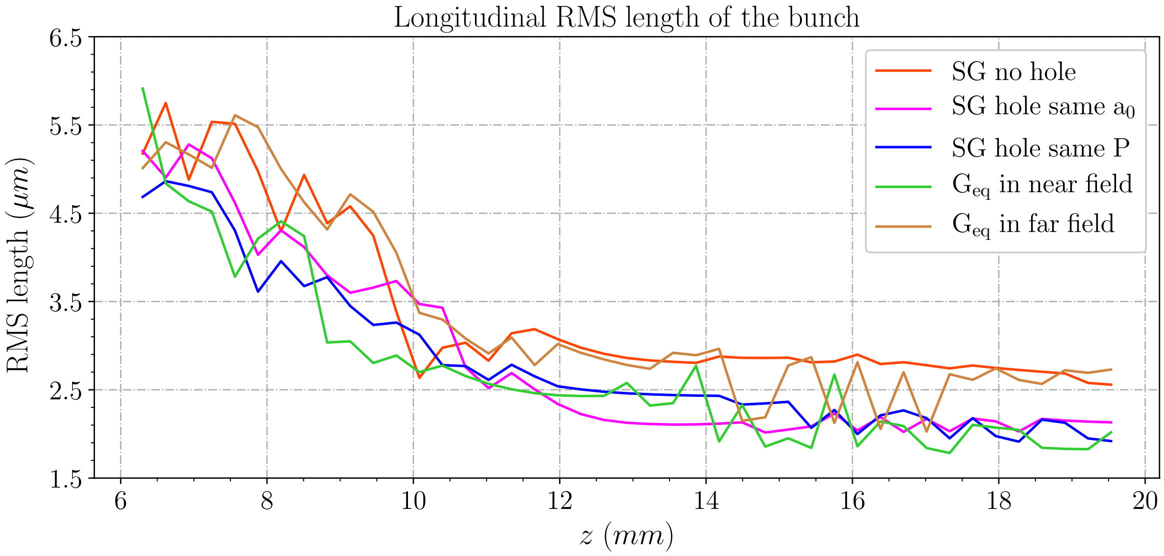

Figure 4.18: Evolution of the RMS longitudinal size of the bunch as a function of the acceleration distance z.

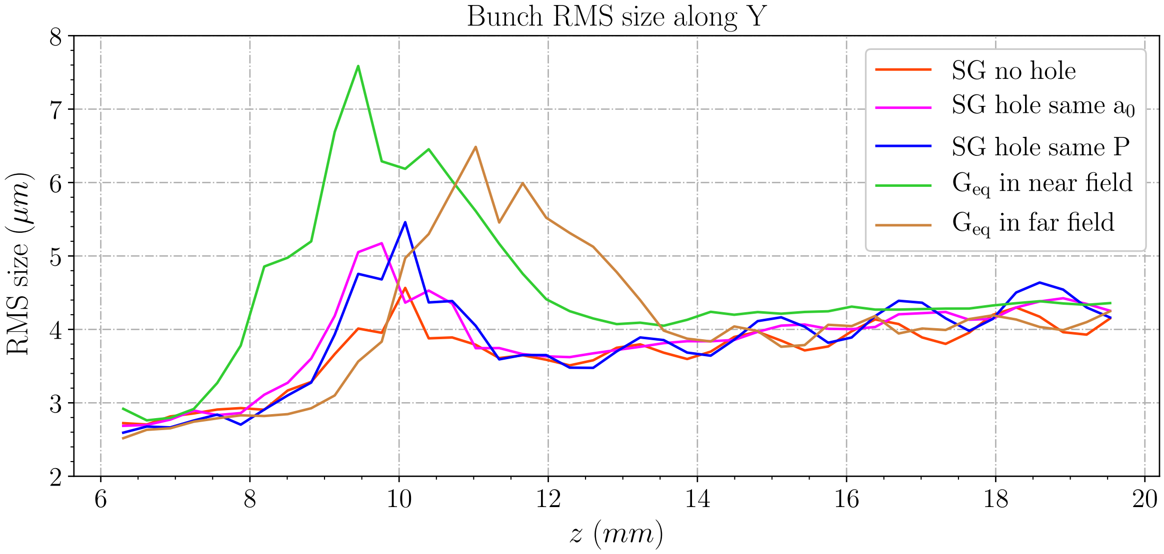

Figure 4.19: Evolution of the RMS transverse size of the bunch in y as a function of the acceleration distance z.

Bunch energy

The peak energy of the bunch presented in fig. 4.15 reflects the efficiency of the energy transfer from the laser to the wakefield and thus to the electrons.

The G_{eq} in near field (green) is the first case where the self-focusing starts and thus the physical processes involved (such as bubble formation) also occur first, which triggers an earlier injection. Therefore, these electrons are accelerated over a longer distance. This explains why

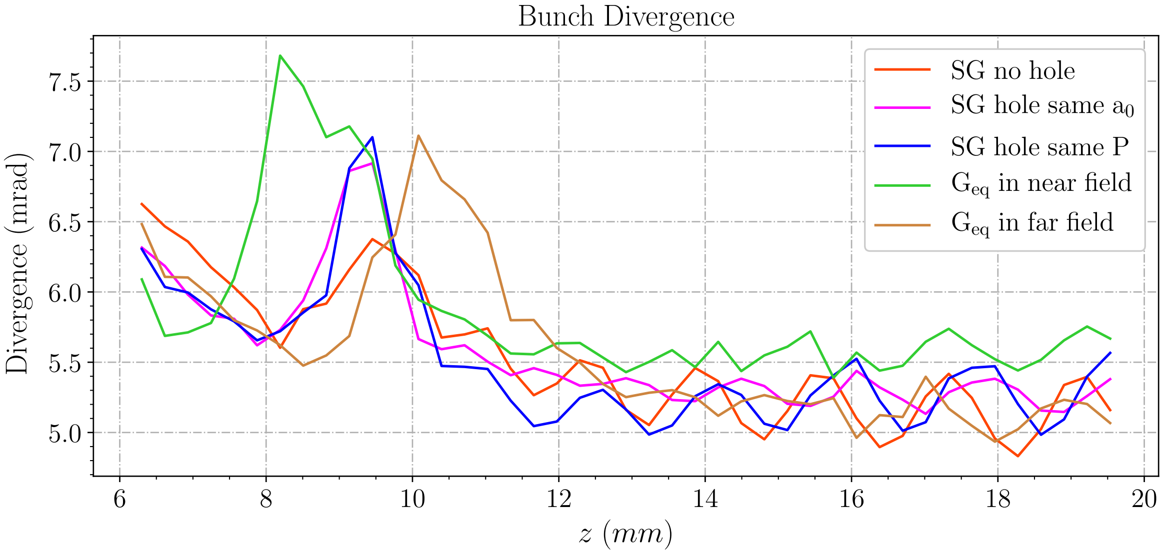

Figure 4.20: Evolution of the bunch's divergence as a function of the acceleration distance z.

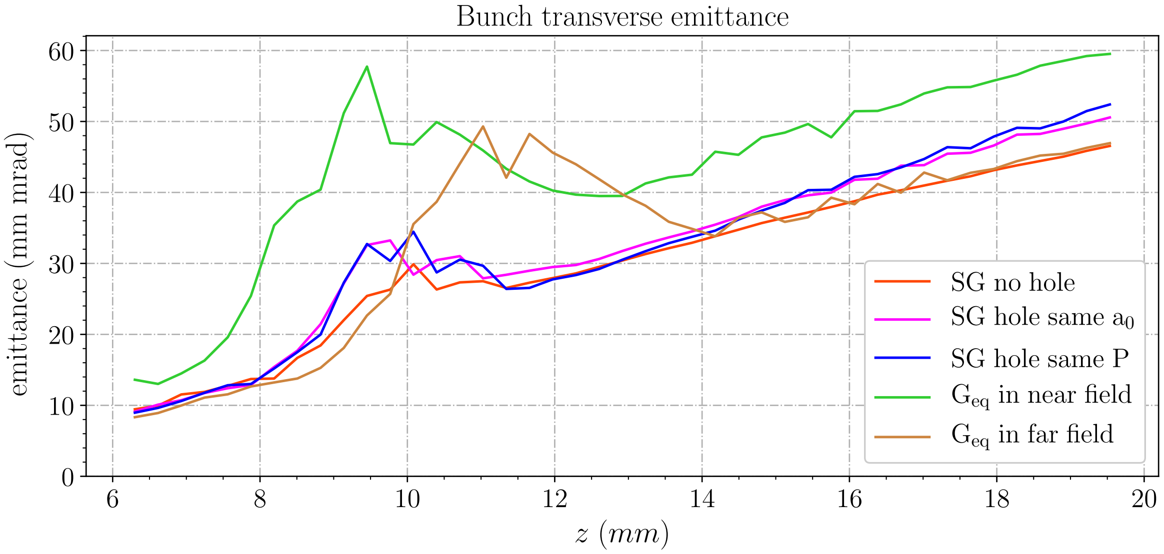

Figure 4.21: Evolution of the bunch's transverse emittance as a function of the acceleration distance z.

in the beginning of the peak energy plot there is a delay between the G_{eq} in near field and the other cases where the injection occurs later. This delay is significantly reduced afterwards for longer acceleration distances.

The trend in the energy peak plot is mainly correlated to the start of the injection. However, the SG hole same P (blue) has the higher energy peak. In fact, in this case the hole seems to help optimizing the conditions for wake excitation. The portion of the laser pulse laying in the wings modifies, by its driven wake, the bubble properties and therefore enhance its accelerating field in some cases [Vieira et al., 2012; Lu et al., 2006b].

Transverse quality of the bunch

In fig. 4.17, the absolute energy spread is increasing with the propagation distance z. However, the relative energy spread (fig. 4.16) corresponding to the absolute energy spread divided by the bunch's peak energy decreases, because the peak energy E_{peak} (fig. 4.15) increases.

The increase in the absolute energy spread in this scenario is explained by the fact that the resulting bunches are relatively long ($\sim 2.5\ \mu m$). Due to the difference between the accelerating field experienced by the front and the back of the bunch, the energy spread tends to increase. In fact, the electrons situated at the back of the bunch experience a higher accelerating field and they already have a higher energy. This is confirmed by comparing the trend in the longitudinal rms-length of the bunch (fig. 4.18) and the absolute or relative energy spread (fig. 4.17 and fig. 4.16) between the different laser profiles. For instance, the SG no hole (red) has the longer bunch and the most important energy spread among all. From fig. 4.18, we can also see that the presence of the hole leads to a shorter bunch and hence a better energy spread. In fact, the hole causes the injection to stop earlier. Therefore, a shorter injection in time leads to a shorter bunch.

The decrease in the longitudinal rms bunch size can be explained by the rotation of the bunch in phase-space (z, p_z) which in return is also responsible for the energy spread growth. In fact, electrons at the back of the bunch have a higher energy and a higher velocity thus slowly catch up with the electrons at the front.

The different bunch-related quantities increase suddenly around $10 - 12\ mm$ of propagation with some delay between the different cases. This increase corresponds approximately to the beginning of the second self-focusing as it can be seen in fig. 4.9. In fact, the second injection is the consequence of a change in the bubble structure. Accordingly, the accelerating and focusing fields felt by the electrons in the bubble also change abruptly which affects the properties of the bunch such as its divergence, transverse size and emittance.

However, this effect vanishes later when the fast modulations start. One can see that these modulations from the successive focusing and defocusing lead also to modulations in the properties of the bunch. This can be confirmed by comparing the period of the two modulations ($\sim 2\ mm$). This is also related to the FWHM bunch definition which is very sensitive to the fast variations in the electrons energy spectrum resulting themselves from the laser modulations.

Due to these modulations, it is hard to distinguish clearly the impact of the hole or the non-Gaussian features on the divergence and on transverse size of the bunch except for the G_{eq} in near field (green) which has the highest values. The SG hole same P (blue) has a slightly more important transverse size and divergence in its bunch.

Finally the transverse emittance, which is an important key parameter to estimate the bunch's transverse quality is illustrated in fig. 4.21. It concatenates the energy spread, the divergence and the transverse bunch size in one relevant quantity.

We recall the expression of the normalized emittance:

$$\epsilon^2_{x,n,rms} = \frac{\Delta E^2}{m_e^2 c^4} \sigma_x^2 \sigma_x'^2 + \langle\gamma\rangle^2 \epsilon^2 \tag{4.11}$$

where ΔE is the energy spread, σ_x is the bunch size, σ'_x is its divergence, $\langle\gamma\rangle$ is the average relativistic factor and ϵ is the un-normalized emittance, one can analyze the correlation between these terms for the previous plots.

In conventional accelerators, the first term is negligible and $\epsilon^2_{x,n,rms} \approx \langle\gamma\rangle^2\epsilon^2$ and remains almost constant thanks to the small value of the energy spread and divergence. However, this is not the case in LWFA where the first term becomes the leader one because of the high values of the energy spread and in the divergence of the produced bunches.

From fig. 4.21, the two cases of the super-Gaussian with a hole (blue and pink) have a more important slope and a higher emittance compared to the SG no hole (red) or G_{eq} in far field (brown) cases. Therefore the hole leads to a slightly worse overall quality of the bunch in the case of long propagations.

4.2.4 Conclusions

From the previous results, lasers exhibiting high-order Gaussian profiles may lead to a better self-focusing and thus to higher bunch charges. However, when the ratio of the maximal intensity in the wings to the intensity in the center of the pulse becomes important, it can lead to less efficient self-focusing and therefore less charge. This is the case for example with the lasers presenting a hole where the hole leads to a more important energy diffracted in the wings.

In fact, the hole in the Apollon laser leads to a shorter self-focusing thus a shorter injection. This results in a shorter bunch with a lower energy spread. The hole also leads to a higher divergence and promotes the transverse emittance growth. Nevertheless, the results are not drastically different and the hole influence is not very important over a long propagation distance like the one presented in this study. Therefore, this technical choice in the design of the Apollon laser is justified at the cost of a small degradation in the bunch quality.

4.3 Influence of experimental laser imperfections on laser wakefield acceleration

4.3.1 Motivation

Laser wakefield acceleration (LWFA) has been demonstrated as an established technique for accelerating electrons efficiently via the interaction of a femtosecond-scale laser pulse with a plasma. The continuous progress in increasing the laser power made it possible to exceed the critical power for relativistic self-focusing [Sun et al., 1987] ($P/P_c > 1$), hence the laser pulses can be self-focused over several Rayleigh lengths. The region where the laser is self-focused triggers a highly nonlinear plasma wave in which plasma electrons are trapped and accelerated to relativistic energies in millimeter distances. Nowadays, the highest acceleration gradients are reached in the bubble regime (section 1.4.2) allowing the generation of multi-GeV electrons. Owing to its simplicity, self-injection (section 1.5.2) is definitely the least experimentally demanding [Benedetti et al., 2013], thus the most commonly used mechanism to produce multi-GeV electrons [Malka, 2013].

However, the self-injection technique offers little control on the injection process because it is very sensitive to both the conditions of the plasma and laser. One major limitation of the particle accelerators based on this technique, compared to conventional accelerators, is the shot-to-shot reproducibility of the beam charge, energy and emittance. The injection process is a key factor to determine the final bunch properties. This emphasis the importance of establishing a more stable and controllable self-injection in order to generate laser-driven electron bunches that meet the requirements in terms of high charge, low emittance and low-energy spread simultaneously.

The improvement of this injection scheme relies intrinsically on understanding the sensitivity of the accelerator's performance to deviations from the ideal physics. In fact, tightly focused femtosecond laser pulses used to accelerate the electrons from the plasma have a complicated structure with asymmetries in the laser's focal spot, aberrations in the wave front and variations in the temporal profile of the pulse. These imperfections affecting the laser pulse propagation [Kaluza et al., 2010; Glinec et al., 2008], also affect the self-injection processes and may lead to poor bunch quality [Ferri et al., 2016; Vieira et al., 2012]. Nevertheless, it has been demonstrated that laser profiles exhibiting higher order Laguerre-Gauss modes may lower the self-trapping thresholds when they are properly tailored [Michel et al., 2006a] and that laser profile imperfections can promote the production of betatron oscillations [Glinec et al., 2008; Mangles et al., 2009; Ferri et al., 2016].

Kinetic simulations provide an ideal venue to investigate and help understanding the response of the LWFA to laser imperfections as it allows to deliberately control the shape of the introduced laser pulse and its associated phase.

So far, most of the theoretical and numerical studies dealing with realistic laser pulses used either higher order Laguerre–Gaussian transverse profiles [Vieira et al., 2012; Genoud et al., 2013] or theoretical fits of the experimental measure: a combination of two Gaussian pulses with the same duration was used in [Nakanii et al., 2016] to mimic the halo effect by shifting the center of the second lower-energy pulse from the axis of the first pulse in the transverse direction. In [Maslarova et al., 2019], the laser beam has been chosen to fit a profile that reaches the super-Gaussian in the focus and in [Cummings and Thomas, 2011] the presence of comatic aberration is modeled by modifying a Gaussian pulse and adding some terms from the expansion of Bessel functions and Zernike Polynomials in the diffraction integral.

In this section, the impact of realistic laser imperfections on the electron bunch formation by the self-injection technique in the bubble regime, is studied numerically via fully relativistic particle-in-cell (PIC) simulations. In this study, the experimental wave front measured in the Apollon laser as well as its intensity profile are included in the simulation and their influence is studied by comparing the results to that of a theoretical fit of the intensity profile with a super-Gaussian along with a flat wave front. Firstly, the simulations carried in 3D Cartesian geometry are compared to evaluate the impact of the laser aberrations on the bunch properties. Subsequently, the same simulations are reproduced in the quasi-cylindrical geometry while varying the number of modes. Then, the sensitivity of the results to the inclusion of higher modes is investigated, by comparing them to the 3D reference simulations.

4.3.2 Effect of realistic laser profiles on 3D Cartesian simulations

In order to enlighten the origin of some trends that may be found in the future experiments of LWFA with the Apollon laser, 3D Cartesian simulations are performed in the bubble regime with the self injection scheme for different laser profiles. In the first scenario, the experimental measure of the intensity laser profile is fitted with a super-Gaussian of order 4 and a flat wave front is assumed. In the second case, the same super-Gaussian fit is used but with the measured wave front. Finally, both the experimentally measured intensity profile and wave front are used.

In the following, first the method of realizing the experimental acquisition and the numerical settings are described. Then, the simulation results on the laser propagation and focusing as well as the electron injection and acceleration are compared. Finally, the influence of the realistic parameters on the simulation are discussed and the conclusions are stated.

Experimental data acquisition and numerical modeling

The experimental data measurement was carried using the Apollon laser facility in Saclay, France. The laser system delivers a linearly polarized pulse of 0.8 μm wavelength with a 25 fs FWHM

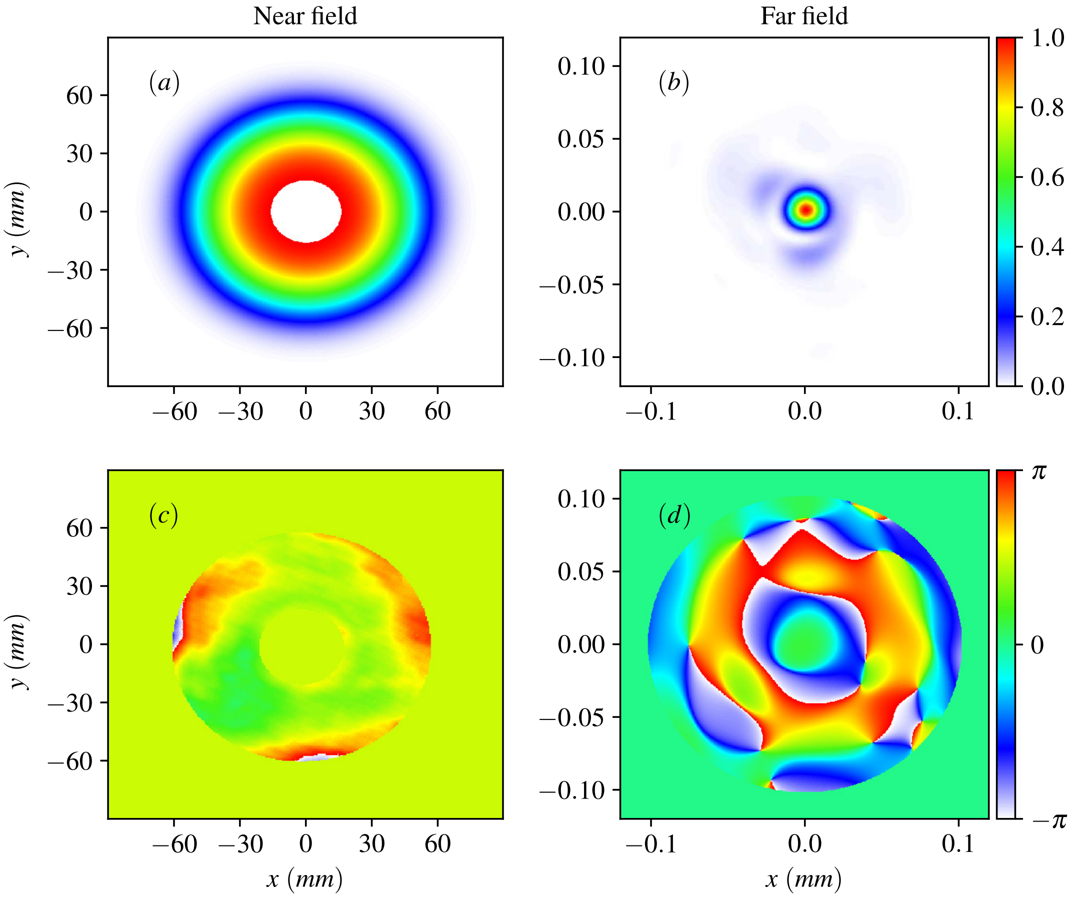

Figure 4.22: (a) and (c) are respectively the super-Gaussian fit SG_4 of the intensity profile and the measured wave front in the near field corresponding to (b) and (d) in the far field at $z = f - 5 \times 10^{-4}$ m.

duration and a total energy of 15 J corresponding to 600 TW power. The experimental results were obtained in the near field after the reflection on the mirror with the hole represented in fig. 4.4.

From shot to shot, the intensity profile in the near field does not vary that much while the wave front does fluctuate. Therefore, The wave front measurement is averaged on over $10 - 100$ shots to have a representative case of the Apollon beam systematic defaults. Note that spatio-temporal distortions i.e spatial dependencies of the temporal properties are not taken into consideration and that the wave front is also averaged over its spectrum.

The raw data from the camera in the near field was interpolated into the computational grid using a quadratic interpolation function taking into account the number of pixels of the camera and the pixel size. Using Fresnel diffraction described in section 4.1, the laser profile in the near field is then focused and propagated up to the far field at the beginning of the plasma target $z = f - 5 \times 10^{-4}$ m where f denotes the focal length of the spherical mirror. Given the information about the laser intensity profile and phase, Fresnel propagation allows a correct calculation of the laser field at any point close enough to the focal plane. Apollon facility offers the possibility of using two focal lengths of 3 m and 9 m. For the upcoming results, the study is carried with the focal length of 3 m, resulting in a tightly focused laser spot size $w_0 \sim 15.5 \approx \mu m$

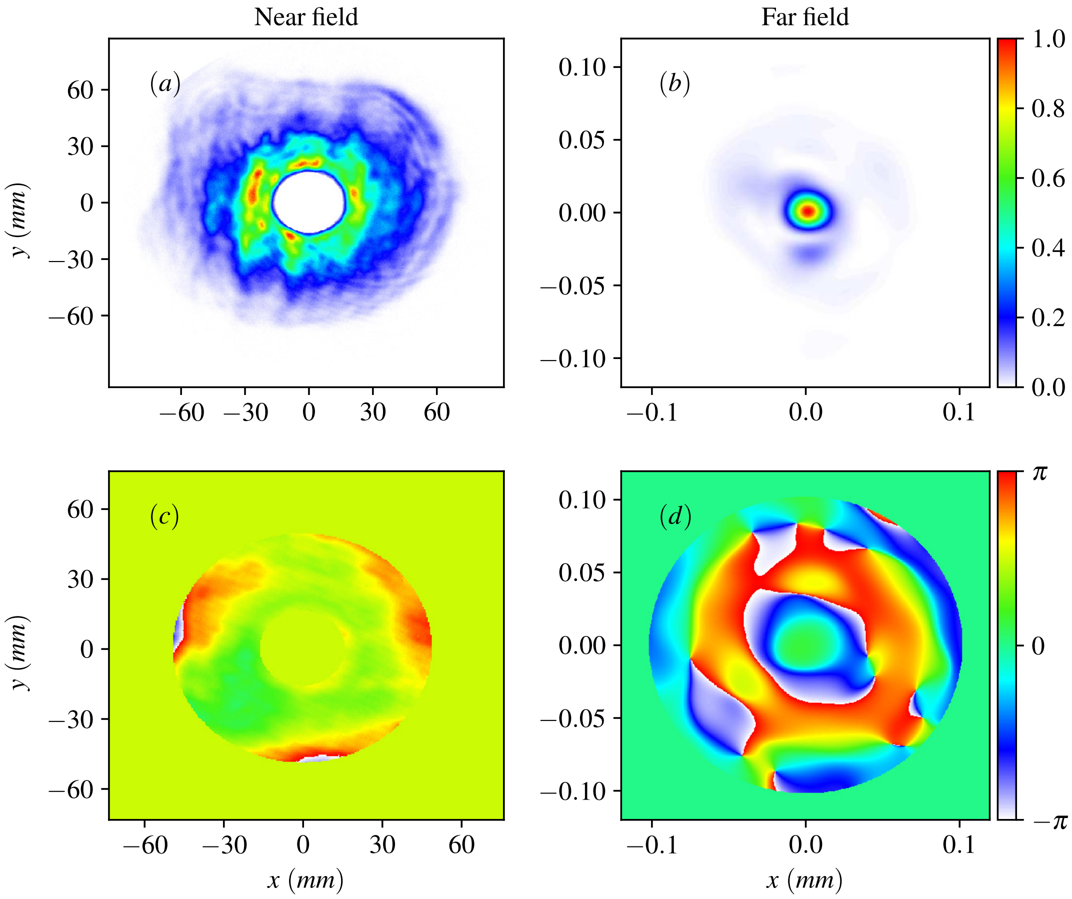

Figure 4.23: (a) and (c) are respectively the experimentally measured intensity profile and wave front in the near field corresponding to (b) and (d) in the far field at $z = f - 5 \times 10^{-4}\ m$.

which corresponds to a $\mathrm{FWHM_I} \approx 25.8\ \mu m$.

The intensity profile and the corresponding wave front are shown in near field and far field for the case of super-Gaussian fit with the measured wave front in fig. 4.22 and for the case of the measured intensity and wave front in fig. 4.23.

In the following, the three cases are referred to as: $\mathrm{SG}_4 + \phi_{\mathrm{flat}}$ for the super-Gaussian fit of order 4 assuming a perfectly flat wave front (null phase), $\mathrm{SG}_4 + \phi_{\mathrm{measured}}$ for the super-Gaussian fit of order 4 with the measured wave front and $\mathrm{I} + \phi_{\mathrm{measured}}$ for the experimentally measured intensity and wave front.

In all the three configurations, the laser beams have the same duration and contain the same total energy which corresponds to the remaining energy after the reflection on the mirror with the hole where a fraction of the energy is lost ($\sim 12\%$). Their waists are also kept close to each other by adequately fitting the super-Gaussian profile to the intensity measurement in the near field, so that only the introduction of the measured wave front and imperfections in the intensity profile are responsible for the differences observed in the results.

The 3D cartesian PIC simulations with the different transverse laser profiles are carried out using the code Smilei in a $6400 \times 640 \times 640$ moving window with cell dimensions of $0.1\ c/\omega_0$ in the longitudinal direction and $2.5\ c/\omega_0$ in the transverse direction and 4 particles per cell. The simulations start with the laser at $z = f - 5 \times 10^{-4}\ m$ so that the focal plane is situated at the end of the 500 μm rising ramp of the pre-ionized plasma plateau of an electronic density $n_e = 8.6 \times 10^{17}$ cm^{-3}. The simulation results are compared up to 1.9 mm of propagation corresponding to $\sim$ 2 Rayleigh length ($Z_r \simeq 0.94$ mm). This distance is limited by the end of the self-guiding.

Laser focusing and electron acceleration results

First, we start investigating the evolution of the energy spectrum of the trapped electrons. An example for the three simulations after a propagation of 1.9 mm is shown in fig. 4.24. The first remarkable difference between them is the presence of a low charge high energy bunch of electrons only in the case of $\mathrm{SG}_4 + \phi_{\mathrm{flat}}$ which is probably originating from an early longitudinal injection [Corde et al., 2013].

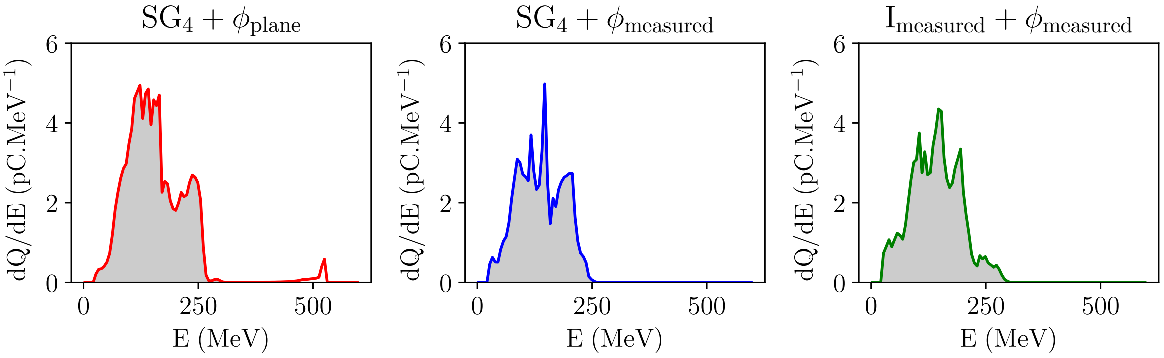

Figure 4.24: Energy spectrum of the electron bunches, after 1.9 mm of propagation. The shaded areas in grey correspond to the selected parts for which the bunch-related quantities are evaluated and compared.

In order to accurately compare the quantities related to the different resulting bunches, this first longitudinal injection is neglected as it entirely vanishes in the two other simulations. In the following analysis, the bunch-related quantities are evaluated only for the main high charge bunches designated by the grey shaded area in fig. 4.24.

To begin, the focusing effect of the different lasers is examined by plotting the evolution of the peak normalized laser field strength a_{max} as a function of the propagation distance fig. 4.25. In all cases, the maximal intensity first increases when the laser self-focuses at the entrance of the plasma, then decreases when the laser is defocused. However, the laser is not well self-guided later in the plasma and diffracts quickly which limits the acceleration length to 1.9 mm in these simulations.

The self-focusing process begins approximately at the same time for the different profiles. Nevertheless, the initial value of a_0 is lower when the experimental features are introduced ($a_0 \simeq 7.5$ for $\mathrm{SG}_4 + \phi_{\mathrm{flat}}$, 6.5 for $\mathrm{SG}_4 + \phi_{\mathrm{measured}}$ and 6.75 for $\mathrm{I}+\phi_{\mathrm{measured}}$). The transverse laser profiles in the far field presented in fig. 4.26 being different, the laser intensity peak is also different in these three cases.

This difference is due to the diffraction of a portion of the laser energy in the wings, out of the central spot, when it propagated from the near field to the far field. Thus, this fraction of energy does not contribute initially to the maximal intensity leading to a less important initial a_0.

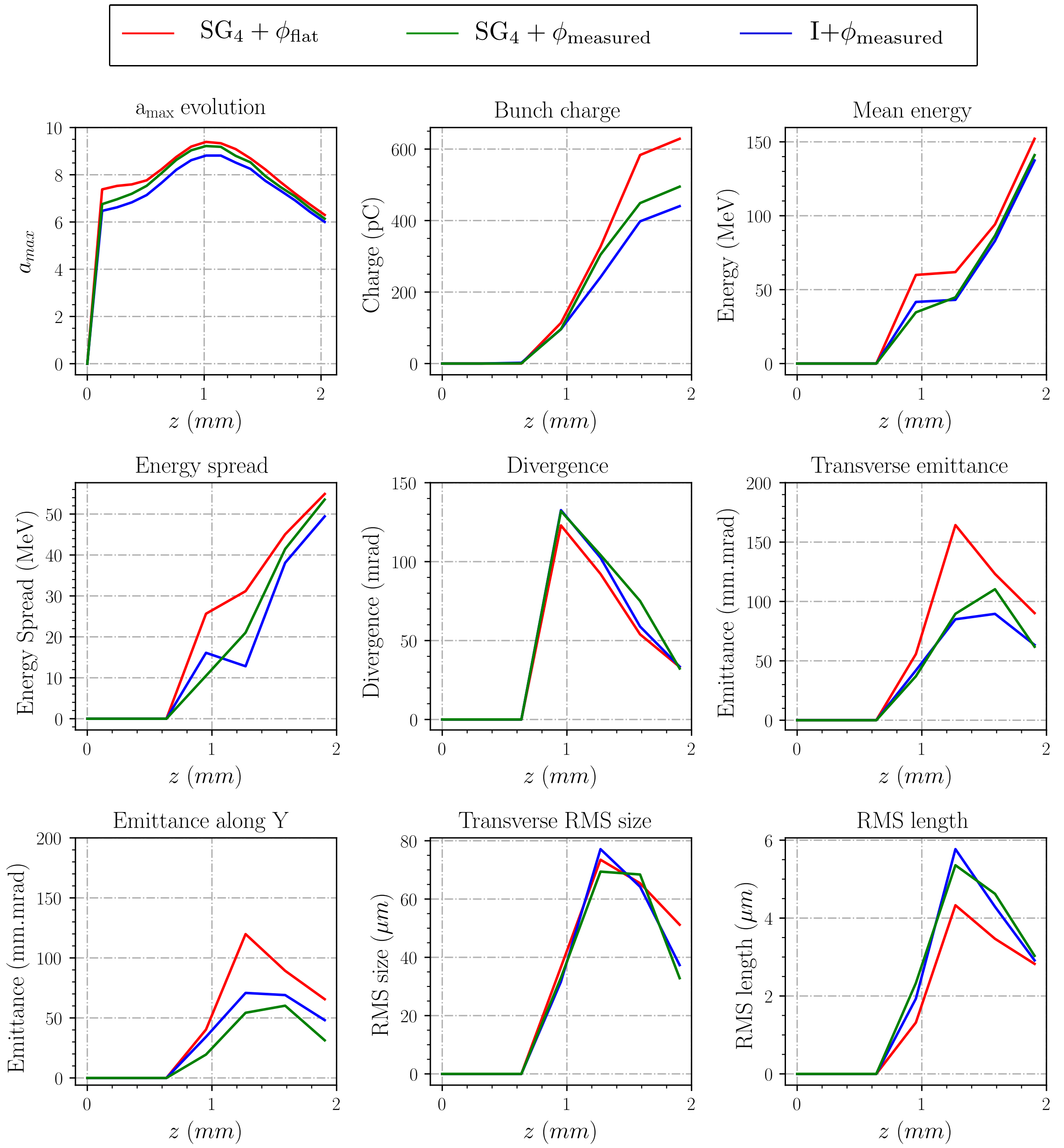

Figure 4.25: The *top left panel* shows the evolution of the peak normalized laser field strength a_{max}. The other panels show the evolution of the bunch-related quantities as a function of the propagation distance z.

With the same initial power in the near field and a similar spatial distribution of the laser in far field, the small difference in the initial a_0 between $SG_4+\phi_{\text{measured}}$ and $I+\phi_{\text{measured}}$ is explained by a compensation of the diffracted portion of the laser power in the wings introduced by the inhomogeneities in the intensity profile. In fact, in the case of $I+\phi_{\text{measured}}$ the correctly focused area from the near field carries in average more intensity compared to the case of $SG_4+\phi_{\text{measured}}$.

Due to the introduction of the realistic wave front, the laser self-focusing evolution is modified.

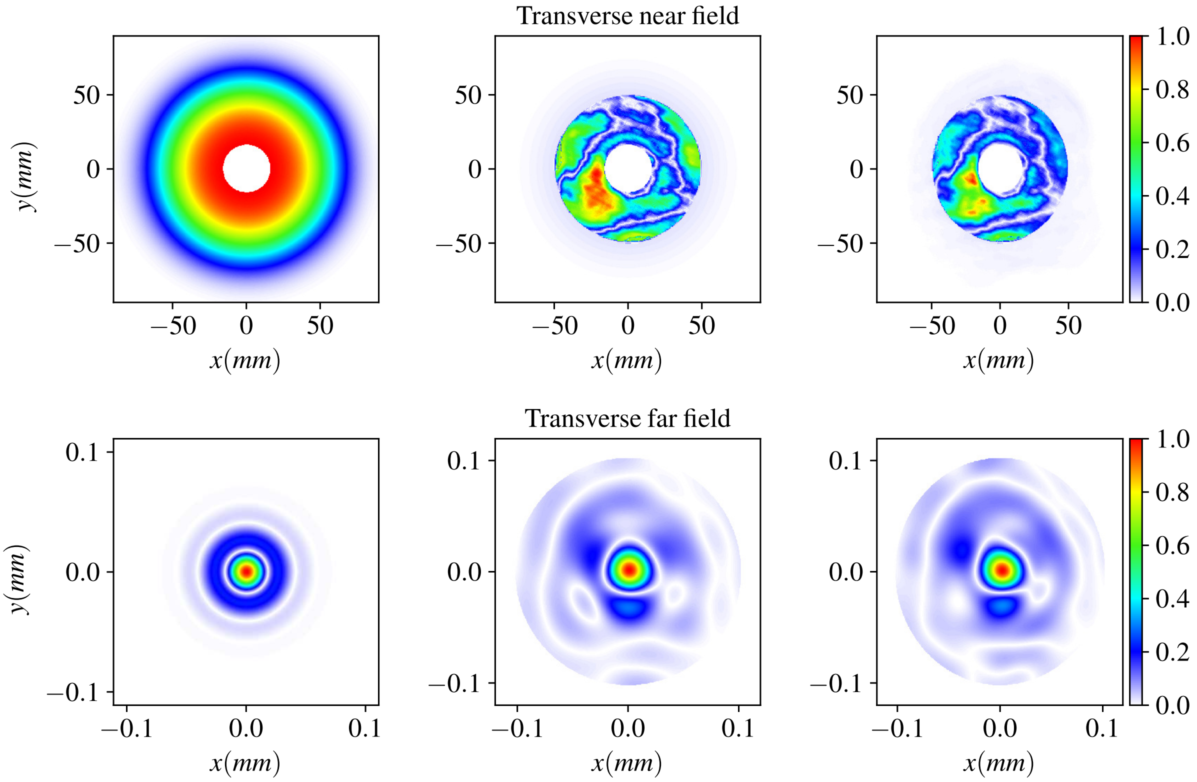

Figure 4.26: From left to right: the laser transverse field of the $SG_4 + \phi_{\text{flat}}$, $SG_4 + \phi_{\text{measured}}$ and $I{+}\phi_{\text{measured}}$ in near field (*top panels*) and in far field at $z = f - 5 \times 10^{-4}\ m$ with $f = 3\ m$ (*lower panels*).

Despite the difference in the initial value of a_0, the laser self-focusing is quicker when the realistic wave front is introduced in either $SG_4{+}\phi_{\text{measured}}$ or $I{+}\phi_{\text{measured}}$ (note the difference in the slope). In fact, the initial gap in the intensity between $SG_4 + \phi_{\text{flat}}$ and the realistic profiles is gradually reduced during the self-focusing, suggesting that a part of the energy contained in the outer part is actually self-focused and guided by the plasma. Therefore, it eventually contributes to the physical processes involved in LWFA like bubble formation and electron acceleration. The maximal intensity with realistic features reaches a comparable, yet slightly inferior, value to the one found with a flat wave front. The effect of the portion of the laser pulse energy situated out of the focus spot, referred to as *halo effect* has been investigated experimentally and numerically in [Nakanii et al., 2016]. In their paper, they demonstrate that the halo of the pulse can be self-focused and thus can also contribute in the self-injection process, given that it has enough power itself.

The gap in the initial a_0 between $SG_4 + \phi_{\text{measured}}$ and $I{+}\phi_{\text{measured}}$ is conserved during the focusing phase of the laser. However, it is slightly reduced during the defocusing phase. This suggests that the wave front effect is dominant compared to imperfections related the intensity profile.

Because of the lower intensity peak in the realistic profiles during their propagation in the plasma, the effective energy transferred from the laser into the plasma is less important resulting in the generation of a wakefield with a lower amplitude. Even though the energy in the wings of laser spot is partially self-focused, the rest of it is actually wasted and not coupled into the plasma wave [Genoud et al., 2013]. Therefore, the quantity of the injected charge is less important when the imperfections of the experimental laser is added ($\sim 30\%$ less than $\mathrm{SG}_4 + \phi_{\text{flat}}$). Since the simulations are carried in the blow-out regime, electrons are almost completely expelled from the region behind the laser pulse around its propagation axis. As a result, an ion cavity surrounded by an electron sheath is formed behind the pulse. This sheath creates a separation between the bubble and the surrounding plasma and bends the laser-pulse wave fronts outwards for $r \gtrsim w_0 \sim R_b$, and inwards for $r \lesssim w_0 \sim R_b$ (R_b is the maximal radius of the bubble). Hence, the blowout region acts as a spatial filter of the laser pulse by confining the main pulse only while the rest of the pulse is lost via diffraction and pump depletion and does not contribute to electrons acceleration [Vieira et al., 2012].

Besides, by looking at the different quantities related to the bunch properties in fig. 4.25 around 1.6 mm of acceleration, one can see that the laser imperfections lead to some differences in the quality of the bunch. The inhomogeneities in the laser pulse lead to a distorted wakefield whose focusing and defocusing properties may affect the electron distribution. As a consequence, the corresponding distribution of accelerated electrons is less collimated than that in the case of $\mathrm{SG}_4 + \phi_{\text{flat}}$. Despite the lower injected charge, the realistic profiles lead to a slightly higher value of divergence.

By evaluating the terms in eq. (4.11), the transverse emittance is rather governed by the energy spread for these cases. As a result, the same trend is found in the energy spread and the transverse emittance. For example $\mathrm{SG}_4 + \phi_{\text{flat}}$ has the highest value of energy spread and thus of transverse emittance. Counter-intuitively, the laser imperfections in this case lead to an enhanced transverse beam emittance particularly in the $y-$direction where the profiles are more distorted in far field. This has been also observed in the simulations conducted in [Cummings and Thomas, 2011] where the wings are referred to as coma aberration. This enhancement can be explained by the difference in the quantity of injected electrons. The aberrations introduced by the experimental profiles also drive a longer bunch yet smaller transversely.

The differences in the quantities indicating the quality of the bunch are considerably reduced afterwards around 1.9 mm of acceleration especially between the $\mathrm{SG}_4+\phi_{\text{measured}}$ and $\mathrm{I}+\phi_{\text{measured}}$. This puts forward the sensitivity of the electron beam distribution to the laser wave front rather than the intensity profile itself [Beaurepaire et al., 2015]. In fact, by examining closely the transverse laser profiles in the far field of $\mathrm{SG}_4 + \phi_{\text{measured}}$ and $\mathrm{I}+\phi_{\text{measured}}$, there is an important resemblance between the far-field laser profiles in the two cases. Therefore, most of the spatial inhomogeneities are rather dictated by the laser wave front distortions.

It also demonstrates the role of the plasma to filter the spatial asymmetries of the transverse wakefield by homogenizing it during the laser propagation. Indeed, the halo of the pulse once self-focused, gives rise to its own wakefield. Because of the difference in the size between the halo and the main laser pulse, the angle of the generated wakefield is different and the interaction between the different wakefields induces some instability at the beginning.

However since the energy contained in the wings is way lower than that of the central part, it is quickly depleted in the plasma leading to a smoother propagation afterwards when the fraction of this energy is dissipated in the plasma. Therefore, the broad distribution of the electrons beam becomes more collimated and its divergence is decreased under the effect of the strong self-focusing field inside the bubble. This is illustrated in fig. 4.27a and fig. 4.27b which show the normalized transverse laser field $E_\perp/E_0$ with $E_\perp = \sqrt{E_x^2 + E_y^2}$ and $E_0 = m_e c\omega_0/e$ and the transverse electron distributions in (θ_x, θ_y) for respectively 1.2 mm and 1.9 mm of propagation.

Figure 4.27b shows that the aberrations in the transverse wakefield are self-corrected by the plasma response, leading to a stable propagation and little deviation in the electron distributions.

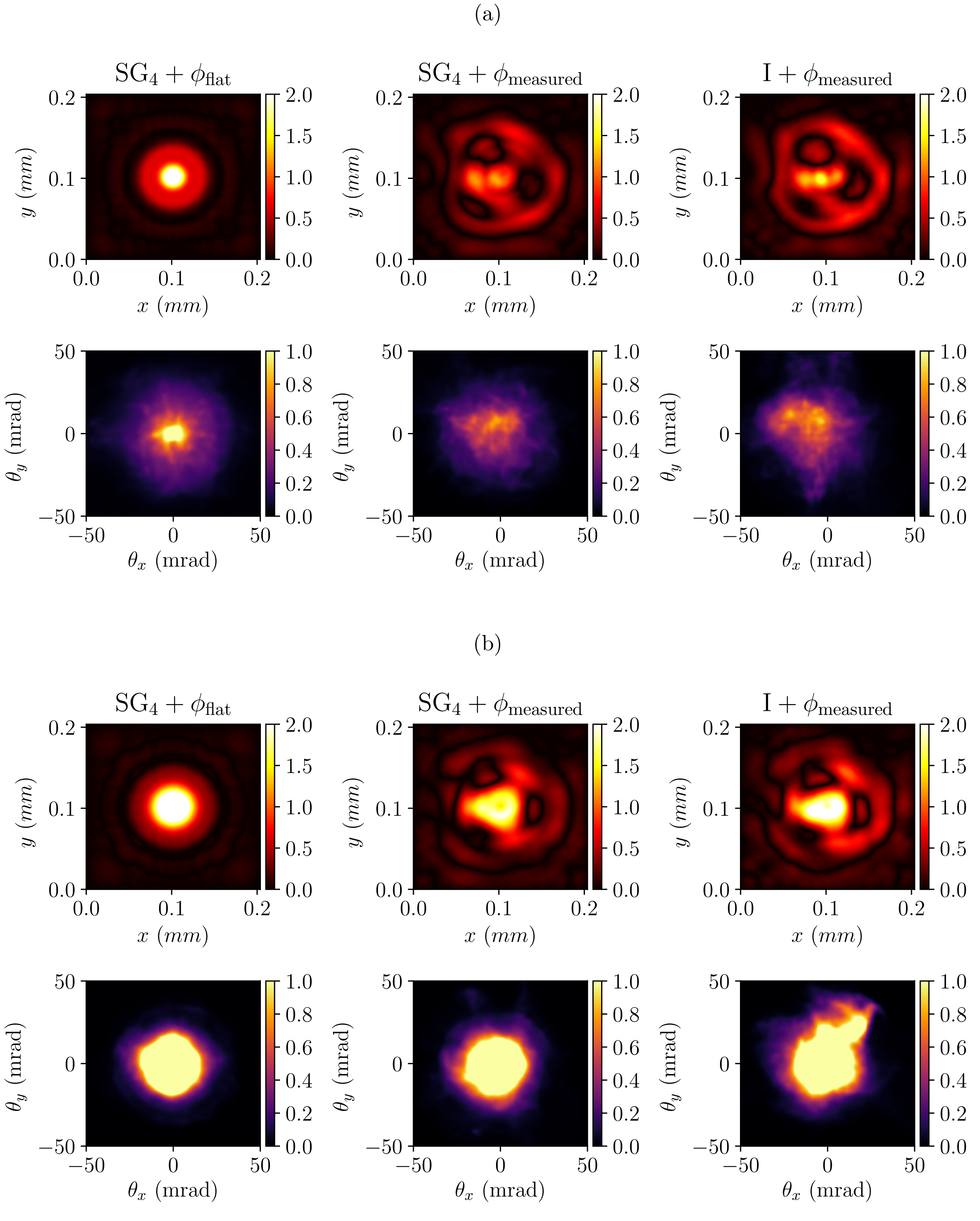

Figure 4.27: From left to right: simulations results for the $SG_4 + \phi_{\text{flat}}$, $SG_4 + \phi_{\text{measured}}$ and $I+\phi_{\text{measured}}$. The *top panels* are the cross-sections of the normalized transverse fields $E_\perp/E_0$ where $E_0 = m_e c\omega_0/e$ and the *lower panels* are the distribution of the electron bunches in (θ_x, θ_y) in (a) after 1.2 *mm* and in (b) after 1.9 *mm* of propagation.

Discussion and conclusion

In this study, the effects of realistic laser profiles have been numerically investigated where both the experimental intensity distribution and wave front are used as input in the simulations. The results are compared with a super-Gaussian profile of order 4 along with a perfectly flat wave front.

Keeping the total laser energy constant, the introduction of realistic features results in a significant drop in the quantity of the injected charge. This clearly emphasizes the limitation of using standard profiles in simulations and put forward the importance of the wave front impact which can be deleterious to the results. It has been shown that the wave front distortions in the near field play an important role in shaping the asymmetries and inhomogeneities present in the laser's far field[Leemans et al., 2014]. These imperfections in the laser pulse result in a complex wakefield pattern that in return influence the electrons injection process and their quality.

This suggests the possibility of boosting the electron bunch quality by properly tailoring the laser wave front, which can be achieved by using a deformable mirror as proposed in [He et al., 2013, 2015]. Presently, the main solution to increase the electron charge or energy relies on rising the laser power. However, this analysis emphasizes the benefit of improving the quality of the laser in far field [Genoud et al., 2013; Mangles et al., 2012]. By controlling the wave front, the pulse energy contained within the central part of the focal spot can be increased while keeping the total energy constant resulting in a better coupling with the plasma and a more efficient energy conversion to the accelerated electrons.

It also has been demonstrated that the plasma plays an important role to focus and guide a portion of the energy in the wings. In [Ferri et al., 2016], this role is highlighted by examining the position of the focal plane with respect to the plasma. A better guiding was found by moving the focal plane further inside the plasma explained by an increase in the homogeneity of the laser spot.

4.3.3 Effect of realistic laser profiles on quasi-cylindrical simulations

In chapter 3, it has been shown that any linear combination of linearly polarized lasers $\boldsymbol{E} = E_0(r,z)\boldsymbol{e}_\alpha$ with a cylindrically-symmetric envelope, i.e E_0 does not depend on θ, can be modeled exclusively by the mode $m = 1$ (3.5). On the other hand, in LWFA the plasma response to a cylindrically-symetric laser envelope is also cylindrically-symetric. In fact, the wake is driven by the ponderomotive force which depends only on the envelope of the laser. Therefore, it is dominated by the mode $m = 0$. Therefore, the infinite sum of modes in eq. (3.3) can be truncated at the first two modes since only the modes $m = 0$ and $m = 1$ are necessary to model laser-wakefield acceleration in this case.

However, ultra-short laser pulses with TW-PW powers are far from being ideal Gaussian beams as it is supposed in most of the theoretical and numerical studies. Furthermore, in the previous section it has been demonstrated that even a fit with an axis-symmetric profile such as a super-Gaussian with a flat wave front is not enough to accurately model the electrons acceleration in LWFA. This definitely highlights the importance of the wave front effects and the imperfections in the intensity profiles which result in complex non-homogeneous structures like the ones presented in fig. 4.26.

In order to accurately model more realistic lasers with the quasi-cylindrical geometry, two modes are not sufficient and it is crucial to include higher modes [Zemzemi et al., 2020]. This is why, $m_{\max}$ the maximal number of modes that can be used is kept as a free parameter in the code.

In this section, the influence of laser aberrations on azimuthal Fourier modes decomposition is studied. The optimal number of modes to describe accurately the realistic laser profiles presented in the previous section is first defined. Then, simulations are run with different modes. Finally, the impact of including higher modes on the simulation results is investigated and the ability of the quasi-cylindrical scheme to reproduce the 3D results is tested by comparing them.

Azimuthal modes decomposition from Cartesian data

In Smilei, the laser field is injected by imposing a corresponding magnetic field at the injection boundary using Silver-Muller condition. This condition has been adapted to inject each mode of the corresponding components in cylindrical geometry, separately as described in section 3.2.3. In the following, we consider a linearly polarized laser pulse along $\boldsymbol{e_y}$ and propagating in z direction.

In order to proceed with the azimuthal modes decomposition, we first start by a canonical transformation to change the variables in the transverse plane into cylindrical coordinates $(x, y) \longmapsto (r, \theta)$. Therefore, the fields that were initially on a (N_x, N_y) Cartesian grid are transformed into a (N_r, N_θ) grid. Subsequently, the field B_y is projected onto the the plane (r, θ) to get the corresponding components B_r and B_θ. Since the fields are sampled with a finite number of points, we apply thereafter a Discrete Fourier Transfrom (DFT) on the θ direction in order to obtain the different modes. Originally, the DFT operator returns both negative and positive modes then the result is rearranged in order to work with only positive modes according to eq. (3.3) where fields modes are designated by $\tilde{F}_m$.

In the following we will simply use B to designate either of the components B_r or B_θ as the exact same principal can be applied in both cases. The injected field B is defined as:

$$\begin{aligned} B(r, \theta, t) =& B_0(r, \theta) \cos(\phi(r, \theta) - \omega_0 t) \\ =& B_0(r, \theta) \left(\cos(\phi(r, \theta)) \cos(\omega_0 t) + \sin(\phi(r, \theta)) \sin(\omega_0 t)\right) \end{aligned} \tag{4.12}$$

Thanks to the linearity of the DFT operator we can write:

$$\mathrm{DFT}_\theta(B(r, \theta, t)) = \mathrm{DFT}_\theta \left[B_0(r, \theta) \cos(\phi(r, \theta))\right] \cos(\omega_0 t) + \mathrm{DFT}_\theta \left[B_0(r, \theta) \sin(\phi(r, \theta))\right] \sin(\omega_0 t) \tag{4.13}$$

Using the complex notation, $\mathcal{B} = B_0(r, \theta) e^{i\phi}$, we can write $\Re(\mathcal{B}(r, \theta)) = B_0(r, \theta) \cos(\phi)$ and $\Im(\mathcal{B}(r, \theta)) = B_0(r, \theta) \sin(\phi)$.

The equation (4.12) can be decomposed in azimuthal Fourier modes using eq. (3.3):

$$B(r, \theta, t) = \sum_{m=-\infty}^{+\infty} \widehat{\Re(\mathcal{B})}_m (r, \theta) e^{-im\theta} \cos(\omega_0 t) + \sum_{m=-\infty}^{+\infty} \widehat{\Im(\mathcal{B})}_m (r, \theta) e^{-im\theta} \sin(\omega_0 t) \tag{4.14}$$

$$= \underbrace{\left[\widetilde{\Re(\mathcal{B})}_0 (r, \theta) + \textstyle\sum_{m=1}^{+\infty} \Re\left(\widetilde{\Re(\mathcal{B})}_m (r, \theta)\right) \cos(m\theta) + \Im\left(\widetilde{\Re(\mathcal{B})}_m (r, \theta)\right) \sin(m\theta)\right]}_{\Re(\mathcal{B})} \cos(\omega_0 t)$$

$$+ \underbrace{\left[\widetilde{\Im(\mathcal{B})}_0 (r, \theta) + \textstyle\sum_{m=1}^{+\infty} \Re\left(\widetilde{\Im(\mathcal{B})}_m (r, \theta)\right) \cos(m\theta) + \Im\left(\widetilde{\Im(\mathcal{B})}_m (r, \theta)\right) \sin(m\theta)\right]}_{\Im(\mathcal{B})} \sin(\omega_0 t)$$

In practice, the infinite sum is replaced with a finite number of modes with m_{max} is the highest mode index such that the total number of modes $N_m = m_{max} + 1$. In fact, the latter is conditioned by the number of points N_θ to discretize the field in θ direction ($N_m \leq N_\theta/2$). To ensure an exact description of the field, N_θ should be chosen large enough. According to a convergence study that is not presented here, the results are converged with $N_\theta = 400$ points, which correspond to 200 modes ($N_\theta = 2N_m$).

However, we are interested in a low value for N_m in order to limit the cost of the simulation and to benefit from the use of this reduced model. In order to determine the optimal number of required modes for an accurate description, we would like to identify the smallest number that minimize the error between the actual laser field and the reconstructed field by fixing a threshold. The reconstructed field is obtained by the truncation of the the infinite sum in eq. (4.15) up to m_{max} modes.

The decomposition procedure described by eq. (4.15), can be divided into two identical and independent steps one for the real part and the other for the imaginary part denoted respectively by $\Re(\mathcal{B})$ and $\Im(\mathcal{B})$ where $\mathcal{B} \in \{\mathcal{B}_r, \mathcal{B}_\theta\}$. Therefore, the reconstruction of each part of each component can also be performed separately. Then the reconstructed fields, denoted by the index *rec* are transformed into the Cartesian frame where the error is calculated $F_{y,rec} = F_{r,rec}\sin(\theta) + F_{\theta,rec}\cos(\theta)$ with $F \in \{\Re(\mathcal{B}), \Im(\mathcal{B})\}$ (in our case the laser is fully described by its B_y component and B_x=0).

$$\begin{aligned}
B_{y,rec}(r,\theta,t) &= B_{r,rec}(r,\theta,t)\sin(\theta) + B_{\theta,rec}(r,\theta,t)\cos(\theta) \\
&= (\Re(\mathcal{B})_{r,rec}(r,\theta)\cos(\omega_0 t) + \Im(\mathcal{B})_{r,rec}(r,\theta)\sin(\omega_0 t))\sin(\theta) \\
&+ (\Re(\mathcal{B})_{\theta,rec}(r,\theta)\cos(\omega_0 t) + \Im(\mathcal{B})_{\theta,rec}(r,\theta)\sin(\omega_0 t))\cos(\theta) \\
&= \underbrace{(\Re(\mathcal{B})_{r,rec}(r,\theta)\sin(\theta) + \Re(\mathcal{B})_{\theta,rec}(r,\theta)\cos(\theta))}_{\Re(\mathcal{B})_{y,rec}}\cos(\omega_0 t) \\
&+ \underbrace{(\Im(\mathcal{B})_{r,rec}(r,\theta)\sin(\theta) + \Im(\mathcal{B})_{\theta,rec}(r,\theta)\cos(\theta))}_{\Im(\mathcal{B})_{y,rec}}\sin(\omega_0 t) \qquad (4.15)
\end{aligned}$$

Determination of the optimal number of modes

To illustrate the influence of the number of modes, the results of the decomposition in the case of both the experimental intensity and wave front $\mathrm{I} + \phi_{\text{measured}}$ are presented.

Qualitatively, from the reconstructed real part of the field in fig. 4.28a and imaginary part in fig. 4.28b, one can remark that the more modes are taken into account, the closer they get to the exact laser field and the more asymmetry appears. For example, the 2 modes (mode 0 + mode 1) reconstructed field has an almost axis-symmetric envelope and a homogeneous intensity distribution surrounding the main spot. However, more contrast and heterogeneity appear in this area with a higher number of modes.

Even though including higher modes in the reconstruction process is important to reproduce the heterogeneity in the field distribution, fig. 4.29a and fig. 4.29b show that most of the energy is contained in mode 1, which is the only non-zero mode in the case of a linearly polarized cylindrically-symmetric laser. On the other hand, small portions are unequally distributed between the rest of the modes: lower modes have more energy than the higher ones whose contributions decrease with the mode index (note the different color bars for each panel).

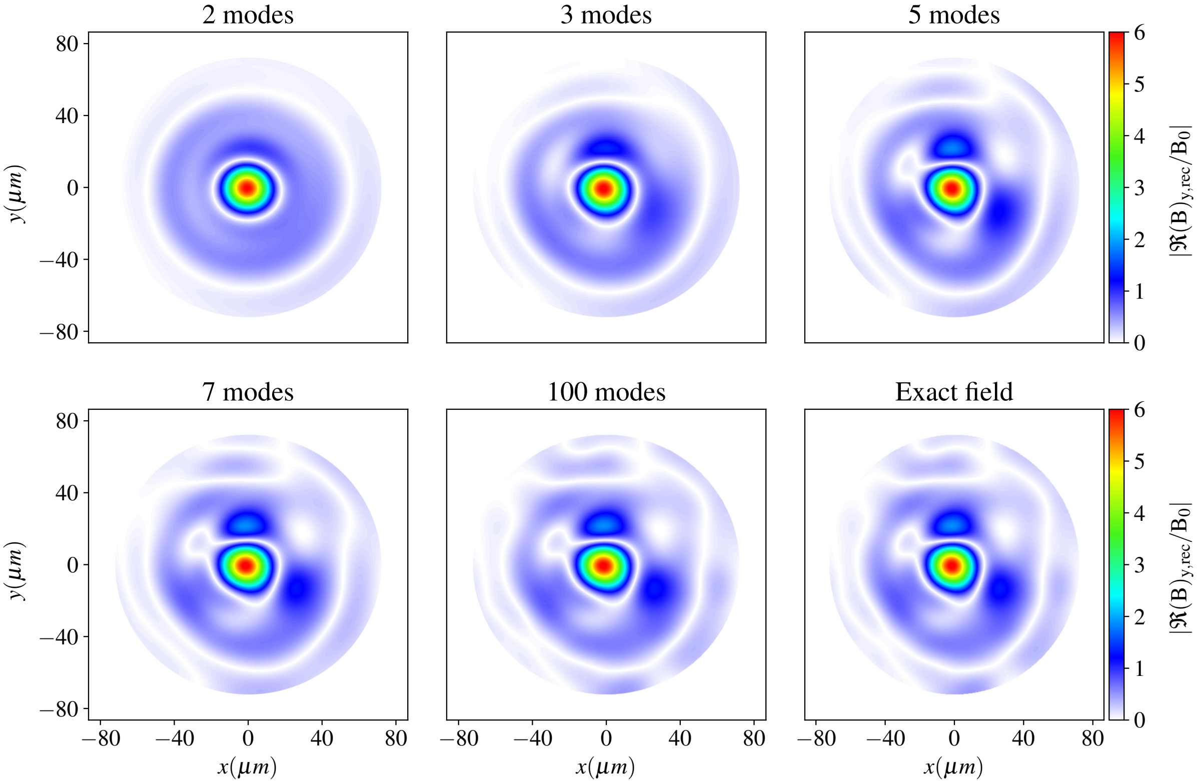

(a) Reconstructed real part of the laser field.

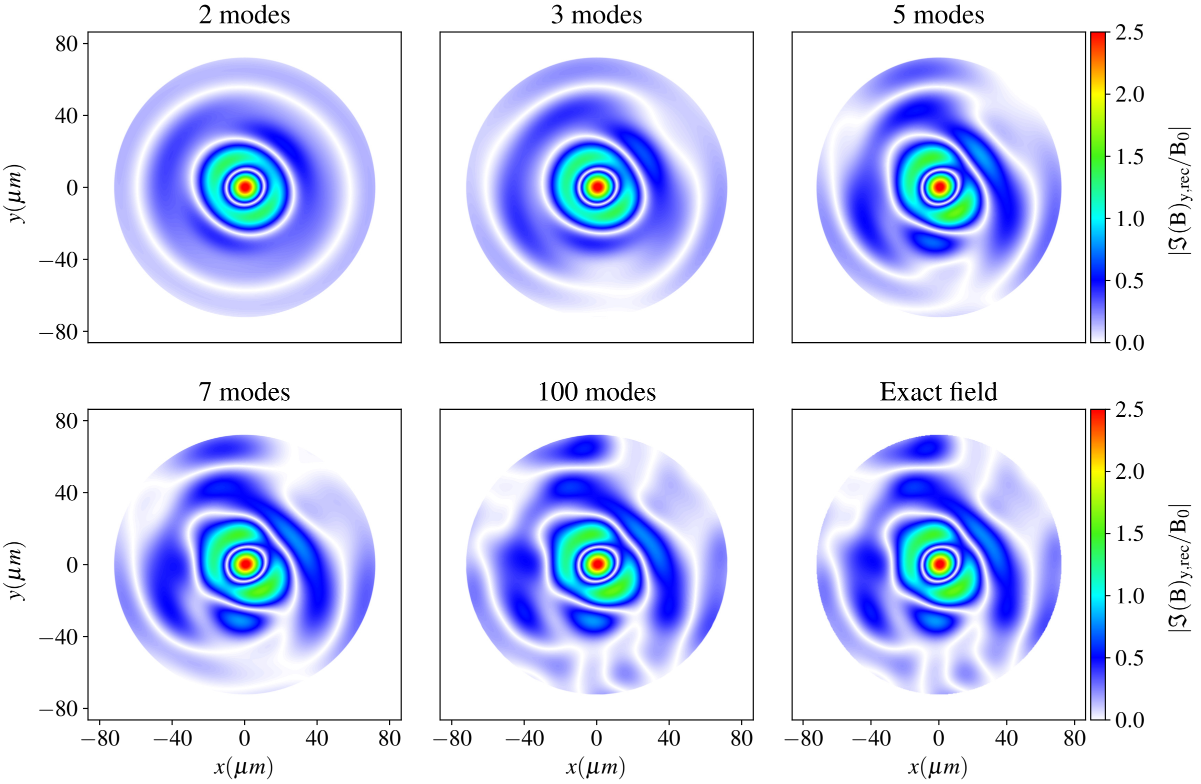

(b) Reconstructed imaginary part of the laser.

Figure 4.28: Reconstructed real part (a) and imaginary part (b) of the I+ϕ_{measured} laser normalized to $B_0 = m_e\omega_0/e$ for different number of modes N_m.

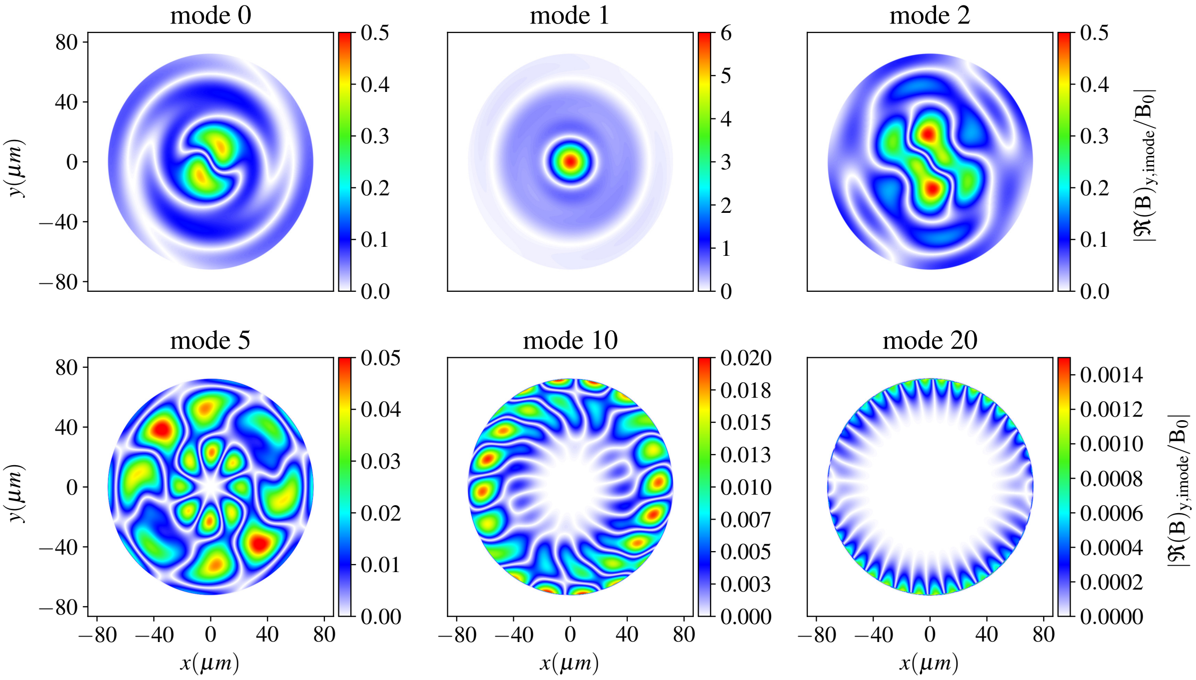

(a) Reconstructed real part of the laser for each mode m.

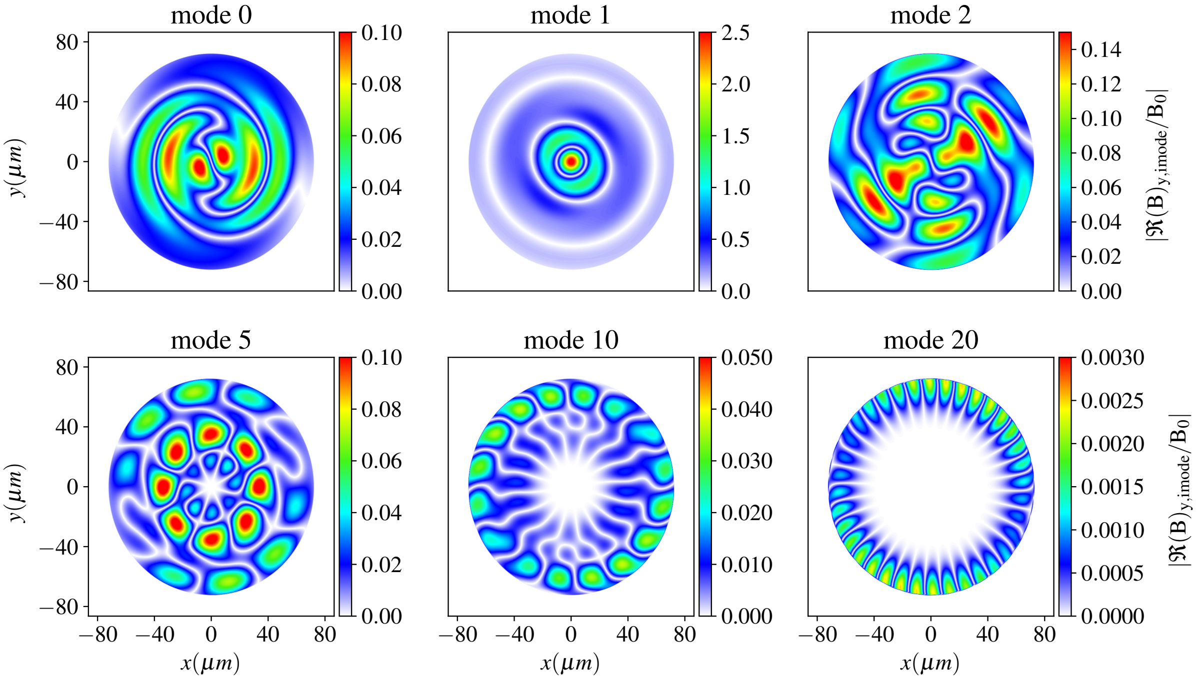

(b) Reconstructed imaginary part of the laser for each mode m.

Figure 4.29: Reconstructed fields of the real part (a) and imaginary part (b) of the I+ϕ_{measured} laser normalized to $B_0 = m_e\omega_0/e$ for different separate modes m.

In order to determine the optimal number of modes, the analysis presented next is based on the estimation of the energy norm. This analysis is a crucial step to determine the number of modes that will be plugged in the simulations of realistic lasers profiles run with the azimuthal cylindrical geometry.

After a canonical coordinates transformation $(r,\theta) \longmapsto (x,y)$ and writing $B_y(x,y,t) = \Re(\mathcal{B}_x)(x,y)\cos(\omega_0 t) + \Im(\mathcal{B}_y)(x,y)\sin(\omega_0 t)$, the relative error can be found via :

$$\frac{\|B_{y,rec} - B_y\|_2}{\|B_y\|_2}(t) = \frac{\|(\Re(\mathcal{B})_{y,rec} - \Re(\mathcal{B})_y)\cos(\omega_0 t) + (\Im(\mathcal{B})_{y,rec} - \Im(\mathcal{B})_y \sin(\omega_0 t))\|_2}{\|\Re(\mathcal{B})_y \cos(\omega_0 t) + \Im(\mathcal{B})_y \sin(\omega_0 t)\|_2} \tag{4.16}$$

where $||x||_2 = \sum_{i,j} |x_{i,j}|^2$.

From eq. (4.16), one can see that the value of the error $\mathcal{E} = \|B_{y,rec} - B_y\|_2 / \|B_y\|_2$ depends on time t, hence on the position since they are inter-dependent. Therefore, it is important when choosing the optimal number of modes, to look at the error variation in time/space and not only at a specific instant/position (for example at the focal plan or at the entry of the simulation box). Another way to look at the problem is that the laser field is more generally described with $|\mathcal{B}(r,\theta)|\cos(\phi(r,\theta) - \omega_0 t + \phi_0)$ where ϕ_0 is an arbitrary phase and this should not change the physics related to the laser evolution. Varying ϕ_0 is equivalent to varying $\omega_0 t$ between 0 and 2π.

The left panels in figs. 4.30a and 4.30b show the evolution of the relative energy norm error of the reconstructed field $\mathcal{E}$ as a function of time while varying the number of modes between 2 and 10. They exhibit a periodic sinusoidal-like pattern with local maximums and minimums. Therefore an accurate criterion should be based on minimizing the maximum value of the error in time. The latter is presented in the right panels of figs. 4.30a and 4.30b as a function of the number of modes N_m in logarithmic scale. The maximal error decreases with the number of modes. However, running the simulation with 10 modes is very expensive. In fact the cost of the simulation in quasi-cylindrical geometry depends on two main factors: first, the number of modes used: a simulation with this geometry using m_{max} modes can be seen as operating $m_{max}\times$ 2D simulations and second, the Courant–Friedrichs–Lewy (CFL) condition which should be respected in order to avoid instabilities induced by the discretization scheme.

In azimuthal FDTD scheme, the latter is given by the relation in eq. (3.76) and depends on m_{max}. It becomes more strict and implies smaller time step Δt when including higher modes. However, we usually use $\Delta z \ll dr$ in order to solve the laser wavelength with typically $\Delta r = 15\Delta z$. This means that for $m_{max} \ll \Delta r/\Delta z$, increasing the number of modes will have little impact on the time step and therefore on the simulation time. For $m_{max} \gg \Delta r/\Delta z$, the time step becomes inversely proportional to m_{max} and the simulation time proportional to m_{max}. The total cost of the simulation is a combination of the two previous factors: it is proportional to m_{max} if $m_{max} \ll \Delta r/\Delta z$ and to m_{max}^2 if $m_{max} \gg \Delta r/\Delta z$. Another factor that can be in play for the cost is the number of particles. Note that using higher number of modes may require a higher number of particles per cell in the θ-direction in order to correctly model the fast variations of currents and charges along θ associated to higher modes.

Based on the previous analysis and from figs. 4.30a and 4.30b, it seems that something between 5 and 7 modes is a good compromise between precision and a reasonable simulation cost. Actually, with these number of modes the error on the norm reaches a value close to the 1%. Besides, running a simulation with 5 modes (respectively with 7 modes) while using the same number of particles per cell, is just 1.7 (respectively 2.3) more expensive than the one with 2 modes. Therefore it is still much less expensive than a 3D simulation, which is almost 22 times more expensive than the 7-modes quasi-cylindrical simulation.

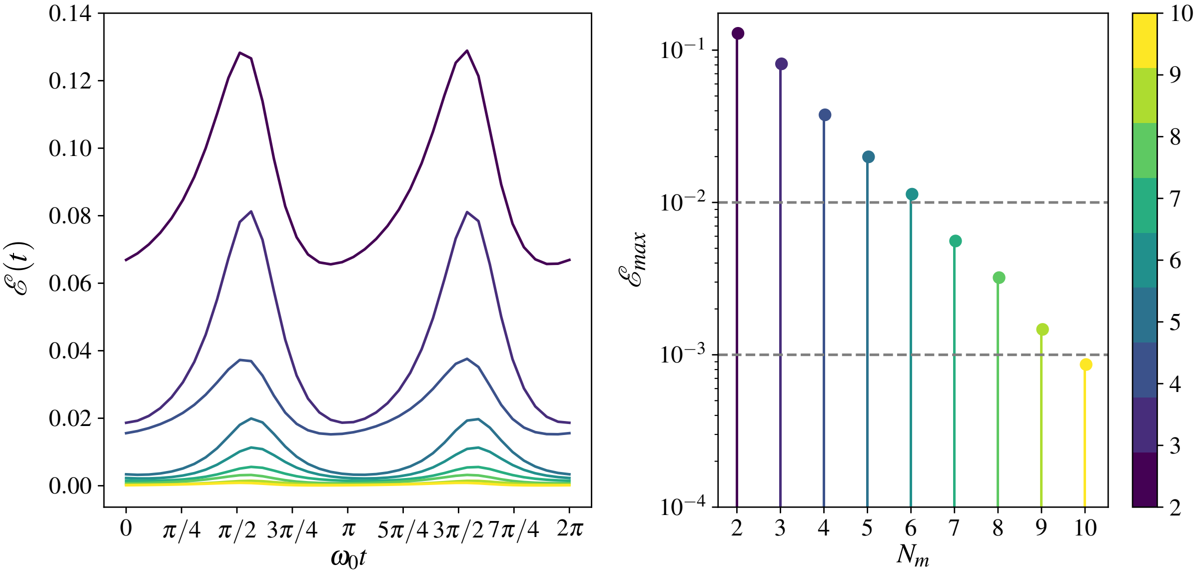

(a) Relative energy errors for the SG+ϕ_{measured} laser.

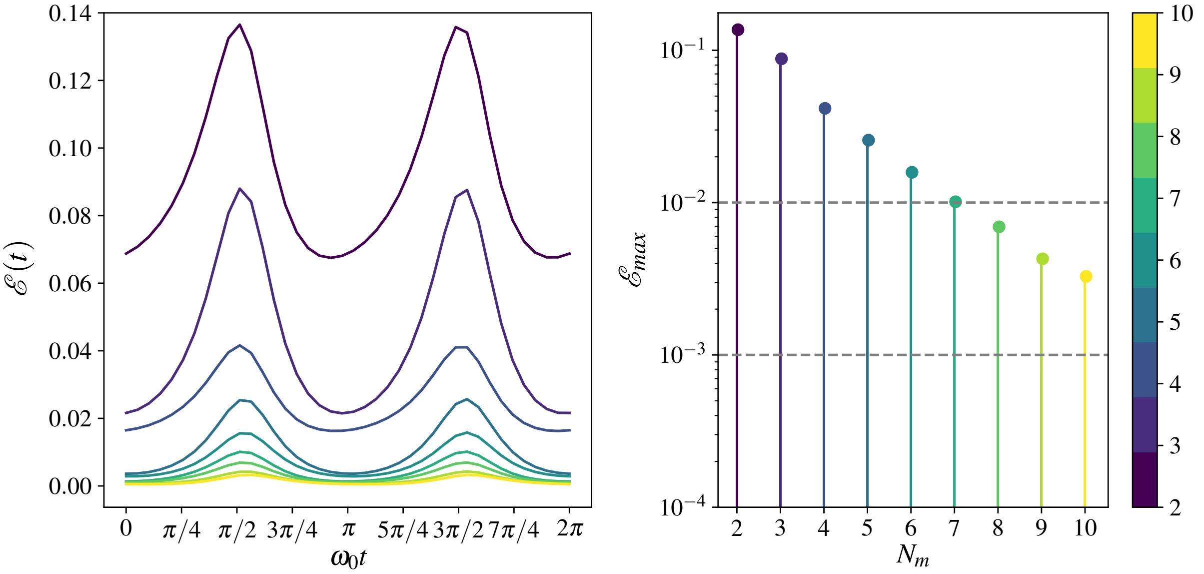

(b) Relative energy errors for the I+ϕ_{measured} laser.

Figure 4.30: *Left panels*: relative energy errors of the reconstructed laser fields as a function of $\omega_0 t$ varied between 0 and 2π for different number of modes N_m. The number of modes for each plot is indicated by the color in the right colorbar. *Right panels*: The maximum relative energy errors are plotted in a logarithmic scale for 2 to 10 modes.

Simulation results and Influence of the number of modes

To understand the influence of including higher modes on the simulation results, 3D cartesian simulations of the laser profiles described in the previous section are reproduced in quasi-cylindrical geometry with the first strictly minimum required 2 modes then 5 modes and 7 modes in the case of $\mathrm{SG}_4 + \phi_{\mathrm{measured}}$ and $\mathrm{I} + \phi_{\mathrm{measured}}$. Note that for these two cases, the mode 0 is not negligible and introduces some asymmetries of the laser as it can be seen in fig. 4.29a and fig. 4.29b for the real and imaginary part of $\mathcal{B}$ in the case of $\mathrm{I} + \phi_{\mathrm{measured}}$. For the $\mathrm{SG}_4 + \phi_{\mathrm{flat}}$ simulation, only the 2 first modes are used because the laser profile is axis-symmetric and thus fully described by the mode 1 while the wakefield is mostly described by the mode 0 [2]. In this study, physical processes such as the bubble formation, wakefield generation and electron acceleration are investigated and the results are compared with their 3D counter parts.

In all the simulations, the laser wavelength is fixed to $\lambda_0 = 0.8\ \mu m$ and a Gaussian time envelope of a duration $\tau_0 = 25\ fs$ is assumed. The lasers propagate in a 500 μm rising plasma ramp followed by a plateau of an electronic density $n_e = 8.6 \times 10^{17}$ cm^{-3}. The numerical parameters for the simulations with different number of modes and for each case are summarized in table 4.2 where Δt_i indicates the specific time step used in the simulation with i modes.

simulation	Numerical params						
	N_z	N_r	Δz	Δr	Δt_2	Δt_5	Δt_7
$\mathrm{SG}_4 + \phi_{\mathrm{flat}}$	6400	640	$0.1\ c/\omega_0$	$2.5\ c/\omega_0$	$0.9974\ \Delta z$	None	None
$\mathrm{SG}_4 + \phi_{\mathrm{measured}}$	7936	1280	$0.1\ c/\omega_0$	$1.5\ c/\omega_0$	$0.99\ \Delta z$	$0.96\ \Delta z$	$0.928\ \Delta z$
$\mathrm{I}+\phi_{\mathrm{measured}}$	7936	1280	$0.1\ c/\omega_0$	$1.5\ c/\omega_0$	$0.99\ \Delta z$	$0.96\ \Delta z$	$0.928\ \Delta z$

Table 4.2: Numerical parameters in the simulations with realistic laser profiles in quasi-cylindrical geometry.

$\underline{\mathrm{SG}_4 + \phi_{\mathrm{flat}}}$:

Figure 4.31 compares respectively the cross sections of the electronic density map and the longitudinal electric field obtained with 3D and quasi-cylindrical simulations after 1.9 mm of propagation, in the case of $\mathrm{SG}_4 + \phi_{\mathrm{flat}}$. As expected, a qualitative agreement between the two simulations is found.

To quantify the convergence between the two geometries, the energy spectrum of the two electron bunches at the end of the acceleration is shown in fig. 4.32. The bunch is defined as the collection of electrons sitting in the accelerating region of the bubble. This region is identified by the profile of the longitudinal electric field.

Both distributions exhibit a high energy (∼ 500 MeV) low charge electron bunch corresponding to first longitudinal injection. However, its energy is slightly higher in the case of 3D simulation. Due to the very small charge quantity in the latter, an energy filter up to 400 MeV is applied in this case and the bunch related quantities are then evaluated only for the main part of the bunch.

---

[2] Note that non-linearities in the wakefield lead to non-zero contributions from higher modes. However, they are still negligible compared to the 0 mode contribution in this case.

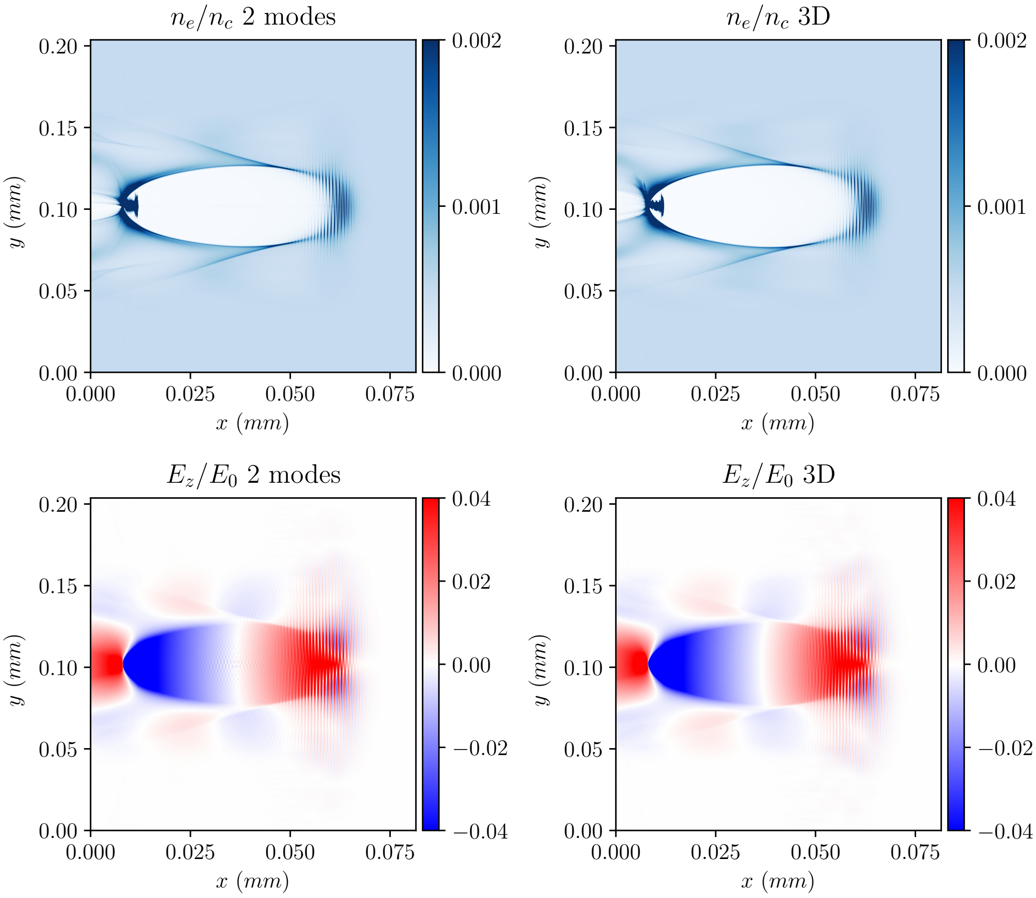

Figure 4.31: Comparison of the simulation results in quasi-cylindrical with 2 modes and in 3D of the $\mathrm{SG}_4+\phi_{\mathrm{flat}}$ laser pulse after 1.9 *mm* of propagation. *Top panels*: colormaps of the normalized electronic densities. *Lower panels*: colormaps of the normalized longitudinal electric fields.

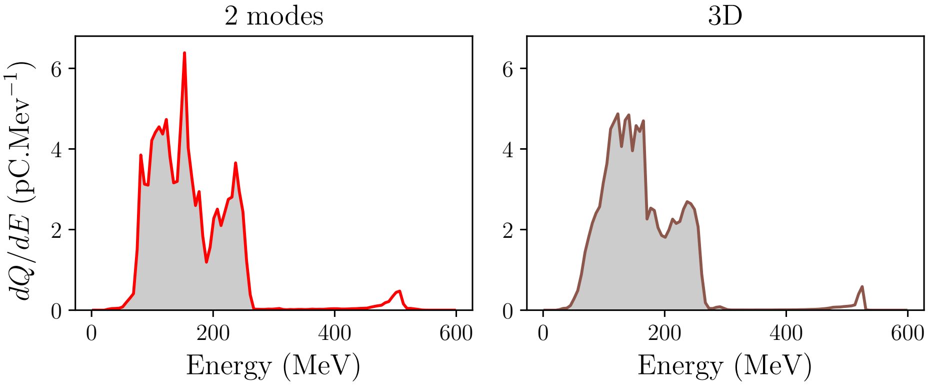

Figure 4.32: Energy spectra of the electrons for the 2-modes quasi-cylindrical and 3D simulations of the $\mathrm{SG}_4+\phi_{\mathrm{flat}}$ laser pulse after 1.9 *mm* of propagation. The selected bunches for which the bunch-related quantities are evaluated in table 4.3, are designated by the shaded areas.

Bunch properties	2 modes	3D
Q (pC)	596	599
Δ E / $\langle$E$\rangle$ (%)	33.5	33.8
$\theta_\perp$ (mrad)	25.9	22
x-rms size (μm)	12.3	20
y-rms size (μm)	29	21.5
z-rms size (μm)	1.9	2.2
$\varepsilon_{n,\perp}$ (mm $\cdot$ mrad)	66.1	47.8

Table 4.3: Summary of the bunch-related quantities for the 2-modes quasi-cylindrical and 3D simulations of the $\mathrm{SG}_4 + \phi_{\mathrm{flat}}$ laser pulse after 1.9 mm of propagation.

From the integrated values of the bunch-related quantities presented in table 4.3, a good agreement is found in terms of the charge quantity and energy spread. Nevertheless, the quasi-cylindrical slightly overestimates the bunch's divergence and emittance in this case.

$\underline{\mathrm{SG}_4 + \phi_{\mathrm{measured}}}$:

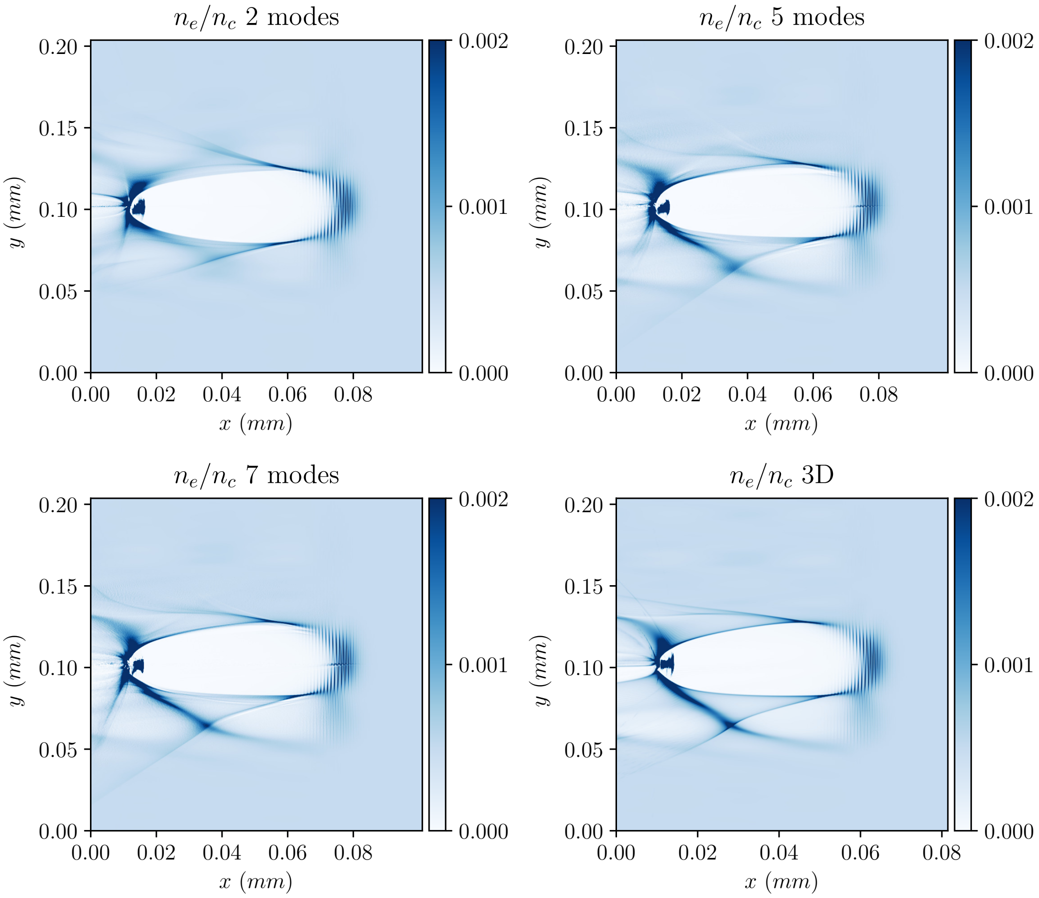

Figure 4.33: Comparison of the normalized electronic density colormaps in 2, 5 and 7-modes quasi-cylindrical and in 3D simulations of the $\mathrm{SG}_4 + \phi_{\mathrm{measured}}$ laser pulse after 1.9 mm of propagation.

By looking at the electronic density map and longitudinal field presented in figs. 4.33 and 4.34 for the different simulations, it is clear that the 2-modes simulation fails to reproduce the inhomogeneity present in the 3D simulation. For instance, the off-axis laser part around $y = 0.06$ mm which drives its own wakefield, is absent in the 2-modes simulation. However, the 2-modes case presents an axis-symmetric ring-like distributed energy around the main laser pulse which creates a weaker wakefield fig. 4.34.

By adding more modes, we can see that the 5 and 7-modes simulations are able to reproduce the 3D features qualitatively. This puts forward the importance of including higher modes in the case of an asymmetric transverse laser field.

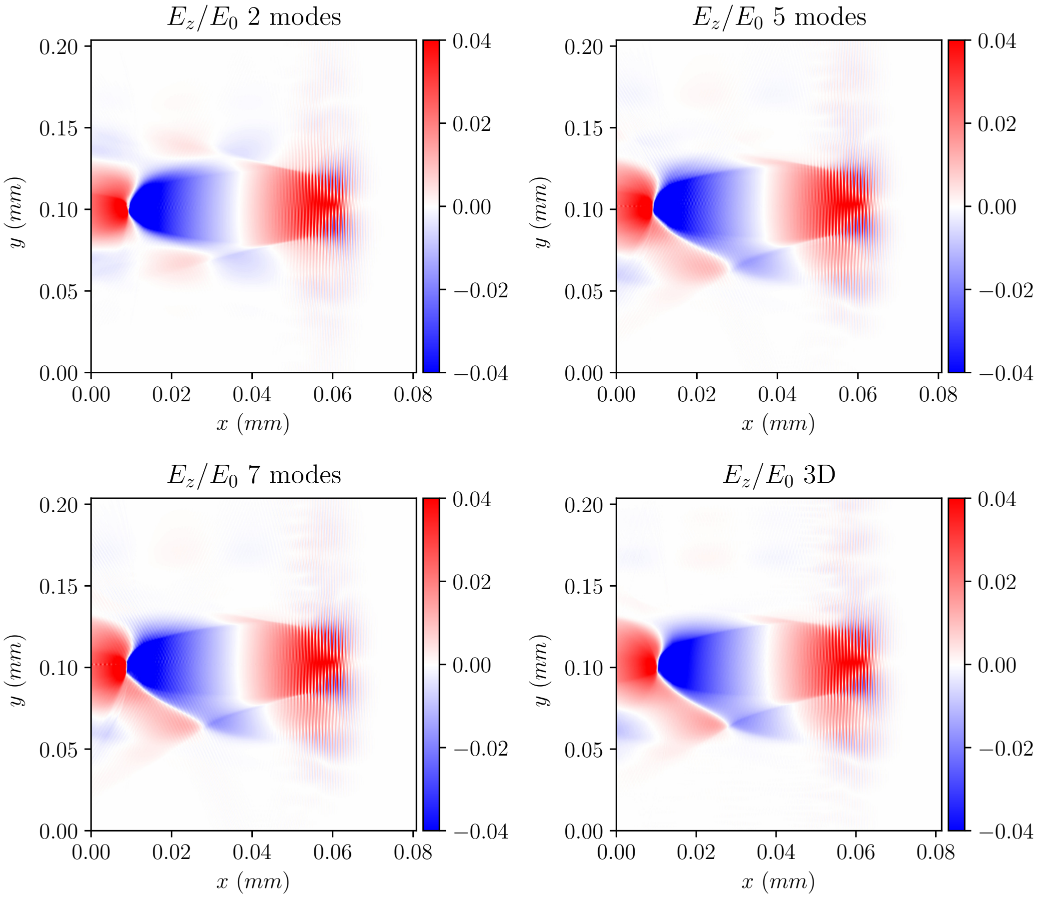

Figure 4.34: Comparison of the normalized longitudinal electric field colormaps in 2, 5 and 7-modes quasi-cylindrical and in 3D simulations of the $\mathrm{SG}_4 + \phi_{\text{measured}}$ laser pulse after 1.9 mm of propagation.

In order to examine the impact of using higher modes on the electrons acceleration from a quantitative point of view, I evaluated the bunch-related quantities presented in table 4.4 by integrating over their spectra. By comparing the overall bunch properties, all the quasi-cylindrical simulations give a good approximation of the injected charge quantity. The rest of the quantities are comparable, however the energy spread, divergence and emittance in the case of the 5 modes and 7 modes simulations are more important. This can be misleading because the values are integrated on the whole bunch. Looking closely to the shape of the energy spectrum after 1.9

mm of propagation in fig. 4.35, the 2 modes distribution is tilted towards the low energies, by adding more modes the pattern gets closer to that of the 3D simulation. For instance, the global shape of the 7-modes distribution tends to become a plateau with spikes as in 3D. The 5 modes distribution exhibits an intermediate pattern between the 2 and 7 modes distributions.

Bunch properties	2 modes	5 modes	7 modes	3D
Q (pC)	405	388	419	418
Δ E / $\langle$E$\rangle$ (%)	29	32	36	32.1
$\theta_\perp$ (mrad)	19.4	22.5	22.4	19.4
x-rms size (μm)	9.2	15.4	13	7.2
y-rms size (μm)	10	18.5	15.5	7
z-rms size (μm)	1.53	1.6	1.63	2
$\varepsilon_{n,\perp}$ (mm $\cdot$ mrad)	19.3	35.8	35	17.1

Table 4.4: Summary of the bunch-related quantities for the 2, 5 and 7-modes quasi-cylindrical and 3D simulations of the $\text{SG}_4 + \phi_{\text{measured}}$ laser pulse after 1.9 mm of propagation.

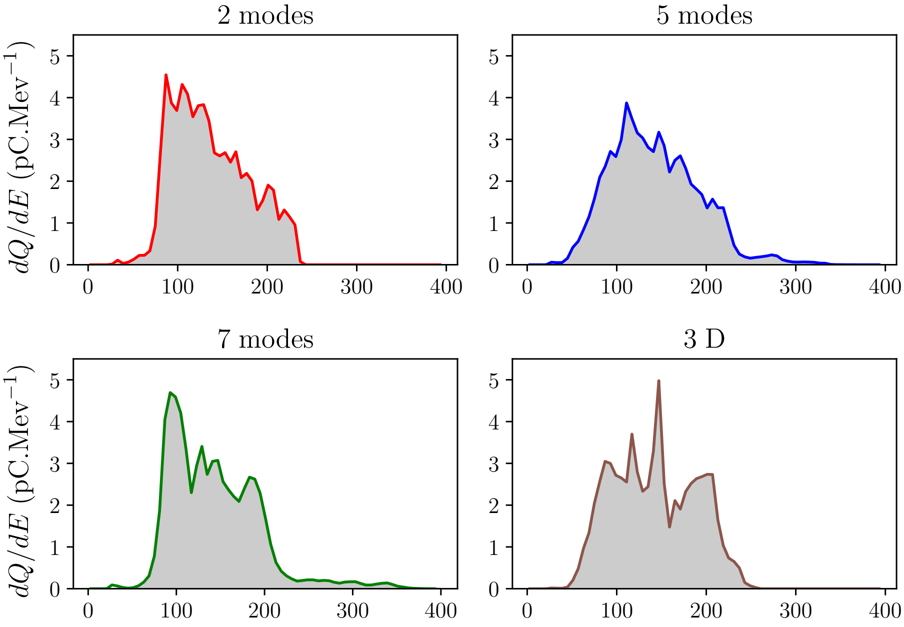

Figure 4.35: Energy spectra of the electrons for the 2, 5 and 7-modes quasi-cylindrical and 3D simulations of the $\text{SG}_4 + \phi_{\text{measured}}$ laser pulse after 1.9 mm of propagation. The selected bunches for which the bunch-related quantities are evaluated in table 4.4, are designated by the shaded areas.

Since it is hard to select a well-defined bunch from the enrgy spectra using the traditional bunch definition, I evaluated some bunch-related quantities per longitudinal slice by decomposing the total bunch length into 20 slices as presented in fig. 4.40. Looking to the charge and the mean energy per slice, we can see that the quasi-cylindrical simulations give a good approximation to the 3D case. In particular, the 5-modes simulation for the charge and the 7-modes for the mean energy. However, for the divergence and transverse-emittance per slice there is an agreement only at the front of the electron bunch and they are overestimated at the back of the bunch where the charge is low, meaning that there are few particles in that slice.

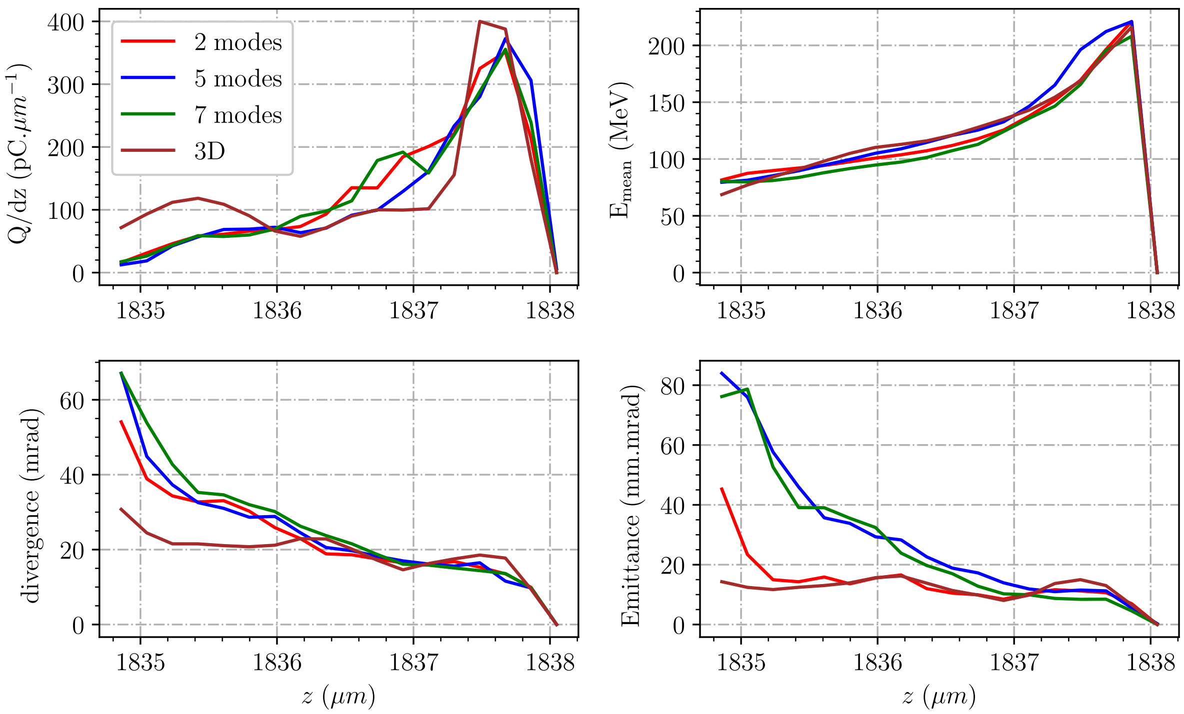

Figure 4.36: Comparison of the bunch-related quantities in the 2, 5 and 7-modes quasi-cylindrical and in 3D simulations of the $SG_4 + \phi_{\text{measured}}$ laser pulse after 1.9 mm of propagation.

$\underline{I + \phi_{\text{measured}}}$:

In regard to the $I + \phi_{\text{measured}}$ case, the influence of higher modes on the shape of the injected electron bunches is even more striking in fig. 4.37. With the measured intensity added to the laser profile, the bunch becomes disrupted in the 3D simulation and separated from the back of the bubble. Once again, the 2-modes simulation is not able to reproduce this effect and contrarily, the injection is continuous and its bunch is symmetric and not separated from the back of the bubble. This disruption in the bunch starts to be visible with the 5-modes and its more obvious with the 7-modes simulation.

As explained previously, the shape of the bunch is affected by the structure of the wakefield. The non-uniformity of the laser pulse leads to a complex structure of the accelerating field presented in fig. 4.38 where the outer part of the laser have enough energy to act as a secondary laser pulse that drives its own wakefield. This induces a sort of instability in the wakefield that disturb the injection and acceleration process.

This time the total quantity of the injected charge is over estimated in the case of 2 modes but it starts to converge to the 3D simulation result with higher modes. The bunch properties metrics in the 7-modes simulation, summarized in table 4.5 are very close to those of the 3D simulation. This convergence with higher modes is also visible in the shape of the energy spectra of the electron bunches as displayed in fig. 4.39. In particular, the high energy part situated above 200 MeV is well reproduced. This demonstrates the importance of the higher modes role for an accurate description.

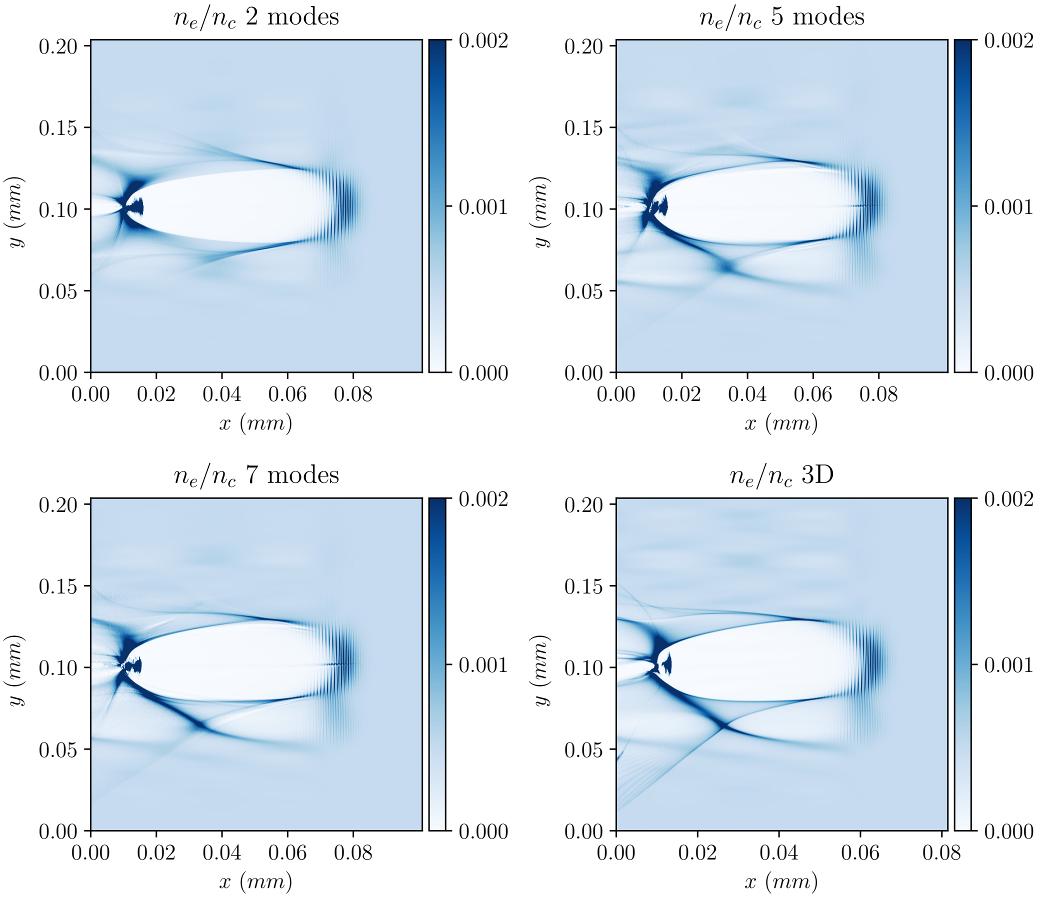

Figure 4.37: Comparison of the normalized electronic density colormaps in 2, 5 and 7-modes quasi-cylindrical and in 3D simulations of the I+ϕ_{measured} laser pulse after 1.9 *mm* of propagation.

This is confirmed by looking to the bunch properties per slice. The 7-modes is a very good approximation for the 3D case in terms of charge and mean energy despite some difference at the back of the bunch. The emittance and the divergence at the front of the bunch, where the charge quantity is important, are correctly modeled. However, these statistical quantities are very sensitive to the number of particles per slice and they tend to increase rapidly when the charge is quiet low.

Conclusion:

To conclude, in the case of an axis-symmetric laser envelope and a flat wave front, such as the case of $\text{SG}_4 + \phi_{\text{flat}}$, the 2-modes quasi-cylindrical is able to describe with fidelity the physics and reproduce with accuracy the results of the 3D simulation. However, some differences are found in the statistical bunch-related quantities.

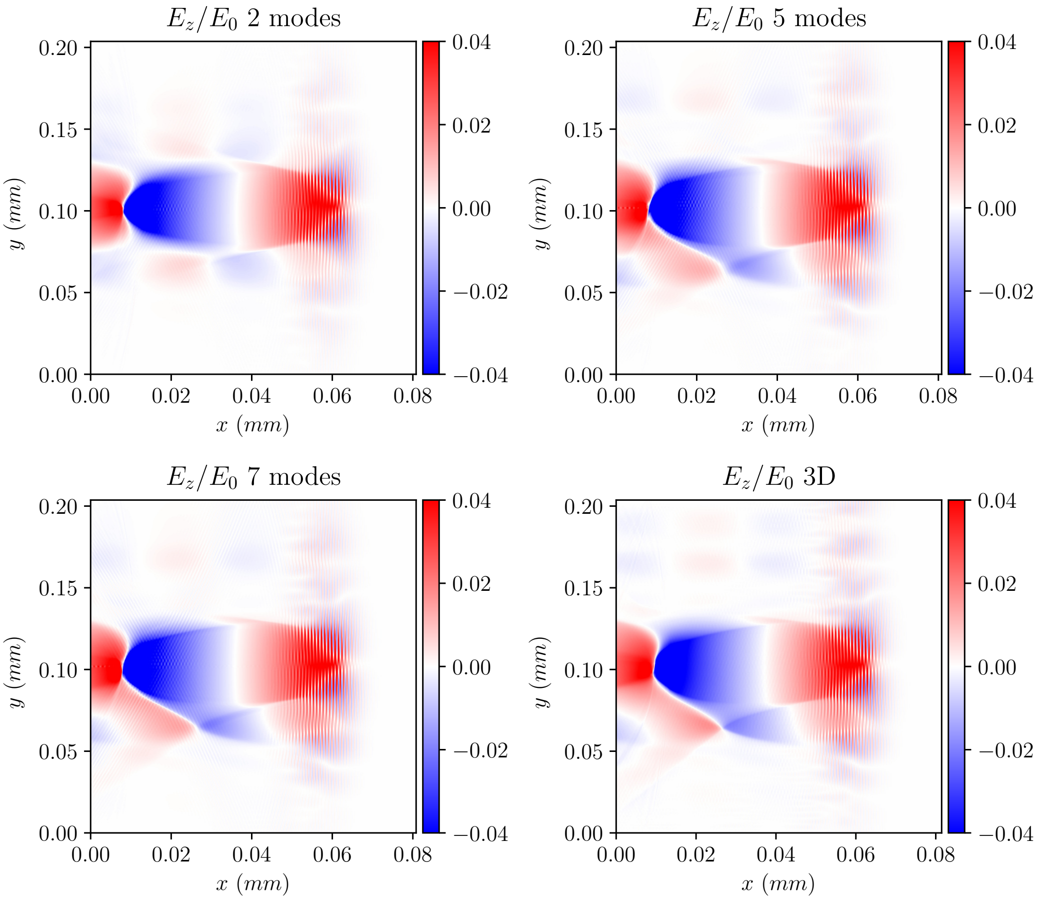

Figure 4.38: Comparison of the normalized longitudinal electric field colormaps in 2, 5 and 7-modes quasi-cylindrical and in 3D simulations of the $\mathrm{I} + \phi_{\text{measured}}$ laser pulse after 1.9 *mm* of propagation.

Bunch properties	2 modes	5 modes	7 modes	3D
Q (pC)	554	463	454	428
Δ E / $\langle$E$\rangle$ (%)	32.5	37	32	29.5
$\theta_\perp$ (mrad)	18.	17.7	19	21.1
x-rms size (μm)	6.5	10.2	9.7	9.2
y-rms size (μm)	5.4	8.6	7.5	5.4
z-rms size (μm)	2.4	2.36	2.31	2.1
$\varepsilon_{n,\perp}$ (mm $\cdot$ mrad)	19.6	17.3	22	21.1

Table 4.5: Summary of the bunch-related quantities for the 2, 5 and 7-modes quasi-cylindrical and 3D simulations of the $\mathrm{I}+\phi_{\text{measured}}$ laser pulse after 1.9 *mm* of propagation.

In the case of $\mathrm{SG}_4+\phi_{\text{measured}}$, the inhomogeneities triggered by the wave front can be reasonably described with 5 modes. Even though the 7-modes simulation gives a slightly better results than the 5-modes simulation, the difference is not very important between the two.

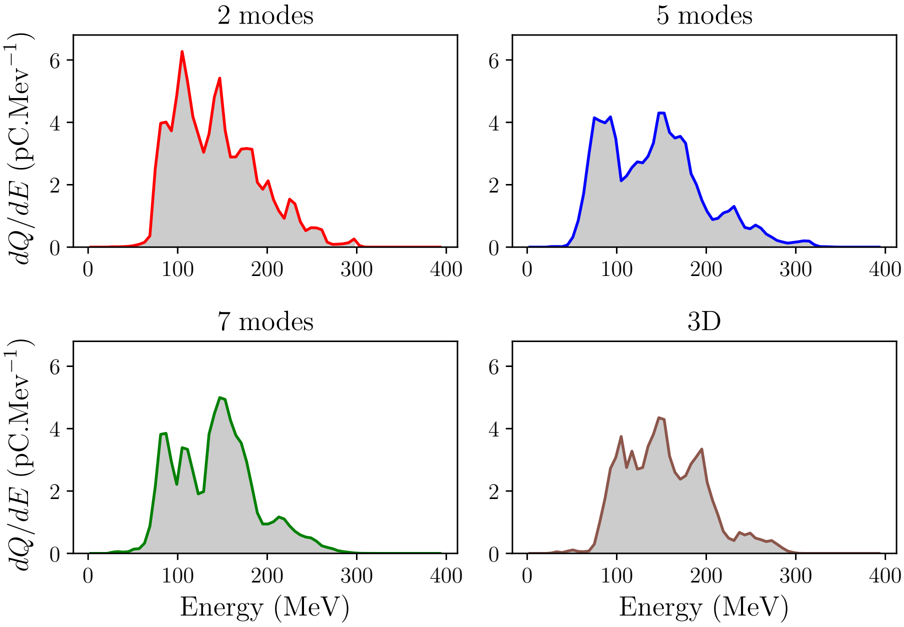

Figure 4.39: Energy spectra of the electrons for the 2, 5 and 7-modes quasi-cylindrical and 3D simulations of the I+ϕ_{measured} laser pulse after 1.9 *mm* of propagation. The selected bunches for which the bunch-related quantities are evaluated in table 4.5, are designated by the shaded areas.

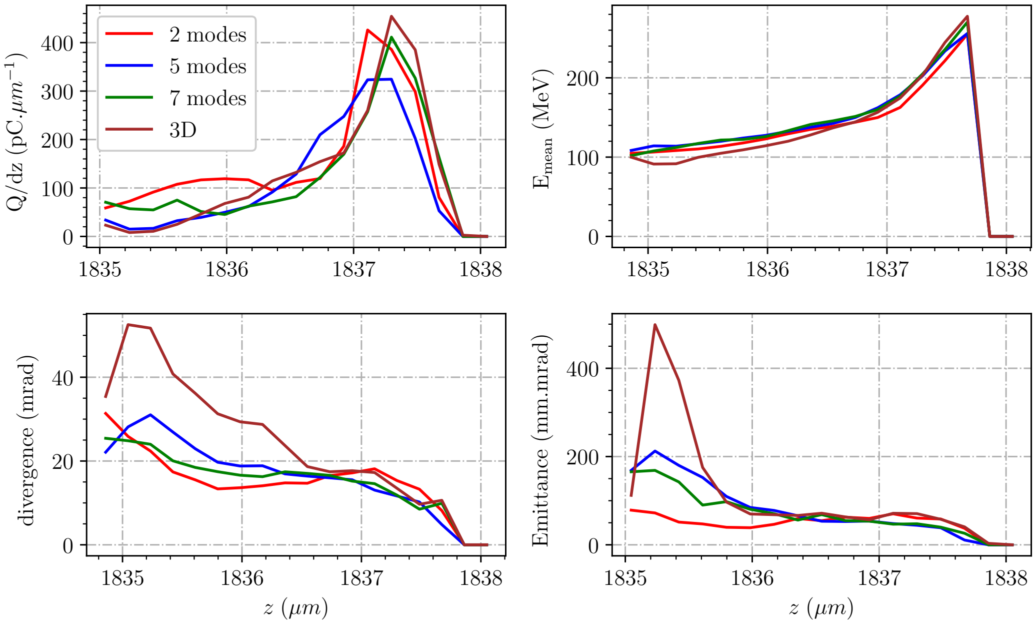

Figure 4.40: Comparison of the bunch-related quantities in the 2, 5 and 7-modes quasi-cylindrical and in 3D simulations of the $\text{I} + \phi_{\text{measured}}$ laser pulse after 1.9 *mm* of propagation.

In the case of $\mathrm{I}+\phi_{\mathrm{measured}}$, the difference between the 5 and 7 modes results becomes slightly more important important. This can be seen, for example, from the charge per slice profile. In fact, adding the intensity profile increase the overall asymmetries and 7 modes are required in this case for a better fidelity.

This trend can be explained from the maximum of the normalized error between the exact field and the reconstructed field plotted in fig. 4.30a for the $\mathrm{SG}_4+\phi_{\mathrm{measured}}$ case and in fig. 4.30b for the $\mathrm{I}+\phi_{\mathrm{measured}}$ case: the slope in the case of $\mathrm{SG}_4+\phi_{\mathrm{measured}}$ is steeper than that of $\mathrm{I}+\phi_{\mathrm{measured}}$ which indicates that the error in higher modes decreases faster. Therefore, the sensitivity of the code to higher modes is more important in the case of the $\mathrm{I}+\phi_{\mathrm{measured}}$ laser. This demonstrates the importance of such a study in order to understand the sensitivity of a given laser to the number of the azimuthal modes used to describe it. This study helps to get a rough estimation of the required number of modes. However, it remains difficult to evaluate an exact estimation of the optimal number of modes in order to reproduce exactly the 3D results.

In the two last cases where the realistic laser features are used, including higher modes is very important to model the homogeneities induced by the laser imperfections and therefore their impact on the wake formation and electrons acceleration.

The quasi-cylindrical simulations are very insightful to run parametric scans. They are not expensive to run and they give a good estimation of the acceleration process, the quantity of the injected charge and its mean energy. This is true even when using realistic lasers that present asymmetries in their profiles, when using a sufficient number of modes. However, the model has its limits when it comes to the estimation of the divergence and emittance. In fact, these statistical metrics are very sensitive to the number of particles. As it has been showed through the plots of the bunch-related quantities per slice, the estimation of the divergence and transverse emittance is correctly modeled only for the parts of the bunch where the charge is sufficiently high. The main differences between the quasi-cylindrical simulations and the 3D ones are found at the back of the bunch, and thus the back of the bubble.

It is not straightforward to find an explanation for this, as this can be related to many possible reasons. Among the possible reasons, one can mention the numerical parameters such as the number of particles per cell, the different numerical dispersion and thus the numerical phase velocity which depends on the mode in the quasi-cylindrical geometry. In fact, simulations with higher modes are more prone to numerical Cherenkov radiation. This can be also related to the on-axis condition in the quasi-cylindrical geometry which leads to a numerical noise.

Simulation	2 modes	5 modes	7 modes	3D
Particles per cell	56	56	56	4
CPU-hours	16496	27483	37413	800000
Number of cores	1536	1536	1536	16000
Vectorization	None	None	None	Adaptative vectorization

Table 4.6: Comparison of the simulation cost between the different quasi-cylindrical simulations and the 3D one.

On the other hand,these simulations are not expensive to run and do not require large computational resources. From table 4.6, the 5-modes simulations are roughly 1.7 times more expensive than the 2-modes ones while the 7-modes are 2.3 times more expensive than the 2-modes simulations if the number of particles per cell is kept the same when varying the number of modes. Using even 7-modes with the quasi-cylindrical geometry, is still 21.5 times cheaper than the 3D simulations despite the fact that the quasi-cylindrical algorithm is still not vectorized yet.

Therefore, a better performance can still be achieved in the future by implementing an adaptative vectorization like the one used in 3D.

Conclusion

Summary of the results

The body of my research work focuses on studying the impact of laser imperfections on laser wakefield acceleration through numerical simulations. In this context, I implemented the azimuthal Fourier field decomposition in cylindrical geometry, referred to as quasi-cylindrical geometry, in the Particle-In-Cell code SMILEI. Then, I used it to carry out a study with realistic laser profiles from the Apollon installation. This section summarizes the main results of this thesis.

First, I implemented the quasi-cylindrical geometry in SMILEI using Finite Difference Time Domain (FDTD) discretization scheme. However, it is known that this scheme may lead to an artificial spurious radiation emitted by the relativistic electrons which hinders the accuracy of PIC simulations and tends to increase the estimation of the emittance. This numerical artifact, called numerical Cherenkov radiation (NCR), can be mitigated by using pseudo-spectral solvers. Therefore, I also implemented a Pseudo Spectral Analytical Time Domain (PSATD) version of this algorithm in PICSAR library. Nevertheless, the precision of this approach comes with a significant increase in the computational cost due to their limited scaling performances and their important memory footprint at large scales. In fact, to guarantee the accuracy of the method, the simulation domain should be decomposed into large subdomains with an important number of ghost cells. Typically 64 ghost cells are used with the 32 order solver.

In order to optimize the performance of the method and benefit from the patch-based load balancing in SMILEI, a special two-level domain decomposition, denoted by Single Domain Multiple Decompositions (SDMD), is used to couple PICSAR with SMILEI. This spatial decomposition allows the use of a coarse-grain decomposition with large subdomains, called regions, where the Maxwell's equations are solved and a fine-grain decomposition with small subdomains, called patches, where operations pertaining to macro-particles are handled. The PSATD implementation is then benchmarked and its results are compared to those of the FDTD scheme. The PSATD solver has been proved to be NCR-free leading to noise-free results and a lower estimation of the transverse emittance as expected.

The second part of my PhD research work focuses on the physics where I leveraged the developed numerical tools to perform LWFA simulations for the future experiments with the Apollon laser.

In the technical design of the Apollon laser, the incoming laser is reflected on a drilled mirror leading to a hole in the laser's near field. To analyze the effect of this hole on the LWFA experiments, I carried out a numerical study with different laser profiles. The choice of the profiles was based on fitting the experimental intensity profile with a super-Gaussian after determining the best order. Then, for each case, the parameters such as the power, the a_0 and the presence of the hole were varied. These profiles also included a Gaussian fit of the measured intensity in near field and an "equivalent" Gaussian in the far field. The results show that the wings in the super-Gaussians may help in the self-focusing process and hence, trigger a more important charge injection. On the other hand, the hole leads to a lower intensity peak in the main pulse and to a more important energy diffracted in the wings. When the energy in the wings is sufficiently high, like in the case of the hole, it can act as a secondary laser pulse that disrupt the wakefield of the main pulse. This leads to a shorter injection in time and thus less injected charge and a shorter bunch length. It also causes a higher divergence and promotes emittance growth. However, it leads to a higher energy peak and to a lower energy spread. In all the cases, the overall quality of the produced bunches is comparable and the differences are not very significant over long acceleration distances like the ones presented in this study. Therefore, the technical choice for the design of the Apollon laser is justified, at the expense of slightly degrading the electron bunch quality.

Using 3D Cartesian simulations, I studied the impact of the Apollon laser imperfections on LWFA and particularly on the quality of the generated electron bunches. The outcome of the results showed the importance of including experimentally measured features. In particular, the wave front has an important impact in shaping the transverse laser profile in the far field, thus on the structure of the wakefield and on the injection process of the electrons and their quality. This suggests that by properly tailoring the wave front, better focal spots and thus better quality of the electrons can be achieved. The same simulations are also run in the quasi-cylindrical geometry. First, an optimal range of the required number of modes is determined from the curve of the normalized error between the reconstructed fields and the actual laser field. Then, the simulations are performed with different number of modes. The comparison between the results highlights the importance of including higher modes to accurately model the laser's asymmetries with realistic profiles.

Future prospects

The presented results open up several prospects regarding the numerical methods to model LWFA with PIC codes on the one hand and the study of realistic laser profiles on the other hand.

Numerical aspect

Despite the use of the SDMD approach to optimize the performance of the PSATD solver, this kind of simulations is still very expensive compared to its FDTD counter-part. This is partially due to the parallelization of the solver currently restricted to the longitudinal direction, which limits the scaling of the code.

In order to optimize the performance of the solver, it should also be parallelized in the transverse direction r. This can be tricky and not straightforward because the Hankel transform employs matrix multiplication which is a non-local operation. A possible way to do that, is to resort to the use of dedicated libraries such as scalapack combined with the adequate algorithms to perform a parallel calculation of matrix multiplication.

Currently, the initialization of the laser with the PSATD solver is done by calculating the electric and magnetic fields of the laser directly in the simulation box. This method is limited to the Gaussian profiles. In order to enable the generalization of the laser profile to any arbitrary function, an antenna should be implemented to inject the laser. This is very important to reproduce the realistic simulations with the PSATD solver.

Another considerable improvement, that can be brought to the code in quasi-cylindrical geometry, is the implementation of the Perfectly Matched Layer (PML). In fact, for the moment the transverse size of the simulation box is chosen to be relatively large in order to avoid any reflections from the upper boundary inside the box. This reflections may lead to an important numerical instability, especially near the axis, and can be detrimental to the accuracy of the results. On the one hand, implementing the PML will help reducing the computational time by allowing the use of smaller boxes and thus less grid points in the radial direction. On the other hand, it will ensure the accuracy of the simulations results by inhibiting any reflections inside the domain.

Physical aspect

The realistic LWFA simulations show that the plasma may focus a part of the laser's halo. In fact, the plasma can act as focusing or defocusing optics for the laser. It is a key factor in determining whether the energy in the wings contributes in the self-focusing and acceleration or it is spatially filtered. Therefore, it is important to study the effect of the laser's imperfections with different plasma densities.

Besides, it has been shown in [Ferri et al., 2016] that the position of the focal plane compared with the beginning of the plasma plateau plays an important role in the evolution of the laser inside the plasma. Thus, it is interesting to also look at how this may affect the results in the case of the Apollon laser.

The presented results concern the case of the Apollon laser with the focal of $f = 3\ m$. However, the installation offers the possibility of using a focal of $f = 9\ m$. The difference in the focal length will lead to a different focal spot and therefore, different results should be expected in this case. In particular, the focal length of $f = 3\ m$ leads to a very intense and a tightly focused laser with a short Rayleigh length while the focal of $f = 9\ m$ offers a larger Rayleigh length. Therefore, it can be self-guided for a longer propagation in the plasma.

Besides, if the same strategy is applied to other lasers with different distortions, then other conclusions can be reached.

Finally, spectral measurements of the Apollon laser have been carried out recently. The same methodology of determining the optimal number of modes can be applied to each spectral component of the laser. Then, these modes can be used in the quasi-cylindrical simulations in order to identify the impact of spatio-spectral coupling in LWFA.

Appendix A

Theory of plasma waves excitation by a laser pulse

The goal of the following part is to establish a model that describes the generation of a plasma wave driven by a laser pulse. For this aim, we define the assumptions for this theoretical framework:

1. We use fluid model to describe the plasma with its macroscopic quantities. Therefore kinetic effects such as trapping and wave breaking are not taken into account.
2. The plasma is cold because the thermal velocity v_{th} is neglected compared to the electrons velocity acquired from the laser field v_e.
3. Plasma ions are supposed to be immobile in the time scale of the electrons motion.
4. The plasma is strongly under-dense $n_0 \ll n_c$. Therefore, $\omega_p \ll \omega_0$ where ω_0 is the laser frequency and ω_p is the plasma frequency.

The starting equations to establish the plasma wave excitation description in the case of a laser driver are the Lorentz equation of motion for the electrons in a cold fluid plasma, plus the Maxwell's equations in the potential formalism under the Coulomb gauge $\nabla \cdot \boldsymbol{A} = 0$. In an under dense plasma, we can distinguish the laser high frequencies from the plasma low frequencies ($\omega_p \ll \omega_0$). Therefore, the coulomb gauge enables us to separate the electromagnetic laser field $\boldsymbol{A}$ from the electrostatic plasma field Φ due to charge separation.

We start with the Poisson equation(1.11) obtained under the Coulomb gauge $\nabla \cdot \boldsymbol{A} = 0$ where $\rho = -e(n_e - n_0)$ is the source term that comes from charge separation in the plasma. The ions are treated as a homogeneous neutralizing background: $n_0 = Zn_i$ with Z the atomic number and n_i the ion density whereas n_e is the displaced electron density. Since, only electrons are displaced we replace f_e by f where f denotes any quantity related to electrons. The displacement of electrons by the laser creates charge separation in the plasma. Therefore the Poisson equation can be written:

$$\nabla^2 \Phi = \frac{e}{\epsilon_0}(n_e - n_0) \tag{A.1}$$

The second equation is the continuity equation:

$$\frac{\partial n_e}{\partial t} + \nabla \cdot (n_e \boldsymbol{v}) = 0 \tag{A.2}$$

Writing Maxwell-Ampere equation (1.2) using potentials results in:

$$\left(\nabla^2 - \frac{1}{c^2}\frac{\partial^2}{\partial t^2}\right)\boldsymbol{A} = \frac{en_e}{\epsilon_0 c^2}\boldsymbol{v} + \frac{1}{c^2}\frac{\partial}{\partial t}\nabla\Phi \tag{A.3}$$

where $\boldsymbol{J}$ has been replaced by the expression $\boldsymbol{J} = -en_e\boldsymbol{v}$.

By replacing the electromagnetic fields with their potential formalism, the equation of motion reads :

$$\left(\frac{\partial}{\partial t} + \boldsymbol{v}\cdot\nabla\right)\boldsymbol{p} = e\left(\nabla\Phi + \frac{\partial \boldsymbol{A}}{\partial t} - \boldsymbol{v}\times\nabla\times\boldsymbol{A}\right)$$

We rearrange this equation to be :

$$\frac{\partial}{\partial t}(\boldsymbol{p} - e\boldsymbol{A}) = e\nabla\Phi + (\boldsymbol{v}\cdot\nabla)\boldsymbol{p} - e\boldsymbol{v}\times(\nabla\times\boldsymbol{A})$$

Using the following property:

$$\nabla\frac{p^2}{2} = (\boldsymbol{p}\cdot\nabla)\boldsymbol{p} + \boldsymbol{p}\times(\nabla\times\boldsymbol{p}) = m\gamma\left[(\boldsymbol{v}\cdot\nabla)\boldsymbol{p} + \boldsymbol{v}\times(\nabla\times\boldsymbol{p})\right]$$

where $\boldsymbol{p} = m\gamma\boldsymbol{v}$ and $\gamma = \sqrt{1 + (\boldsymbol{p}/mc)^2)}$, we find that:

$$\nabla\gamma = \frac{1}{m^2c^2\gamma}\nabla\frac{\boldsymbol{p}^2}{2} = \frac{1}{mc^2}\left[(\boldsymbol{v}\cdot\nabla)\boldsymbol{p} + \boldsymbol{v}\times(\nabla\times\boldsymbol{p})\right]$$

Thus:

$$(\boldsymbol{v}\cdot\nabla)\,\boldsymbol{p} = mc^2\nabla\gamma - \boldsymbol{v}\times(\nabla\times\boldsymbol{p})$$

Inserting this identity in the equation of motion, the latter reads:

$$\frac{\partial}{\partial t}(\boldsymbol{p} - e\boldsymbol{A}) = \nabla(e\Phi - mc^2\gamma) + \boldsymbol{v}\times\left[\nabla\times(\boldsymbol{p} - e\boldsymbol{A})\right]$$

where $\boldsymbol{v}\times[\nabla\times(\boldsymbol{p} - e\boldsymbol{A})] = 0$. This can be proved by applying the rotational operator to the previous equation[3]:

$$\frac{\partial}{\partial t}\boldsymbol{g} = \nabla\times\boldsymbol{v}\times\boldsymbol{g}$$

where $\boldsymbol{g} = \nabla\times(\boldsymbol{p} - e\boldsymbol{A})$. Since at t=0 $\boldsymbol{v} = \boldsymbol{p} = \boldsymbol{A} = 0$, $\boldsymbol{g} = 0 = \partial g/\partial t_{t=0} = 0$. Thus, then the quantity $e\nabla\times(\boldsymbol{p} - e\boldsymbol{A}) = 0, \quad \forall t$. Finally the equation of motion after simplification becomes:

$$\frac{\partial \boldsymbol{p}}{\partial t} = e\nabla\Phi + e\frac{\partial \boldsymbol{A}}{\partial t} - mc^2\nabla\gamma \tag{A.4}$$

Using the normalized quantities: $\phi = e\Phi/mc^2$, $\boldsymbol{a} = e\boldsymbol{A}/mc$, $\boldsymbol{u} = \boldsymbol{p}/mc = \gamma\boldsymbol{v}/c = \gamma\boldsymbol{\beta}$ and $\gamma = \sqrt{1 + \boldsymbol{u}^2)}$ in eq. (A.1), eq. (A.2), eq. (A.3) and eq. (A.4) , we obtain the following system of equations:

$$\nabla^2\phi = k_p^2\left(\frac{n}{n_0} - 1\right) \tag{A.5}$$

---

[3] Note that $\nabla\times\left[\nabla(e\Phi - mc^2\gamma)\right] = 0$

$$\frac{\partial n}{\partial t} + c\nabla \cdot \left(\frac{n\boldsymbol{u}}{\gamma} \right) = 0 \tag{A.6}$$

$$\left(\nabla^2 - \frac{1}{c^2}\frac{\partial^2}{\partial t^2} \right) \boldsymbol{a} = k_p^2 \frac{n\boldsymbol{u}}{\gamma n_0} + \frac{1}{c}\frac{\partial}{\partial t}\nabla\phi \tag{A.7}$$

$$\frac{\partial \boldsymbol{u}}{\partial t} = c\nabla(\phi - \gamma) + \frac{\partial \boldsymbol{a}}{\partial t} \tag{A.8}$$

where $k_p = \omega_p/c = \sqrt{e^2 n_0/\epsilon_0 m_e c^2}$ is the wave number of the plasma.

Appendix B

Comoving coordinates

In an under-dense plasma, it is assumed that the laser driver and the corresponding wakefield propagate very close to the speed of light i.e $v_g \sim c$ and $v_\phi \sim c$, so it is practical to use the copropagating coordinates, also called coordinates in the laboratory frame , in order to follow the laser pulse when the latter is short. In the case of a laser propagating along z, the transformation is $\tau = t$ and $\xi = z - ct$. This implies :

$$\frac{\partial}{\partial t} = \frac{\partial}{\partial \tau} - c\frac{\partial}{\partial \xi} \tag{B.1}$$

$$\frac{\partial}{\partial z} = \frac{\partial}{\partial \xi} \tag{B.2}$$

$$\frac{\partial^2}{\partial^2 t} = \frac{\partial^2}{\partial \tau^2} + c^2\frac{\partial^2}{\partial \xi^2} - 2c\frac{\partial^2}{\partial \tau \partial \xi} \tag{B.3}$$

$$\frac{\partial^2}{\partial z^2} = \frac{\partial^2}{\partial \xi^2} \tag{B.4}$$

However, in reality the laser propagation velocity slightly differs from the light speed ($v_g \neq c$). It becomes more important to take into account this velocity instead of c when it comes to relativistic particles acceleration where relativistic effects become important such as dephasing. Therefore, when using the transformation $\tau = t$ and $\xi = z - v_g t$ instead of $\xi = z - ct$ and supposing that the wake velocity $v_p \simeq v_g$ we have:

$$\frac{\partial}{\partial t} = \frac{\partial}{\partial \tau} - v_g\frac{\partial}{\partial \xi} \tag{B.5}$$

$$\frac{\partial}{\partial z} = \frac{\partial}{\partial \xi} \tag{B.6}$$

$$\frac{\partial^2}{\partial^2 t} = \frac{\partial^2}{\partial \tau^2} + v_g^2\frac{\partial^2}{\partial \xi^2} - 2v_g\frac{\partial^2}{\partial \tau \partial \xi} \tag{B.7}$$

$$\frac{\partial^2}{\partial z^2} = \frac{\partial^2}{\partial \xi^2} \tag{B.8}$$

Appendix C

One dimensional model of plasma waves excitation theory in the case of a laser pulse driver

In this appendix, we propose to solve the system of equations given by eq. (1.54), eq. (1.55), eq. (1.56) and eq. (1.57) in the limit of 1D. Hence, all quantities depend only on (z, t) and $\nabla = \frac{\partial}{\partial z}\boldsymbol{e_z}$. In this case, the Coulomb gauge $\nabla \cdot \boldsymbol{A} = 0$ implies that $A_z = 0$ and that the laser is purely transverse $\boldsymbol{a} = \boldsymbol{a}_\perp$. The longitudinal and transverse component of the equation of motion eq. (1.57) obey respectively to:

$$\frac{\partial(\gamma\beta_z)}{\partial t} = c\frac{\partial(\phi - \gamma)}{\partial z} \tag{C.1}$$

$$\frac{\partial(\boldsymbol{u}_\perp - \boldsymbol{a})}{\partial t} = 0 \tag{C.2}$$

This entails that the transverse electrons motion is only due to the laser field $\boldsymbol{u}_\perp = \boldsymbol{a}$. We can also rewrite the Lorentz factor as:

$$\gamma = (1 - \beta_\perp^2 - \beta_z^2)^{-1/2} = \frac{(1 + a^2)^1/2}{(1 - \beta_z)^{1/2}} \tag{C.3}$$

Afterwards, we decompose eq. (1.56) into its longitudinal and transverse part. We obtain:

$$\left(\nabla^2 - \frac{1}{c^2}\frac{\partial^2}{\partial t^2}\right)\boldsymbol{a} = \frac{nk_p^2}{n_0\gamma}\boldsymbol{a} \tag{C.4}$$

$$\frac{1}{c}\frac{\partial^2\phi}{\partial t\partial z} = -\frac{nk_p^2}{n_0\gamma}u_z \tag{C.5}$$

Adopting the transformation of the comoving coordinates in the laser frame ($\tau = t, \xi = z - ct$) described in appendix B supposing that it propagates at a velocity $v_g \simeq c$ implies:

$$\frac{\partial^2\phi}{\partial\xi^2} = k_p^2\left(\frac{n_e}{n_0} - 1\right) \tag{C.6}$$

$$\frac{\partial n_e}{\partial\tau} = c\frac{\partial}{\partial\xi}\left(n_e(1 - \beta_z)\right) \tag{C.7}$$

$$\frac{\partial(\gamma\beta_z)}{\partial\tau} = c\frac{\partial}{\partial\xi}\left(\phi - \gamma(1-\beta_z)\right) \tag{C.8}$$

$$\left(\frac{2}{c}\frac{\partial^2}{\partial\xi\partial\tau} - \frac{1}{c^2}\frac{\partial^2}{\partial\tau^2}\right)\boldsymbol{a} = \frac{nk_p^2}{n_0\gamma}\boldsymbol{a} \tag{C.9}$$

According to the quasi-static approximation introduced in section 1.4, we can neglect temporal derivatives $\partial/\partial\tau$. Therefore under this assumption,eq. (C.7) and eq. (C.9) become after integration:

$$n_e(1-\beta_z) = n_0 \tag{C.10}$$

$$\gamma(1-\beta_z) = 1 + \phi \tag{C.11}$$

Using the above relations in eq. (C.6) and eq. (C.8) gives us the coupled equations to describe the laser $\boldsymbol{a}$ and the potential ϕ evolution along the propagation axis:

$$\frac{\partial^2\phi}{\partial\xi^2} = \frac{k_p^2}{2}\left[\frac{1+a^2}{(1+\phi)^2 - 1}\right] \tag{C.12}$$

$$\frac{\delta n_e}{n_0} = \frac{1}{2}\left[\frac{1+a^2}{(1+\phi)^2 - 1}\right] \tag{C.13}$$

However, when relativistic effects become important, the laser propagation velocity can no longer be confused with the light speed ($v_g \neq c$). Therefore, when using the transformation $\tau = t$ and $\xi = z - v_g t$ instead of $\xi = z - ct$ and supposing that the wake velocity $v_p \simeq v_g$ and after some math the potential equation reads:

$$\frac{1}{w_p^2}\frac{\partial^2\phi}{\partial\xi^2} = \gamma_g^2\left[\beta_g\left(1 - \frac{1+a^2}{\gamma_g^2(1+\phi)^2}\right)^{-1/2} - 1\right] \tag{C.14}$$

Bibliography

(2012). *Introduction to plasma dynamics.* CRC press.

A. Ghaith, M. E. C. e. a. (2020). Undulator design for laser plasma based free electron laser. *(submitted).*

Akhiezer, A. I. and Polovin, R. V. (1956). Theory of wave motion of an electron plasma.

Antici, P., Alberto, B., Benedetti, C., Chiadroni, E., Ferrario, M., Rossi, A., Lancia, L., Migliorati, M., Mostacci, A., Palumbo, L., and Serafini, L. (2012). Laser-driven electron beamlines generated by coupling laser-plasma sources with conventional transport systems. *Journal of Applied Physics*, 112.

Azmayesh-Fard, S. M. (2013). Gaussian beam propagation: comparison of the analytical closed-form fresnel integral solution to the simulations of the huygens, fresnel, and rayleigh sommerfeld approximations. *J. Opt. Soc. Am. A*, 30(4):640–644.

Bauer, D., Mulser, P., and Steeb, W. H. (1995). Relativistic ponderomotive force, uphill acceleration, and transition to chaos. *Phys. Rev. Lett.*, 75:4622–4625.

Beaurepaire, B., Vernier, A., Bocoum, M., Böhle, F., Jullien, A., Rousseau, J.-P., Lefrou, T., Douillet, D., Iaquaniello, G., Lopez-Martens, R., Lifschitz, A., and Faure, J. (2015). Effect of the laser wave front in a laser-plasma accelerator. *Phys. Rev. X*, 5:031012.

Beck, A., Derouillat, J., Lobet, M., Farjallah, A., Massimo, F., Zemzemi, I., Perez, F., Vinci, T., and Grech, M. (2019). Adaptive simd optimizations in particle-in-cell codes with fine-grain particle sorting. *Computer Physics Communications*, 244:246 – 263.

Ben-Ismail, A., Lundh, O., Rechatin, C., Lim, J. K., Faure, J., Corde, S., and Malka, V. (2011). Compact and high-quality gamma-ray source applied to 10 μm-range resolution radiography. *Applied Physics Letters*, 98(26):264101.

Benedetti, C., Schroeder, C. B., Esarey, E., Geddes, C. G. R., and Leemans, W. P. (2010). Efficient modeling of laser-plasma accelerators with inf&rno. *AIP Conference Proceedings*, 1299(1):250–255.

Benedetti, C., Schroeder, C. B., Esarey, E., Rossi, F., and Leemans, W. P. (2013). Numerical investigation of electron self-injection in the nonlinear bubble regime. *Physics of Plasmas*, 20(10):103108.

Benedetti, C., Schroeder, C. B., Geddes, C. G. R., Esarey, E., and Leemans, W. P. (2017). Efficient modeling of laser-plasma accelerator staging experiments using inf&rno. *AIP Conference Proceedings*, 1812(1):050005.

Berezhiani, V. and Murusidze, I. (1990). Relativistic wake-field generation by an intense laser pulse in a plasma. *Physics Letters A*, 148(6):338 – 340.

Berezhiani, V. I. and Murusidze, I. G. (1992). Interaction of highly relativistic short laser pulses with plasmas and nonlinear wake-field generation. *Physica Scripta*, 45(2):87–90.

Birdsall, C. and Langdon, A. (2004). *Plasma Physics via Computer Simulation*. Series in Plasma Physics. Taylor & Francis.

Boris, J. (1970). Relativistic plasma simulation-optimization of a hybrid code. In *Proceeding of the Fourth Conference on Numerical Simulations of Plasmas*. Naval Research Laboratory.

Boris, J. P. and Lee, R. (1973). Nonphysical self forces in some electromagnetic plasma-simulation algorithms. *Journal of Computational Physics*, 12(1):131 – 136.

Bourgeois, N., Cowley, J., and Hooker, S. M. (2013). Two-pulse ionization injection into quasi-linear laser wakefields. *Phys. Rev. Lett.*, 111:155004.

Bourgeois, P.-L. and Davoine, X. (2020). New mitigation approach to numerical cherenkov radiation in pic simulations of wakefield accelerators. *Journal of Computational Physics*, 413:109426.

Brantov, A. V., Esirkepov, T. Z., Kando, M., Kotaki, H., Bychenkov, V. Y., and Bulanov, S. V. (2008). Controlled electron injection into the wake wave using plasma density inhomogeneity. *Physics of Plasmas*, 15(7):073111.

Buck, A., Wenz, J., Xu, J., Khrennikov, K., Schmid, K., Heigoldt, M., Mikhailova, J. M., Geissler, M., Shen, B., Krausz, F., Karsch, S., and Veisz, L. (2013). Shock-front injector for high-quality laser-plasma acceleration. *Phys. Rev. Lett.*, 110:185006.

Bulanov, S., Naumova, N., Pegoraro, F., and Sakai, J. (1998). Particle injection into the wave acceleration phase due to nonlinear wake wave breaking. *Phys. Rev. E*, 58:R5257–R5260.

Bulanov, S. V., Inovenkov, I. N., Kirsanov, V. I., Naumova, N. M., and Sakharov, A. S. (1992). Nonlinear depletion of ultrashort and relativistically strong laser pulses in an underdense plasma. *Physics of Fluids B: Plasma Physics*, 4(7):1935–1942.

Buneman, O. (1993). The 3-d electromagnetic particle code. *Computer space plasma physics*, pages 67–84.

Burza, M., Gonoskov, A., Svensson, K., Wojda, F., Persson, A., Hansson, M., Genoud, G., Marklund, M., Wahlström, C.-G., and Lundh, O. (2013). Laser wakefield acceleration using wire produced double density ramps. *Phys. Rev. ST Accel. Beams*, 16:011301.

C. Lejeune, J. A. (1980). Emittance and brightness: Definitions and measurements in applied charged particle optics. *A. Septier, Academic Press, New York*, 159-259.

Corde, S., Thaury, C., Lifschitz, A., Lambert, G., Ta Phuoc, K., Davoine, X., Lehe, R., Douillet, D., Rousse, A., and Malka, V. (2013). Observation of longitudinal and transverse self-injections in laser-plasma accelerators. *Nat Commun*, 4.

Couperus, J. P., Pausch, R., Köhler, A., Zarini, O., Krämer, J. M., Garten, M., Huebl, A., Gebhardt, R., Helbig, U., Bock, S., Zeil, K., Debus, A., Bussmann, M., Schramm, U., and Irman, A. (2017). Demonstration of a beam loaded nanocoulomb-class laser wakefield accelerator. *Nature Communications*, 8(1):487.

Courant, R., Friedrichs, K., and Lewy, H. (1967). On the partial difference equations of mathematical physics. *IBM Journal of Research and Development*, 11(2):215–234.

Cowan, B. M., Bruhwiler, D. L., Cary, J. R., Cormier-Michel, E., and Geddes, C. G. R. (2013). Generalized algorithm for control of numerical dispersion in explicit time-domain electromagnetic simulations. *Phys. Rev. ST Accel. Beams*, 16:041303.

Cros, B., Courtois, C., Matthieussent, G., Di Bernardo, A., Batani, D., Andreev, N., and Kuznetsov, S. (2002). Eigenmodes for capillary tubes with dielectric walls and ultraintense laser pulse guiding. *Phys. Rev. E*, 65:026405.

Cummings, P. and Thomas, A. G. R. (2011). A computational investigation of the impact of aberrated gaussian laser pulses on electron beam properties in laser-wakefield acceleration experiments. *Physics of Plasmas*, 18(5):053110.

Davidson, A., Tableman, A., An, W., Tsung, F. S., Lu, W., Vieira, J., Fonseca, R. A., Silva, L. O., and Mori, W. B. (2014). Implementation of a hybrid particle code with a PIC description in r-z and a gridless description in ϕ into OSIRIS. *ArXiv e-prints*.

Davidson, A. W. (2016). *Methods of Generating High-Quality Beams in Laser Wakefield Accelerators through Self-Injectio*. PhD thesis, UCLA.

Davoine, X., Lefebvre, E., Faure, J., Rechatin, C., Lifschitz, A., and Malka, V. (2008). Simulation of quasimonoenergetic electron beams produced by colliding pulse wakefield acceleration. *Physics of Plasmas*, 15(11):113102.

Davoine, X., Lefebvre, E., Rechatin, C., Faure, J., and Malka, V. (2009). Cold optical injection producing monoenergetic, multi-gev electron bunches. *Phys. Rev. Lett.*, 102:065001.

Dawson, J. M. (1959). Nonlinear electron oscillations in a cold plasma. *Phys. Rev.*, 113:383–387.

Dawson, J. M. (1983). Particle simulation of plasmas. *Rev. Mod. Phys.*, 55:403–447.

Derouillat, J. and Beck, A. (2020). Single domain multiple decompositions for particle-in-cell simulations. *Journal of Physics: Conference Series*, 1596:012052.

Derouillat, J., Beck, A., Pérez, F., Vinci, T., Chiaramello, M., Grassi, A., Flé, M., Bouchard, G., Plotnikov, I., Aunai, N., Dargent, J., Riconda, C., and Grech, M. (2018). Smilei : A collaborative, open-source, multi-purpose particle-in-cell code for plasma simulation. *Computer Physics Communications*, 222:351 – 373.

Desforges, F., Hansson, M., Ju, J., Senje, L., Audet, T., Dobosz-Dufrénoy, S., Persson, A., Lundh, O., Wahlström, C.-G., and Cros, B. (2014). Reproducibility of electron beams from laser wakefield acceleration in capillary tubes. *Nuclear Instruments and Methods in Physics Research Section A: Accelerators, Spectrometers, Detectors and Associated Equipment*, 740:54–59.

Esarey, E., Hubbard, R. F., Leemans, W. P., Ting, A., and Sprangle, P. (1997). Electron injection into plasma wakefields by colliding laser pulses. *Phys. Rev. Lett.*, 79:2682–2685.

Esarey, E. and Pilloff, M. (1995). Trapping and acceleration in nonlinear plasma waves. *Physics of Plasmas*, 2(5):1432–1436.

Esarey, E., Schroeder, C. B., and Leemans, W. P. (2009). Physics of laser-driven plasma-based electron accelerators. *Rev. Mod. Phys.*, 81:1229–1285.

Esarey, E., Shadwick, B. A., Schroeder, C. B., and Leemans, W. P. (2004). Nonlinear Pump Depletion and Electron Dephasing in Laser Wakefield Accelerators. In Yakimenko, V., editor, *American Institute of Physics Conference Series*, volume 737 of *American Institute of Physics Conference Series*, pages 578–584.

Esarey, E., Sprangle, P., Krall, J., and Ting, A. (1996). Overview of plasma-based accelerator concepts. *IEEE Transactions on Plasma Science*, 24(2):252–288.

Esarey, E., Ting, A., Sprangle, P., and Joyce, G. (1989). The laser wakefield accelerator. 12(4):191–204.

Esirkepov, T. (2001). Exact charge conservation scheme for particle-in-cell simulation with an arbitrary form-factor. *Computer Physics Communications*, 135(2):144 – 153.

Esirkepov, T., Bulanov, S. V., Yamagiwa, M., and Tajima, T. (2006). Electron, positron, and photon wakefield acceleration: Trapping, wake overtaking, and ponderomotive acceleration. *Phys. Rev. Lett.*, 96:014803.

Faure, J., Glinec, Y., Pukhov, A., Kiselev, S., Gordienko, S., Lefebvre, E., Rousseau, J. P., Burgy, F., and Malka, V. (2004a). A laser–plasma accelerator producing monoenergetic electron beams. *Nature*, 431(7008):541–544.

Faure, J., Glinec, Y., Pukhov, A., Kiselev, S., Gordienko, S., Lefebvre, E., Rousseau, J.-P., Burgy, F., and Malka, V. (2004b). A laser-plasma accelerator producing monoenergetic electron beams. *Nature*, 431(7008):541–544.

Faure, J., Rechatin, C., Lundh, O., Ammoura, L., and Malka, V. (2010). Injection and acceleration of quasimonoenergetic relativistic electron beams using density gradients at the edges of a plasma channel. *Physics of Plasmas (1994-present)*, 17(8):083107.

Faure, J., Rechatin, C., Norlin, A., Lifschitz, A., Glinec, Y., and Malka, V. (2006a). Controlled injection and acceleration of electrons in plasma wakefields by colliding laser pulses. *Nature (London)*, 444:737–739.

Faure, J., Rechatin, C., Norlin, A., Lifschitz, A., Glinec, Y., and Malka, V. (2006b). Controlled injection and acceleration of electrons in plasma wakefields by colliding laser pulses. *Nature*, 444(7120):737—739.

Ferrario, M. (2016). Injection, Extraction and Matching. In *CAS - CERN Accelerator School: Plasma Wake Acceleration*, pages 159–179, Geneva. CERN.

Ferri, J., Davoine, X., Fourmaux, S., Kieffer, J. C., Corde, S., Ta Phuoc, K., and Lifschitz, A. (2016). Effect of experimental laser imperfections on laser wakefield acceleration and betatron source. *Scientific Reports*, 6(1):27846.

Floettmann, K. (2003). Some basic features of the beam emittance. *Phys. Rev. ST Accel. Beams*, 6:034202.

Fourmaux, S., Corde, S., Phuoc, K. T., Lassonde, P., Lebrun, G., Payeur, S., Martin, F., Sebban, S., Malka, V., Rousse, A., and Kieffer, J. C. (2011). Single shot phase contrast imaging using laser-produced betatron x-ray beams. *Opt. Lett.*, 36(13):2426–2428.

Geddes, C. G. R., Nakamura, K., Plateau, G. R., Toth, C., Cormier-Michel, E., Esarey, E., Schroeder, C. B., Cary, J. R., and Leemans, W. P. (2008). Plasma-density-gradient injection of low absolute-momentum-spread electron bunches. *Phys. Rev. Lett.*, 100:215004.

Geddes, C. G. R., Toth, C., van Tilborg, J., Esarey, E., Schroeder, C. B., Bruhwiler, D., Nieter, C., Cary, J., and Leemans, W. P. (2004a). High-quality electron beams from a laser wakefield accelerator using plasma-channel guiding. *Nature*, 431(7008):538–541.

Geddes, C. G. R., Toth, C., van Tilborg, J., Esarey, E., Schroeder, C. B., Bruhwiler, D., Nieter, C., Cary, J., and Leemans, W. P. (2004b). High-quality electron beams from a laser wakefield accelerator using plasma-channel guiding. *Nature*, 431(7008):538–541.

Geddes, C. G. R., Tóth, C., van Tilborg, J., Esarey, E., Schroeder, C. B., Bruhwiler, D., Nieter, C., Cary, J., and Leemans, W. P. (2005). Production of high-quality electron bunches by dephasing and beam loading in channeled and unchanneled laser plasma accelerators. *Physics of Plasmas*, 12(5):056709.

Genoud, G., Bloom, M. S., Vieira, J., Burza, M., Najmudin, Z., Persson, A., Silva, L. O., Svensson, K., Wahlström, C.-G., and Mangles, S. P. D. (2013). Increasing energy coupling into plasma waves by tailoring the laser radial focal spot distribution in a laser wakefield accelerator. *Physics of Plasmas*, 20(6):064501.

Gibbon, P. (2005). *Short Pulse Laser Interactions with Matter: An Introduction.*

Gjonaj, E., Lau, T., and Weiland, T. (2006). Low-dispersion wake field calculation tools.

Glinec, Y., Faure, J., Lifschitz, A., Vieira, J. M., Fonseca, R. A., Silva, L. O., and Malka, V. (2008). Direct observation of betatron oscillations in a laser-plasma electron accelerator. *EPL (Europhysics Letters)*, 81(6):64001.

Glinec, Y., Faure, J., Malka, V., Fuchs, T., Szymanowski, H., and Oelfke, U. (2006). Radiotherapy with laser-plasma accelerators: Monte carlo simulation of dose deposited by an experimental quasimonoenergetic electron beam. *Medical Physics*, 33(1):155–162.

Godfrey, B. B. (1974). Numerical cherenkov instabilities in electromagnetic particle codes. *Journal of Computational Physics*, 15(4):504 – 521.

Goldstein, H., Poole, C., and Safko, J. (1980). Classical mechanics addison-wesley. *Reading, MA*, 426.

Golovin, G., Chen, S., Powers, N., Liu, C., Banerjee, S., Zhang, J., Zeng, M., Sheng, Z., and Umstadter, D. (2015). Tunable monoenergetic electron beams from independently controllable laser-wakefield acceleration and injection. *Phys. Rev. ST Accel. Beams*, 18:011301.

Gonsalves, A. J., Nakamura, K., Daniels, J., Benedetti, C., Pieronek, C., de Raadt, T. C. H., Steinke, S., Bin, J. H., Bulanov, S. S., van Tilborg, J., Geddes, C. G. R., Schroeder, C. B., Tóth, C., Esarey, E., Swanson, K., Fan-Chiang, L., Bagdasarov, G., Bobrova, N., Gasilov, V., Korn, G., Sasorov, P., and Leemans, W. P. (2019). Petawatt laser guiding and electron beam acceleration to 8 gev in a laser-heated capillary discharge waveguide. *Phys. Rev. Lett.*, 122:084801.

Gonsalves, A. J., Nakamura, K., Lin, C., Panasenko, D., Shiraishi, S., Sokollik, T., Benedetti, C., Schroeder, C. B., Geddes, C. G. R., van Tilborg, J., Osterhoff, J., Esarey, E., Toth, C., and Leemans, W. P. (2011). Tunable laser plasma accelerator based on longitudinal density tailoring. *Nat. Phys.*, 7:862–866.

Gorbunov, L. M. and Kirsanov, V. I. (1987). The excitation of plasma waves by an electromagnetic wave packet. *Zhurnal Eksperimentalnoi i Teoreticheskoi Fiziki*, 93:509–518.

Gordienko, S. and Pukhov, A. (2005). Scalings for ultrarelativistic laser plasmas and quasimonoenergetic electrons. *Physics of Plasmas*, 12(4):043109.

Guillaume, E., Döpp, A., Thaury, C., Lifschitz, A., Goddet, J.-P., Tafzi, A., Sylla, F., Iaquanello, G., Lefrou, T., Rousseau, P., Phuoc, K. T., and Malka, V. (2015a). Physics of fully-loaded laser-plasma accelerators. *Phys. Rev. ST Accel. Beams*, 18:061301.

Guillaume, E., Döpp, A., Thaury, C., Ta Phuoc, K., Lifschitz, A., Grittani, G., Goddet, J.-P., Tafzi, A., Chou, S. W., Veisz, L., and Malka, V. (2015b). Electron rephasing in a laser-wakefield accelerator. *Phys. Rev. Lett.*, 115:155002.

Hafizi, B., Ting, A., Sprangle, P., and Hubbard, R. F. (2000). Relativistic focusing and ponderomotive channeling of intense laser beams. *Phys. Rev. E*, 62:4120–4125.

Hansson, M., Aurand, B., Davoine, X., Ekerfelt, H., Svensson, K., Persson, A., Wahlström, C.-G., and Lundh, O. (2015). Down-ramp injection and independently controlled acceleration of electrons in a tailored laser wakefield accelerator. *Phys. Rev. ST Accel. Beams*, 18:071303.

Hansson, M., Aurand, B., Ekerfelt, H., Persson, A., and Lundh, O. (2016). Injection of electrons by colliding laser pulses in a laser wakefield accelerator. *Nuclear Instruments and Methods in Physics Research Section A: Accelerators, Spectrometers, Detectors and Associated Equipment*, 829:99 – 103. 2nd European Advanced Accelerator Concepts Workshop - EAAC 2015.

He, Z. H., Hou, B., Lebailly, V., Nees, J. A., Krushelnick, K., and Thomas, A. G. R. (2015). Coherent control of plasma dynamics. *Nature Communications*, 6(1):7156.

He, Z.-H., Hou, B., Nees, J. A., Easter, J. H., Faure, J., Krushelnick, K., and Thomas, A. G. R. (2013). High repetition-rate wakefield electron source generated by few-millijoule, 30 fs laser pulses on a density downramp. *New Journal of Physics*, 15(5):053016.

Hockney, R. and Eastwood, J. (1988). *Computer Simulation Using Particles.* Taylor & Francis.

Hückel, E. and Debye, P. (1923). The theory of electrolytes: I. lowering of freezing point and related phenomena. *Phys. Z*, 24(185-206):1.

Hughes, P. A. and Bregman, J. N., editors (2006). *Proceedings, Relativistic Jets: The Common Physics of AGN, Microquasars, and Gamma-Ray Bursts: Ann Arbor, Michigan, December 14-17, 2005*, volume 856.

Humphries, S. (1990). *Charged particle beams.* A Wiley-Interscience publication. Wiley.

Huygens, C. (1962). Treatise on light. *Dover.*

I. Haber, R. Lee, H. K. and Boris, J. (1973). Advances in electromagnetic plasma simulation techniques. *Proc. Sixth Conf. on Num. Sim. Plasmas, Berkeley, CA.*

Innocenti, M., Beck, A., Markidis, S., and Lapenta, G. (2016). Momentum conservation in multi-level multi-domain (mlmd) simulations. *Journal of Computational Physics*, 312:14 – 18.

Irman, A., Couperus, J. P., Debus, A., Köhler, A., Krämer, J. M., Pausch, R., Zarini, O., and Schramm, U. (2018). Improved performance of laser wakefield acceleration by tailored self-truncated ionization injection. *Plasma Physics and Controlled Fusion*, 60(4):044015.

Jackson, J. D. (1998). *Classical Electrodynamics Third Edition*. Wiley, third edition.

Jalas, S., Dornmair, I., Lehe, R., Vincenti, H., Vay, J.-L., Kirchen, M., and Maier, A. R. (2017). Accurate modeling of plasma acceleration with arbitrary order pseudo-spectral particle-in-cell methods. *Physics of Plasmas*, 24(3):033115.

Johnson, L. C. and Chu, T. K. (1974). Measurements of electron density evolution and beam self-focusing in a laser-produced plasma. *Phys. Rev. Lett.*, 32:517–520.

Kallala, H. (2020). *Massively parallel algorithms for realistic PIC simulations of ultra high intensity laser-plasma interaction, application to attosecond pulses separation of Doppler harmonics*. Theses, Université Paris-Saclay.

Kalmykov, S., Yi, S. A., Khudik, V., and Shvets, G. (2009). Electron self-injection and trapping into an evolving plasma bubble. *Phys. Rev. Lett.*, 103:135004.

Kalmykov, S. Y., Beck, A., Yi, S. A., Khudik, V. N., Downer, M. C., Lefebvre, E., Shadwick, B. A., and Umstadter, D. P. (2011). Electron self-injection into an evolving plasma bubble: Quasi-monoenergetic laser-plasma acceleration in the blowout regime. *Physics of Plasmas*, 18(5):056704.

Kaluza, M. C., Mangles, S. P. D., Thomas, A. G. R., Najmudin, Z., Dangor, A. E., Murphy, C. D., Collier, J. L., Divall, E. J., Foster, P. S., Hooker, C. J., Langley, A. J., Smith, J., and Krushelnick, K. (2010). Observation of a long-wavelength hosing modulation of a high-intensity laser pulse in underdense plasma. *Phys. Rev. Lett.*, 105:095003.

Karsch, S., Osterhoff, J., Popp, A., Rowlands-Rees, T. P., Major, Z., Fuchs, M., Marx, B., Hörlein, R., Schmid, K., Veisz, L., Becker, S., Schramm, U., Hidding, B., Pretzler, G., Habs, D., Grüner, F., Krausz, F., and Hooker, S. M. (2007). GeV-scale electron acceleration in a gas-filled capillary discharge waveguide. *New Journal of Physics*, 9(11):415–415.

Katsouleas, T. and Mori, W. B. (1988). Wave-breaking amplitude of relativistic oscillations in a thermal plasma. *Phys. Rev. Lett.*, 61:90–93.

Katsouleas, T., Wilks, S., Chen, P., Dawson, J. M., and Su, J. J. (1987). Beam loading in plasma accelerators. *Particle Accelerators*, 22:81–99.

Kim, H. T., Pae, K. H., Cha, H. J., Kim, I. J., Yu, T. J., Sung, J. H., Lee, S. K., Jeong, T. M., and Lee, J. (2013). Enhancement of electron energy to the multi-gev regime by a dual-stage laser-wakefield accelerator pumped by petawatt laser pulses. *Phys. Rev. Lett.*, 111:165002.

Kim, J. U., Hafz, N., and Suk, H. (2004). Electron trapping and acceleration across a parabolic plasma density profile. *Phys. Rev. E*, 69:026409.

Kirchen, M., Lehe, R., Jalas, S., Shapoval, O., Vay, J.-L., and Maier, A. R. (2020). Scalable spectral solver in galilean coordinates for eliminating the numerical cherenkov instability in particle-in-cell simulations of streaming plasmas. *Phys. Rev. E*, 102:013202.

Kneip, S., Nagel, S. R., Martins, S. F., Mangles, S. P. D., Bellei, C., Chekhlov, O., Clarke, R. J., Delerue, N., Divall, E. J., Doucas, G., Ertel, K., Fiuza, F., Fonseca, R., Foster, P., Hawkes, S. J., Hooker, C. J., Krushelnick, K., Mori, W. B., Palmer, C. A. J., Phuoc, K. T., Rajeev, P. P., Schreiber, J., Streeter, M. J. V., Urner, D., Vieira, J., Silva, L. O., and Najmudin, Z. (2009). Near-gev acceleration of electrons by a nonlinear plasma wave driven by a self-guided laser pulse. *Phys. Rev. Lett.*, 103:035002.

Kostyukov, I., Nerush, E., Pukhov, A., and Seredov, V. (2010). A multidimensional theory for electron trapping by a plasma wake generated in the bubble regime. *New Jour. Phys.*, 12:045009.

Kostyukov, I., Pukhov, A., and Kiselev, S. (2004). Phenomenological theory of laser-plasma interaction in “bubble” regime. *Physics of Plasmas*, 11(11):5256–5264.

Krall, N. A. and Trivelpiece, A. W. (1973). Principles of plasma physics. *American Journal of Physics*, 41(12):1380–1381.

Kruer, W. (2003). *The Physics of Laser Plasma Interactions.* Frontiers in physics. Westview Press.

Lapenta, G. (2015). Kinetic plasma simulation: Particle in cell method.

Lee, P. and Vay, J.-L. (2016). Efficiency of the perfectly matched layer with high-order finite difference and pseudo-spectral maxwell solvers. *AIP Conference Proceedings*, 1777(1):050002.

Leemans, W. P., Catravas, P., Esarey, E., Geddes, C. G. R., Toth, C., Trines, R., Schroeder, C. B., Shadwick, B. A., van Tilborg, J., and Faure, J. (2002). Electron-yield enhancement in a laser-wakefield accelerator driven by asymmetric laser pulses. *Phys. Rev. Lett.*, 89:174802.

Leemans, W. P., Gonsalves, A. J., Mao, H.-S., Nakamura, K., Benedetti, C., Schroeder, C. B., Tóth, C., Daniels, J., Mittelberger, D. E., Bulanov, S. S., Vay, J.-L., Geddes, C. G. R., and Esarey, E. (2014). Multi-gev electron beams from capillary-discharge-guided subpetawatt laser pulses in the self-trapping regime. *Phys. Rev. Lett.*, 113:245002.

Leemans, W. P., Nagler, B., Gonsalves, A. J., Toth, C., Nakamura, K., Geddes, C. G. R., Esarey, E., Schroeder, C. B., and Hooker, S. M. (2006). Gev electron beams from a centimetre-scale accelerator. *Nat. Phys.*, 2:696.

Lefebvre, E., Cochet, N., Fritzler, S., Malka, V., Aleonard, M.-M., Chemin, J.-F., Darbon, S., Disdier, L., Faure, J., Fedotoff, A., Landoas, O., Malka, G., Meot, V., Morel, P., Rabec Le Gloahec, M., Rouyer, A., Rubbelynck, C., Tikhonchuk, V., Wrobel, R., Audebert, P., and Rousseaux, C. (2003). Electron and photon production from relativistic laser–plasma interactions. *Nuclear Fusion*, 43(7):629.

Lehe, R., Kirchen, M., Andriyash, I. A., Godfrey, B. B., and Vay, J.-L. (2016). A spectral, quasi-cylindrical and dispersion-free particle-in-cell algorithm. *Computer Physics Communications*, 203:66 – 82.

Lehe, R., Lifschitz, A., Thaury, C., Malka, V., and Davoine, X. (2013a). Numerical growth of emittance in simulations of laser-wakefield acceleration. *Phys. Rev. ST Accel. Beams*, 16:021301.

Lehe, R., Lifschitz, A. F., Davoine, X., Thaury, C., and Malka, V. (2013b). Optical transverse injection in laser-plasma acceleration. *Phys. Rev. Lett.*, 111:085005.

Lifschitz, A. F., Davoine, X., Lefebvre, E., Faure, J., Rechatin, C., and Malka, V. (2009). Particle-in-cell modelling of laser-plasma interaction using fourier decomposition. *J. Comput. Phys.*, 228(5):1803–1814.

Liu, Q. (1997). The pstd algorithm: A time-domain method requiring only two cells per wavelength.

Lobet, M. (2015). *Radiative and quantum electrodynamics effects in extreme intensity laser-matter interaction.* Theses, Université de Bordeaux.

Lu, W., Huang, C., Zhou, M., Mori, W. B., and Katsouleas, T. (2006a). Nonlinear theory for relativistic plasma wakefields in the blowout regime. *Phys. Rev. Lett.*, 96:165002.

Lu, W., Huang, C., Zhou, M., Tzoufras, M., Tsung, F. S., Mori, W. B., and Katsouleas, T. (2006b). A nonlinear theory for multidimensional relativistic plasma wave wakefields. *Physics of Plasmas (1994-present)*, 13(5):056709.

Lu, W., Tzoufras, M., Joshi, C., Tsung, F. S., Mori, W. B., Vieira, J., Fonseca, R. A., and Silva, L. O. (2007a). Generating multi-gev electron bunches using single stage laser wakefield acceleration in a 3d nonlinear regime. *Phys. Rev. ST Accel. Beams*, 10:061301.

Lu, W., Tzoufras, M., Joshi, C., Tsung, F. S., Mori, W. B., Vieira, J., Fonseca, R. A., and Silva, L. O. (2007b). Generating multi-gev electron bunches using single stage laser wakefield acceleration in a 3d nonlinear regime. *Phys. Rev. ST Accel. Beams*, 10:061301.

Malka, V. (2013). Review of Laser Wakefield Accelerators. In *4th International Particle Accelerator Conference*, page MOYBB101.

Malka, V., Fritzler, S., Lefebvre, E., Aleonard, M.-M., Burgy, F., Chambaret, J.-P., Chemin, J.-F., Krushelnick, K., Malka, G., Mangles, S. P. D., Najmudin, Z., Pittman, M., Rousseau, J.-P., Scheurer, J.-N., Walton, B., and Dangor, A. E. (2002). Electron acceleration by a wake field forced by an intense ultrashort laser pulse. *Science*, 298(5598):1596–1600.

Malka, V., Fritzler, S., Lefebvre, E., Aleonard, M.-M., Burgy, F., Chambaret, J.-P., Chemin, J.-F., Krushelnick, K., Malka, G., Mangles, S. P. D., Najmudin, Z., Pittman, M., Rousseau, J.-P., Scheurer, J.-N., Walton, B., and Dangor, A. E. (2002). Electron acceleration by a wake field forced by an intense ultrashort laser pulse. *Science*, 298(5598):1596–1600.

Mangles, S. P. D., Genoud, G., Bloom, M. S., Burza, M., Najmudin, Z., Persson, A., Svensson, K., Thomas, A. G. R., and Wahlström, C.-G. (2012). Self-injection threshold in self-guided laser wakefield accelerators. *Phys. Rev. ST Accel. Beams*, 15:011302.

Mangles, S. P. D., Genoud, G., Kneip, S., Burza, M., Cassou, K., Cros, B., Dover, N. P., Kamperidis, C., Najmudin, Z., Persson, A., Schreiber, J., Wojda, F., and Wahlström, C.-G. (2009). Controlling the spectrum of x-rays generated in a laser-plasma accelerator by tailoring the laser wavefront. *Applied Physics Letters*, 95(18):181106.

Mangles, S. P. D., Murphy, C. D., Najmudin, Z., Thomas, A. G. R., Collier, J. L., Dangor, A. E., Divall, E. J., Foster, P. S., Gallacher, J. G., Hooker, C. J., Jaroszynski, D. A., Langley, A. J., Mori, W. B., Norreys, P. A., Tsung, F. S., Viskup, R., Walton, B. R., and Krushelnick, K. (2004a). Monoenergetic beams of relativistic electrons from intense laser–plasma interactions. *Nature*, 431(7008):535–538.

Mangles, S. P. D., Murphy, C. D., Najmudin, Z., Thomas, A. G. R., Collier, J. L., Dangor, A. E., Divall, E. J., Foster, P. S., Gallacher, J. G., Hooker, C. J., Jaroszynski, D. A., Langley, A. J., Mori, W. B., Norreys, P. A., Tsung, F. S., Viskup, R., Walton, B. R., and Krushelnick, K. (2004b). Monoenergetic beams of relativistic electrons from intense laser-plasma interactions. *Nature*, 431(7008):535–538.

Mangles, S. P. D., Thomas, A. G. R., Lundh, O., Lindau, F., Kaluza, M. C., Persson, A., Wahlström, C.-G., Krushelnick, K., and Najmudin, Z. (2007). On the stability of laser wakefield electron accelerators in the monoenergetic regime. *Physics of Plasmas*, 14(5):056702.

Marder, B. (1987). A method for incorporating gauss' law into electromagnetic pic codes. *Journal of Computational Physics*, 68(1):48 – 55.

Marder, B. (1993). Eliminating Boundary-Induced Errors in the Pseudo-Current Method. *Journal of Computational Physics*, 104(1):273–273.

Maslarova, D., Krus, M., Horny, V., and Psikal, J. (2019). Laser wakefield accelerator driven by the super-gaussian laser beam in the focus. *Plasma Physics and Controlled Fusion*, 62(2):024005.

McGuffey, C., Thomas, A. G. R., Schumaker, W., Matsuoka, T., Chvykov, V., Dollar, F. J., Kalintchenko, G., Yanovsky, V., Maksimchuk, A., Krushelnick, K., Bychenkov, V. Y., Glazyrin, I. V., and Karpeev, A. V. (2010). Ionization induced trapping in a laser wakefield accelerator. *Phys. Rev. Lett.*, 104:025004.

Mehrling, T., Grebenyuk, J., Tsung, F. S., Floettmann, K., and Osterhoff, J. (2012). Transverse emittance growth in staged laser-wakefield acceleration. *Phys. Rev. ST Accel. Beams*, 15:111303.

Michel, P., Esarey, E., Schroeder, C. B., Shadwick, B. A., and Leemans, W. P. (2006a). Efficient electron injection into plasma waves using higher-order laser modes. *Physics of Plasmas*, 13(11):113112.

Michel, P., Schroeder, C. B., Shadwick, B. A., Esarey, E., and Leemans, W. P. (2006b). Radiative damping and electron beam dynamics in plasma-based accelerators. *Phys. Rev. E*, 74:026501.

Mirzaie, M., Li, S., Zeng, M., Hafz, N. A. M., Chen, M., Li, G. Y., Zhu, Q. J., Liao, H., Sokollik, T., Liu, F., Ma, Y. Y., Chen, L. M., Sheng, Z. M., and Zhang, J. (2015). Demonstration of self-truncated ionization injection for gev electron beams. *Scientific Reports*, 5(1):14659.

Modena, A., Najmudin, Z., Dangor, A. E., Clayton, C. E., Marsh, K. A., Joshi, C., Malka, V., Darrow, C. B., Danson, C., Neely, D., and Walsh, F. N. (1995a). Electron acceleration from the breaking of relativistic plasma waves. *Nature*, 377(6550):606–608.

Modena, A., Najmudin, Z., Dangor, A. E., Clayton, C. E., Marsh, K. A., Joshi, C., Malka, V., Darrow, C. B., Danson, C., Neely, D., and Walsh, F. N. (1995b). Electron acceleration from the breaking of relativistic plasma waves. *Nature*, 377(6550):606 – 608.

Mora, P. and Antonsen, T. M. (1996). Electron cavitation and acceleration in the wake of an ultraintense, self-focused laser pulse. *Phys. Rev. E*, 53:R2068–R2071.

Mora, P. and Antonsen, Jr., T. M. (1997). Kinetic modeling of intense, short laser pulses propagating in tenuous plasmas. *Physics of Plasmas*, 4(1):217–229.

Mori, M., Kondo, K., Mizuta, Y., Kando, M., Kotaki, H., Nishiuchi, M., Kado, M., Pirozhkov, A. S., Ogura, K., Sugiyama, H., Bulanov, S. V., Tanaka, K. A., Nishimura, H., and Daido, H. (2009). Generation of stable and low-divergence 10-mev quasimonoenergetic electron bunch using argon gas jet. *Phys. Rev. ST Accel. Beams*, 12:082801.

Mori, W. B., Decker, C. D., and Leemans, W. P. (1993). Relativistic harmonic content of nonlinear electromagnetic waves in underdense plasmas. *IEEE Transactions on Plasma Science*, 21(1):110–119.

Morse, R. L. and Nielson, C. W. (1971). Numerical simulation of the weibel instability in one and two dimensions. *The Physics of Fluids*, 14(4):830–840.

Nakajima, K. (2008). Compact x-ray sources: Towards a table-top free-electron laser. *Nat. Phys.*, 4:92 – 93.

Nakanii, N., Hosokai, T., Iwasa, K., Pathak, N. C., Masuda, S., Zhidkov, A. G., Nakahara, H., Takeguchi, N., Mizuta, Y., Otsuka, T. P., Sueda, K., Nakamura, H., and Kodama, R. (2016). Effect of halo on the stability of electron bunches in laser wakefield acceleration. *EPL (Europhysics Letters)*, 113(3):34002.

Nuter, R., Grech, M., Gonzalez de Alaiza Martinez, P., Bonnaud, G., and d'Humières, E. (2014). Maxwell solvers for the simulations of the laser-matter interaction. *The European Physical Journal D*, 68(6):177.

Osterhoff, J., Popp, A., Major, Z., Marx, B., Rowlands-Rees, T. P., Fuchs, M., Geissler, M., Hörlein, R., Hidding, B., Becker, S., Peralta, E. A., Schramm, U., Grüner, F., Habs, D., Krausz, F., Hooker, S. M., and Karsch, S. (2008). Generation of stable, low-divergence electron beams by laser-wakefield acceleration in a steady-state-flow gas cell. *Phys. Rev. Lett.*, 101:085002.

P., M. (2013). Introduction aux plasmas créés par laser.

Pak, A., Marsh, K. A., Martins, S. F., Lu, W., Mori, W. B., and Joshi, C. (2010). Injection and trapping of tunnel-ionized electrons into laser-produced wakes. *Phys. Rev. Lett.*, 104:025003.

Plateau, G. R., Geddes, C. G. R., Thorn, D. B., Chen, M., Benedetti, C., Esarey, E., Gonsalves, A. J., Matlis, N. H., Nakamura, K., Schroeder, C. B., Shiraishi, S., Sokollik, T., van Tilborg, J., Toth, C., Trotsenko, S., Kim, T. S., Battaglia, M., Stöhlker, T., and Leemans, W. P. (2012). Low-emittance electron bunches from a laser-plasma accelerator measured using single-shot x-ray spectroscopy. *Phys. Rev. Lett.*, 109:064802.

Pollock, B. B., Clayton, C. E., Ralph, J. E., Albert, F., Davidson, A., Divol, L., Filip, C., Glenzer, S. H., Herpoldt, K., Lu, W., Marsh, K. A., Meinecke, J., Mori, W. B., Pak, A., Rensink, T. C., Ross, J. S., Shaw, J., Tynan, G. R., Joshi, C., and Froula, D. H. (2011). Demonstration of a narrow energy spread, ~ 0.5 gev electron beam from a two-stage laser wakefield accelerator. *Phys. Rev. Lett.*, 107:045001.

Pukhov, A. (1999). Three-dimensional electromagnetic relativistic particle-in-cell code vlpl (virtual laser plasma lab). *Journal of Plasma Physics*, 61(03):425–433.

Pukhov, A. (2020). X-dispersionless maxwell solver for plasma-based particle acceleration. *Journal of Computational Physics*, 418:109622.

Pukhov, A. and Meyer-ter Vehn, J. (2002). Laser wake field acceleration: the highly non-linear broken-wave regime. *Applied Physics B*, 74(4-5):355–361.

Pukhov, A., Sheng, Z.-M., and Meyer-ter Vehn, J. (1999). Particle acceleration in relativistic laser channels. *Physics of Plasmas*, 6(7):2847–2854.

Qiang, J., Ryne, R. D., Habib, S., and Decyk, V. (2000). An object-oriented parallel particle-in-cell code for beam dynamics simulation in linear accelerators. *Journal of Computational Physics*, 163(2):434 – 451.

Rax, J. M. (2005). *Physique des plasmas: Cours et applications.* Dunod.

Rechatin, C., Davoine, X., Lifschitz, A., Ismail, A. B., Lim, J., Lefebvre, E., Faure, J., and Malka, V. (2009a). Observation of beam loading in a laser-plasma accelerator. *Phys. Rev. Lett.*, 103:194804.

Rechatin, C., Faure, J., Ben-Ismail, A., Lim, J., Fitour, R., Specka, A., Videau, H., Tafzi, A., Burgy, F., and Malka, V. (2009b). Controlling the phase-space volume of injected electrons in a laser-plasma accelerator. *Phys. Rev. Lett.*, 102:164801.

Reiser, M. (2008). *Theory and Design of Charged Particle Beams.* Wiley Series in Beam Physics and Accelerator Technology. Wiley.

Rosenzweig, J. B., Breizman, B., Katsouleas, T., and Su, J. J. (1991a). Acceleration and focusing of electrons in two-dimensional nonlinear plasma wake fields. *Phys. Rev. A*, 44:R6189–R6192.

Rosenzweig, J. B., Breizman, B., Katsouleas, T., and Su, J. J. (1991b). Acceleration and focusing of electrons in two-dimensional nonlinear plasma wake fields. *Phys. Rev. A*, 44:R6189–R6192.

Rosenzweig, J. B., Cline, D. B., Cole, B., Figueroa, H., Gai, W., Konecny, R., Norem, J., Schoessow, P., and Simpson, J. (1988). Experimental observation of plasma wake-field acceleration. *Phys. Rev. Lett.*, 61:98–101.

Schlenvoigt, H.-P., Haupt, K., Debus, A., Budde, F., Jackel, O., Pfotenhauer, S., Schwoerer, H., Rohwer, E., Gallacher, J. G., Brunetti, E., Shanks, R. P., Wiggins, S. M., and Jaroszynski, D. A. (2008). A compact synchrotron radiation source driven by a laser-plasma wakefield accelerator. *Nat Phys*, 4:130–133.

Schmid, K., Buck, A., Sears, C. M. S., Mikhailova, J. M., Tautz, R., Herrmann, D., Geissler, M., Krausz, F., and Veisz, L. (2010). Density-transition based electron injector for laser driven wakefield accelerators. *Phys. Rev. ST Accel. Beams*, 13:091301.

Schreiber, J., Bellei, C., Mangles, S. P. D., Kamperidis, C., Kneip, S., Nagel, S. R., Palmer, C. A. J., Rajeev, P. P., Streeter, M. J. V., and Najmudin, Z. (2010). Complete temporal characterization of asymmetric pulse compression in a laser wakefield. *Phys. Rev. Lett.*, 105:235003.

Schroeder, C. B., Esarey, E., Geddes, C. G. R., Benedetti, C., and Leemans, W. P. (2010). Physics considerations for laser-plasma linear colliders. *Phys. Rev. ST Accel. Beams*, 13:101301.

Schroeder, C. B., Esarey, E., Shadwick, B. A., and Leemans, W. P. (2006). Trapping, dark current, and wave breaking in nonlinear plasma waves. *Physics of Plasmas*, 13(3):033103.

Shadwick, B. A., Schroeder, C. B., and Esarey, E. (2009). Nonlinear laser energy depletion in laser-plasma accelerators. *Physics of Plasmas*, 16(5):056704.

Shaw, J. L., Lemos, N., Amorim, L. D., Vafaei-Najafabadi, N., Marsh, K. A., Tsung, F. S., Mori, W. B., and Joshi, C. (2017). Role of direct laser acceleration of electrons in a laser wakefield accelerator with ionization injection. *Phys. Rev. Lett.*, 118:064801.

Siegman, A. E. (1986). *Lasers*. University Science Books.

Singh, K. P. and Sajal, V. (2009). Quasimonoenergic collimated electrons from the ionization of nitrogen by a chirped intense laser pulse. *Physics of Plasmas*, 16(4):043113.

Sirois, F. and Grilli, F. (2015). Potential and limits of numerical modelling for supporting the development of HTS devices. *Superconductor Science and Technology*, 28(4):043002.

Sprangle, P., Esarey, E., Krall, J., and Joyce, G. (1992). Propagation and guiding of intense laser pulses in plasmas. *Phys. Rev. Lett.*, 69:2200–2203.

Sprangle, P., Esarey, E., and Ting, A. (1990). Nonlinear theory of intense laser-plasma interactions. *Phys. Rev. Lett.*, 64:2011–2014.

Sprangle, P., Esarey, E., Ting, A., and Joyce, G. (1988). Laser wakefield acceleration and relativistic optical guiding. *Applied Physics Letters*, 53(22):2146–2148.

Sprangle, P., Hafizi, B., Peñano, J. R., Hubbard, R. F., Ting, A., Moore, C. I., Gordon, D. F., Zigler, A., Kaganovich, D., and Antonsen, T. M. (2001). Wakefield generation and gev acceleration in tapered plasma channels. *Phys. Rev. E*, 63:056405.

Sprangle, P., Tang, C., and Esarey, E. (1987). Relativistic self-focusing of short-pulse radiation beams in plasmas. *IEEE Transactions on Plasma Science*, 15(2):145–153.

Startsev, E. A. and McKinstrie, C. J. (1997). Multiple scale derivation of the relativistic ponderomotive force. *Phys. Rev. E*, 55:7527–7535.

Steinhauer, L. C. and Ahlstrom, H. G. (1971). Propagation of coherent radiation in a cylindrical plasma column. *Physics of Fluids (1958-1988)*, 14(6):1109–1114.

Strickland, D. and Mourou, G. (1985). Compression of amplified chirped optical pulses. *Optics Communications*, 55(6):447 – 449.

Sun, G., Ott, E., Lee, Y. C., and Guzdar, P. (1987). Self-focusing of short intense pulses in plasmas. *The Physics of Fluids*, 30(2):526–532.

Swanson, K. K., Tsai, H.-E., Barber, S. K., Lehe, R., Mao, H.-S., Steinke, S., van Tilborg, J., Nakamura, K., Geddes, C. G. R., Schroeder, C. B., Esarey, E., and Leemans, W. P. (2017). Control of tunable, monoenergetic laser-plasma-accelerated electron beams using a shock-induced density downramp injector. *Phys. Rev. Accel. Beams*, 20:051301.

TAJIMA, T. (2010). Laser acceleration and its future. *Proceedings of the Japan Academy, Series B*, 86(3):147–157.

Tajima, T. and Dawson, J. M. (1979). Laser electron accelerator. *Phys. Rev. Lett.*, 43:267–270.

Teychenné, D., Bonnaud, G., and Bobin, J. (1994). Oscillatory relativistic motion of a particle in a power-law or sinusoidal-shaped potential well. *Physical review. E, Statistical physics, plasmas, fluids, and related interdisciplinary topics*, 49(4):3253—3263.

Thaury, C., Guillaume, E., Lifschitz, A., Ta Phuoc, K., Hansson, M., Grittani, G., Gautier, J., Goddet, J.-P., Tafzi, A., Lundh, O., and Malka, V. (2015). Shock assisted ionization injection in laser-plasma accelerators. *Scientific Reports*, 5:16310.

Thaury, C. and Quéré, F. (2010). High-order harmonic and attosecond pulse generation on plasma mirrors: basic mechanisms. *Journal of Physics B: Atomic, Molecular and Optical Physics*, 43(21):213001.

Ting, A., Esarey, E., and Sprangle, P. (1990). Nonlinear wake-field generation and relativistic focusing of intense laser pulses in plasmas. *Physics of Fluids B: Plasma Physics*, 2(6):1390–1394.

Tonks, L. and Langmuir, I. (1929). Oscillations in ionized gases. *Phys. Rev.*, 33:195–210.

Tzoufras, M., Lu, W., Tsung, F. S., Huang, C., Mori, W. B., Katsouleas, T., Vieira, J., Fonseca, R. A., and Silva, L. O. (2008). Beam loading in the nonlinear regime of plasma-based acceleration. *Phys. Rev. Lett.*, 101:145002.

Umstadter, D., Chen, S.-Y., Maksimchuk, A., Mourou, G., and Wagner, R. (1996a). Nonlinear optics in relativistic plasmas and laser wake field acceleration of electrons. *Science*, 273(5274):472–475.

Umstadter, D., Kim, J. K., and Dodd, E. (1996b). Laser injection of ultrashort electron pulses into wakefield plasma waves. *Phys. Rev. Lett.*, 76:2073–2076.

Vay, J.-L. (2007). Noninvariance of space- and time-scale ranges under a lorentz transformation and the implications for the study of relativistic interactions. *Phys. Rev. Lett.*, 98:130405.

Vay, J.-L. (2008a). Simulation of beams or plasmas crossing at relativistic velocity. *Physics of Plasmas (1994-present)*, 15(5):056701.

Vay, J.-L. (2008b). Simulation of beams or plasmas crossing at relativistic velocity. *Physics of Plasmas*, 15(5):056701.

Vay, J.-L., Geddes, C., Cormier-Michel, E., and Grote, D. (2011). Numerical methods for instability mitigation in the modeling of laser wakefield accelerators in a lorentz-boosted frame. *Journal of Computational Physics*, 230(15):5908 – 5929.

Vay, J.-L. and Godfrey, B. B. (2014). Modeling of relativistic plasmas with the particle-in-cell method. *Comptes Rendus Mécanique*, 342(10):610 – 618. Theoretical and numerical approaches for Vlasov-maxwell equations.

Vay, J.-L., Haber, I., and Godfrey, B. B. (2013). A domain decomposition method for pseudo-spectral electromagnetic simulations of plasmas. *Journal of Computational Physics*, 243:260 – 268.

Vieira, J., Martins, S. F., Fiúza, F., Huang, C. K., Mori, W. B., Mangles, S. P. D., Kneip, S., Nagel, S., Najmudin, Z., and Silva, L. O. (2012). Influence of realistic parameters on state-of-the-art laser wakefield accelerator experiments. *Plasma Physics and Controlled Fusion*, 54(5):055010.

Villasenor, J. and Buneman, O. (1992). Rigorous charge conservation for local electromagnetic field solvers. *Computer Physics Communications*, 69(2-3):306–316.

Vincenti, H., Lobet, M., Lehe, R., Sasanka, R., and Vay, J.-L. (2017). An efficient and portable simd algorithm for charge/current deposition in particle-in-cell codes. *Comput. Phys. Commun.*, 210:145–154.

Vincenti, H. and Vay, J.-L. (2016). Detailed analysis of the effects of stencil spatial variations with arbitrary high-order finite-difference maxwell solver. *Computer Physics Communications*, 200:147 – 167.

Walker, P. A., Bourgeois, N., Rittershofer, W., Cowley, J., Kajumba, N., Maier, A. R., Wenz, J., Werle, C. M., Karsch, S., Grüner, F., Symes, D. R., Rajeev, P. P., Hawkes, S. J., Chekhlov, O., Hooker, C. J., Parry, B., Tang, Y., and Hooker, S. M. (2013). Investigation of GeV-scale electron acceleration in a gas-filled capillary discharge waveguide. *New Journal of Physics*, 15(4):045024.

Wang, W. T., Li, W. T., Liu, J. S., Zhang, Z. J., Qi, R., Yu, C. H., Liu, J. Q., Fang, M., Qin, Z. Y., Wang, C., Xu, Y., Wu, F. X., Leng, Y. X., Li, R. X., and Xu, Z. Z. (2016). High-brightness high-energy electron beams from a laser wakefield accelerator via energy chirp control. *Phys. Rev. Lett.*, 117:124801.

Wang, X., Zgadzaj, R., Fazel, N., Li, Z., Yi, S. A., Zhang, X., Henderson, W., Chang, Y.-Y., Korzekwa, R., Tsai, H.-E., Pai, C.-H., Quevedo, H., Dyer, G., Gaul, E., Martinez, M., Bernstein, A. C., Borger, T., Spinks, M., Donovan, M., Khudik, V., Shvets, G., Ditmire, T., and Downer, M. C. (2013). Quasi-monoenergetic laser-plasma acceleration of electrons to 2 gev. *Nat Commun*, 4. 1988.

Welford, W. T. (1975). Principles of optics (5th Edition). M. Born, E. Wolf Pergamon Press, Oxford, 1975, pp xxviii + 808, £9.50. *Optics Laser Technology*, 7(4):190–191.

Whittum, D. H. (1997). Transverse two-stream instability of a beam with a bennett profile. *Physics of Plasmas*, 4(4):1154–1159.

Wiggins, S., Issac, R., Welsh, G., Brunetti, E., Shanks, R., Anania, M., Cipiccia, S., Manahan, G., Aniculaesei, C., Ersfeld, B., Islam, M., Burgess, R., Vieux, G., Gillespie, W., MacLeod, A., van der Geer, S., de Loos, M., and Jaroszynski, D. (2010). High quality electron beams from a laser wakefield accelerator. *Plasma Physics and Controlled Fusion*, 52(12):–.

Xie, B.-S., Wu, H.-C., Wang, H., Wang, N.-Y., and Yu, M. Y. (2007). Analysis of the electromagnetic fields and electron acceleration in the bubble regime of the laser-plasma interaction. *Physics of Plasmas*, 14(7):073103.

Yee, K. (1966). Numerical solution of initial boundary value problems involving maxwell's equations in isotropic media. *Antennas and Propagation, IEEE Transactions on*, 14(3):302 –307.

Zemzemi, I., Massimo, F., and Beck, A. (2020). Azimuthal decomposition study of a realistic laser profile for efficient modeling of laser WakeField acceleration. *Journal of Physics: Conference Series*, 1596:012054.

Résumé

Le sujet de ma thèse porte sur le développement et l'exploitation d'un modèle réduit pour les codes de simulation cinétiques du type Particle-In-Cell (PIC). Cette approche implémentée dans le code libre Smilei, exploite la symétrie azimutale du problème pour en réduire la dimensionnalité et donc permettre un gain important en temps de calcul. Dans le cadre de ma thèse, j'ai mis le code en oeuvre pour réaliser des simulations numériques d'accélération d'électrons par sillage laser dans des plasmas sous denses.

L'accélération laser-plasma est un domaine de recherche visant à développer les accélérateurs de particules de demain. Le plasma est un état de la matière, dans lequel les atomes sont partiellement ou totalement ionisés. Ces particules ionisées répondent de manière collective à l'influence des champs électromagnétiques qu'ils soient externes ou générés par le plasma lui-même. Depuis près d'un siècle, la physique des plasmas est devenue un domaine de recherche très actif, tant d'un point de vue fondamental qu'applicatif. Parallèlement à l'essor de la physique des plasmas, les technologies laser ont, elles aussi, connu un progrès très important. L'utilisation de la technique de CPA (Chirped Pulse Amplification), dont la mise au point a été récompensée par le prix Nobel de physique de 2018, a permis d'augmenter considérablement la puissance des lasers à plusieurs PetaWatts (10^{15} W) tout en réduisant leurs durées à quelques dizaines de femtosecondes (10^{-15} s). Focalisés sur la matière, ces lasers ionisent complètement les milieux avec lesquels ils interagissent, donnant lieu à des plasmas, dans lesquels une large panoplie de phénomènes complexes peut avoir lieu. La physique UHI (Ultra-High-Intensity) est la branche de la physique qui s'intéresse à la compréhension de tels phénomènes. Un des volets les plus importants en physique UHI est l'étude des mécanismes d'accélération de particules par laser dans les plasmas sous denses. Proposée en 1979 par Tajima & Dawson, l'accélération par sillage laser peut avoir lieu lorsqu'on envoie une impulsion laser ultra courte et ultra intense dans un plasma obtenu par ionisation d'un gaz dilué. Le laser va se propager dans le plasma ainsi créé, et générer dans son sillage une onde de Langmuir. Cette onde constitue une structure accélératrice pour les électrons qui y sont injectés. Les champs accélérateurs dans cette structure peuvent atteindre 100 GeV/m, ce qui dépasse de plusieurs ordres de grandeur, l'amplitude des champs d'accélération obtenus dans les accélérateurs conventionnels.

Le développement de cette physique et l'amélioration de la qualité des faisceaux d'électrons reposent énormément sur l'exploitation des outils de simulation numérique. La méthode PIC est une approche cinétique très puissante pour modéliser des plasmas hors équilibre. Elle est notamment très utilisée pour modéliser des expériences d'interaction laser-plasma. Une description précise des phénomènes en jeu nécessite cependant de réaliser des simulations premier-principe en géométrie 3D. Ces simulations sont néanmoins très coûteuses à cause des volumes de données massives qui sont en jeu et qui peuvent atteindre plusieurs dizaines de terabytes et nécessiter plusieurs millions d'heures de calcul.

L'optimisation du temps de calcul de ces simulations est donc une problématique très critique dans les codes PIC. À cet égard, on peut exploiter la symétrie azimutale des données physiques dans le cadre des simulations d'accélération par sillage laser, pour développer un formalisme numérique réduit. Dans ce formalisme, les données de simulation sont projetées dans une base réduite composée des modes de Fourier fondamentaux associés à la variable angulaire azimutale en coordonnées cylindriques. Ainsi on peut obtenir une description 3D avec un coût de simulation comparable avec celui de 2D.

J'ai implémenté ce modèle réduit dans le code open source, massivement parallèle, SMILEI développé par la communauté UHI du plateau de Saclay. Dans cette implémentation, les équations de Maxwell sont résolues à chaque pas de temps par un schéma de différences finies. Cette approche est massivement parallélisable mais peut induire des instabilités numériques qui peuvent dégrader les résultats de la simulation. Pour pallier ces limites, j'ai également implémenté un solveur de Maxwell pseudo-spectral qui offre une précision inégalée. Cette implémentation a été réalisée dans PICSAR dans le cadre d'une collaboration avec Lawrence Berkeley National Laboratory (LBNL). PICSAR est une librairie PIC open source de routines de calcul optimisées, pensée à rendre exploitable par d'autres codes PIC.

Pendant la deuxième partie de ma thèse, j'ai exploité ce travail pour épauler numériquement les physiciens exploitant le laser Apollon pour réaliser des expériences d'accélération d'électrons. J'ai utilisé les mesures du profil laser réalisés par des collaborateurs pour faire des simulations réalistes tenant compte des défauts du laser en 3D. Ceci afin de mieux rendre compte des effets physiques induits par les défauts présents dans le profil du laser et donner une prévision la plus fidèle possible et la plus proche des résultats qui pourront être obtenus pendant les expériences. Cette analyse a montré qu'inclure les défauts du laser mènent à des différences dans les résultats obtenus et que ces derniers dégradent la performance des accélérateurs laser-plasma notamment en termes de quantité de charge injectée. Ensuite, j'ai développé des algorithmes de reconstitution de profils compatibles avec la méthode azimutale et j'ai étudié sa capacité à modéliser correctement les processus physiques présents en déterminant le nombre de modes nécessaires et en comparant ses résultats avec ceux issus des simulations 3D en géométrie Cartésienne. Cette étude a montré l'importance d'inclure des modes supérieurs pour avoir une modélisation fidèle et précise.

Ces simulations, instructives pour les futures expériences d'accélération d'électrons par le laser Apollon, mettent en avant la nécessité d'inclure les mesures expérimentales dans la simulation pour aboutir à des résultats précis d'une part, et la possibilité d'utiliser la géométrie quasi-cylindrique avec un nombre de modes suffisant pour ce type d'étude d'autre part.

Mots-clés: accélération laser-plasma, simulations Particle-In-Cell, modèle réduit, lasers réalistes

ECOLE DOCTORALE

Titre : Calcul haute-performance et simulation numérique pour l'accélération d'électrons par sillage laser avec des profils laser réalistes

Mots clés : accélération laser-plasma, simulations Particle-In-Cell, modèle réduit, lasers réalistes

Résumé : Le développement des lasers ultra-courts à de hautes intensités a permis l'émergence de nouveaux domaines de recherche en relation avec l'interaction laser-plasma. En particulier, les lasers petawatt femtoseconde ont ouvert la voie vers la possibilité de concevoir une nouvelle génération d'accélérateurs de particules. La modélisation numérique a largement contribué à l'essor de ce domaine d'accélération des électrons par sillage laser. Dans ce contexte, les codes Particle-In-Cell sont les plus répandus dans la communauté. Ils permettent une description fiable de l'interaction laser plasma et surtout de l'accélération par sillage laser. Cependant, une modélisation précise de la physique en jeu nécessite de recourir à des simulations 3D particulièrement coûteuses. Une manière pour accélérer efficacement ce type de simulations est l'utilisation de modèles réduits qui, tout en assurant un gain en temps de calcul très important, garantissent une modélisation fiable du problème. Parmi ces modèles, la décomposition des champs en modes de Fourier dans la direction azimutale est particulièrement adaptée à l'accélération laser plasma. Dans le cadre de ma thèse, j'ai implémenté ce modèle dans le code open-source SMILEI, dans un premier temps, avec un schéma différences finies (FDTD) pour discrétiser les équations de Maxwell. Néanmoins, ce type de solveur peut induire un effet de Cherenkov numérique qui corrompt les résultats de la simulation. Pour mitiger cet artéfact, j'ai également implémenté une version pseudo-spectrale du solveur de Maxwell qui présente de nombreux avantages en termes de précision numérique. Cette méthode est ensuite mise en oeuvre pour étudier l'impact de profils de lasers réalistes sur la qualité du faisceau d'électrons en exploitant des mesures réalisées sur le laser Apollon. Sa capacité à modéliser correctement les processus physiques présents est analysée en déterminant le nombre de modes nécessaires et en comparant les résultats avec ceux issus des simulations 3D en géométrie Cartésienne. Cette étude montre qu'inclure les défauts du laser mène à des différences dans les résultats et que ces derniers dégradent la performance des accélérateurs-laser plasma notamment en termes de quantité de charge injectée. Ces simulations, instructives pour les futures expériences d'accélération d'électrons par le laser Apollon, mettent en avant la nécessité d'inclure les mesures expérimentales dans la simulation et particulièrement celle du front de phase, pour aboutir à des résultats précis.

Title : High performance computing and numerical simulation for laser wakefield acceleration with realistic laser profiles

Keywords : laser-wakefield acceleration, Particle-In-Cell simulations, reduced models, realistic lasers

Abstract : The advent of ultra-short high-intensity lasers has paved the way to new and promising, yet challenging, areas of research in laser-plasma interaction physics. The success of building petawatt femtosecond lasers offers a promising path for designing future particle accelerators and light sources. Achieving this goal intrinsically relies on the combination of experiments and numerical modeling. So far, Particle-In-Cell (PIC) codes have been the ultimate tool to accurately describe the laser-plasma interaction especially in the field of Laser WakeField Acceleration (LWFA). Nevertheless, the numerical modeling of laser-plasma accelerators in 3D can be a very challenging task due to their high computational cost. A useful approach to speed up such simulations consists of employing reduced numerical modes which simplify the problem while retaining a high fidelity. Among these models, Fourier field decomposition in azimuthal modes for the cylindrical geometry is particularly well suited for physical problems with close to cylindrical symmetry, which is the case in LWFA. During my Ph.D., I first implemented this method in the open-source code SMILEI in the Finite Difference Time Domain (FDTD) discretization scheme for the Maxwell solver. However, this kind of solvers may suffer from numerical Cherenkov radiation (NCR). To mitigate this artifact, I also implemented Maxwell's solver in the Pseudo Spectral Analytical Domain (PSATD) scheme which offers better accuracy of the results. This method is then employed to study the impact of realistic laser profiles from the Apollon facility on the quality of the accelerated electron beam. Its ability to correctly model the involved physical processes is investigated by determining the optimal number of modes and benchmarking its results with full 3D Cartesian simulations. It is shown that the imperfections in the laser pulse lead to differences in the results compared to theoretical profiles. They degrade the performance of laser-plasma accelerators especially in terms of the quantity of injected charge. These simulations, insightful for the future experiments of LWFA that will be held soon with the Apollon laser, put forward the importance of including realistic lasers in the simulation to obtain reliable results.

Institut Polytechnique de Paris
91120 Palaiseau, France